2015

PHYSICS-BASED MODELING AND CONTROL OF POWERTRAIN SYSTEMS INTEGRATED WITH LOW TEMPERATURE COMBUSTION ENGINES

Mehran Bidarvatan
Michigan Technological University, mbidarva@mtu.edu

PHYSICS-BASED MODELING AND CONTROL OF POWERTRAIN SYSTEMS INTEGRATED WITH LOW TEMPERATURE COMBUSTION ENGINES

By

Mehran Bidarvatan

A DISSERTATION

Submitted in partial fulfillment of the requirements for the degree of

DOCTOR OF PHILOSOPHY

In Mechanical Engineering-Engineering Mechanics

MICHIGAN TECHNOLOGICAL UNIVERSITY

2015

This dissertation has been approved in partial fulfillment of the requirements for the Degree of DOCTOR OF PHILOSOPHY in Mechanical Engineering-Engineering Mechanics.

Department of Mechanical Engineering-Engineering Mechanics

Dissertation Advisor: *Dr. Mahdi Shahbakhti*

Committee Member: *Dr. Jeffrey D. Naber*

Committee Member: *Dr. Rush D. Robinett III*

Committee Member: *Dr. John E. Beard*

Committee Member: *Dr. Jeffrey B. Burl*

Department Chair: *Dr. William W. Predebon*

Dedication

To many years' efforts of my father, Dr. Atapour Bidarvatan on number theory.

Contents

List of Figures

List of Tables

Preface

Results in the chapters are partially based on 8 papers. The granted permissions form the publishers of the papers are found in Appendix E. The contribution of the author of this dissertation as well as the contributions of the co-authors for each of the papers are as follows:

- Contribution for Chapter 2([1]): Modeling, experimental validation of the model, control design, and evaluation of the controller in simulation were done by the author, M. Bidarvatan. C.R. Koch provided the experimental data and technical comments, and edited the manuscript. M. Shahbakhti analyzed the experimental data, provided technical comments and edited the manuscript. S.A. Jazayeri provided technical comments and edited the manuscript.

- Contribution for Chapter 3([2]): Modeling, a partial analysis of the experimental data, experimental validation of the model, control design, evaluation of the controller in simulation, and writing the paper were done by the author, M. Bidarvatan. M. Shahbakhti analyzed the experimental data, provided technical comments and edited the manuscript.

- Contribution for Chapter 4: For [5], Analysis of the experimental data and creating the performance maps, development of the control algorithm, control

design, evaluation of the controller in simulation, and writing the paper were done by the author, M. Bidarvatan. M. Shahbakhti provided technical comments and edited the manuscript. For [4], modeling, experimental validation of the model, and writing the paper were done by the author, M. Bidarvatan. M. Shahbakhti provided technical comments and edited the manuscript. For [3], Modeling and experimental validation of the model, development of the Genetic algorithm, control design, evaluation of the controller in simulation, and writing the paper were done by the author, M. Bidarvatan. Partial modeling, experimental validation of the model, and partial writing of the paper were done by V. Thakkar. B. Bahri and A.A. Aziz provided partial experimental data. M. Shahbakhti provided technical comments and edited the manuscript.

- Contribution for Chapter 5 ([6]): Partial modeling and experimental validation of the model, control design, evaluation of the controller in simulation, and writing the paper were done by the author, M. Bidarvatan. Modeling and experimental validation of the model, partial control design and evaluation of the controller in simulation were done by D. Kothari. M. Shahbakhti provided technical comments and edited the manuscript.

- Contribution for Chapters 6 and 7 ([7, 11]): Modeling and experimental validation of the model, energy management control design, evaluation of the controller in simulation, and writing the paper were done by the author, M. Bidarvatan. M. Shahbakhti provided technical comments and edited the manuscript.

Acknowledgments

It is a great pleasure for me to take this opportunity to thank many people who have helped or supported through the course of my PhD research. I am very thankful to my advisor, Dr. Mahdi Shahbakhti, who always encouraged to build up my research skills and supported to accomplish this work. At the same time Dr. Shahbakhti has been a great counselor. He has always given me valuable advice to overcome both research and teaching challenges during my Ph.D. I would also like to thank Dr. B. Predebon, the ME-EM department chair to give me a great opportunity to teach a senior level undergraduate course as a Distinguished Doctoral Teaching Fellow.

I am grateful to Dr. B. Koch from the University of Alberta and Dr. B. Bahri and Dr. A.A. Aziz from the Universiti Teknologi Malaysia for their support in providing a part of the experimental data used in this research. I graciously acknowledge Dr. Hamit Solmaz and Kaushik Kannan for their contributions in collecting the experimental data from our LTC engine setup at MTU used for this work. Many thanks are deserved to my colleagues in the Simulation team and the co-authors of my papers, M. Razmara, D. Kothari, and Vishal Thakkar. Their efforts significantly contributed to the quality of this dissertation. Special thanks to the examination committee for their valuable feedbacks on the research of this dissertation.

Thanks to all my friends at Michigan Tech University for all the good time we have had during these three and half years specially my close friends Meysam Razmara, Pouya Arabizadeh, Mehdi and Mojdeh Malekrah, and Mehdi Mortazavi. Lastly, my parents (Sima and Atapour), my lovely wife (Nooshin), and other family members are those whom I will be always grateful for their love, encouragement and support throughout my PhD studies.

List of Abbreviations

Acronyms

aBDC	After Bottom Dead Center
ANN	Artificial Neural Networks
aTDC	After Top Dead Center
BDC	Bottom Dead Center
CAD	Crank Angle Degree
CA50	Crank Angle for 50% Burnt Fuel
CO	Carbon Monoxide
COM	Control Oriented Model
DP	Dynamic Programming
DSMC	Discrete Sliding Mode Controller
DSSMC	Discrete Suboptimal Sliding Mode Control
E-machine	Electric-machine
EGR	Exhaust Gas Recirculation
EOC	End of Combustion
EPA	Environmental Protection Agency
EVC	Exhaust Valve Closing
EVO	Exhaust Valve Opening

GB/GA	Grey-box Genetic Algorithm
HCCI	Homogenous Charge Compression Ignition
HEV	Hybrid Electric Vehicle
ICE	Internal Combustion Engine
IMEP	Indicated Mean Effective Pressure
IVC	Intake Valve Closing
IVO	Intake Valve Opening
LCOM	Linear Control Oriented Model
LQG	Linear Quadratic Gaussian
LQR	Linear Quadratic Regulator
LTC	Low Temperature Combustion
LVD	Longitudinal Vehicle Dynamics
MKIM	Modified Knock Integral Model
MIMO	Multiple Input Multiple Output
MISO	Multiple Input Single Output
MPC	Model Predictive Controller
MSE	Mean Square Error
NCOM	Nonlinear Control Oriented Model
NHTSA	National Highway Traffic Safety Administration
NMOG	Non-Methane Organic Gas
NO_x	Nitrogen Oxides

OCP	Optimum Combustion Phasing
ON	Octane Number
PCCI	Premixed Charge Compression Ignition
PI	Proportional Integral
PID	Proportional Integral Derivative
PM	Particulate Matter
PPM	Parts Per Million
PRF	Primary Reference Fuel
RCCI	Reactivity Controller Charge Compression Ignition
RMSE	Root Mean Square Error
rpm	Revolution per Minute
SI	Spark Ignition
SISO	Single Input Single Output
SMC	Sliding Mode Control
SOC	Start of Combustion but Battery State of Charge in Chapters 6 and 7
std (STD)	Standard Deviation
TDC	Top Dead Center
THC	Total Hydrocarbon
TWC	Three Way Catalyst
UDDS	Urban Dynamometer Driving Schedule

uHC	Unburned Hydrocarbon
VVA	Variable Valve Actuation

Symbols

A	Area (m^2) but Vehicle Front Area (m^2) in Chapters 6 and 7
a	Vehicle Acceleration ($\frac{m}{s^2}$)
AEI	Aftertreatment Efficiency Index (-)
AFR	Air Fuel Ratio (-)
BSFC	Brake Specific Fuel Consumption ($\frac{g}{kW.h}$)
C_D	Discharge Coefficient (-)
C_d	Aerodynamic Drag Coefficient (-)
$\bar{C}_v$	Average Constant-volume Specific Heat Capacity ($\frac{kJ}{kg.K}$)
C_p	Constant Pressure Specific Heat Capacity ($\frac{kJ}{kg.K}$)
CA50	Crank Angle for 50% Burnt Fuel (CADaTDC)
CO	Carbon Monoxide Concentration (%)
CoC	Completeness of Combustion (%)
d_v	Diameter of Exhaust Valve (m)
ΔT_{comb}	Temperature Increase due to the Combustion Process (K)
E	Total Energy (kJ)
e	Fuel Consumption Error for Engine Model ($\frac{g}{h}$)
EGR	Exhaust Gas Recirculation Fraction (-)
η	Efficiency (-)

F	Force (N)
$FMEP$	Friction Mean Effective Pressure (kPa)
h	Convective Heat Transfer Coefficient ($\frac{W}{m^2K}$)
I	Current (A)
IMEP	Indicated Mean Effective Pressure (bar)
J	Mass Moment of Inertia (kgm^2)
k_{ay2}	Synchromesh Engaged Damping Constant ($\frac{Nms}{rad}$)
k_{ayl}	Slipping Stiffness Constant for Engine Side Shaft ($\frac{Nm}{rad}$)
K_i	Integral Control Gain in PI Control
K_p	Proportional Control Gain in PI Control
l	Gain Vector of Kalman Filter
λ	AFR over Stoichiometric AFR (-)
LHV	Low Heating Value (kJ/kg)
LI	Load Index (-)
M	Vehicle Gross Mass (kg)
m	Mass (g) but (kg) in Chapter 2 Except Table 2.3 and Figure 2.9
$\dot{m}$	Mass Flow Rate (kg/s) or (g/s)
N	Engine Speed (rpm), but rotational speed in Chapters 6 and 7
N_u	Feed-forward Gain Vector

NO_x	Nitrogen Oxides Concentration (ppm)
n	Ratio of Specific Heat Capacities (-)
n_d	Differential Gear Ratio (-)
ω	Rotational Speed ($\frac{rad}{s}$)
ON	Octane Number (-)
$\mathcal{P}$	Power (kW)
P	Pressure (kPa)
p	Pressure (kPa), but (bar) in Eq. (7.4)
p_r	Pressure Ratio (-)
ϕ	Fuel Equivalence Ratio (-)
PI	Performance Index (-)
Q_c	Overall Battery Energy Capacity (Ah)
Q_{corr}	Heat Transfer (Other than Convection) Between the Exhaust Gases and the Exhaust Manifold (kJ)
Q_f	Energy Released from Burning Fuel (kJ)
Q_w	Heat Loss from In-cylinder Gas to Surrounding Walls (kJ)
R	Radius (m)
$\bar{R}$	Average Gas Constant ($\frac{kJ}{kgK}$)
R_d	Battery Equivalent Resistance (Ohm)
REI	Raw Emission Index (-)
RGF	Residual Gas Fraction (-)

ρ	Density ($\frac{kg}{m^3}$)
σ	Fuel Consumption Standard Deviation of Error for Engine Model ($\frac{g}{h}$)
S_{sl}	Sliding Surface
SOC	Start Of Combustion Moment (CADaTDC)
T	Temperature (K) but (°C) in Eqs. 2.4 and 2.6; Torque in Chapters 6 and 7
t	Time (sec)
τ	Fuel Dynamics Time Constant (sec)
TEI	Tailpipe Emission Index (-)
Θ	Temperature (K)
θ	Crank Angle (°)
U	Internal Energy (kJ)
u	Control Input
V	Volume (m^3), but Voltage (V) in Chapters 6 and 7
$\mathbb{V}$	Vehicle Velocity ($\frac{km}{h}$)
V_d	Engine Displacement Volume (m^3)
W	Work (kJ), but vehicle Gross Mass (N) in Chapters 6 and 7
w	Disturbance Vector
x	Model State Vector, but Fraction of Fuel Delivered to

	Intake System (-) in Chapter 7
X_r	Residual Gas Fraction (-)
y	Plant Output

Subscripts

ac	Airflow into Cylinder
ad	Adiabatic
amb	Ambient
ave	Average
b	Burned, but Battery in Chapters 6 and 7
c	Compression,but Clutch in Chapters 6 and 7
ce	(Flow) from Cylinder to Exhaust
$comb$	Combustion
$cool$	Engine Coolant
d	Displacement, but Aerodynamic Drag in Chapters 6 and 7
dur	Burning Duration
dyn	Dynamic
e	Expansion, but Engine in Chapters 6 and 7
ec	(Flow) from Exhaust to Cylinder
eoc	End of Combustion
evc	Exhaust Valve Closure
evo	Exhaust Valve Opening

exh	Exhaust Gas
f	Fuel
fc	Fuel Conversion
f,c	Cumulative Fuel Consumption
f,f	Fuel Film
f,i	Injected Fuel
f,v	Fuel Vapor Phase
f/p	Friction and Pumping
g	Grey-box
gen	Generating Mode
hv	Heating Value
i	Indicated
iso	Iso-Octane
ivc	Intake Valve Closing
ivo	Intake Valve Opening
k	Engine Cycle Index
l	Load
m	Motor (E-machine)
man	Manifold
max	Maximum
mix	Mixture

mot	Motoring Mode
nc	New Charge to the Engine Cylinder
nH	n-Heptane
oc	Battery Open Circuit
p	Physical Model
pen	Penalty
r	Rolling Resistance
ref	Reference
req	Request
rg	Residua Gas
soc	Start of Combustion
st	Stoichiometric, but Steady-state in Chapter 7
$surf$	Surface of the Exhaust Manifold
t	Total
w	Cylinder Walls, but Wheel in Chapters 6 and 7

Abstract

Low Temperature Combustion (LTC) holds promise for high thermal efficiency and low Nitrogen Oxides (NO_x) and Particulate Matter (PM) exhaust emissions. Fast and robust control of different engine variables is a major challenge for real-time model-based control of LTC. This thesis concentrates on control of powertrain systems that are integrated with a specific type of LTC engines called Homogenous Charge Compression Ignition (HCCI). In this thesis, accurate mean value and dynamic cycle-to-cycle Control Oriented Models (COMs) are developed to capture the dynamics of HCCI engine operation. The COMs are experimentally validated for a wide range of HCCI steady-state and transient operating conditions. The developed COMs can predict engine variables including combustion phasing, engine load and exhaust gas temperature with low computational requirements for multi-input multi-output real-time HCCI controller design. Different types of model-based controllers are then developed and implemented on a detailed experimentally validated physical HCCI engine model. Control of engine output and tailpipe emissions are conducted using two methodologies: i) an optimal algorithm based on a novel engine performance index to minimize engine-out emissions and exhaust aftertreatment efficiency, and ii) grey-box modeling technique in combination with optimization methods to minimize engine emissions. In addition, grey-box models are experimentally validated and their prediction accuracy is compared with that from black-box only or clear-box

only models.

A detailed powertrain model is developed for a parallel Hybrid Electric Vehicle (HEV) integrated with an HCCI engine. The HEV model includes sub-models for different HEV components. The HCCI map model is obtained based on extensive experimental engine dynamometer testing. The LTC-HEV model is used to investigate the potential fuel consumption benefits archived by combining two technologies including LTC and electrification. An optimal control strategy including Model Predictive Control (MPC) is used for energy management control in the studied parallel LTC-HEV. The developed HEV model is then modified by replacing a detailed dynamic engine model and a dynamic clutch model to investigate effects of powertrain dynamics on the HEV energy consumption. The dynamics include engine fuel flow dynamics, engine air flow dynamics, engine rotational dynamics, and clutch dynamics. An enhanced MPC strategy for HEV torque split control is developed by incorporating the effects of the studied engine dynamics to save more energy compared to the commonly used map-based control strategies where the effects of powertrain dynamics are ignored.

LTC is promising for reduction in fuel consumption and emission production however sophisticated multi variable engine controllers are required to realize application of LTC engines. This thesis centers on development of model-based controllers for powertrain systems with LTC engines.

Chapter 1

Introduction

The global fossil fuel consumption is expected to increase to 92.2 quadrillion Btu per year by 2040. In addition, Global Green House Gas (GHG) emissions production is expected to increase by 29% from 2015 to 20130 [12]. Transportation sector accounts for 23% global GHG emissions as by 2010 [13].

The US Department of Transportation's National Highway Traffic Safety Administration (NHTSA) requires the vehicle corporate average fuel economy to be increased by 53% (from 15.1 to 23.2 $\frac{km}{l}$) for light duty vehicles from 2016 to 2025 [14]. In addition, the 2014 US Environmental Protection Agency (EPA) emission standards (Tier III and LEV III) regulate that emissions of Nitrogen Oxides and Non-Methane Organic Gas (NO_x+NMOG) reduces from current 99.2 $\frac{mg}{km}$ to 18.6 $\frac{mg}{km}$ in 2025 on fleet

average for light duty vehicles [15]. Thus, there is now a high demand for powertrain technologies with low fuel consumption and low NO_x emissions.

One major solution to reduce emissions and fuel consumption in transportation systems is to utilize cleaner and more efficient combustion technologies in Internal Combustion Engines (ICEs). One candidate is diesel or Compression Ignition (CI) engines since CI combustion has higher thermal efficiency compared to Spark Ignition (SI) engines. However, CI engines suffer from high NO_x and soot emissions. Soot can be reduced using a Diesel Particulate Filter (DPF) effectively; however, DPFs require continuous regeneration (means removal of collected soot), which leads to high fuel consumption [16]. Additionally, since CI engines typically operate under lean mixture conditions, the exhaust oxygen concentrations are too high to convert NO_x to nitrogen using a Three Way Catalyst (TWC). Efforts to operate CI engines under stoichiometric mixture condition such that a TWC can be used for NO_x reduction, have yielded poor fuel efficiency [17].

One promising combustion technology to reach low fuel consumption and low emissions is to use Low Temperature Combustion (LTC) engines [18, 19]. LTC engines have negligible Particulate Matter (PM) or soot emissions and low NO_x emissions due to low temperature of combustion and homogeneity of the air-fuel mixture. There are different combustion strategies to achieve LTC. Homogenous Charge Compression Ignition (HCCI), Premixed Charge Compression Ignition (PCCI), and Reactivity

Controller Charge Compression Ignition (RCCI) are examples of LTC strategies. In HCCI strategy, a homogenous air-fuel mixture (premixed in the intake manifold) is inducted into the cylinders and combusted as a result of compression. For PCCI strategy, direct in-cylinder fuel injection with early injection timing (usually early in the compression stroke) is used to prepare a premixed air-fuel mixture inside the cylinders. However, compared to HCCI mode, the level of homogeneity is less in PCCI. Different types of fuels with different levels of reactivity can be used in HCCI and PCCI strategies depending on the engine compression ratio. In addition, multiple fuel injections can be employed for mixture preparation. In RCCI, two types of fuels are utilized: 1) a low reactivity fuel (e.g., gasoline or natural gas) which is injected into the intake manifold to prepare the premixed air-fuel mixture and 2) a high reactivity fuel (e.g., n-Heptane or diesel fuel) which is directly injected into the cylinders to control the reactivity of the total mixture [20, 21]. Figure 1.1 shows conventional CI combustion and LTC strategies in relation to NO_x and soot formations at different local fuel equivalence ratios (ϕ) and local temperatures [8]. As seen in Figure 1.1, LTC strategies overcome CI combustion mode with lower soot and NO_x emissions. RCCI and PCCI have greater local ϕ values compared to HCCI due to the direct fuel injection and less homogeneity; in addition, HCCI and PCCI have no soot formations. The focus of this thesis is on HCCI engines which can be easily retrofitted from conventional engines, and can operate with one fuel. HCCI has the lowest soot formation compared to PCCI and RCCI as shown in Figure 1.1.

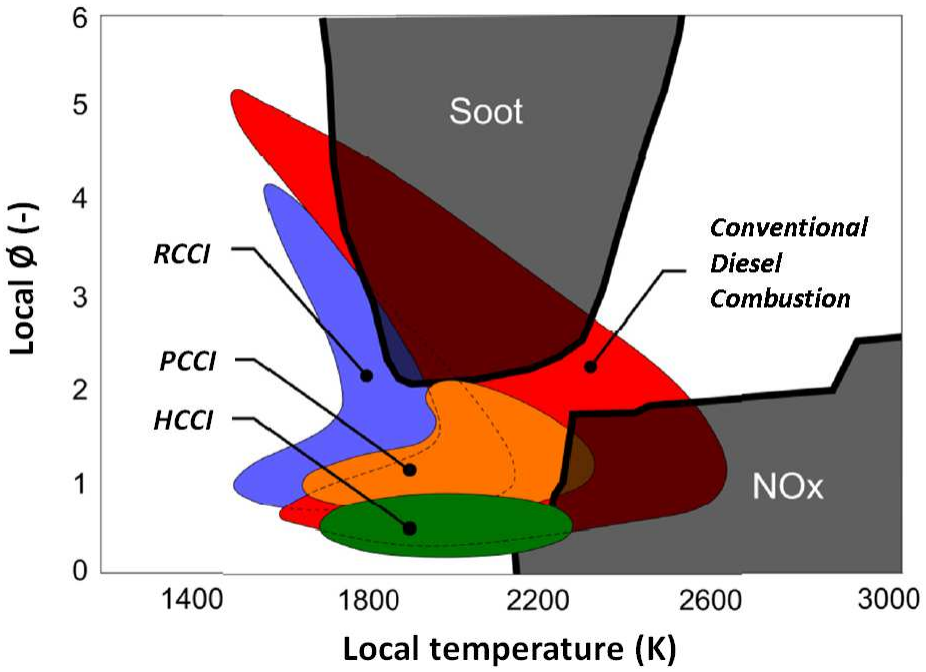

Figure 1.1: Soot and NO_x regions for LTC and diesel engines in ϕ-T space (adapted from [8]).

1.1 HCCI Engines

1.1.1 HCCI Benefits and Challenges

Figure 1.2 shows major HCCI benefits (shown in light green) and drawbacks (shown in red). HCCI has low fuel consumption and indicated thermal efficiency as high as 50% [22] with negligible PM and lower NO_x emissions compared to conventional diesel and SI engines and also low cyclic variations [23, 24]. However these benefits are accompanied by major drawbacks such as limited operating range and high levels

of unburned Hydrocarbon (uHC) and Carbon Monoxide (CO) emissions [25, 26] (due to low temperature combustion). In addition, HCCI lacks a direct means to initiate combustion due to the dependency on the charge properties ([27, 28]). Control of HCCI combustion is the major challenge that needs to be overcome to realize HCCI benefits [29, 30].

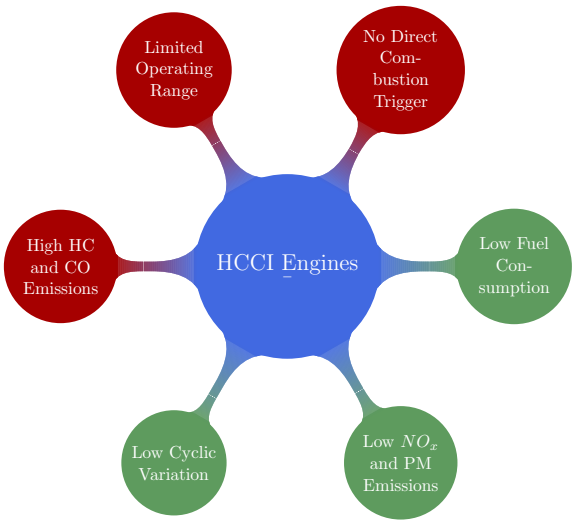

Figure 1.2: HCCI engine benefits (shown in green) and drawbacks (shown in red).

1.1.2 Control of HCCI Powertrain Systems

Optimal combustion phasing can reduce HCCI emission levels ([26, 31, 32]) and it also influences the HCCI operating range and affects the magnitude of cyclic variations ([10, 33, 34, 35]). Lack of a direct means to initiate combustion and the complexity of HCCI combustion control call for a sophisticated controller strategy which can adjust

charge properties cycle-to-cycle to obtain desired combustion phasing.

In addition, uHC and CO abatement by oxidation catalysts is limited in HCCI engines since HCCI typically has a low T_{exh}, as low as 120 °C [36] while the light-off temperature (the temperature at which the catalyst becomes more than 50 percent effective) is about 250 to 300 °C [37, 38] for most catalysts. Thus, control of T_{exh} is essential to increase the exhaust aftertreatment efficiency.

Another control requirement/variable is the desired engine load that should be met while meeting the engine constraints such as knock limit. Therefore, major HCCI control variables include combustion phasing, engine load, and T_{exh}. Integrated control of these three engine variables is critical to overcome major challenges in HCCI engines.

HCCI control studies in the literature are divided into four main categories as shown in Figure 1.3. Depending on the control variables involved, there are four major groups: 1) control of combustion phasing, 2) control of engine load, 3) control of exhaust aftertreatment efficiency (or exhaust gas temperature), and 4) control of HCCI dynamics for mode switching between HCCI and conventional SI, diesel, Electric-machine (E-machine) (Hybrid Electric Vehicle, HEV) mode. The first group focuses on single control of combustion phasing that can be realized mostly by controlling the crank angle when 50% of the fuel mass is burned (CA50) or the crank angle at the maximum pressure ($\theta_{P_{max}}$). Studies in [39, 40, 41, 42, 43, 44, 45, 46, 47, 48, 49, 50] are

some examples of this group. The second category focuses on control of engine load or output work that is realized by controlling the Indicated Mean Effective Pressure (IMEP) or Net Mean Effective Pressure (NMEP). Studies in [40, 47, 51] are examples for this group on simultaneous control of load and CA50. The third group includes control of T_{exh} to ensure high conversion efficiency of the exhaust aftertreatment system. In [52], simultaneous control of T_{exh} and maximum pressure (P_{max}) was studied while in [53], T_{exh} was adjusted to be above a certain threshold as a constraint in control of the HCCI engine.

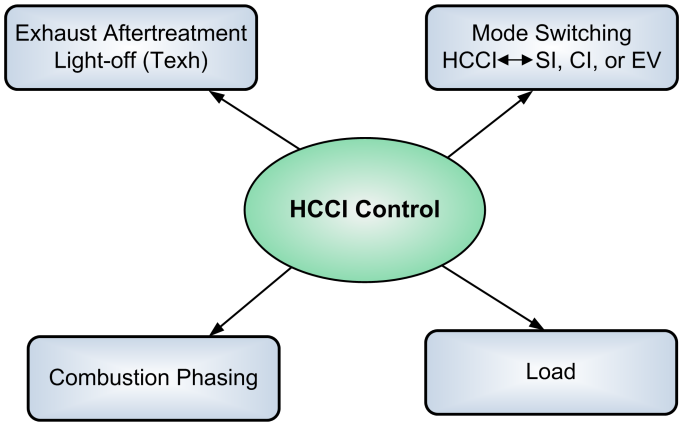

Figure 1.3: Different categories of HCCI engine control.

The fourth category of HCCI control studies is dedicated to control of combustion mode switching between HCCI and either SI [53] or Compression Ignition (CI) [54, 55, 56]. Energy management and control of mode switching between propulsion sources of HCCI engine and Electric-machine (E-machine) in an HEV powertrain are also included in this category. Most studies in the literature are on control of SI engine based HEVs ([57, 58, 59, 60, 61, 62, 63, 64, 65]) or CI engine based HEVs ([58, 66,

67, 68, 69, 70, 71, 72, 73]). There are not many studies in the literature on control of HCCI engine based HEVs. In [74, 75, 76] energy management between the dual mode SI-HCCI and the E-machine is conducted in simulation for different levels of hybridization and different HEV configurations. This thesis focuses on i) the first three HCCI control categories, and ii) control of mode switching between HCCI and E-machine in an HEV powertrain.

Figure 1.4 summarizes the previous studies on these specific categories along with different types of HCCI controllers designed. The controllers consist of a variety of types including i) empirical tuned Proportional Integral (PI) and Proportional Integral Derivative (PID) controllers, ii) model-based controllers including integral state feedback, Linear Quadratic Regulator (LQR) and Linear Quadratic Gaussian (LQG), Model Predictive Control (MPC), sliding mode, H_2, and constraint-based controllers) to control HCCI engine, and iii) Rule Based Controllers (RBCs) to control the mode switching in HCCI-HEV. In the empirical studies, a manual technique is used to tune a PID controller without incorporating a model of engine dynamics ([44, 77, 78, 79]). For model-based controllers, an accurate model is required to dynamically predict HCCI engine operation. In this study, model-based controls is utilized for control of HCCI engine based powertrain systems.

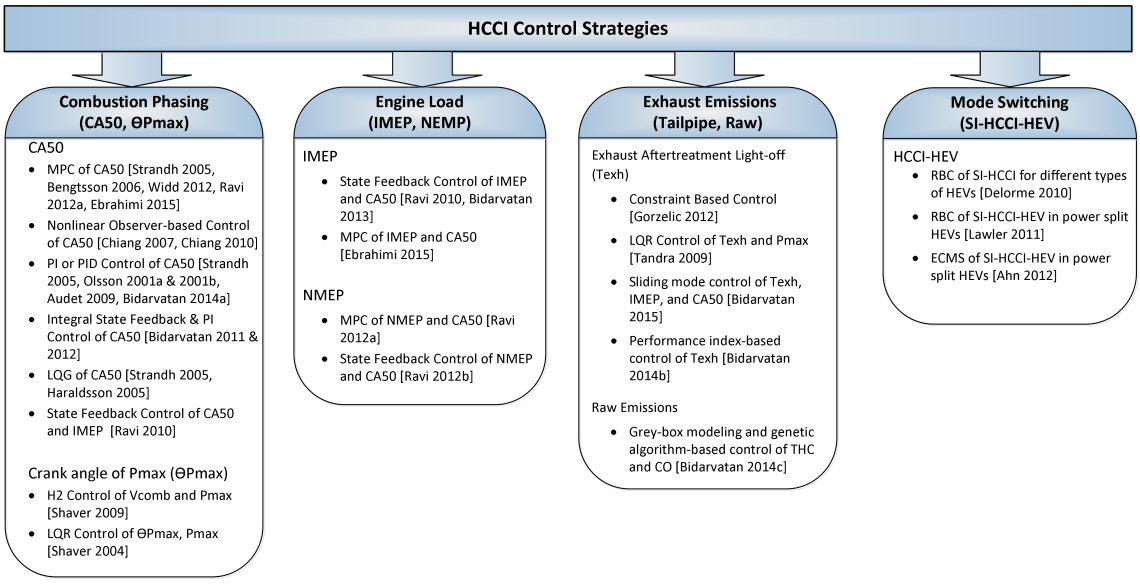

Figure 1.4: Background of HCCI control categories.

1.1.3 Thesis Organization

This thesis is organized into eight chapters as depicted in Figure 1.5. Chapter 1 is the Introduction and Background. In Chapter 2, a physic-based Control Oriented Model (COM) is developed to predict HCCI engine operation. The COM is then used to design a model-based Sliding Mode Controller (SMC) to control HCCI combustion phasing. In Chapter 3, the developed COM is extended to predict engine load and then a Multiple Input Multiple Output (MIMO) controller is designed and tested to control combustion phasing and load. Chapter 4 explains methodologies for indirect control of T_{exh} and engine-out emissions to be utilized in the HCCI engine MIMO control structure. Two methodologies including 1) an optimal methodology based on a new performance index and 2) grey-box modeling with genetic algorithm are used

for this purpose. The COM from Chapter 3 is then extended in Chapter 5 to predict T_{exh}. The new COM is used to design and test model-based controllers for direct control of combustion phrasing, load, and T_{exh}. Chapter 6 explains development of a parallel HEV powertrain model including an HCCI engine model. The HEV model is used to design MPC as an optimal energy management control strategy for control of energy split between ICE and E-machine. The goal is to investigate the fuel economy benefits achieved by hybridizing LTC-based powertrain. Chapter 7 includes a study on the effects of ICE dynamics and clutch dynamics on torque split management and fuel consumption in a parallel HEV. An experimentally validated dynamic ICE model along with a dynamic clutch model is used in the HEV plant model. An MPC strategy is developed that accounts for the effects of the studied dynamics for HEV torque split management. The simulation results will show the energy consumption benefits of the new designed MPC strategy.

Figure 1.5: Schematic of the thesis organization.

Chapter 2

Control Oriented Model (COM) Development and Model-based Control of Combustion Phasing[1]

Fast and robust control of combustion phasing is major challenge for real-time model-based control of HCCI. In this chapter a discrete Control Oriented Model (COM) for predicting HCCI combustion phasing on a cycle-to-cycle basis is developed and validated against experimental data from a single cylinder blended fuel Ricardo engine. A Discrete Sliding Mode Controller (DSMC) coupled with a Kalman filter is designed to control combustion phasing by adjusting the ratio of two Primary Reference Fuels

[1]The results of this chapter are partially based on [1] (Reprinted with permission from Elsevier as shown in Appendix E, Section E.1).

(PRFs). Performance of the DSMC in tracking the desired combustion phasing trajectories is studied. In addition, performance of the DSMC is studied for maintaining the stability of the engine in a wide operation range under conditions of physical disturbances of engine speed, intake manifold temperature, and fueling. Results are then compared with those from a commonly used empirical Proportional Integral (PI) controller.

2.1 Introduction

The main HCCI dynamic controllers for combustion phasing are divided into two main categories - empirical controllers and model-based controllers (Figure 2.1). In the first category, a manual technique is used to tune a PID controller without incorporating a model of engine dynamics ([44, 77, 78, 79]). Model-based controllers where an accurate model is required to dynamically predict HCCI combustion phasing is the secondary category. Depending on which type of model is used in the synthesis of the controller, the model-based controllers are further subdivided into two groups: system identification-based controllers and physics-based controllers. The first group includes the controllers which are based on empirical models such as system identification or black-box modeling ([43, 45, 80]). The second group relates to model-based controllers derived from physical models such as thermodynamic models of the HCCI engine cycle. Examples of physical HCCI models are ([9, 60, 81, 82, 83, 84, 85, 86, 87]).

For real-time control implementation and stability analysis ([88]), simple COMs have been proposed in literature ([1, 41, 47, 49, 89]). In this chapter, a discrete Nonlinear Control Oriented Model (NCOM) is developed for predicting HCCI combustion phasing on a cycle-to-cycle basis. The NCOM has sufficient accuracy and low processing time that makes it suitable for real-time control. CA50 is used as the measure of HCCI combustion phasing since it is a robust feedback indicator of HCCI combustion phasing due to the steep heat release in the main stage of HCCI combustion ([90]).

Figure 2.1 also lists different control actuators which are used for control of HCCI combustion phasing. Examples of control actuators for HCCI include blended fuel ratio modulation ([43, 45, 46, 91]), charge temperature manipulation by lift adjustment of secondary exhaust valve opening ([41, 42]), thermal management ([48]), and Variable Valve Actuation (VVA) by Intake Valve Closing (IVC) timing ([43, 49, 92]), adjustment of exhaust valve closing (EVC) ([93]), start of fuel injection timing ([53]), simultaneous adjustment of IVC timing and the negative valve overlap (NVO) ([47, 78, 89]), and simultaneous timing of EVC and pilot fuel injection ([40]). Dual fuel control of LTC engines has received a lot of attention in the literature during recent years ([94, 95]). This study presents dual fuel control of HCCI combustion phasing by manipulating the ratio of two Primary Reference Fuels (PRFs). This study uses a blend of iso-Octane (PRF100) with the octane number (ON) of 100 and n-Heptane (PRF0) with the ON of 0. The reason for using a PRF fuel blend is that these fuels

are standard fuels and are used to test the control to fuel octane number changes. The control strategy developed can then be suitably modified and applied to other blends of fuels.

Different types of controllers have been used in the literature to control HCCI combustion phasing as shown in Figure 2.1. Examples of these controllers include PI control ([45, 92]), integral state feedback ([46, 47]), Linear Quadratic Regulator (LQR) and Linear Quadratic Gaussian (LQG) ([43, 53]), H2 controller ([49]), MPC ([39, 89, 90]), and nonlinear observer based controller ([41, 42]). Sliding Mode Control (SMC) is a robust non-linear control method to reject system uncertainty and disturbances. In this study, a discrete type of SMC called Discrete Suboptimal Sliding Mode Control (DSSMC) is designed for HCCI combustion phasing control. To the author's knowledge, this is the first application of DSSMC for HCCI combustion control.

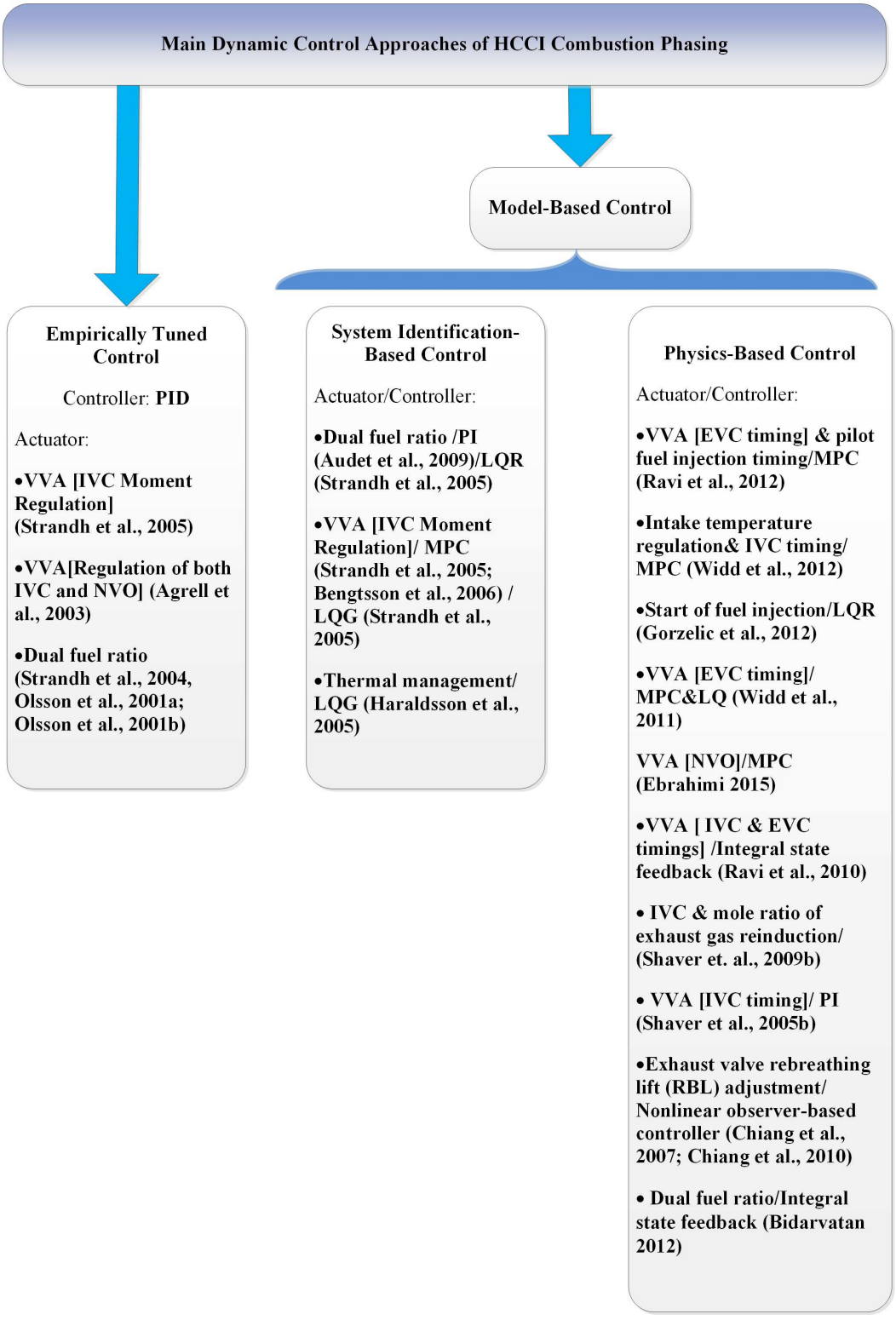

Figure 2.1: HCCI combustion phasing control approaches in the literature.

The following section describes details on development of a discrete NCOM for HCCI combustion phasing prediction. Then, the model performance is investigated by validating it against both experimental data and simulations results from a more detailed physical HCCI model ([9]). Next, a DSSMC controller along with a Kalman filter observer is designed. Tracking performance of the controller is studied under conditions of having noisy measurements and with physical disturbances. Variations in the intake manifold temperature, intake manifold pressure and the injected fuel equivalence ratio (as an engine load indicator) are considered to be physical disturbances to the HCCI engine. Finally, the control results are compared with those of a manually tuned PI controller and summary of this chapter is reached.

2.2 Control Oriented Model Development

2.2.1 Model States and Disturbances

A discrete NCOM is developed in this section to predict cycle-to-cycle HCCI combustion phasing. The NCOM simulates an HCCI cycle by incorporating physical-empirical models to describe phenomena occurring during the HCCI cycle. The model comprises the following five states:

1. CA50

2. Temperature at Start Of Combustion (SOC) moment (T_{soc})

3. In-Cylinder pressure at SOC moment (P_{soc})

4. Residual gas temperature (T_{rg})

5. Mass of trapped residual gases at EVC (m_{evc})

These five states are dominant variables affecting HCCI combustion phasing since they strongly influence the thermodynamic conditions of the in-cylinder mixture in an HCCI cycle. T_{soc} and P_{soc} directly influence the location of SOC, while T_{rg} and m_{evc} affect the charge temperature of the next cycle.

2.2.2 Model Description

The NCOM detailed in this section models the HCCI cycle as a series of events beginning with the intake stroke and ending with the calculation of the residual gas properties at the end of exhaust stroke. The NCOM is then parameterized for a single cylinder Ricardo engine with the specifications listed in Table 2.1. The physical-empirical equations of the NCOM are described next and values of constant parameters in the NCOM are listed in Appendix A.1.

Table 2.1
Single cylinder Ricardo engine specifications.

Parameter	Value
Bore	80 mm
Stroke	88.90 mm
Compression ratio	10 : 1
Displacement	447 cc
Number of valves	4
Intake valve opening	$-175\,^\circ$ aBDC*
Intake valve closing	$+55\,^\circ$ aBDC
Exhaust valve opening	$-70\,^\circ$ aBDC
Exhaust valve closing	$-175\,^\circ$ aBDC

*after bottom dead center (BDC) point

2.2.2.1 Intake Stroke ($IVO \rightarrow IVC$)

Thermodynamic States of Fresh Charge at IVC Moment

Mixture pressure and temperature at IVC moment (P_{ivc} and T_{ivc}) are estimated by two semi-empirical correlations [9]:

$$P_{ivc,k+1} = \left[\frac{N_k{}^{\bar{a}}\phi_k{}^{\bar{b}}}{T^{\bar{c}}_{man,k}}\right] P_{man,k} \tag{2.1}$$

$$T_{ivc,k+1} = \left(a_1 T^2_{man,k} + a_2 T_{man,k} + a_3\right) \frac{\phi_k{}^{b_1} N^{b_2}}{(1+EGR)^{b_3}} \tag{2.2}$$

where EGR is the rate of external exhaust gas recirculation fraction and ranges from 0 to 1. N [rpm] is the engine speed and P_m [kPa] and T_m [°C] are the intake manifold pressure and the intake manifold temperature, respectively. The index $k+1$ denotes

the current engine cycle and the index k denotes the previous engine cycle.

Mixing Temperature at IVC

In-cylinder trapped residual gas from the previous cycle (cycle k) mixes with the inducted fresh charge (cycle $k+1$). By assuming ideal gases and energy conservation in the mixing process, the gas mixture temperature at IVC (T_{mix}) is obtained by:

$$T_{mix,k+1} = (1 - X_{r_g,k})\frac{\bar{C}_{v,n_c}}{\bar{C}_{v,t}}T_{ivc,k+1} + X_{r_g,k}\frac{\bar{C}_{v,n_c}}{\bar{C}_{v,t}}T_{rg,k} \tag{2.3}$$

where X_{rg} [-] is the residual gas mass fraction. $\bar{C}_v$ $[kJ/kgK]$ is the average of gas specific heat capacity. Subscripts "t", "nc" and "rg" denote total mixture, new charge, and residual gas, respectively. By using T_{man}, the charge cooling effects are already considered in the modeling.

2.2.2.2 Polytropic Compression ($IVC \rightarrow SOC$)

By assuming a polytropic process for compression [37], the instantaneous values of gas temperature and pressure are calculated between IVC and SOC as:

$$T_{soc,k+1} = T_{mix,k+1}\left(\frac{V_{ivc,k+1}}{V_{soc,k+1}}\right)^{k_{c-1}} \tag{2.4}$$

$$P_{soc,k+1} = P_{ivc,k+1}\left(\frac{V_{ivc}}{V_{soc,k+1}}\right)^{k_c} \tag{2.5}$$

where k_c is the specific heat capacity ratio in the compression process. V_{ivc} and V_{soc} are the cylinder volume at the instant of IVC and SOC. Cylinder volume at each crank angle is calculated using a slider crank mechanism equations [37].

2.2.2.3 Combustion Period ($SOC \rightarrow EOC$)

Combustion Phasing Prediction: MKIM Simplification

A Modified Knock Integral Model (MKIM) [96] is used to predict HCCI auto ignition phasing (θ_{soc}) [9]:

$$\int_{\theta_{ivc}}^{\theta_{soc,k+1}} \frac{{\phi_k}^b}{Eexp\left(\frac{c(P_{ivc,k+1}V_c^{k_c})^D}{T_{mix,k+1}V_c^{k_c-1}}\right)N_k} d\theta = 1 \tag{2.6}$$

where θ_{ivc} is the crank angle at IVC moment. V_c and E are calculated by:

$$V_c = \frac{V_{ivc}}{V_\theta} \qquad E = e_1 X_d + e_2 \tag{2.7}$$

where:

$$X_d = \frac{EGR + X_{r_g}}{1 - X_{r_g}}. \tag{2.8}$$

Although this MKIM is accurate in predicting θ_{soc}, the structure and nonlinearity limit its real-time control application to HCCI combustion phasing. Mixture temperature at IVC, fuel octane number, and concentrations of the fuel and oxygen are the

three dominant parameters influencing HCCI auto ignition phasing (i.e., θ_{soc}) [10, 41] and the fuel equivalence ratio is considered to be an indicator of the fuel and oxygen concentrations [96]. The MKIM is reduced to a fitted correlation considering these three major influential parameters:

$$\theta_{soc,k+1} = f(T_{mix,k+1}, ON_k, \phi_k) \tag{2.9}$$

CA50 is then obtained as a function of θ_{soc} and combustion duration ($\delta\theta_{comb}$), assuming a constant fuel burn rate:

$$CA50_{k+1} = \theta_(soc, k+1) + 0.5\Delta(\theta)_{comb}, \tag{2.10}$$

resulting in:

$$CA50_{k+1} = g(T_{mix,k+1}, ON_k, \phi_k), \tag{2.11}$$

and defining the correlation as:

$$g(T_{mix,k+1}, ON_k, \phi_k) = C_1\phi_k T_(mix, k+1) + C_2\phi_k + C_3 ON_k + C_4. \tag{2.12}$$

The correlation given in Eq. (2.12) is parameterized without having external EGR and over an engine speed range of 800-1000 rpm. Values of the constant coefficients and more discussion about the correlation structure are found in Appendix A.1.

Thermodynamic States at EOC

The mixture temperature increase (δT_{comb}) assuming adiabatic combustion is determined as:

$$\Delta T_{comb_k+1} = \frac{m_{f,k+1} LHV_f \overline{CoC}}{m_{t,k+1} \bar{C}_v} \tag{2.13}$$

where m_f is the mass of the inducted fuel. LHV_f is the Lower Heating Value of the blended fuel and it is a function of fuel density (ρ), volume percentage ($\%V$) and LHV of each PRF (nH denotes n-Heptane and iso stands for iso-Octane). $\overline{CoC}$ is the average completeness of combustion. The lower heating value is based on the two fuels as follows:

$$LHV_f = \frac{\%V_{n_H} \rho_{n_H} LHV_{n_H} + \%V_{iso} \rho_{iso} LHV_{iso}}{\%V_{n_H} \rho_{n_H} + \%V_{iso} \rho_{iso}}. \tag{2.14}$$

Eq. (2.13) is modified to express δT_{comb} as a function of ϕ and X_r as:

$$\Delta T_{comb_k+1} = \frac{LHV_f \overline{CoC}}{(1 + X_{r,k})({\phi_k}^{-1} AFR_{st} + 1)\bar{C}_v}, \tag{2.15}$$

where AFR_{st} is the stoichiometric air-fuel ratio. The mixture temperature at the End Of Combustion (EOC) is obtained from:

$$T_{eoc,k+1} = T_{soc,k+1} + \Delta T. \tag{2.16}$$

The mixture pressure at EOC is obtained by assuming an ideal gas ($PV = m\bar{R}T$) and mass conservation during the combustion period as:

$$P_{eoc,k+1} = \frac{P_{soc,k+1}V_{soc,k+1}}{V_{eoc,k+1}} \frac{T_{eoc,k+1}}{T_{soc,k+1}} \frac{R_{eoc}}{R_{soc}}, \tag{2.17}$$

where R_{soc} and R_{eoc} are averages of the gas constants at SOC and EOC moments, respectively. The average values are calculated for a range of ON and ϕ variations.

2.2.2.4 Polytropic Expansion ($EOC \rightarrow EVO$)

Expansion of burned gases after EOC is modeled as a polytropic process [37] to obtain the temperature and pressure when the exhaust valve opens (EVO) as:

$$T_{evo,k+1} = \frac{T_{eoc,k+1}V_{eoc,k+1}}{{V_{evo}}^{(k_e-1)}}, \tag{2.18}$$

$$P_{evo,k+1} = \frac{P_{eoc,k+1}V_{eoc,k+1}}{{V_{evo}}^{k_e}}, \tag{2.19}$$

where k_e is the specific heat capacity in the expansion process.

2.2.2.5 Exhaust Stroke ($EVO \rightarrow EVC$)

The residual gas temperature (T_{rg}) is determined by assuming a polytropic relation for the exhaust stroke [47, 49, 60] as:

$$T_{r,k+1} = T_{evo,k+1}(\frac{V_{evo}}{V_{evc}})^{(k_e-1)}. \tag{2.20}$$

The exhaust manifold pressure is considered to be at atmospheric pressure (P_o). Finally m_{evc} is obtained by applying the ideal gas state equation at Exhaust Valve Closing (EVC):

$$m_{evc,k+1} = \frac{P_o V_{evc}}{R_{evc} T_{r,k+1}}, \tag{2.21}$$

where R_{evc} is the gas constant at EVC. The residual gas fraction is obtained as a mass fraction of residual gases to the entire combustion mixture and hence is calculated by:

$$X_{r,k+1} = \frac{m_{evc,k+1}}{m_{t,k+1}}. \tag{2.22}$$

2.2.3 Model Summary

The discrete NCOM described above captures dynamics of an HCCI engine cycle as well as the thermal coupling between two consecutive engine cycles through the

exhaust recirculation. The NCOM is compared with a detailed physical model simulation from previous work [9] in Figure 2.2. The complexity and nonlinearities in the NCOM are significantly reduced from the detailed physical model. Model-based control design is easier and real time implementation of HCCI combustion phasing controller is more computationally efficient for the NCOM.

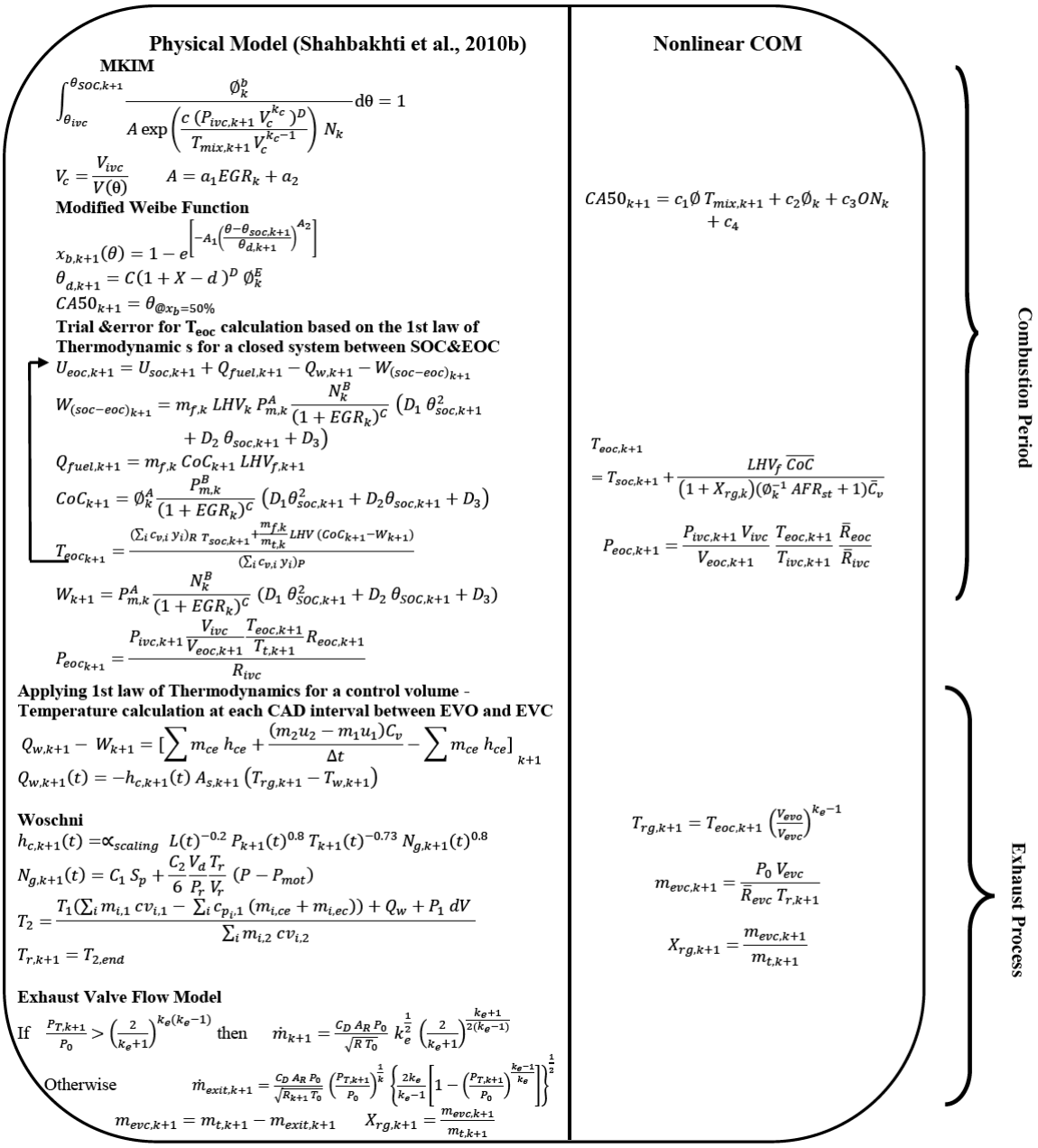

Figure 2.2: Equation summary and comparison of NCOM and physical model from [9]; permission from Elsevier is found in Appendix E, Section E.1.

Summarizing the equations in Section 2.2.2, the model state space and output equations are:

$$x_{k+1} = F(x_k, u_k), \tag{2.23}$$

$$y_k = G(x_k), \tag{2.24}$$

$$y_k = G(x_k), \tag{2.25}$$

where u is the model input, y is the output and x is the model state vector. The NCOM and the detailed physical model [9] are simulated for the same transient input conditions in Figure 2.3. The NCOM performance is studied by comparing it to the detailed model as shown in Figure 2.4. The NCOM and the detailed model show that the NCOM has good agreement for predicting the model states that are not easily measurable in practice (T_{soc}, T_{rg}, and m_{evc}). CA50 can be predicted by the NCOM with an average error and a RMSE less than 0.5 CAD. The processing of 100 cycles of the physical model on a 2.67 GHz Intel processor in Fig. 4 is approximately 5 seconds. The NCOM only needs 5 ms per 100 engine cycles; a speed improvement of approximately 1000. Acceptable processing time and good accuracy in predicting CA50 make the NCOM suitable for real-time model-based control of HCCI combustion phasing.

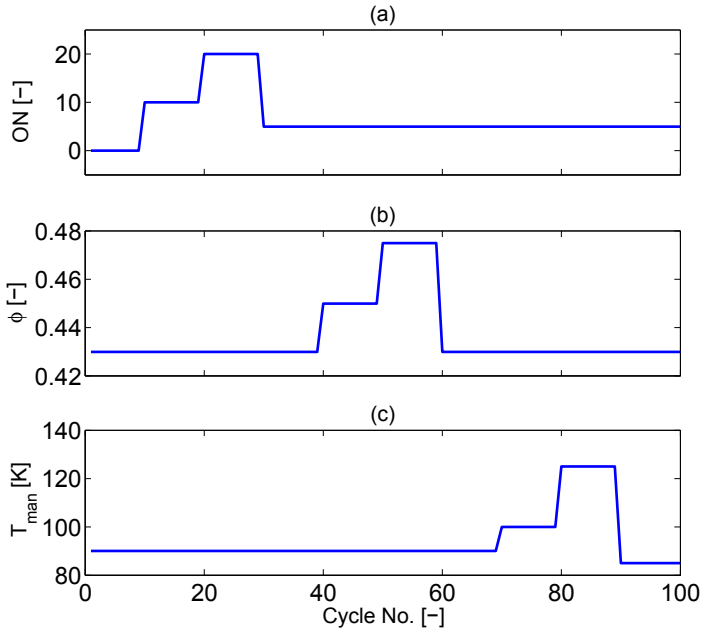

Figure 2.3: Operating conditions for performance comparison test of the NCOM vs. the detailed physical model (P_m=110 kPa, N= 800 rpm).

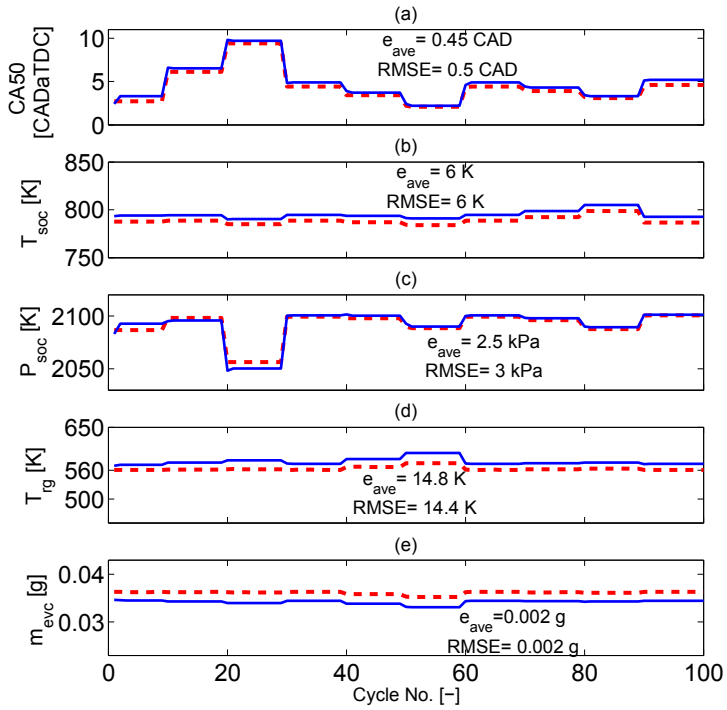

Figure 2.4: Operating conditions for performance comparison test of the NCOM vs. the detailed physical model (P_m=110 kPa, N= 800 rpm).

2.3 Experimental Validation of NCOM

Before performing the control design, experimental data from the single-cylinder Ricardo engine is compared with the NCOM and the physical model to validate the models. First, both the physical model and NCOM are validated against the steady state experimental data. Experimental data at 57 steady state engine operating conditions listed in Table 2.2 are used to evaluate both models. The results are shown in Figure 2.5 and they indicate that both physical model and NCOM can capture CA50 with average errors of 1.3 CAD and 1.8 CAD respectively, while the standard deviation (STD) of errors in comparison with the experimental results are less than 2 CAD for both models.

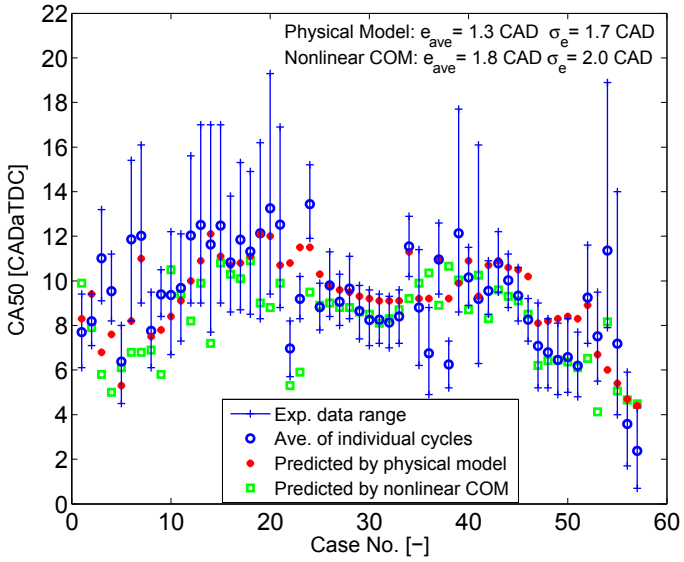

Figure 2.5: CA50 steady-state validation of the COM and physical model.

Table 2.2
Steady-state engine operating conditions used for validating the COM.

Parameter	Value
Fuel	PRF0, PRF10, PRF20, PRF40
N [rpm]	800-1000
T_{man}(°C)	79-148
P_{man}(kPa)	89-135
ϕ (-)	0.38-0.72

Figures 2.6-2.8 show the performance of the NCOM and the physical model in predicting CA50 during transient fueling experiments. The models are tested against variations in ϕ and ON and the output CA50 is predicted. Results show that both models have good accuracy in predicting CA50 when compared to experimental engine data for the 1335 cycles tested in Figures 2.6-2.8 with an average error and an uncertainty of error[2] of less than 1.5 CAD as well as RMSE of less than 2.0 CAD. This confirms the fidelity of the NCOM for design of model based HCCI combustion timing controllers.

[2]Uncertainty is calculated based on standard deviation of the errors between predicted (output of the NCOM) and experimental values of CA50.

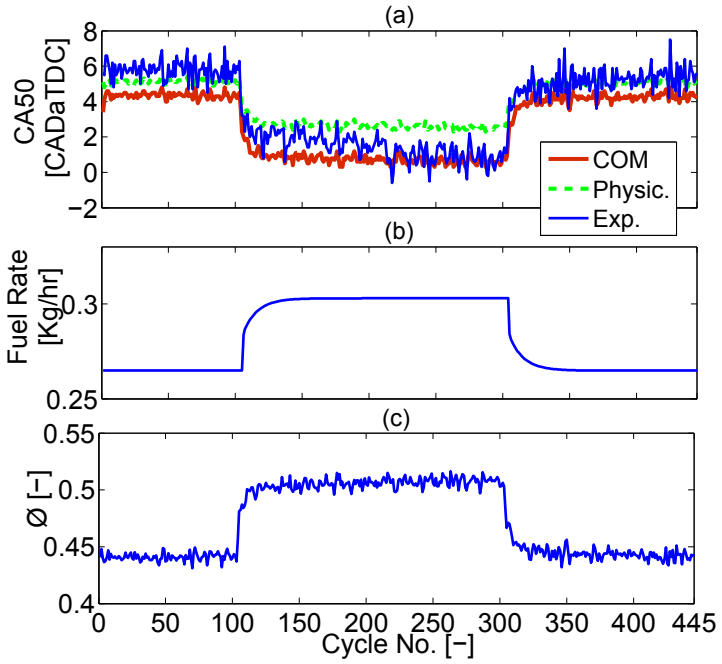

Figure 2.6: One cycle ahead prediction of the COM and physical model compared to experimental data for a fuel equivalence ratio step change (ON= 0; P_m= 100 kPa, T_m = 67 °C, External EGR= 0%, P_{exh}= 97.3 kPa, $N \simeq 815$ rpm).

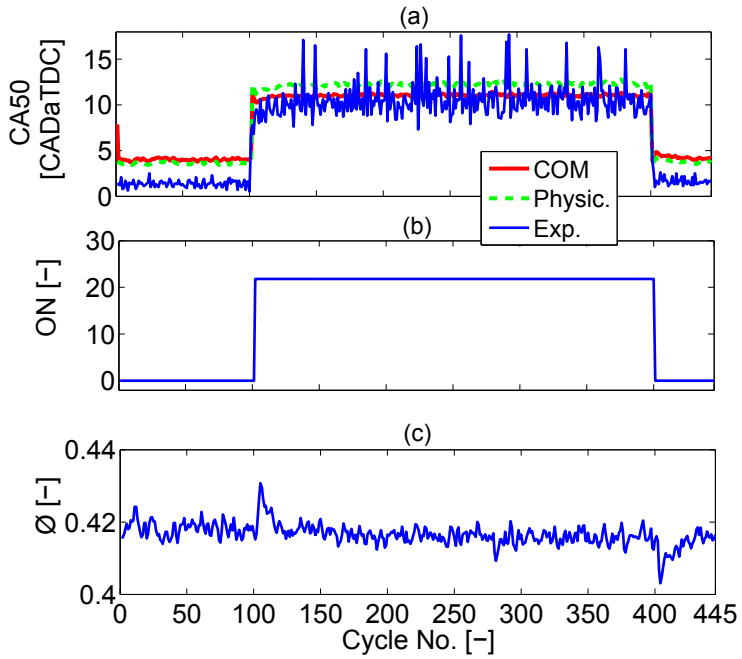

Figure 2.7: One cycle ahead prediction of COM and physical model compared to experimental data for a fuel octane number step change (P_m= 110 kPa, T_m= 91 °C, External EGR = 0%, P_{exh}= 99 kPa, $N \simeq 815$ rpm).

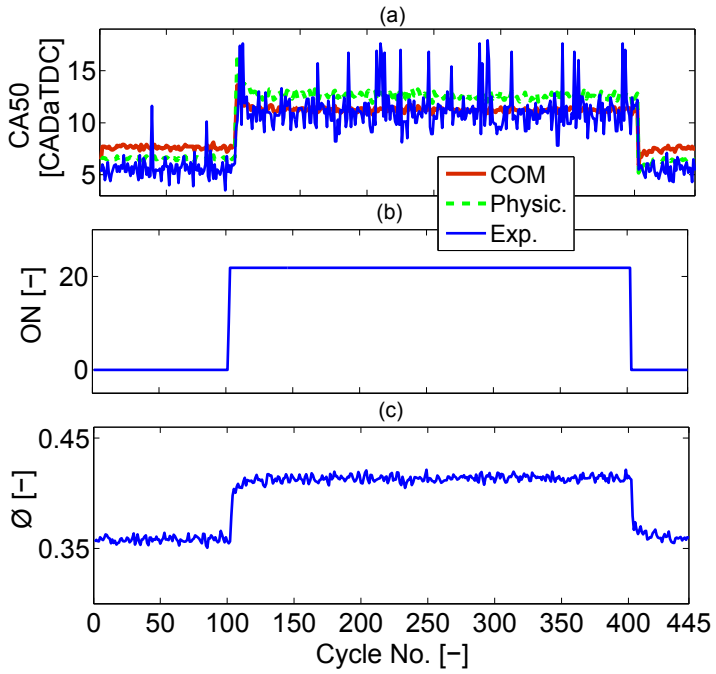

Figure 2.8: One cycle ahead prediction of COM and physical model compared to experimental data for a simultaneous fuel equivalence ratio and octane number step changes ($P_m = 110$ kPa, $T_m = 91$ °C, External EGR = 0%, $P_{exh} = 99$ kPa, $N \simeq 815$ rpm).

2.4 Model Linearization

The NCOM is now linearized around a nominal operating point shown in Table 2.3. The nominal operating point is chosen using the experimental observations in [10] to ensure that the selected operating point is located in a desirable HCCI operation region. The linearized version is the following standard state space form:

$$\bar{x}_{k+1} = A\bar{x}_k + B\bar{u}_k, \tag{2.26}$$

$$\bar{y}_k = C\bar{x}_k, \tag{2.27}$$

Table 2.3
Nominal operating point around which the nonlinear COM is linearized

Parameter	Value
CA50	6 CAD aTDC
T_{soc}	795 K
P_{soc}	2104 kPa
T_r	577 K
m_{evc}	0.0342 g
ON	8 (-)
Φ	0.43 (-)
T_{man}	90 °C
P_{man}	110 kPa
External EGR	0 %
N	800 rpm

where $\tilde{x}$, $\tilde{y}$ and $\tilde{u}_k$ are deviations of the state vector, the output, and the input from the nominal conditions, respectively. The discrete time state space matrices A, B, and C of Eqs. (2.26) and (2.27) linearized about the conditions in Table 2.3 are shown in Appendix A.1.

At this nominal operating point the linearized system $\tilde{x} = [C\tilde{A}50, \tilde{T}_{soc}, \tilde{P}_{soc}, \tilde{T}_{rg}, \tilde{m}_{evc}]^T$ is stable. This system has five states (n=5), one input, and one output. Accuracy of the linear COM (LCOM) is tested for the experimental transient fueling conditions (Figure 2.9). Results show that the average error and the standard deviation of error are about 1.6 and 1.7 CAD, respectively.

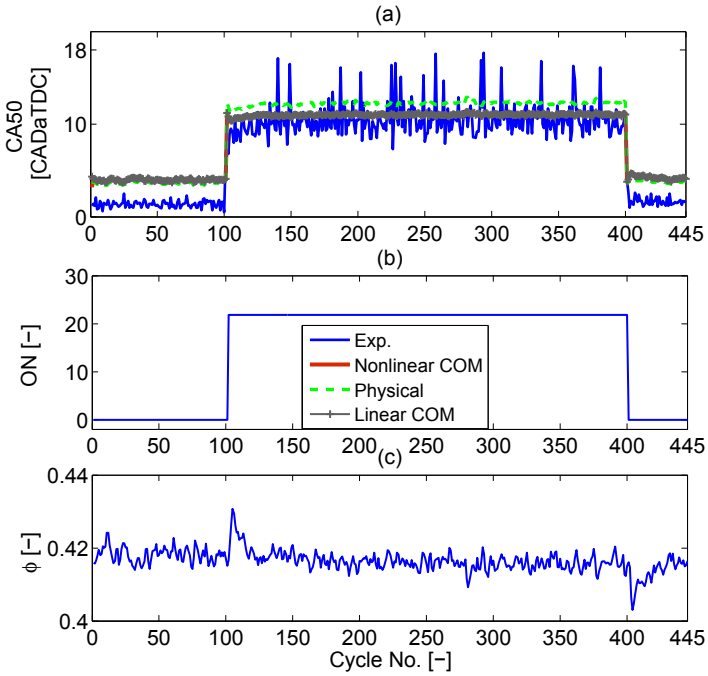

Figure 2.9: One cycle ahead prediction of LCOM, NCOM, and physical model compared to experimental data for a simultaneous fuel equivalence ratio and octane number step changes (P_m= 110 kPa, T_m= 91 °C, External EGR = 0%, P_{exh}= 99 kPa, $N \simeq$ 815 rpm).

2.5 Controller Design

2.5.1 Discrete-Time Sliding Mode Control (DSMC)

Discrete-time sliding mode control (DSMC), also known as quasi sliding mode control, [97, 98, 99] is chosen for HCCI ignition timing control since it provides a controller design which is robust to external disturbances and uncertainties of model

parameters [100]. Different DSMC designs are found in literature depending on what approach is used in determining sliding surface and designing switching laws. Here, a type of DSMC called discrete sub-optimal sliding mode control (DSSMC) [101] is used to control HCCI combustion phasing. In this type of controller, an optimal control law is used in determining the desirable sliding surface and the reaching phase. A Kalman filter is used to estimate the model states since most of them are difficult to measure on the engine.

2.5.1.1 Discrete Sub-optimal Sliding Mode Control (DSSMC) with Feed-Forward Gain

Discrete Sub-optimal Sliding Mode Control is a discrete optimization based control method that combines the advantage of optimal control with the robustness advantage of sliding mode control [101]. A discrete Linear Quadratic Regulator (LQR) suboptimal control law is used for determining the sliding surface and for driving the controlled system to the determined surface. In this method, the suboptimal approach is applied to deal with backward in time calculation problem. An online-disturbance rejection rule discussed by [102] is used to replace other conventional complex estimation methods [103, 104]. The DSSMC law is obtained by the following relation [101]:

$$u_k = -(C_s B)^{-1}[C_s A x_k + C_s E w_{k-1}], \tag{2.28}$$

$$C_s = \begin{bmatrix} G & 1 \end{bmatrix} T, \tag{2.29}$$

$$TB = \begin{bmatrix} 0_{n-m\times 1} & I_m \end{bmatrix}. \tag{2.30}$$

where $\tilde{w}$ is deviation of the vector of external disturbances to the controlled system from the nominal conditions, C_s is the sliding surface and T is an orthogonal transformation matrix that meets Eq. (2.30), m is a nonzero scalar, and G is calculated by:

$$G = K - S. \tag{2.31}$$

The K matrix in Eq. (2.31) is obtained by LQ optimization method and matrix S is found as a function of T and a constant positive definite symmetrical matrix (P) [101]:

$$S = -Q_{21}Q_{22}^{-1} \tag{2.32}$$

where:

$$Q = (T^{-1})^T H T^{-1} = \begin{bmatrix} Q_{11} & Q_{12} \\ Q_{21} & Q_{22} \end{bmatrix} \tag{2.33}$$

$Q_{11} \epsilon \Re^{n-m\times n-m}$, $Q_{12} \epsilon \Re^{n-m\times m}$, $Q_{21} \epsilon \Re^{m\times n-m}$, and $Q_{22} \epsilon \Re^{m\times m}$. The first term of Eq. 2.28 mainly relates to regulation characteristic of DSSMC while the second term is related to robustness and its disturbance rejection property. The main characteristic of DSSMC is robustness to external disturbances [101]. These disturbances can be in terms of uncertainties in the inputs. The designed DSSMC can mitigate uncertainties

in fueling amount, intake manifold temperature, and engine speed. But it cannot mitigate uncertainties in the boost pressure and mixture dilution (EGR).

A feed-forward gain (N_u) is added to enhancing the controller tracking performance [105] and the modified control law is:

$$u_k = -(C_s B)^{-1}[C_s A x_k + C_s E w_{k-1}] + N_u \bar{y}_{ref}, \tag{2.34}$$

where N_x and N_u are feed-forward gain matrices used to track the reference output trajectory ($\tilde{y}_{ref}$):

$$N_x \tilde{y}_{ref} = \tilde{x}_{ref} \qquad N_u \tilde{y}_{ref} = \tilde{u}_{ref}. \tag{2.35}$$

N_u is obtained for a system of n states (here n=5) by [105]:

$$\begin{bmatrix} N_x \\ N_u \end{bmatrix} = \begin{bmatrix} A - I_n & B \\ C & 0 \end{bmatrix}^{-1} \begin{bmatrix} 0_{n\times 1} \\ I_m \end{bmatrix} \tag{2.36}$$

where I represents the identity matrix that is a scalar due to the unity of output.

2.5.1.2 Constant Gain Kalman Filter

The states of the COM ($CA50$,T_{soc}, P_{soc}, T_{rg}, and m_{evc}) are not easily measurable on a real engine, so a constant gain Kalman filter state observer is designed. The

observed state vector ($\hat{X}$) is obtained by the following equation:

$$\hat{X}_{k+1} = A\hat{X}_k + B\hat{u}_k + B_1\tilde{w}_k + I(\tilde{y}_k - \hat{y}_k). \tag{2.37}$$

where $\hat{y}$ is the estimated value of model output and l is the Kalman gain vector found by solving an algebraic Riccati equation by using covariance of the engine plant measurement noise [106]. CA50 can be obtained by using an in-cylinder pressure sensor. If an in-cylinder pressure sensor is used P_{soc} can be measured too but accurate detection of SOC can be challenging for HCCI combustion. Thus accurate measurement of P_{soc} is not always possible. Experimentally CA50 [90] is often used. CA50 measurement includes cyclic variability and measurement noise. Cyclic variability can be deterministic or stochastic. In this study, the focus is on the stochastic cyclic variability. Stochastic cyclic variability and measurement noise are combined in a noise term for Kalman filter design.

2.5.1.3 Application of DSSMC for HCCI Combustion Phasing Control

Fluctuations in engine load (i.e. equivalence ratio, ϕ), intake manifold temperature, and engine speed are considered as disturbances to the HCCI engine. Thus, Eq. 2.26 is modified to:

$$\tilde{X}_{k+1} = A\tilde{X}_k + B\tilde{u}_k + B_1\tilde{w}_k, \tag{2.38}$$

where,

$$\tilde{w} = \begin{bmatrix} \tilde{\phi} & \tilde{T}_{man} & \tilde{N} \end{bmatrix}^T, \tag{2.39}$$

$$B_1 = \begin{bmatrix} -52.980 & -0.0572 & 0.085 \\ -9.7340 & 0.4500 & 0 \\ 577.60 & 0.1140 & -0.2720 \\ 466.70 & 0.0732 & 0.0024 \\ -0.0276 & 0 & 0 \end{bmatrix}, \tag{2.40}$$

By applying the DSSMC from to the linearized model, the sliding surface matrix is determined for HCCI combustion phasing control:

$$C_s = \begin{bmatrix} -0.0268 & 0.0107 & 0.1170 & -0.0476 & -0.1501 \end{bmatrix} \tag{2.41}$$

The observer gain vector obtained for this engine plant is:

$$I = \begin{bmatrix} 0.0972 & -0.0388 & -0.4243 & 0.1726 & 0 \end{bmatrix}^T \tag{2.42}$$

The structure of the DSSMC coupled with the Kalman filter is shown in Figure 2.10.

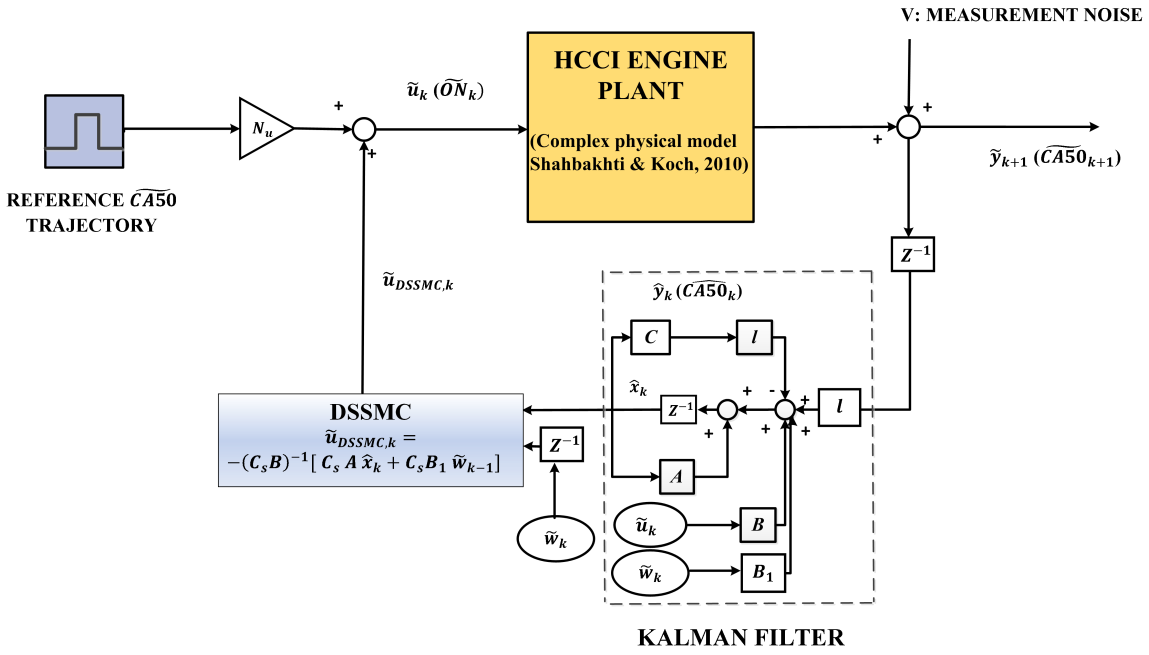

Figure 2.10: Schematic of HCCI combustion phasing controller.

2.5.2 Proportional Integral (PI) Controller

A discrete PI controller using Trapezoidal rule is designed to compare to the designed DSSMC. The discrete PI controller is:

$$G_c(z) = K_p + K_i \frac{T_s}{2} \frac{z+1}{z-1}, \tag{2.43}$$

where K_p= 0.8 and K_i= 5.35 and T_s=150 ms. The PI controller gains (k_p and k_i) are initially set using Ziegler and Nichols method. Then both gains are varied to examine the effect on rise time and maximum overshoot. T_s=150 ms is the simulation sample

time according to the engine speed at the nominal condition. More details for selecting optimal PI gains are found in the following.

2.5.2.1 Selection of PI Controller Gains

Variations in the controller gains are shown in Figures B.1 and B.2. These two figures show that for the selected values of gains (K_i=5.35,K_p=0.08), optimum control metrics including the maximum overshoot and rise time are achievable around the studied nominal operating point.

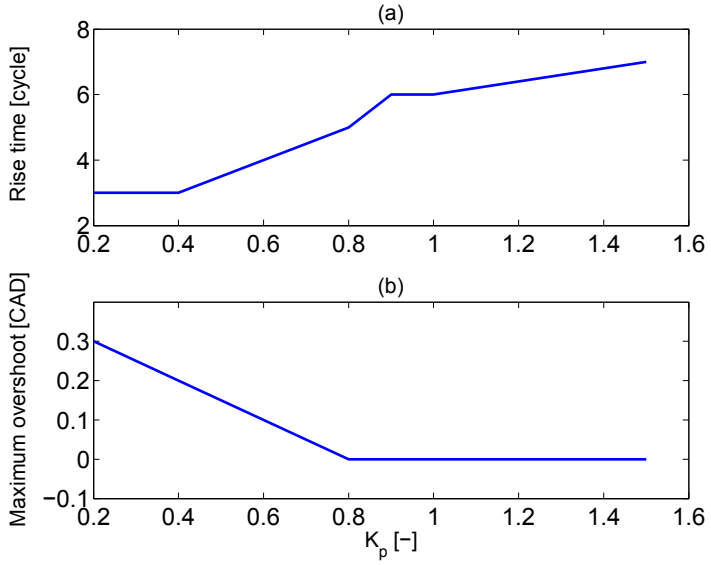

Figure 2.11: Variation of control metrics for different values of K_p (K_i=5.35).

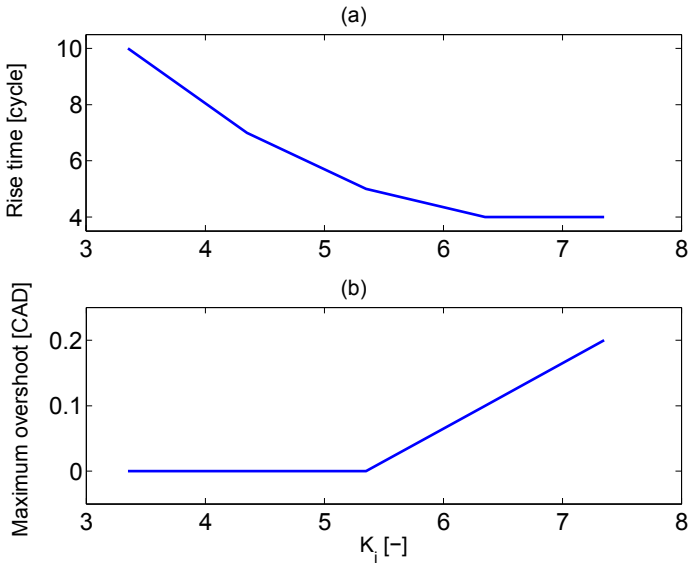

Figure 2.12: Variation of control metrics for different values of K_i (K_p=0.08).

2.6 Control Results

Using the detailed physical HCCI model [9] the DSSMC is tested. Performance of the DSSMC is then compared with the manually tuned discrete PI controller.

2.6.1 Tracking Performance

A comparison of tracking performance between the DSSMC and the PI controller for 100 engine cycles is shown in Figure 2.13. In this figure, the octane number input is adjusted by the controller to track the desired CA50s while all other variables are

constant. Both controllers perform well and no overshoot is observed in CA50 tracking results. However, the DSSMC has a 2 cycle faster rise time than the PI controller (rise times for the DSSMC and the PI controller are about 3 and 5 simulation engine cycles, respectively). Control results of DSSMC show a small steady state error (about 0.3 CAD). This is due to the model mismatch between the NCOM and the physical model.

Figure 3.6 shows the observer states corresponding to Figure 2.13. The accuracy of state estimation (RMSE) is also shown in Figure 2.13. The RMSE values indicate the designed observer estimates the model states with a good accuracy.

Next, the performance of the DSSMC and PI controllers are evaluated for sensor noise using noisy measurements of CA50. The noise model assumes a Gaussian distribution with a STD of 1.5 CAD to emulate CA50 cyclic variations and STDCA50 of 1.5 CAD is chosen based on the experimental observations in [10] for the normal level of cyclic variations in the Ricardo HCCI engine. The resulting simulation is shown in Figure 2.15. Under the sensor noise conditions, DSSMC has better performance with less cyclic variations as listed in Table 2.4. This is attributed to the observer attenuating the measurement noise.

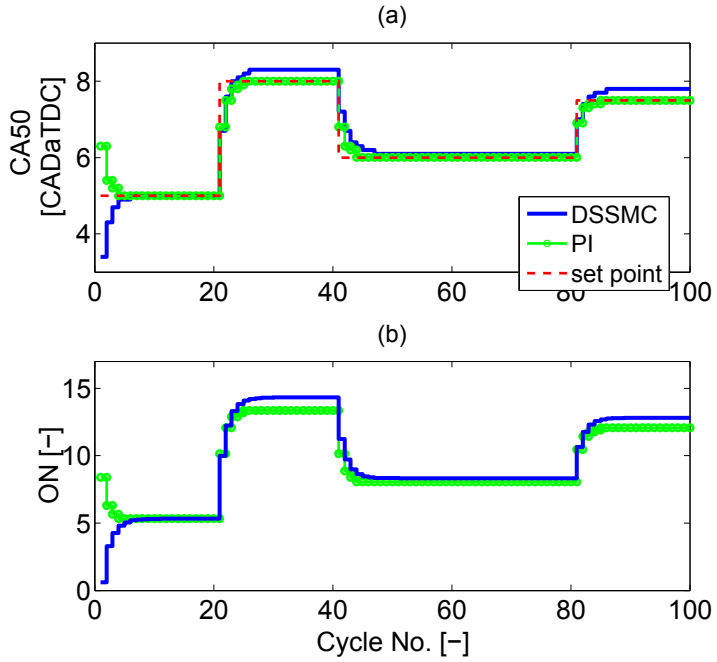

Figure 2.13: DSSMC and PI controllers tracking performance: (a) plant (complex model) output, (b) control input.

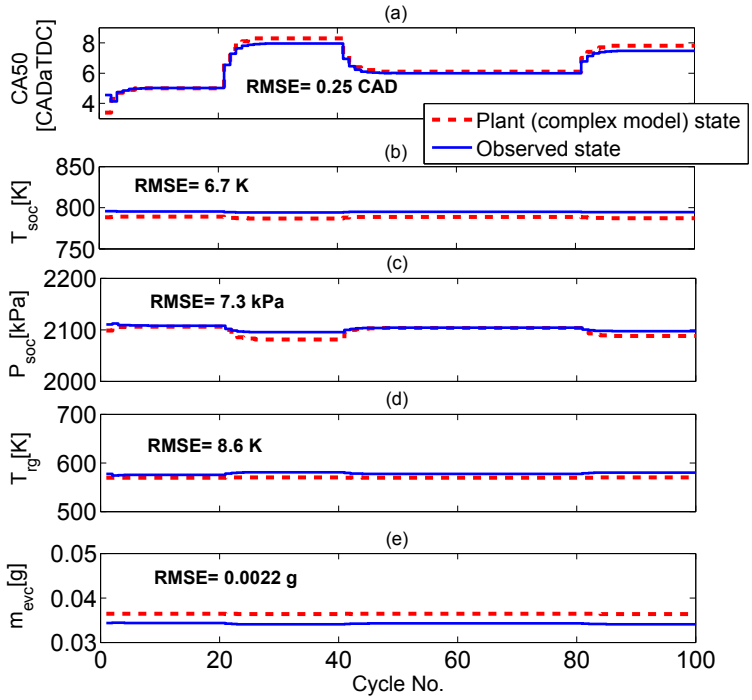

Figure 2.14: State estimation of observer states corresponding to Figure 2.13. RMSE is the root mean square of error values between states of the plant (complex model) and the estimated states.

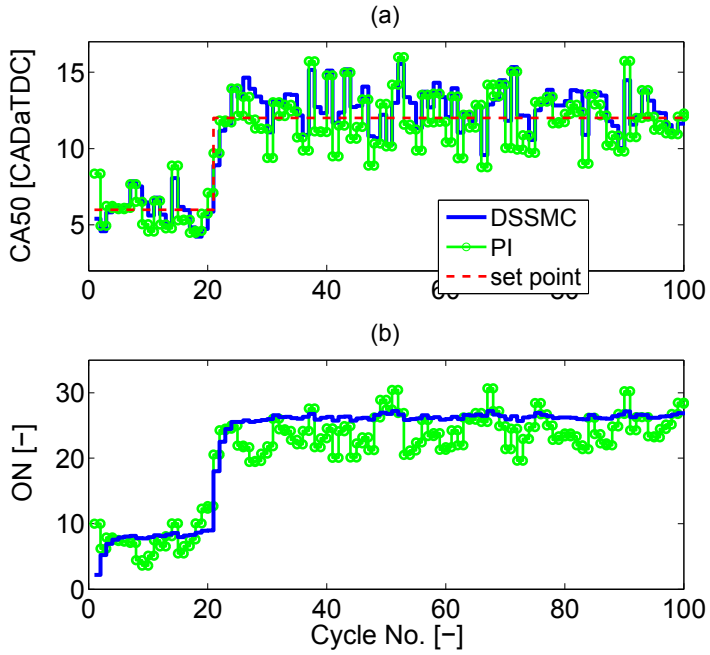

Figure 2.15: Performance of controllers with measurement noise ($STD_{noise} = 1.5CAD$): (a) plant (complex model) output, (b) control input.

Table 2.4
Average cyclic errors in tracking performance of DSSMC and PI controllers in Figure 2.15

Engine cycles	STD	
	DSSMC	PI
1-20	1.01	1.30
21-100	1.35	1.70

2.6.2 Robustness to Disturbances

A comparison for positive and negative step changes in disturbances of engine load, intake manifold temperature, and engine speed are shown in Figs. 14-16. Here the

output (CA50= 5 CADaTDC) is constant as the optimum set point using experimental data in [10]. To judge disturbance rejection, the maximum deviation from the desired CA50 and the number of engine cycles each controller takes to stabilize CA50 to the desired steady value (within 2%) are listed in Table 2.5. The DSSMC outperforms the PI controller for rejecting disturbances. For load disturbance rejection, the DSSMC has about 3.5 CAD less average deviation to retain the desired CA50 compared to that of the PI controller. Similarly the DSSMC better rejects intake temperature and engine speed disturbances since it can retain the desired CA50 with 1.7 CAD less maximum deviation. The DSSMC has also faster response (about 3 cycles faster) in rejecting CA50 deviations resulted from the disturbances.

Compared to the PI controller, the model-based DSSMC is able to incorporate knowledge of the system parametric changes. Although the integral action of the PI control is mainly responsible for robustness to the physical disturbances, applying the simple on-line disturbance rejection rule [102] inside the DSSMC structure enhances robustness property of this model-based controller in comparison with the PI controller. The model-based DSSMC can be utilized for other HCCI engines by parameterzing the controller model to correspond to the dynamics of a new engine.

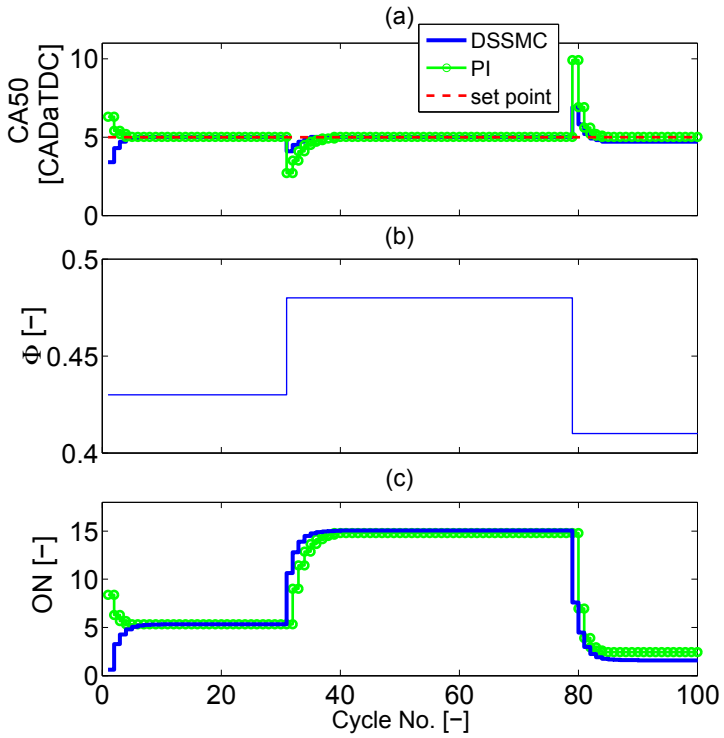

Figure 2.16: Disturbance rejection: fuel equivalence ratio (engine load) step changes: 0.43-0.48-0.41. (a) plant (complex model) output, (b) disturbance, (c) control input.

Table 2.5
Comparison of controller rejection to the physical disturbances

Disturbance	Controller	Max. Deviation [CAD]	Rejection Speed [cycle]
Φ	PI	5.0	7
	DSSMC	1.8	4
T_{man}	PI	1.5	5
	DSSMC	1.0	4
N	PI	4.5	6
	DSSMC	2.8	3

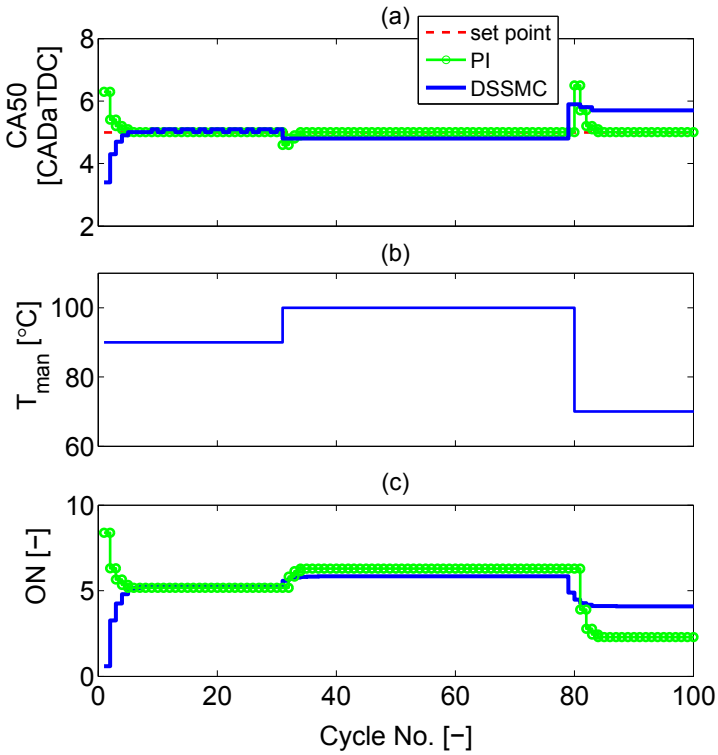

Figure 2.17: Disturbance rejection: intake temperature step changes: 90-100-70 °C (a) plant (complex model) output, (b) disturbance, (c) control input.

2.7 Summary

A NCOM is developed for predicting cycle-to-cycle HCCI combustion phasing. The NCOM is based on relations directly linked to thermodynamics of a blended-fuel HCCI engine cycle. First the model is validated against a detailed physical model and then is validated for transient operating conditions using experimental measurements. Sufficient accuracy in predicting HCCI combustion phasing and high computational efficiency make this model suitable for real-time engine control. Model processing

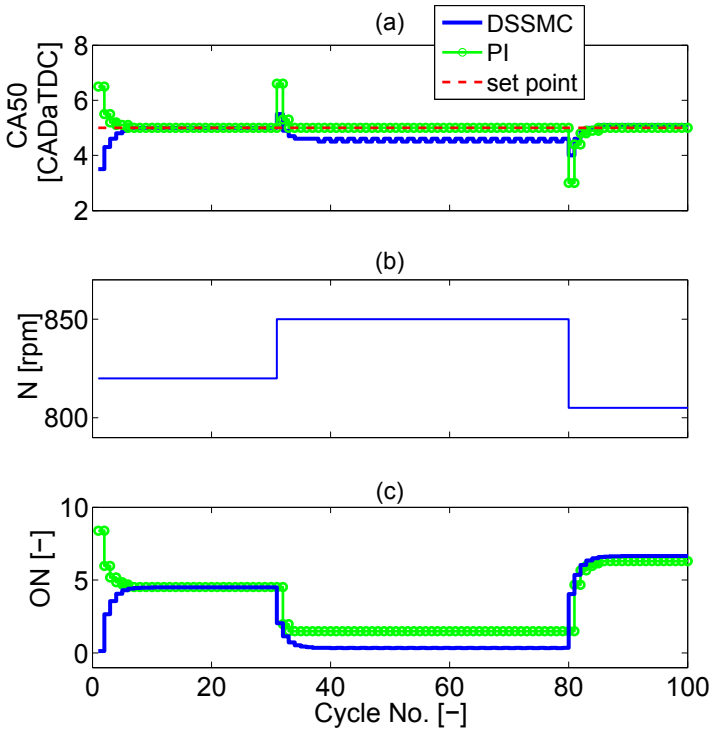

Figure 2.18: Disturbance rejection: engine speed step changes: 800 rpm- 850 rpm- 750 rpm (a) plant (complex model) output, (b) disturbance, (c) control input.

time for one engine cycle on a 2.67 GHz Intel processor is less than 1 ms.

The NCOM is used to design a model-based HCCI combustion controller by linearization around a nominal operating point. The point is chosen using the previous experimental observations in [10] to ensure that it is located in a desirable HCCI operation region. A discrete sub-optimal sliding mode controller along with feed-forward gain is designed to control HCCI combustion phasing (CA50) in a range of operating conditions. The controller adjusts the injected ratio of two fuels to change octane number and obtain a desired CA50. Performance of the controller is compared using a detailed physical model. Simulation results show the designed controller regulates

CA50 within a maximum of three engine cycles with no overshoot or chattering. Subject to step disturbances, the designed controller outperforms a PI controller for rejecting step disturbances of engine load, intake temperature, and engine speed and appears promising for real-time HCCI combustion timing control.

Chapter 3

Development of MIMO COM and Control of Combustion Phasing and Load[1]

This chapter outlines a framework for simultaneous control of HCCI combustion phasing and load (i.e., IMEP) on a cycle-to-cycle basis. The dynamic COM form Chapter 2 is extended to predict IMEP. Performance of the model is validated by comparison with the experimental data for 60 different steady state and transient HCCI conditions of the single cylinder Ricardo engine. A two-input two-output controller is

[1]The results of this chapter are partially based on [2] (Reprinted with permission from SAE International as shown in Appendix E, Section E.2).

designed to control combustion phasing and IMEP by adjusting fuel equivalence ratio and blending ratio of two PRFs. The designed controller consists of a Discrete Sliding Mode Controller (DSMC) and a feed-forward integral controller. The controller is tested on a detailed complex HCCI model to study tracking performance of both IMEP and combustion phasing over a range of HCCI operating conditions. In addition, disturbance rejection performance of the designed controller is studied for physical disturbances of engine speed and intake manifold temperature.

3.1 Introduction

Previous HCCI control studies in literature are divided into two main groups: single control and multiple control. Figure 3.1 outlines some of major HCCI control studies from these two groups along with the control variables and types of the HCCI controllers designed. In single control studies, one major variable of HCCI combustion phasing is adjusted by a single control input. [39, 41, 42, 43, 44, 48, 53] are examples of this group. CA50 is the most common combustion phasing variable used in HCCI control as explained in Chapter 2. Volume at the constant volume combustion event (V_{comb}) [49] and the crank angle at the peak pressure ($\theta_{P_{max}}$) [50] are other combustion timing variables used in HCCI control. Single control approach is very common in HCCI control, however multiple control approach is found in a number of HCCI control studies [40, 47, 49, 50, 51, 52]. In these studies, a secondary variable is

controlled besides the combustion phasing, including maximum in-cylinder pressure (P_{max}) [49, 50], Indicated Mean Effective Pressure (IMEP) [47, 89], Net Mean Effective Pressure (NMEP) [40, 51], and the exhaust gas temperature (T_{exh}) [52]. IMEP is the major indicator of the engine output work and is used in this work as the second control variable.

Figure 3.1 also shows different types of controllers which have been used for HCCI control. These include 1) manually tuned controllers such as Proportional Integral (PI) controller [45, 46], and Proportional Integral Derivative (PID) controller [43, 44]; 2) linear model-based controllers such as Linear Quadratic Regulator (LQR) [50, 52], Linear Quadratic Gaussian [43, 48], Pole placement state feedback controller [51], Integral state feedback controller [46, 47], H2 controller [49], and Model Predictive Controller (MPC) [39, 40, 89]; 3) nonlinear model-based controllers such as nonlinear observer-based controller [41, 42]. Fast tracking and strong disturbance rejection properties are the major requirements for a desirable HCCI engine controller. For multiple control approach, HCCI controllers should be able to simultaneously track the desired trajectories of the both outputs while maintaining the engine in the desired range against physical disturbances. In this work, a discrete type of Sliding Mode Controller (SMC) along with a feed-forward integral controller is used for simultaneous control of HCCI combustion phasing and IMEP. SMC is chosen for HCCI combustion timing control since it provides a controller design that is robust to external disturbances and uncertainties of model parameters. CA50 and IMEP are the

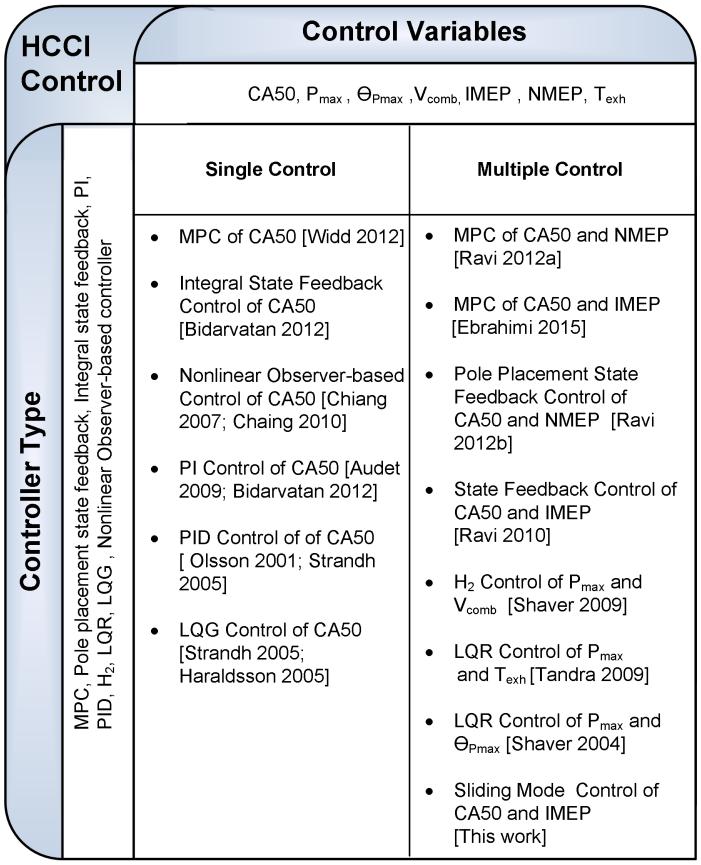

Figure 3.1: HCCI control background in the literature.

major indicators of combustion phasing and output work in HCCI engines. Thus, simultaneous control of CA50 and IMEP is critical for HCCI engines. CA50 can affect IMEP since CA50 directly influences the in-cylinder pressure trace. But IMEP depends on other engine variables such as injected fuel energy. Thus, combined control of CA50 and IMEP is required because single control of CA50 cannot offer a proper control over IMEP. Figure 2 confirms this speculation since IMEP in this figure does not necessarily follow the same trend as CA50. IMEP and CA50 both decrease in Figure 2(a) as the engine condition varies but the IMEP increases as the CA50 decreases

in Figure 2(b). Simultaneous control of CA50 and IMEP is a challenging HCCI control problem which is addressed in this work. The contribution from this chapter is twofold. First, a Control Oriented Model (COM) from Chapter 2 is extended and experimentally validated to predict both IMEP and CA50 in HCCI engines. Second, the application of DSMC for HCCI control is illustrated for combustion phasing and IMEP control. In the following section the COM from Chapter 2 is used and extended

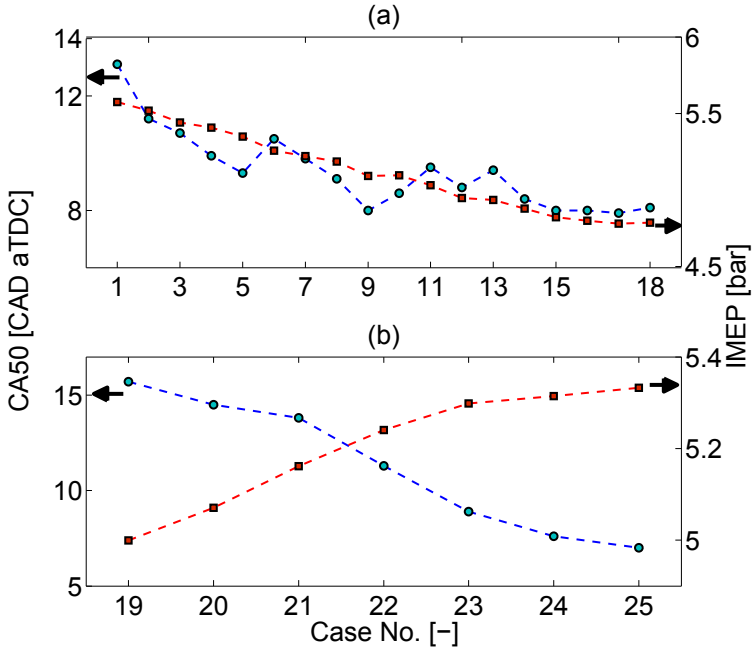

Figure 3.2: Variations of CA50 and IMEP for (a) variable fuel equivalence ratio and intake manifold temperature operation, (b) variable fuel equivalence ratio and intake manifold pressure operation. Engine conditions: (a) PRF40, N=810 rpm, EGR=0%, P_{man}= 89 kPa, ϕ sweep 0.66-0.71 and T_{man} sweep 80-123 °C, (b) PRF40, N=810 rpm, EGR=0%, ϕ sweep 0.42-0.61 and P_{man} sweep 96-127 kPa. Experimental data is taken from [10].

to predict both IMEP and CA50 in HCCI engines. Then, the model is experimentally validated at a large number of steady state and transient operating conditions. Next, a two-input two-output controller is designed for simultaneous control of CA50

and IMEP. Then, tracking performance of the new controller is tested by using a complex physical HCCI model from the previous work [9]. The disturbance rejection properties of the designed controller are also investigated against engine speed and intake manifold temperature disturbances. Finally, the summary from this chapter are presented.

3.2 control model description

The previous model from Chapter 2 is extended to predict cycle-to-cycle variation of both IMEP and combustion timing in an HCCI engine. The resulting physics-based COM will be able to capture behavior of HCCI engine in a complete engine cycle.

3.2.1 Definition of inputs, outputs, and model states

The inputs to the system are considered to be the following:

1. The fuel equivalence ratio (ϕ),

2. The octane number of the blended fuel mixture (ON), i.e. the volume percentage of iso-Octane in the mixture of iso-Octane and n-Heptane fuels.

The main outputs are the IMEP and CA50. The fuel equivalence ratio is used to vary the input fuel energy that directly affects the engines IMEP. HCCI combustion phasing is controlled by adjusting the ON value of the fuel. The following physical state variables are considered for modeling an HCCI engine cycle:

1. CA50
2. Temperature at the start of combustion (SOC), T_{soc}
3. Pressure at SOC, P_{soc}
4. In-cylinder mass at the exhaust valve closing (EVC), m_{evc}
5. Temperature of the trapped residual gases after EVC, T_{rg}

These five state variables are linked through state equations to describe the thermodynamics of engine operating cycle. Thermodynamic states of the in-cylinder air/fuel mixture at SOC are determined by T_{soc} and P_{soc}. Residual gasses of each engine cycle are mixed with the fresh charge of the next cycle. The resulting air/fuel mixture temperature at the intake valve closing (IVC) will affect the combustion phasing of the next engine cycle. Therefore residual gas properties (m_{evc} and T_{rg}) are selected in the list of states, so the residual gas coupling effect on HCCI combustion phasing is included.

3.2.2 IMEP Modeling

The developed COM was then extended to capture variations in IMEP. The IMEP was calculated using the pressure trace in the following equation:

$$IMEP_{k+1} = \frac{1}{V_{dis}} \oint PdV \tag{3.1}$$

where V_{dis} is the engine cylinder displacement volume. Eq. (3.1) was converted to the following equation by capturing the temperature variations during the compression and expansion strokes:

$$IMEP_{k+1} = m_{t,k+1} \frac{C_v}{V_{dis}} (T_{mix,k+1} - T_{soc,k+1} + T_{eoc,k+1} - T_{evc,k+1}) \tag{3.2}$$

3.3 Experimental Validation of the COM

The resulting COM is validated against the experimental data collected from the single cylinder Ricardo engine [26, 107]. The validation is done for both steady state and transient operating conditions.

3.3.1 Steady State Operation

Experimental data at 57 steady state engine operating conditions listed in Table 3.1 are used to evaluate the COM. The results are shown in Figure 3.3 and they indicate the COM can predict CA50 and IMEP with average errors of 1.3 CAD and 0.17 bar respectively for a large range of engine operation. Too late ignitions typically lead to larger cyclic variation of CA50 and IMEP as shown in Figure 3.3 (e.g., see data point numbers 20 and 21).

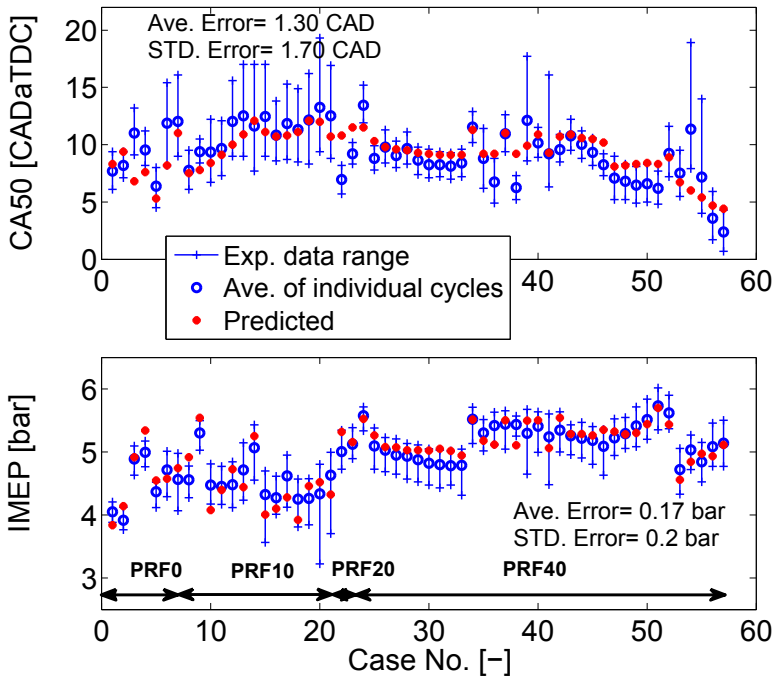

Figure 3.3: Steady-state validation of the COM.

Table 3.1
Steady state engine operating conditions used for validating the COM (57 operating points as in Figure 3.3.

Parameter	**Range**
Fuel	PRF0, PRF10, PRF20, PRF40
Φ (-)	0.38-0.72
N (rpm)	800-1000
T_{man}	79-148 °C
P_{man}	89-125 kPa

3.4 Transient Operation

Performance of the COM is also tested at transient fueling conditions. Figures 3.4-3.6 show comparison of the predicted and experimental CA50 and IMEP for step changes in the fuel equivalence ratio and octane number. Table 3.2 lists the quantitative values of the COM prediction for CA50 and IMEP under the experimental conditions shown in Figures 3.4-3.6. Results show that the COM has acceptable performances for predicting CA50 and IMEP. Simulation processing time of the COM on a 2.67 GHz Intel processor is about 0.10 sec for 445 engine cycles, i.e. 0.2 ms per engine cycle. Low processing time makes the COM a desirable simulation test bed to design real-time model-based CA50 and IMEP controllers.

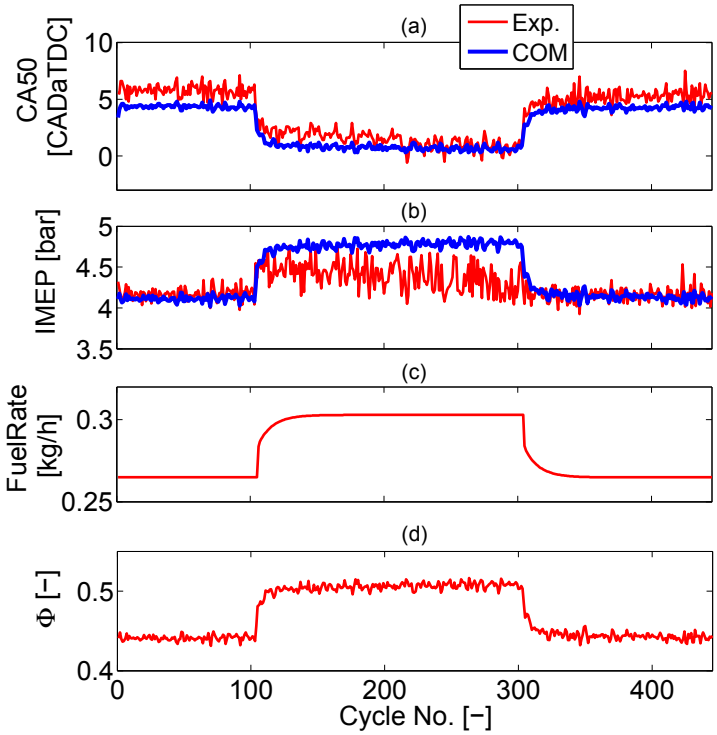

Figure 3.4: Cycle-to-cycle experimental validation of the two-input two-output COM for a step change in fuel equivalence ratio (ON= 0; P_m= 100 kPa, T_m = 67 °C, External EGR= 0%, P_{exh}= 97.3 kPa, $N \simeq$ 815 rpm).

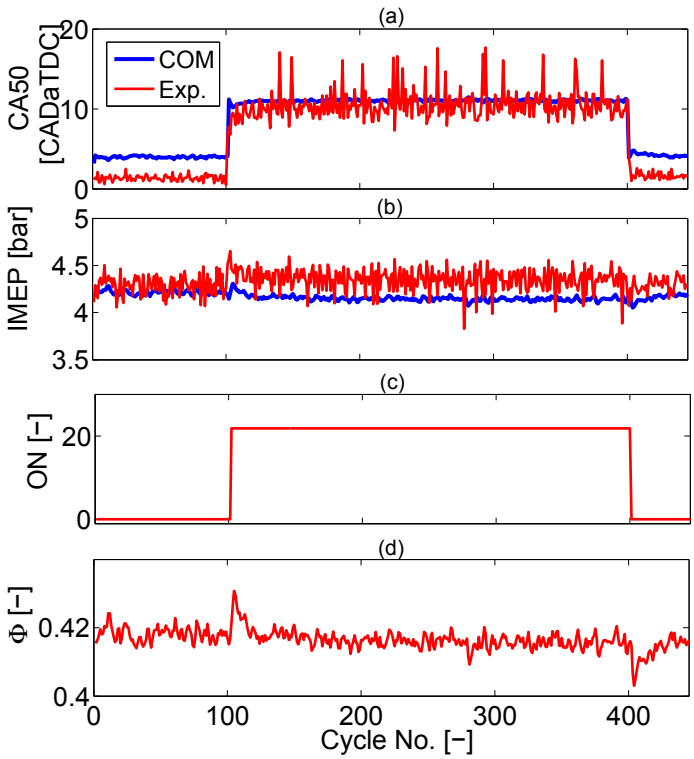

Figure 3.5: Cycle-to-cycle experimental validation of the two-input two-output COM for a step change in fuel octane number (P_m= 110 kPa, T_m = 91 °C, $\Phi \simeq 0.42$, External EGR= 0%, P_{exh}= 99 kPa, $N \simeq 815$ rpm).

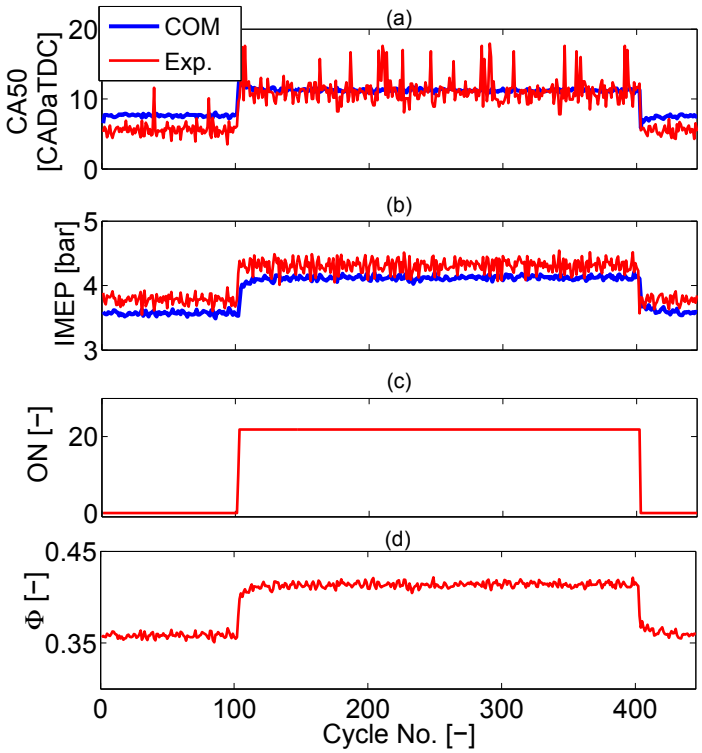

Figure 3.6: Cycle-to-cycle experimental validation of the two-input two-output COM for a step change in fuel equivalence ratio and octane number (P_m= 110 kPa, T_m = 91 °C, External EGR= 0%, P_{exh}= 99 kPa, $N \simeq$ 815 rpm).

Table 3.2
Accuracy of the COM in predicting CA50 and IMEP for the transient experiments in Figures 3.4-3.6.

Prediction accuracy	CA50 [CAD]	IMEP [bar]
Uncertainty[1]	±1.4	±0.16
Average error	1.4	0.23
RMSE[2]	1.7	0.19

[1]The prediction uncertainty is calculated based on the standard deviation of errors between the predicted and experimental CA50 or IMEP. [2]Root mean square of error between predicted and experimental results.

3.5 Model Equation Summary

The nonlinear COM in this chapter consists of the the COM described in Chapter 2 for CA50 prediction and the newly added IMEP submodel. The model states ($x = [CA50, T_{soc}, P_{soc}, T_{rg}, m_{evc}]$) and the first output y_1 ($CA50$) are obtained as functions of the model states of the previous cycle and the first input u_1 (ON).

$$\begin{aligned} x_{k+1} &= F(x_k, u_{1,k}) \\ y_{1,k} &= G(x_k, u_{1,k}) \end{aligned} \tag{3.3}$$

Variation of IMEP in relation to ϕ is determined by solving the equations of the nonlinear COM including the IMEP submodel equations in 3.1 and 3.1. The results are then used to form a condensed physical $IMEP - \phi$ map which is used for the IMEP controller design.

3.5.1 Model Linearization

The nonlinear COM is linearized around a nominal operating point. Operating condition at this point is shown in Table 3.3. This point is selected according to the experimental results in [10] to ensure that the selected point is located inside the

engine optimal operating region with low cyclic variations. The resulting linear state-space model is:

$$\bar{x}_{k+1} = Ax_k + Bu_k, \tag{3.4}$$

$$y_k = Cx_k, \tag{3.5}$$

Table 3.3
Nominal operating point around which the nonlinear COM is linearized

Parameter	Value
CA50	8 CAD aTDC
T_{soc}	795 K
P_{soc}	2078 kPa
T_r	563 K
m_{evc}	0.035 g
ON	10 (-)
Φ	0.40 (-)
T_{man}	363 K
P_{man}	110 kPa
External EGR	0 %
N	815 rpm

Values of the elements of the linear model matrices are shown in Appendix A.2. Poles of the system are: $0.0018 \pm i002$, 0, 0; all are inside the unit circle so the system is stable around the selected operating point.

3.6 Controller Design

Experimental results in [9, 10, 27] show that variation of ON can be used to advance or retard HCCI combustion phasing, while has a strong impact on IMEP. Here, CA50 and IMEP are controlled by two separate controllers using two independent inputs. CA50 is controlled by adjusting ON, while IMEP is controlled by adjusting ϕ. The two-input two-output controller in this work includes 1) a DSSMC to track the desired CA50 trajectory by manipulating the ratio of the blended fuel mixture, and 2) an integral feed-forward sub-controller for IMEP control. Changes in the engine operating conditions such as changes in the intake temperature or the engine speed affect CA50 and IMEP in HCCI engines [10]. Here, both controllers are designed such that they can reject any physical disturbances from the engine. Furthermore, each sub-controller (e.g. CA50 controller) can reject any disturbance caused by the input actuated by the other sub-controller (e.g. IMEP controller). Details of DSSMC design were presented in Chapter 2. The state observer in this chapter is different. Thus, only details of the observer and IMEP sub-controller are discussed in this chapter.

3.6.1 State Observer Design

A Luenberger state observer [105] is designed to estimate the model state variables since most of the states are not easily measurable in practice. The observed states are then used by the DSSMC to determine the appropriate control input to the engine plant. Eq. (3.6) shows how the model states ($\hat{X}$) at k+1 cycle are determined using the previously estimated states, the estimated output ($\hat{y}_1$), and the engines physical disturbances from the previous cycle (k).

$$\hat{X}_{k+1} = A\hat{X}_k + B\hat{u}_{1,k} + B_1\tilde{w}_k + l(\tilde{y}_{1,k} - \hat{y}_{1,k}). \tag{3.6}$$

where l is the Luenberger gain vector which is found by a pole placement technique [105]. $w = [\phi, T_{man}, N]^T$ is the vector of physical disturbances.

3.6.2 Feed-forward Integral IMEP Sub-controller

An IMEP-ϕ map is obtained by running a detailed physical HCCI model [9] for a range of operating conditions to determine the engines IMEP in response to the changes in the fuel equivalence ratio:

$$u_{2,k_{map}} = c_1 y_{2,k} + c_2. \tag{3.7}$$

In addition, an integral gain (K_i) is added to cancel any steady state error. The integral controller is able to reject the effects of the engine physical disturbances including T_m and N on the engine plant IMEP. The sampling time of 150 ms is selected for the integral controller, taking into account the engines nominal speed of 815 rpm. Eventually the second control input is calculated by:

$$u_{2,k} = u_{2,k_{map}} + u_{2,k_i}, \tag{3.8}$$

where u_{2,k_i} is the control input actuated by the integral controller. Structure of the combined CA50 and IMEP controller is shown in Figure 3.7. Values of the controller parameters are as follows:

$$C_s = \begin{bmatrix} -0.0619 & 0.0791 & 0.8536 & -0.1182 & -0.0125 \end{bmatrix} \tag{3.9}$$

$$N_u = 3.1415$$

$$l = \begin{bmatrix} 0.0014 & 0.3564 & -0.3409 & -0.0001 & 0 \end{bmatrix}^T$$

$$K_i = 30.$$

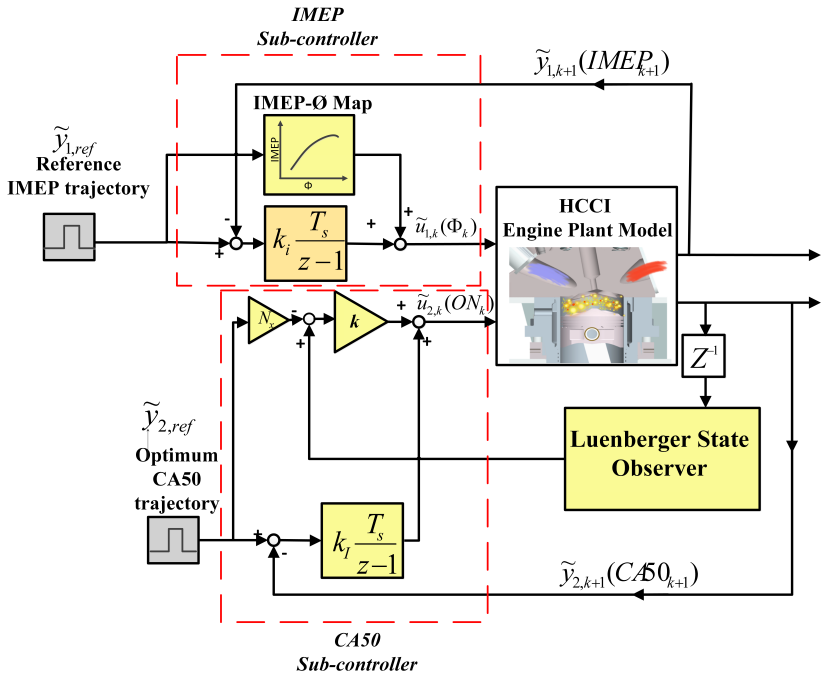

Figure 3.7: Structure of CA50 and IMEP controller.

3.7 Control Results

The complex physical HCCI model from [9] is used to test the performance of the designed two-input two-output HCCI controller. In this section, the tracking and regulation performance of the controller is studied. Next, the disturbance rejection properties of the controller are evaluated for step changes in the engine speed and the intake manifold temperature.

3.7.1 Tracking and Regulation Performance

Tracking performances of controllers are tested for positive and negative step changes in the desired CA50 and IMEP. Figure 3.8(a) shows the tracking results when one of the CA50 and IMEP setpoints are changed, while Figure 3.8(b) shows the tracking results when CA50 and IMEP setpoints are simultaneously changed. In the first simulation period (cycles: 1 to 70) in Figure 3.8(a), positive and negative step changes of desired IMEP evaluate the tracking performance of the IMEP sub-controller. While a constant desired CA50 is considered to study how the DSSMC can regulate output CA50 at the desired value (i.e., 8 CAD aTDC) and cancel effects of the ϕ variations on it. In the second simulation period (up to cycle ♯140), the tracking performance of the DSSMC is studied for positive and negative step changes of the desired CA50 while the IMEP sub-controller is responsible to regulate the output IMEP at the desired constant value of 4 bars. Figure 3.8(b) shows how the controller tracks CA50 and IMEP while there are simultaneous step changes in the desired values. No overshoot and chattering are observed in sliding mode control of CA50. Quantitative performance metrics for tracking and regulation performance of the controllers are shown in Table 3.4. The steady state error for CA50 tracking is due to the mismatch between the COM and the complex physical model [9]. Results show that the two-input two-output controller is able to track both CA50 and IMEP within 3 simulation engine cycles.

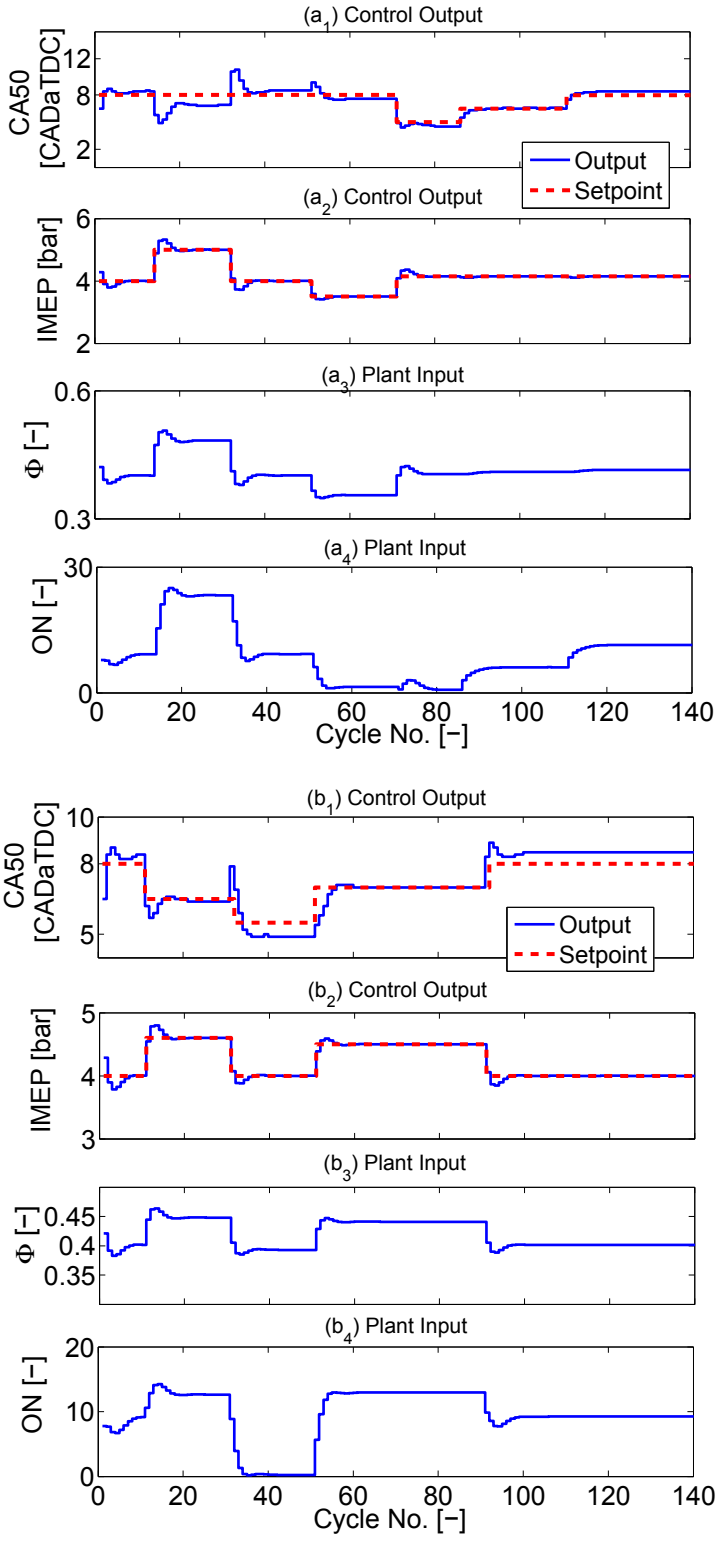

Figure 3.8: Tracking performance of the CA50 and IMEP controller: (a) Single tracking of CA50 and IMEP, (b) Simultaneous tracking of CA50 and IMEP.

Table 3.4
Average tracking performance metrics for CA50 and IMEP controller in Figure 3.8 (RT: Rise Time, SSE= Steady-state Error).

Performance metric	CA50 sub-controller	IMEP sub-controller
RT	3 cycles	1 cycle
Maximum overshoot	0 CAD	0.35 bar
SSE	0.5 CAD	0 bar
Cycle needed for regulation	4 cycles	4 cycles

Performance of the designed Luenberger observer for tracking the reference trajectories of Figure 3.8 is demonstrated in Figure 9. The Luenberger state observer performance is tested under condition of having variation in CA50 or IMEP setpoint (Figure 3.9(a)) and also condition of having simultaneous step variations in both CA50 and IMEP setpoints (Figure 3.9(b)). Average error (e_{ave}) and standard deviation error (σ_e) between estimated and complex model states are less than 0.5 CAD for CA50 and less than 2% for other four states. Thus, the designed state observer is accurate enough for use in the DSSMC.

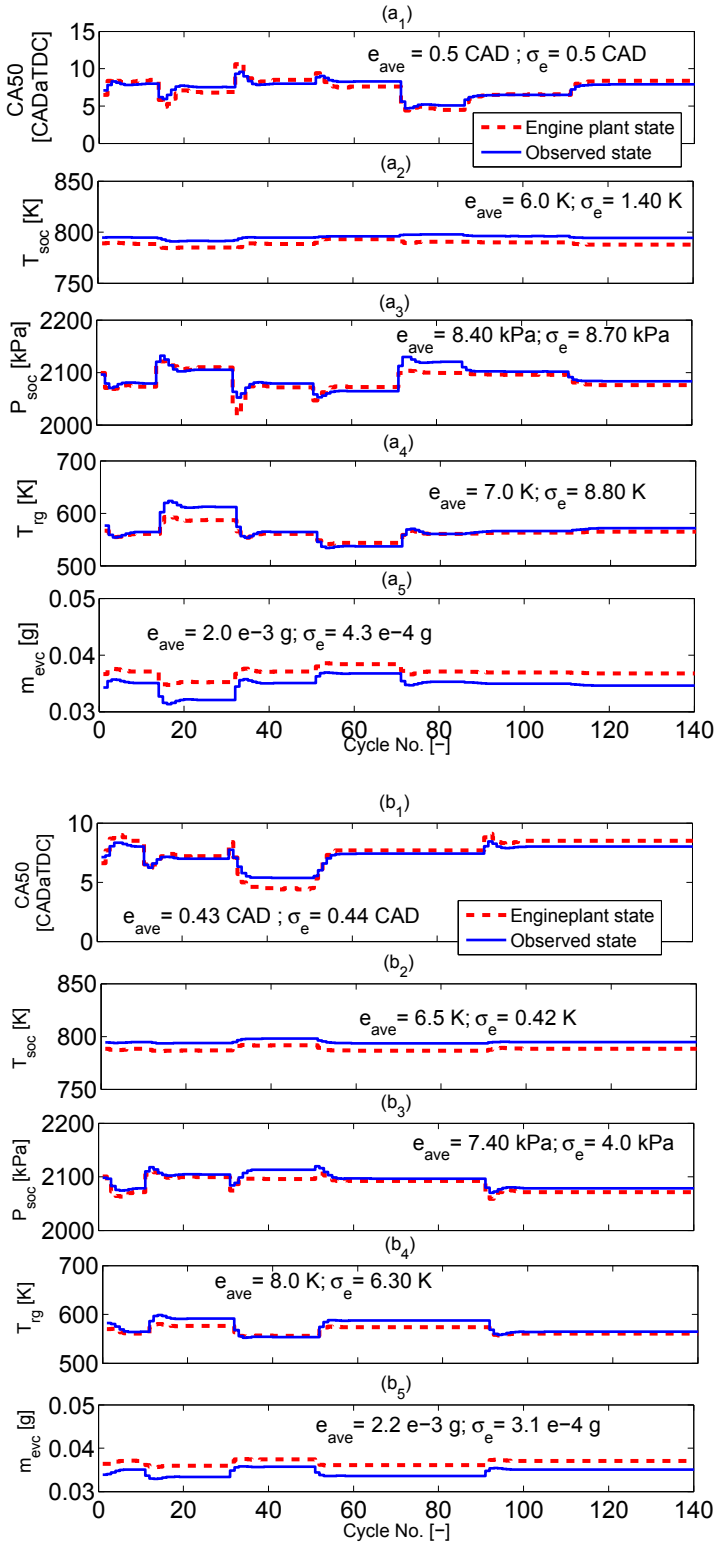

Figure 3.9: Performance of the state observer for estimation of model states during tracking conditions in Figure 3.8 (e_{ave} : average error,σ_e: standard deviation of error).

3.7.2 Disturbance Rejection Performance

Performance of the designed two-input two-output controller is now studied under conditions of having physical disturbances (i.e. variations in engine speed and intake manifold temperature). Figures 10 and 11 show how the controller can reject positive and negative step disturbances and cancel their effects on the output CA50 and IMEP. Here a constant CA50 of 7 CAD aTDC is selected as the optimum set point using the experimental data in [5]. An open loop control system is also included for comparison. The metrics for the disturbance rejection performance of the controller are listed in Table 7. They include the maximum deviations of CA50 and IMEP from the reference values and the number of engine cycles takes to stabilize the outputs. For the disturbance conditions tested in Figures 10 and 11, the designed model-based controller regulates CA50 and IMEP within 3-6 simulation engine cycles while the maximum CA50 deviation is 50% less than the open loop control system.

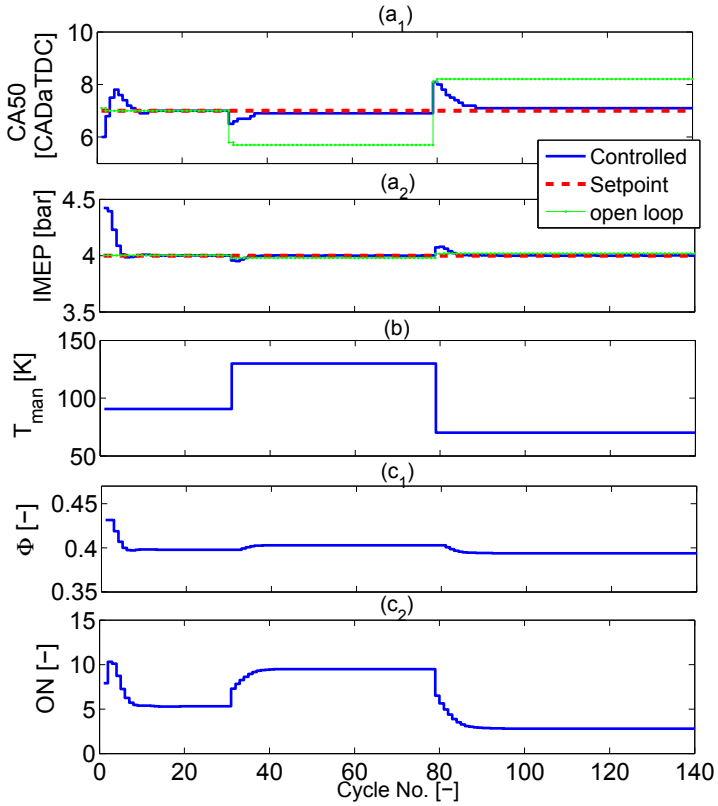

Figure 3.10: Disturbance rejection: Intake manifold temperature step changes (90-130-70 °C): (a) Plant (complex HCCI model) outputs, (b) Physical disturbance, (c) Control inputs.

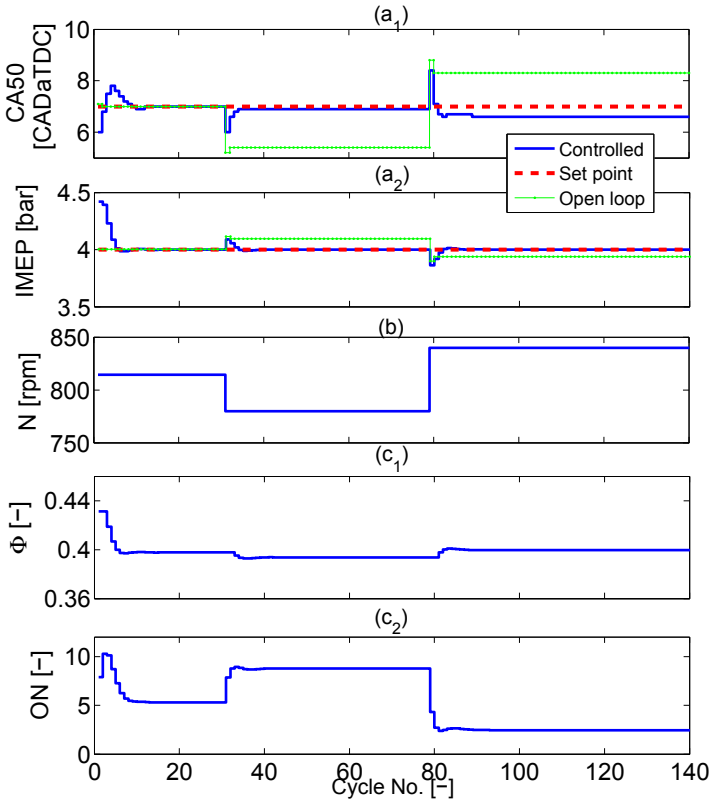

Figure 3.11: Disturbance rejection: Engine speed step changes (815 rpm-780 rpm-840 rpm): (a) Plant (complex HCCI model) outputs, (b) Physical disturbance, (c) Control inputs.

Table 3.5
Disturbance rejection performance metrics of the CA50 and IMEP controller.

Disturbance	Control output	Max. absolute deviation	Max. absolute open-loop deviation	Rejection speed [cycle]
T_{man}	CA50 [CADaTDC]	1.1	2.5	6
	IMEP [bar]	0.1	0.1	4
N	CA50 [CADaTDC]	1.5	3.4	3
	IMEP [bar]	0.14	0.14	3

3.8 Summary

A COM was extended to predict cycle-to-cycle IMEP and CA50 for a blended fuel HCCI engine. The COM was validated with the HCCI experimental data at 57 steady state and 3 transient operating conditions. The validation results indicate the COM can predict CA50 and IMEP with an average error of 1.4 CAD and 0.2 bar respectively. The COM is computationally efficient and it only requires 0.2 ms to simulate an engine cycle on a 2.67 GHz Intel processor. The COM was then utilized to design a two-input two-output HCCI controller for tracking desired cycle-to-cycle IMEP and CA50. The new controller is a model-based engine controller which combines a DSMC with a feed-forward integral controller. This is, to the authors knowledge, the first application of DSMC for HCCI engine control. The designed controller can track the desired IMEP and CA50 trajectory in a maximum of 4 engine cycles. No overshoot and chattering were observed in sliding mode control of combustion phasing. Performance of the controller was also evaluated under physical disturbances when the intake manifold temperature and the engine speed suddenly change. The simulation results show that the controller can reject these two physical disturbances in 3 to 6 engine cycles, while maintaining CA50 and IMEP deviation within 1.5 CAD and 0.1 bar. Given the low computational time and good prediction accuracy, the new COM and the designed model-based combustion controller are suitable for real-time HCCI engine control.

Chapter 4

Control of Combustion Phasing and Load with Indirect Control of Exhaust Gas Temperature and Emissions[1]

Control of HCCI combustion phasing, load, and exhaust aftertreatment system is essential for realizing high efficiency HCCI engines, while maintaining low THC and CO emissions. This chapter introduces two different new methodologies for integrated HCCI engine control. In the first methodology, a novel performance index is defined to

[1]The results of this chapter are partially based on [3, 4, 5] with permissions from Elsevier and ASME as shown in Appendix E, Section E.3.

characterize different HCCI operating regions. The experimental data from the single cylinder engine at 214 operating conditions is used to determine the performance index for the blended fuel HCCI engine. The new performance index is then used to design an optimum reference trajectory for a multi-input multi-output HCCI controller. The optimum trajectory is designed for control of combustion phasing and IMEP, while meeting catalyst light-off requirements for the exhaust aftertreatment system. The designed controller is tested on a previously validated physical HCCI engine model.

In the second methodology, a computationally efficient grey-box model is developed for predicting major HCCI engine variables. The grey-box model consists of a combination of physical models and three feed-forward artificial neural networks models to estimate six major HCCI variables including combustion phasing, load, exhaust gas temperature, Total Hydrocarbon (THC), CO, and NO_x emissions. The grey-box model is experimentally validated over a large range of HCCI engines operation including 309 steady state and transient test conditions for two different HCCI engine applications. A Genetic Algorithm optimization method is applied to simulation results from the grey-box model to determine the optimum CA50s leading to minimum HCCI emissions at different engine loads. The optimum CA50 trajectory is then utilized in design of a model-based CA50-IMEP controller to simultaneously control combustion phasing and load while minimizing the HCCI engine-out emissions.

4.1 Introduction

HCCI typically has a low T_{exh}, as low as 120 °C [36] while the light-off temperature (the temperature at which the catalyst becomes more than 50 percent effective) is about 250 to 300 °C [37, 38] for most catalysts. Therefore, abatement of THC and CO by oxidation catalysts is limited in HCCI engines; thus, control of T_{exh} is essential to increase the exhaust aftertreatment efficiency. This chapter centers on developing methodologies to determine an optimum combustion phasing as an integrated target to minimize tailpipe exhaust emissions and raw emissions while providing required engine load.

Figure 4.1 outlines some of the major HCCI control studies along with the control variables and types of HCCI controllers designed. Studies can be divided into three major groups, depending on the control variables involved: 1) combustion phasing, 2) engine load, 3) exhaust gas temperature and raw. The first two groups were explained in Chapter 3. The third group includes control of i) T_{exh} to ensure high conversion efficiency of the exhaust aftertreatment system, and 2) engine raw emissions. In [52], simultaneous control of T_{exh} and maximum pressure (P_{max}) was studied while in [53], a constraint-based control technique was used for T_{exh}. An integrated control of all three major engine outputs (i.e. load, CA50, and T_{exh}) is essential for realizing HCCI as a viable solution. In this chapter a model-based control framework is presented to

adjust CA50 and IMEP, while indirectly controlling T_{exh} based on an optimum CA50 to lower tailpipe exhaust emissions.

In addition, a comprehensive grey-box MIMO model is proposed that can predict all the major HCCI engine variables including combustion phasing, load, T_{exh}, and engine-out emissions of THC, CO, and NO_x. To the best of the author's knowledge, this is the first study on developing a MIMO HCCI grey-box model that can predict both the engine performance parameters and the main HCCI engine emissions. The grey-box model is experimentally validated and can be used for either evaluation or design of model-based HCCI controllers. The grey-box model is combined with an optimization genetic algorithm to find the optimum combustion phasing which minimizes engine-out emissions of THC and CO. Therefore a framework is achieved for simultaneous control of CA50, IMEP, and engine-out emissions.

All the previous studies [1, 2, 39, 40, 41, 42, 43, 44, 45, 46, 47, 48, 49, 50, 51, 52, 53, 79, 80, 89, 108] have used a constant trajectory for desired CA50, but these two approaches are not suitable for an integrated HCCI control. This is because CA50 affects three main factors including HCCI emissions, exhaust gas temperature, and engine load [36]. Desired CA50 is different among these three factors and it varies by changing engine operation region. Thus, desired CA50 should be variable to include different changing factors. To the best of the author's knowledge, this work provides the first study to determine a varying desired CA50 trajectory for an

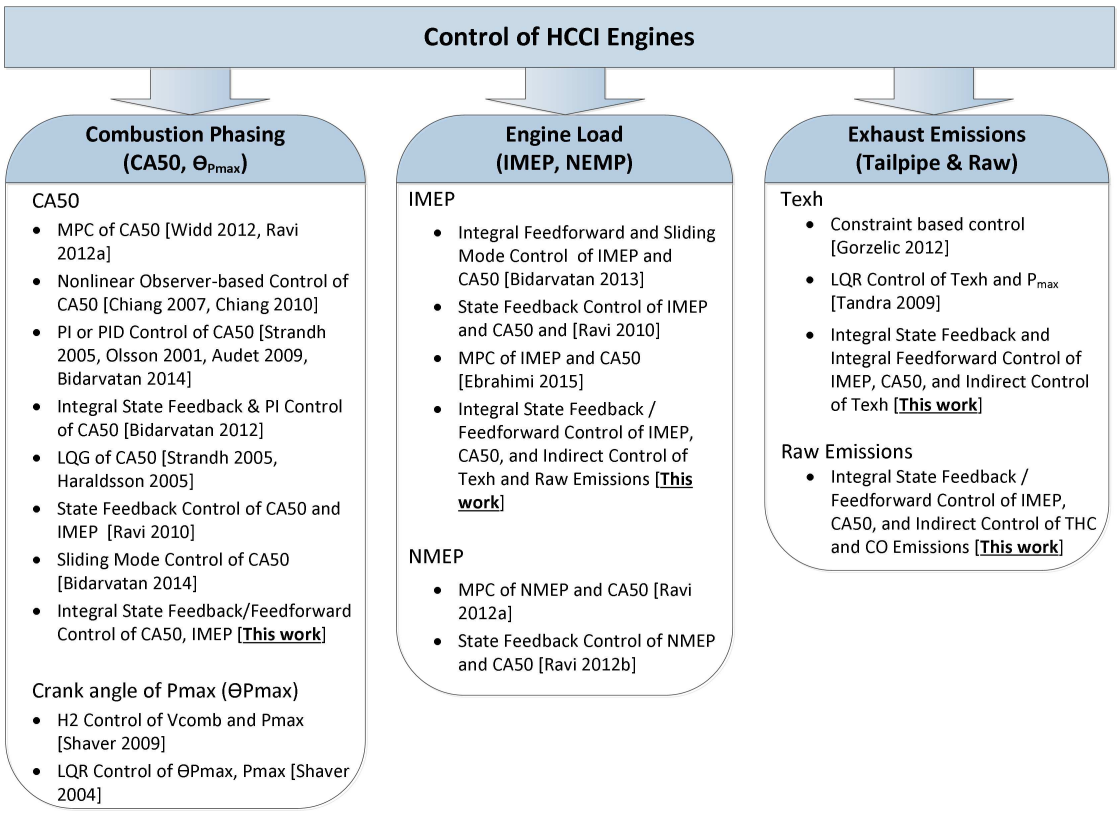

Figure 4.1: Background of HCCI engine control in the literature based on the control variables.

integrated HCCI control. In the first methodology, the desired CA50 is determined by using a performance index which incorporates considerations for engine raw emissions, exhaust aftertreatment efficiency, and engine load. In the second methodology, the desired CA50 is determined by using combination of a grey-box model and genetic algorithm.

The contribution from this chapter is four fold. First, two novel methodologies for integrated HCCI engine control based on i) an integrated performance index and ii) grey-box modeling are developed. Second, a new algorithm is developed to determine Optimum Combustion Phasing (OCP) trajectory for HCCI control based on

the developed performance index. Third, the first MIMO grey-box model that can predict major HCCI engine output variables is presented. Fourth, the applications of both proposed performance index-based and grey-box model-based methodologies are illustrated for control of IMEP and CA50 in an HCCI engine.

4.2 Integrated HCCI Engine Control Based on a Performance Index

In this section, a methodology based on a proposed performance index of HCCI engine is presented. The methodology is used to find the OCP for optimal indirect control of engine raw emissions and aftertreatment efficiency.

4.2.1 Experimental Data Analysis

HCCI experimental data from [26] at 214 steady state operating conditions is used in this study. The experimental data is collected from a single cylinder HCCI Ricardo engine with the same specifications as listed in Chapter 2. The experimental data includes a large range of HCCI engine operation as shown in Figure 4.2. Three different blends of two Primary Reference Fuels (PRFs), i.e. iso-Octane (PRF100) with octane number of 100 and n-Heptane (PRF0) with octane number of 0 are used

in this study. These fuel blends include PRF0, PRF20 (20% iso-Octane and 80% n-Heptane), and PRF40 (40% iso-Octane and 60% n-Heptane).

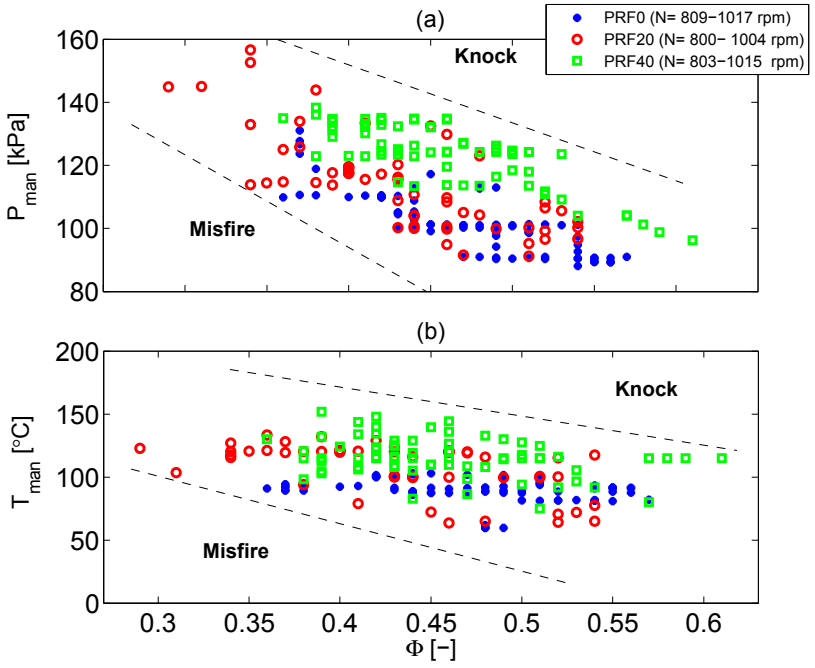

Figure 4.2: Engine operating range for 214 steady-state experimental data points (EGR0%).

The major engine variables in the experimental data include ϕ, P_{man}, and T_{man}. The HCCI engine operation is limited by knock and misfire limits as observed in Figure 4.2. To avoid knock, only lean air-fuel mixtures ($0.3<\phi<0.6$) are used, as seen in Figure 4.2. Running the engine at higher values of ϕ could have been done by using EGR. Figure 4.3 shows ranges of engine output conditions (i.e. engine load, exhaust gas temperature, and exhaust gas concentrations) for the same data points as in Figure 4.2.

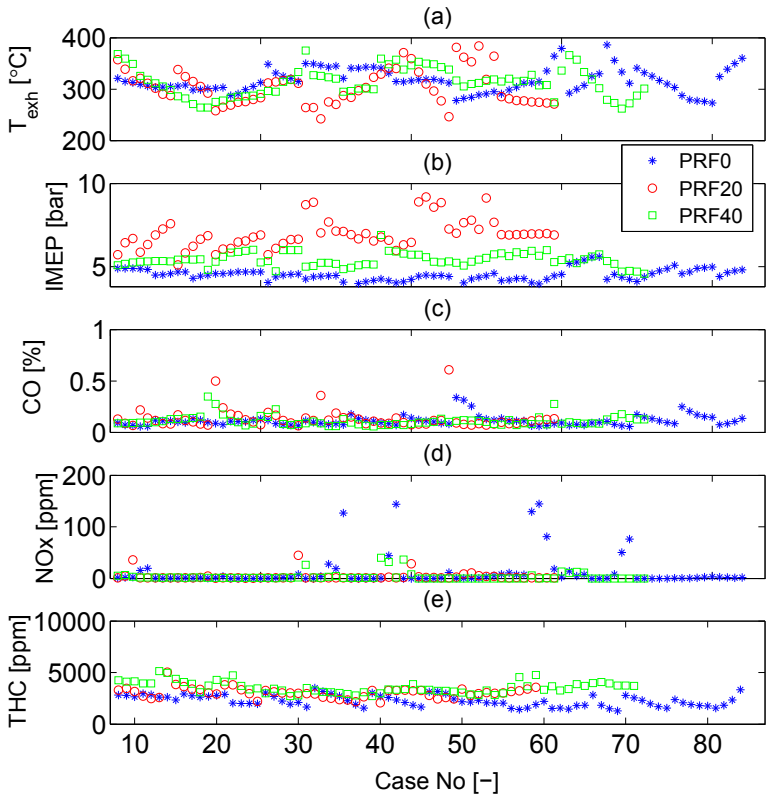

Figure 4.3: Range of the load, exhaust temperature, and exhaust emission concentrations for the experimental data points shown in Figure 4.2.

Results in Figure 4.3 show that about 33% of the data points have T_{exh} less than 300 °C while Texh can be as low as 240 °C. The light-off temperature (the temperature at which the catalyst becomes more than 50 percent effective) is about 250–300 °C for most catalysts ([37, 38, 109]). It is important to ensure that exhaust temperature remains above catalyst light-off temperature, thus high HC and CO emissions in HCCI can be mitigated by an oxidation catalyst. Results in Figure 4.3 also show that NOx is negligible for most HCCI conditions. Thus, HC and CO emissions are the critical factors for an HCCI controller to minimize engine-out emissions.

4.2.2 Performance Index for HCCI Control

A new Performance Index (PI) is proposed to determine the optimum trajectory for HCCI combustion phasing. The performance index is defined based on the engine load, engine raw emission concentrations, and exhaust aftertreatment efficiency:

$$PI = \frac{1}{2}(LI + TEI) \tag{4.1}$$

where LI is the load index as the ratio of IMEP to the maximum IMEP.

$$LI = \frac{IMEP}{IMEP_{max}} \tag{4.2}$$

TEI is the tailpipe emission index including raw emissions and aftertreatment efficiency:

$$TEI = \frac{1}{2}(REI + AEI) \tag{4.3}$$

where REI is the engine raw emission index and AEI is the aftertreatment efficiency index:

$$REI = 1 - \frac{1}{3}(\frac{CO}{CO_{max}} + \frac{NOx}{NOx_{max}} + \frac{THC}{THC_{max}}) \tag{4.4}$$

$$AEI = \frac{T_exh}{T_{exh,max}} \tag{4.5}$$

CO (in percentage), NO_x (in ppm), and THC (in ppm) are concentrations of carbon monoxide, nitrogen oxides, and unburned hydrocarbon respectively. The subscript max denotes the maximum value, which is determined based on the collected experimental data for an engine (e.g. Figure 4.3).

Figure 4.4 shows normalized variation in the engine performance index with respect to normalized changes in the engine load, exhaust gas temperature, and exhaust emission indices. To have a better understanding of the relative variations in the performance index, $\pm 2\%$ variation in PI is shown by two horizontal dashed lines. Figure 4.4 shows that 2% absolute PI variation corresponds to 4% variation in IMEP, 8% in Texh, and about 20% variation in the emission gas concentrations. Thus, 2% change in PI causes an important change in HCCI engine operation. In this work, ΔPI=2% is selected as a design parameter in the OCP algorithm which will be discussed later.

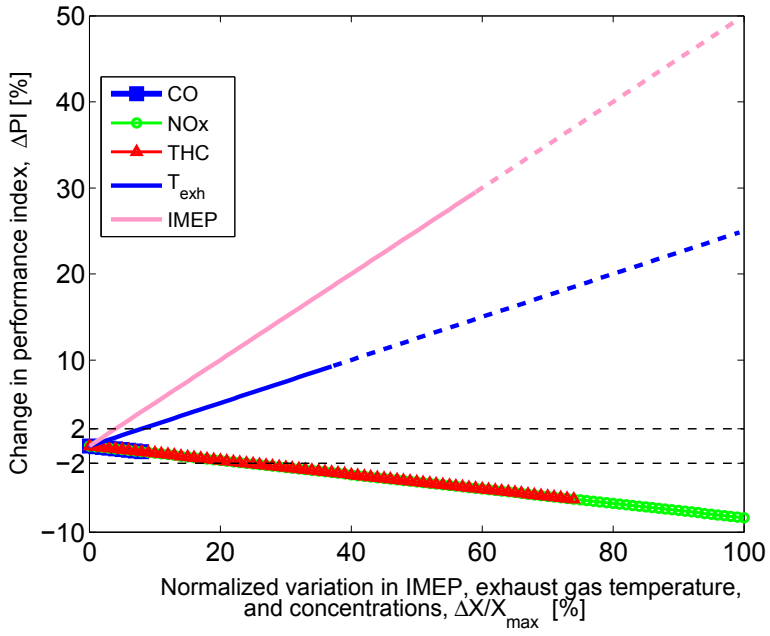

Figure 4.4: Variation of the HCCI engine performance index versus variations in the engine load, emission concentrations, and exhaust gas temperature. The solid lines show the range of experimental data (according to Figure 4.3) and the dashed lines show the projection up to 100% normalized variation. The two black horizontal dashed lines show $\Delta PI = \pm 2\%$.

Figure 4.5 shows the engine REI contours with respect to IMEP and CA50 variations for the studied operating range. Steady state data points (Figure 4.3) are shown with solid points. Three regions are noticed in Figure 4.5 including misfire, knock, and dilution limited high load regions. At low loads and late combustion phasing, misfire occurs while at high loads and early CA50, the engine is prone to knock. To extend the engine operation to higher load range at late ignitions (i.e. high CA50), a high level of dilution by EGR can be utilized [110, 111]. For the data in this study, no EGR is applied (Figure 4.3), thus the engine operation is limited at high load with late CA50. REI is mostly varied in a definite range (0.7-0.75), however, it has

higher values close to High Load Range through High Dilution region due to higher combustion efficiency [112].

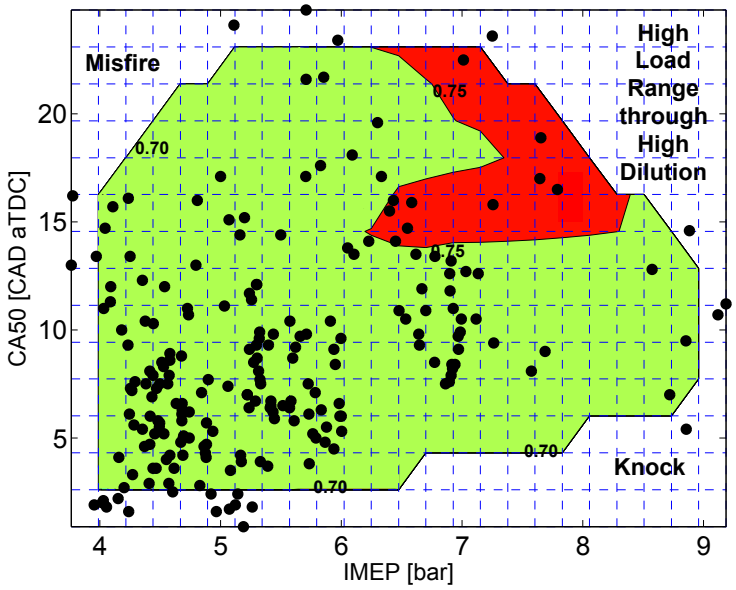

Figure 4.5: Engine REI contour versus the IMEP and CA50 variations. Black dots in the figure indicate the location of experimental data.

Figure 4.6 shows AEI contours in the studied operating range of IMEP and CA50. It can be seen that by a diagonal movement in the figure (i.e. retarding CA50 and increasing engine load), the AEI increases. This is because while shifting from early to late combustion, most of the energy is released part of the way down the expansion stroke and this increases the exhaust temperature and efficiency of aftertreatment. Thus HCCI operation close to the "High Load Range through High Dilution" region leads to the highest AEI. Close to the knock limit, AEI decreases due to early ignition with short combustion duration, leading to low Texh.

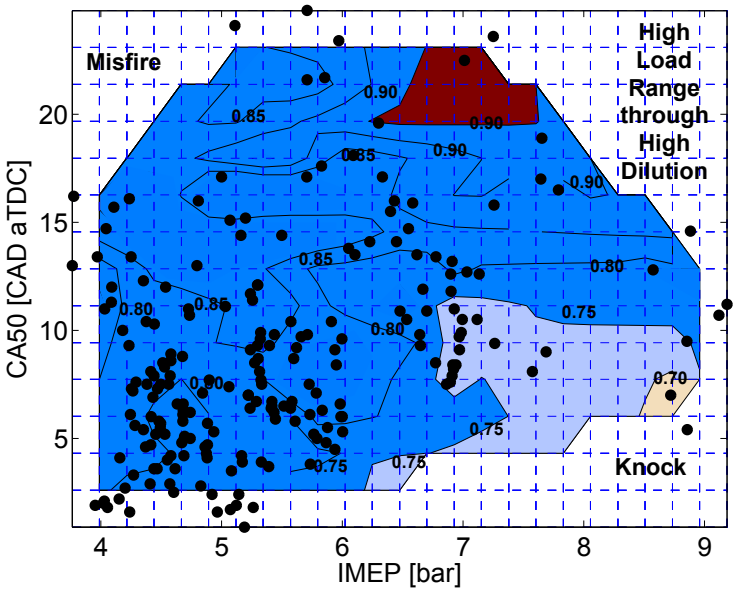

Figure 4.6: Engine AEI contour versus the IMEP and CA50 variations.

Figure 4.7 shows variations in PI in the same studied range of load and combustion phasing. At a constant CA50, a higher PI is achievable at higher engine loads while at a constant engine load, a higher PI is achievable at a later CA50. The best performance index is seen at high load with relatively late ignitions to prevent knock occurrence. Similar observation is found in other studies [9, 112]. Figure 4.7 suggests that at higher loads, a more delayed CA50 is needed to have a higher PI. This figure clearly indicates that an OCP is not a fixed desired value and it varies by moving from one region to another region. The next section describes an algorithm to find the OCP for a HCCI engine.

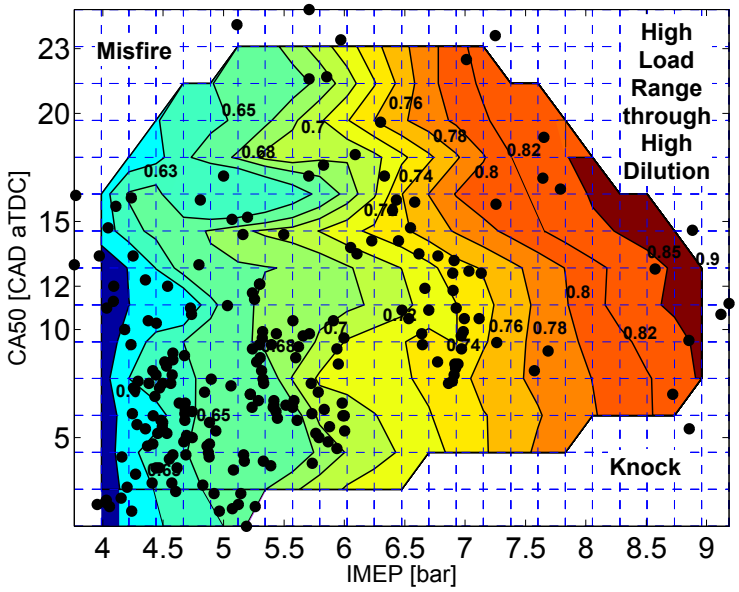

Figure 4.7: Engine PI contour versus the IMEP and CA50 variations.

4.2.3 OCP Algorithm

The optimum CA50 trajectory for HCCI control is determined based on an algorithm denoted here as Optimum Combustion Phasing (OCP). A schematic of the algorithm is shown in Figure 4.8. The OCP algorithm takes the desired IMEP trajectory as an input and calculates optimum CA50 trajectory as an output, using experimentally determined PI values (Figure 4.7). For each required change in the desired IMEP, the possible operating range for the new CA50 is determined according to the PI-CA50-IMEP map from the previous section. Then the maximum PI is found at the desired IMEP and the corresponding CA50 is obtained. As expected, PI is dominated by

TEI when IMEP remains constant.

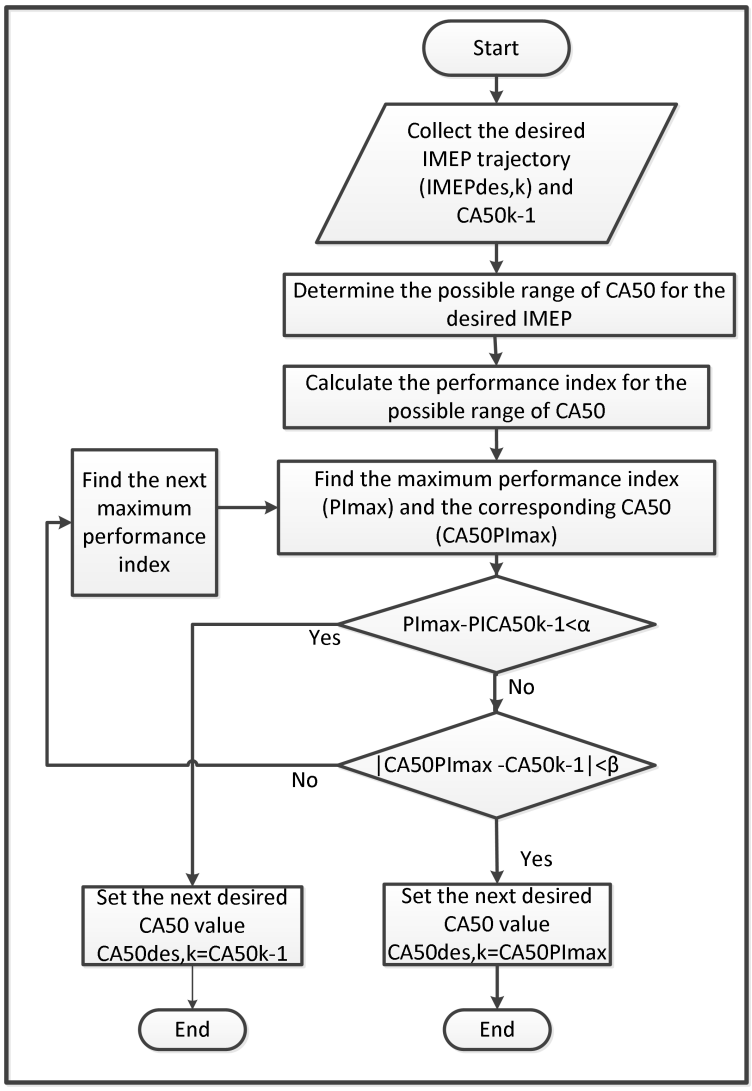

Figure 4.8: A schematic representation of the OCP algorithm.

The OCP algorithm has two design parameters including α and β. The parameter α sets the minimum ΔPI to take a control action. The main purpose is to minimize control efforts. For this purpose, the new PI is compared with the PI of the previous desired CA50 if the difference between these two PIs is more than α, then a new

desired CA50 is set. This avoids the HCCI controller to keep changing CA50 for a small gain in the PI.

The design parameter β is used as a saturation limit to avoid large variations in the desired CA50 trajectory. β is used as a conservative factor to ensure that the engine will not fall into unknown regions that have a high possibility of instability. β is an arbitrary parameter which should be chosen based on the accuracy of the experimentally determined PI contours particularly close to HCCI operation limits. If the absolute difference between the previous and next desired CA50s is less than β, the new desired CA50 is assigned; otherwise the next maximum PI is found and the same steps are followed as a loop.

Figure 4.9 shows the optimum CA50 trajectories found by the OCP algorithm. α=0.02 is selected based on the results in the previous section (Figure 4). β=5 CAD is selected that allows a conservative change in CA50. A higher value for β can be chosen if a more aggressive control action is desired. Values of α and β should be designed for each HCCI engine based on available experimental data and desired control speed which can be limited by the response time of actuators (e.g., a variable valve actuation system has a fast response time versus slow response time in a heater to increase intake charge temperature). This chapter focuses more on developing a general methodology rather than focusing on the absolute values of the parameters (e.g., α and β).

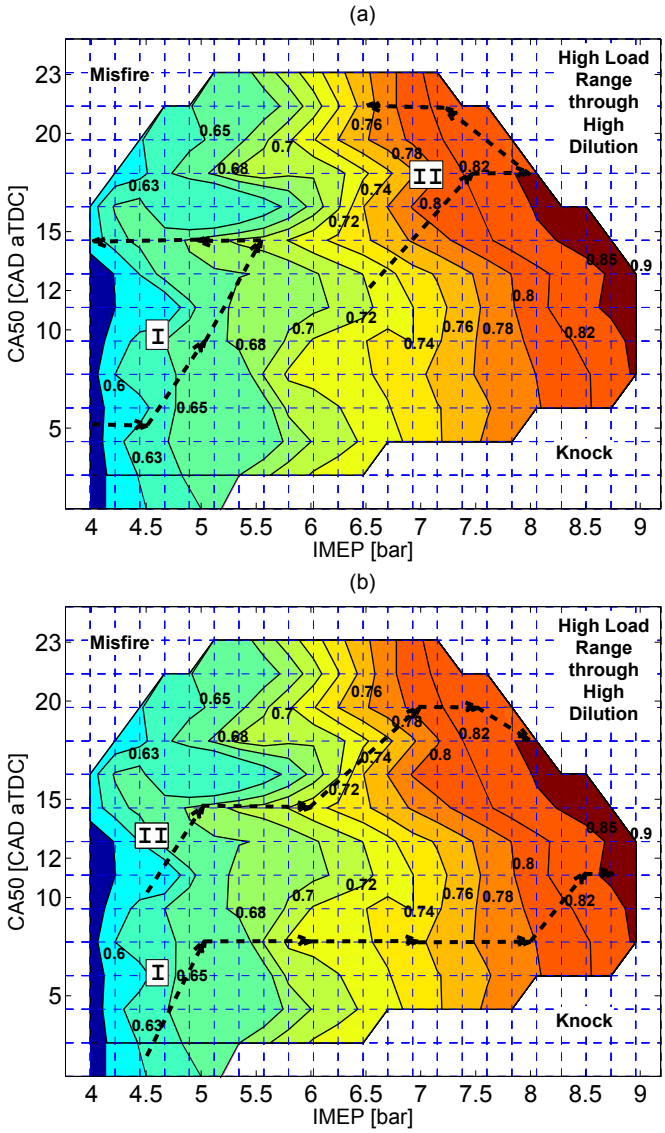

Figure 4.9: Calculated desired CA50 trajectories: (a) in local low load and high load regions, (b) transition from low load region to high load region (α=0.02, β=5 CAD).

Figure 4.9(a) shows the CA50 trajectories for two moderate load transitions while Figure 4.9(b) shows the optimum CA50 trajectories for large load transitions from a low load to a high load. For case I in Figure 4.9(a), the desired engine load changes

4 bar→4.5 bar→5.5 bar→4 bar and the desired CA50 is determined based on the OCP algorithm. Figure 4.10 details the case I from Figure 4.9(a). As seen, the desired CA50 does not change for IMEP change from 4 to 4.5 bar and similarly for the change from 5.5 to 5 bar. The constraint α=0.02 does not allow selection of any desired CA50 which cannot offer a minimum of 2% improvement compared to the previous point of trajectory. The same for β=5 CAD when it prevents selection of any desired CA50 with absolute difference more than 5 CAD compared to the previous point of trajectory.

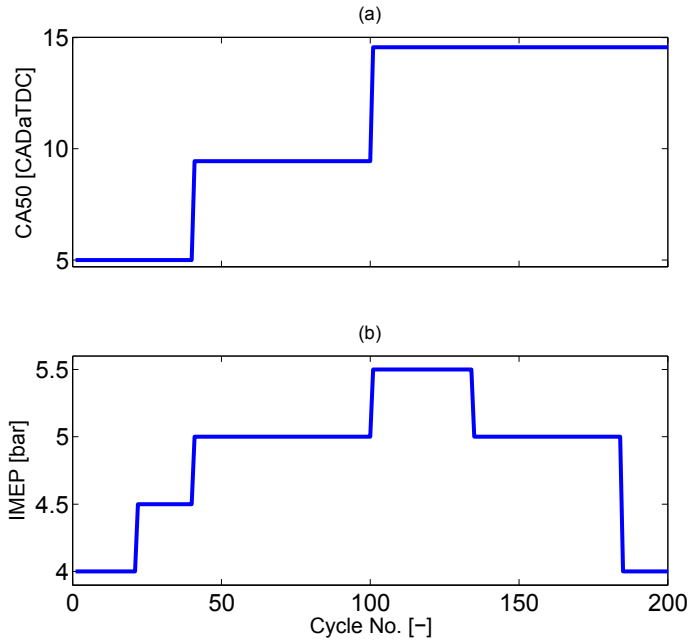

Figure 4.10: Desired trajectories for Figure 4.9(a) case I: (a) determined desired CA50 trajectory, and (b) input desired IMEP trajectory (α=0.02, β=5 CAD).

4.2.4 Performance Index based HCCI Control

In this section, application of the OCP algorithm is illustrated for a two-input two-output HCCI controller for engine load and CA50. The OCP algorithm is used to determine the optimum CA50 trajectory for the HCCI controller. The controller is designed based on a control oriented model (COM) from Chapter 3 and then is tested on a more complex physical HCCI engine model that has been experimentally validated in [9].

4.2.4.1 Controller Design

The controller is designed based on the discrete two-input two-output HCCI COM from Chapter 3which consists of a series of physical events beginning with the intake stroke and ending with the calculation of the residual gas properties at the end of the exhaust stroke. The inputs to the model are as follows:

1. ϕ at a constant air mass flow rate
2. The volumetric ratio of two PRFs, i.e. fuel ON.

The outputs of the COM are IMEP and CA50. Variation of ϕ has a strong impact on IMEP, while ON can be used to advance or retard HCCI combustion phasing [9, 27,

105, 112]. Here the two outputs are controlled by two separate sub-controllers using two independent inputs. IMEP is controlled by adjusting ϕ and CA50 is controlled by adjusting the ON values of blended fuel. The two-input two-output controller includes: 1) an integral feedforward sub-controller to control IMEP, and 2) an integral state feedback controller to track the desired CA50 trajectory determined by the OCP algorithm. Exhaust tailpipe emissions and Texh are controlled indirectly by adjusting CA50 such that it maximizes the PI value.

Integral Feedforward IMEP Controller

A map for IMEP-ϕ is obtained by running a detailed physical HCCI model [113] for a range of operating conditions so that the engines IMEP can be determined in response to the variations in ϕ:

$$u_{1map,k} = c_1 y_{1,k} + c_2 \tag{4.6}$$

where $u_1 = \phi$, y_1=IMEP, and c_1 and c_2 are constants. An integral gain (k_i) is added to cancel any steady state error. Eventually the control input is calculated by:

$$u_{1,k} = u_{1map,k} + u_{1i,k} \tag{4.7}$$

where u_{1i} is actuated by the integral controller. Values of the controller parameters are as follows:

$$c_1 = 0.071$$
$$c_2 = 0.114 \tag{4.8}$$
$$k_i = 0.003$$

Integral State Feedback CA50 Controller

The CA50 controller is designed based on the COM with five states including: CA50, T_{soc}, P_{soc}, T_{rg}, and m_{evc}. The COM is linearized around a nominal operating point shown in Table 4.1.

Table 4.1
Nominal operating point around which the nonlinear COM is linearized

Parameter	Value
CA50	12 CAD aTDC
T_{soc}	787 K
P_{soc}	2260 kPa
T_{rg}	572 K
m_{evc}	0.0393 g
ON	20 (-)
Φ	0.40 (-)
T_{man}	363 K
P_{man}	125 kPa
External EGR	0 %
N	800 rpm

The linearized COM in the standard state space form is:

$$\tilde{X}_{k+1} = A\tilde{X}_k + B\tilde{u}_{2,k}\tilde{y}_{2,k} = C\tilde{X}_k \tag{4.9}$$

where $X = [C\tilde{A}50, \tilde{T}_{soc}, \tilde{P}_{soc}, \tilde{T}_{rg}, \tilde{m}_{evc}]$, $\tilde{y}_2 = C\tilde{A}50$, and $\tilde{u}_2 = \tilde{ON}$. $\tilde{X}$, $\tilde{y}_2$, and $\tilde{u}_2$ are the state vector, the output, and the input, respectively. The tilde accents show deviations from the nominal conditions. The index $k+1$ denotes the current engine cycle and the index k denotes the previous engine cycle. Values of elements for the discrete time state space matrices (A, B, and C) are shown in Appendix A.3.

Eigen values of A are: -1.03 e-22.3 e-22, 3 e-49 e-4, and 1.93 e-2. All the eigen values are inside the unit circle so the system is stable around the studied operating point.

The state feedback controller regulates the model states at the operating point condition while the integral action is responsible for tracking as well as cancelling the steady state error. The integral action can also enable the CA50 sub-controller to reject the disturbance from variations of ϕ (actuated by the IMEP sub-controller). By adding the integral action to the state feedback controller, the order of the model is increased by a unit [41], resulting in the following state equation:

$$\begin{bmatrix} \tilde{X}_I \\ \tilde{X} \end{bmatrix}_{k+1} = \begin{bmatrix} 1 & C \\ 0 & A \end{bmatrix} \begin{bmatrix} \tilde{X}_I \\ \tilde{X} \end{bmatrix}_k + \begin{bmatrix} 0 \\ B \end{bmatrix} \tilde{u}_{2,k} \tag{4.10}$$

where x is the unaugmented state vector and X_I is the integral state. The state feedback control input is:

$$\tilde{u}_{2,k} = -\begin{bmatrix} k_I & k \end{bmatrix} \begin{bmatrix} \tilde{X}_I \\ \tilde{X} \end{bmatrix}_k \tag{4.11}$$

where k_I is the integral controller gain and k is the state feedback gain vector. The matrices and parameters for the augmented model are:

$$\begin{gathered} A_{aug} = \begin{bmatrix} 1 & C \\ 0 & A \end{bmatrix}, B_{aug} = \begin{bmatrix} 0 \\ B \end{bmatrix}, C_{aug} = C \\ k_{aug} = \begin{bmatrix} k_I & k \end{bmatrix}, \tilde{X}_{aug} = \begin{bmatrix} \tilde{X}_I \\ \tilde{X} \end{bmatrix} \end{gathered} \tag{4.12}$$

To determine the control gain vectors, a Linear Quadratic (LQ) optimization is carried out on the model states to minimize the following cost function:

$$J_{aug} = \sum_{i=1}^{\infty} [\tilde{X}_{aug}(i)^T Q \tilde{X}_{aug}(i) + \tilde{u}_2(i)^T R \tilde{u}_2(i)] \tag{4.13}$$

Q is a symmetric positive definite matrix and R is a positive definite scalar. k_{aug} is found by the following equation:

$$k_{aug} = (R + {B_{aug}}^T P B_{aug})^{-1} {B_{aug}}^T P A_{aug} \tag{4.14}$$

where P is found by solving the discrete Riccati equation. A feedforward gain vector (N_x) is also used to enhance the tracking performance:

$$N_x \tilde{y}_{2,ref} = \tilde{X}_{ref} \tag{4.15}$$

where the subscript ref denotes reference. N_x is found by the following equation (here n=5):

$$\begin{bmatrix} N_x \\ N_y \end{bmatrix} = \begin{bmatrix} A - I_n & B \\ C & 0 \end{bmatrix}^{-1} \begin{bmatrix} 0_{n\times 1} \\ I \end{bmatrix} \tag{4.16}$$

where I represents the identity matrix that is a scalar due to the unity of output.

Since most of the model states are not easily measurable in practice, a Luenberger state observer is designed:

$$\hat{X}_{k+1} = A\tilde{X}_k + B\tilde{u}_{2,k} + l(\tilde{y}_{2,k} - \hat{y}_{2,k}) \tag{4.17}$$

where $\hat{y}_2$ is the estimated CA50 and l is the Luenberger gain vector found by pole placement [105]. Values of the parameters for the CA50 sub-controller and the state observer are found in the following equations.

$$\begin{aligned} k &= \begin{bmatrix} 0.195 & -0.012 & 0.004 & -0.064 & -240.213 \end{bmatrix} \\ k_I &= 1.40 \end{aligned} \tag{4.18}$$

$$l = \begin{bmatrix} -4e-21 & -6e-13 & -2e-2 & 2e-1 & 0 \end{bmatrix} \tag{4.19}$$

The final control input for the CA50 sub-controller is determined as follows:

$$\tilde{u}_{2,k} = -\begin{bmatrix} k_I & k \end{bmatrix} \begin{bmatrix} \tilde{X}_I \\ \tilde{X} - N_x \tilde{y}_{2,ref} \end{bmatrix}_k + N_x \tag{4.20}$$

The structure of the combined IMEP-CA50 controller is shown in Figure 4.11. The desired CA50 trajectory ($y_{2,r}$) is determined by the OCP algorithm based on a desired IMEP trajectory ($y_{1,r}$).

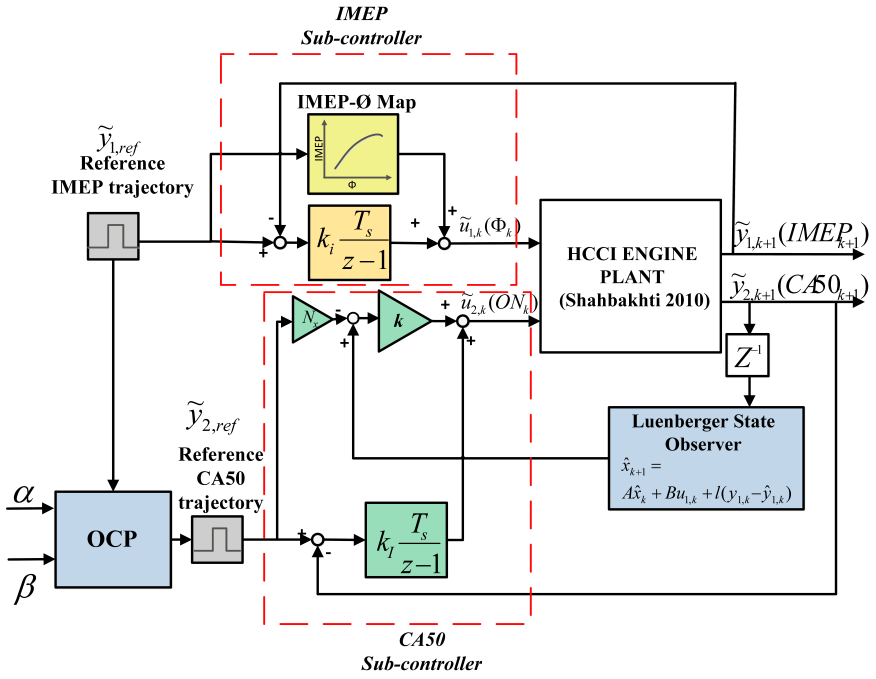

Figure 4.11: Schematic of the control structure using OCP algorithm.

4.2.5 Performance Results

The controller is designed in MATLAB and tested on an HCCI engine model [9], which is significantly more detailed than the COM used to design the controller in this work. Figure 4.12 shows the performance of the controller for simultaneously tracking the desired IMEP trajectory and the optimum CA50 trajectory determined by the OCP algorithm. The given desired IMEP condition is the same as that is shown in Figure 4.10. Results show that the controller is able to track the desired IMEP step changes within an average speed of 1-2 engine cycles. For tracking the desired CA50 step changes, the average speed is about 3 simulation engine cycles. Both sub-controllers are able to cancel the effects of variations caused by the other sub-controller, e.g. the CA50 sub-controller cancels CA50 variations caused by the ϕ changes commanded by the IMEP sub-controller. The average speed of the CA50 sub-controller to reject disturbances from ϕ variation is about 3 simulation engine cycles. With successful implementation of the PI-based CA50-IMEP controller, two major HCCI performance targets will be met. First, the controller directly adjusts the engine load (IMEP). Second, THC and CO tailpipe emissions are minimized by choosing optimum CA50. The optimum CA50 leads to minimizing engine-out emissions while maximizing exhaust aftertreatment efficiency by using hot exhaust gases (high Texh) to heat up the catalyst.

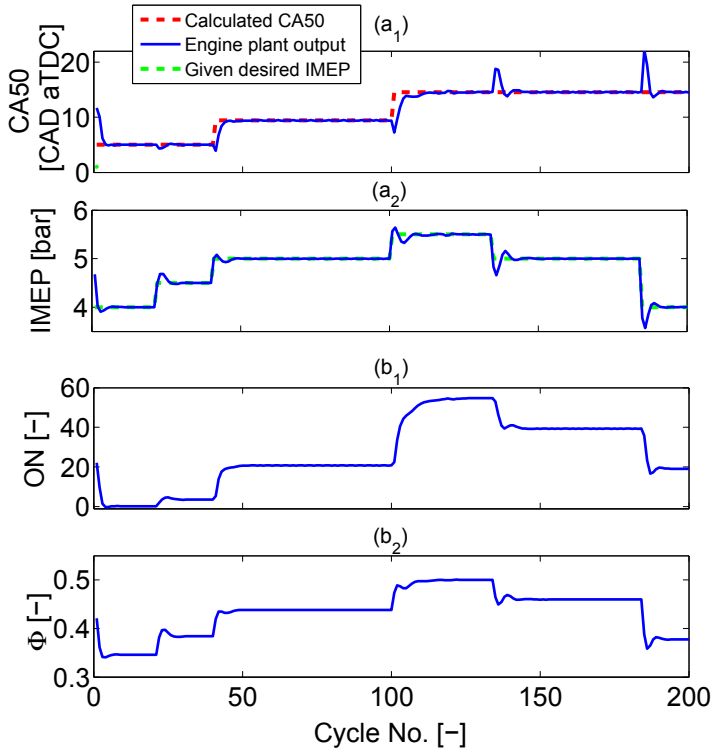

Figure 4.12: Tracking control results: (a) control outputs, (b) control inputs.

Table 4.2 compares PI variation at each step change in the desired IMEP for both the OCP algorithm and constant desired CA50 trajectory (i.e. 5 CAD aTDC). Results in Table 4.2 show that using the OCP algorithm for determining the desired CA50 trajectory leads to the total 11% improvement in PI for the same given IMEP trajectory as in Figure 10(b).

Table 4.2
PI variation for HCCI control at each step of IMEP by using OCP model and constant desired CA50 trajectory

Desired IMEP (bar)	PI by OCP (%)	PI by constant desired CA50 (%)	ΔPI (%)
4	58	58	0
4.5	64	64	0
5	67	66	1
5.5	71	68	3
5	69	66	3
4	62	58	4

ΔPI=11%

Table 4.3 shows variation of $\sum \Delta PI$ for different values of α and β, using the same desired IMEP trajectory as in Figure 10(b). Relaxing the constraint for a minimum desirable PI gain by choosing a lower α leads to improvement in the total $\sum \Delta PI$ as seen in Table 4.3. Choosing a lower α value results in a more aggressive behavior by the controller, which accepts to change the desired CA50 for a smaller gain in PI. This can lead to a high cyclic variation in CA50. A higher value relaxes the constraint for allowable CA50 variation. This can lead to more improvement in the total $\sum \Delta PI$ of the HCCI engine, provided the boundaries of the engine operating map are accurately characterized, thus the engine does not end up into an unstable operating region by a large change in CA50. For the case study in Figure 4.10, reducing α to 0.01 leads to 3% increase in the total $\sum \Delta PI$ while decreasing β by half, improves the total $\sum \Delta PI$ by 8%. It should be added that in this study, engine control is done at constant loads (IMEPs) and since CA50 is controlled by adjustment of ON, then ϕ

is constant at each load. Therefore, the emission concentrations in the units of PPM are used; otherwise, the specific emission concentrations ($\frac{g}{kWh}$) can be used.

Table 4.3
The $\sum \Delta PI$ for different values of α and β

α	β (CAD)	$\sum \Delta PI$ (%)
0.02	5	11
0.01	5	14
0.02	10	19

4.3 Grey-box Modeling for Control of HCCI Engines

HCCI control models can be divided into three main groups as shown in Figure 4.13. These groups include empirical or black-box models, physics-based models, and grey-box models. The first group includes System Identification (SYID) based models [43, 45, 48, 80] and Artificial Neural Networks (ANN) models. ANN models have been widely used in internal combustion engine applications [114, 115, 116, 117, 118, 119, 120]. [121, 122, 123, 124, 125] are examples of ANN models used for HCCI engine control applications. The empirical models can be used to capture the behavior of HCCI engines without enough knowledge of the physics of the processes. However, due to the lack of physical knowledge, the empirical models will not be able to compensate easily for the system dynamics change in response

to parametric variations. The second group includes physical models that capture characteristics of HCCI operation by using mathematical modeling of the engine cycle. Studies in [1, 2, 39, 40, 41, 42, 46, 47, 49, 50, 51, 52, 86, 87, 89, 126, 127, 128] are examples of this group. Depending on the level of complexity, there is a variety of physical HCCI models ranging from detailed thermo-kinetic models [127] and multi-zone models [128, 129] to simple physics-based control-oriented models [1, 2, 39, 40, 41, 42, 46, 47, 49, 50, 51, 52, 86, 87, 89, 126]. All of these model types can capture physical parametric changes due to their physical understanding of the system process. However, there is a limitation for real-time control application of the physical models particularly when low order computationally efficient models are required. Grey-box models [130] provide benefits of both groups of physical models (clear-box models) and black-box models, by combining these two model types. This chapter centers on developing a grey-box model to predict HCCI engine operation for performance analysis and control applications.

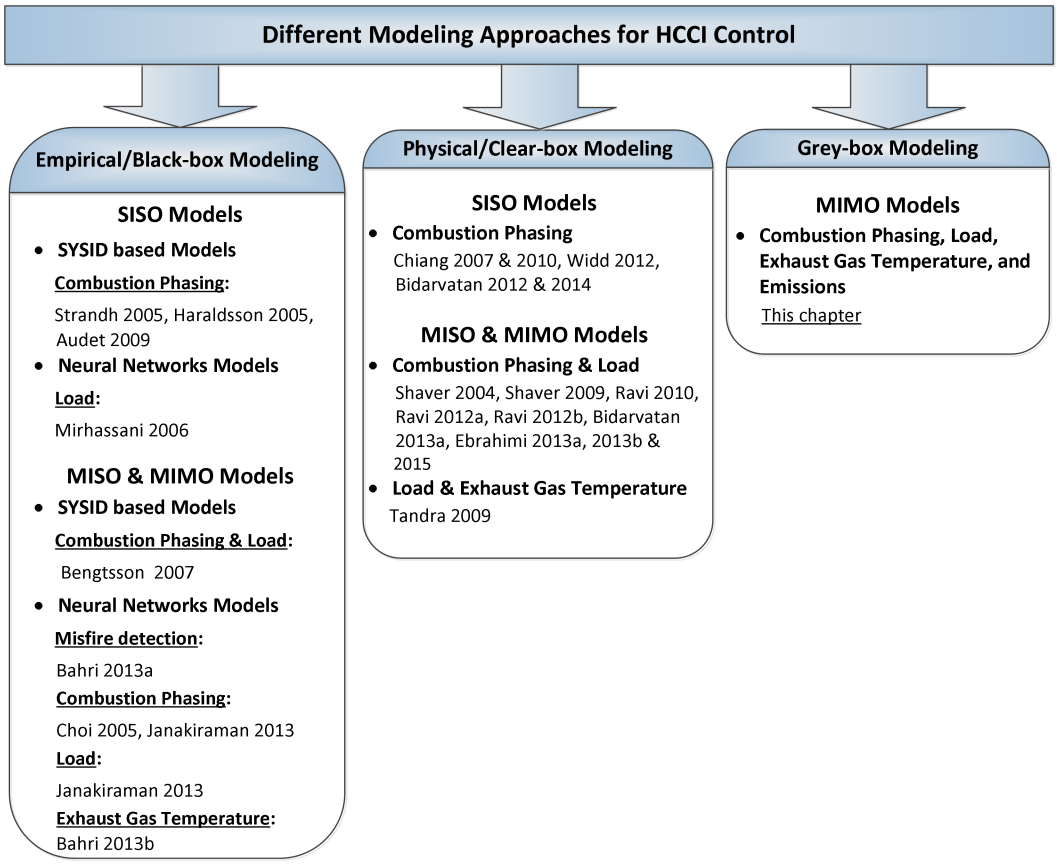

Figure 4.13: Background of HCCI engine control modeling in literature.

The HCCI models in the literature can also be categorized into three groups with respect to the number of inputs and outputs as depicted in Figure 4.13. Single Input Single Output (SISO), Multi Input Single Output (MISO), and Multi Input and Multi Output (MIMO) models constitute these groups. [1, 39, 41, 42, 43, 45, 46, 48] are examples of SISO models used for predicting combustion phasing. Another example of a SISO HCCI model is [122] in which the engine load (IMEP) is predicted. [121, 123, 124, 125] are examples of MISO models for predicting combustion phasing, separate control of load and combustion phasing, detection of misfire, and predicting exhaust

gas temperature, respectively. Some examples of MIMO models are [80] and [2, 40, 47, 49, 50, 51, 89] that simultaneously predict the engine combustion phasing and load. The model in [52] predicts load and exhaust gas temperature while [130] proposes a model for simultaneous prediction of combustion phasing, load, and exhaust gas temperature.

There is no *comprehensive* control model in the literature for predicting HCCI engine performance parameters and exhaust emissions. Available HCCI emission models in the literature are computationally expensive for use in control applications. In this study, a comprehensive grey-box MIMO model is proposed that can predict all the major HCCI engine variables including combustion phasing, load, exhaust gas temperature, and engine-out emissions of THC, CO, and NOx. To the best of the authors' knowledge, this is the first study on developing a MIMO HCCI grey-box model that can predict both the engine performance parameters and the main HCCI engine emissions. Accuracy of the model is tested by experimental validation over a large operating range of two HCCI engines under 309 steady state and transient conditions. In addition, application of the HCCI grey-box modeling is shown for control of HCCI engines.

4.3.1 Experimental Data

Experimental data from [26] for a single cylinder HCCI Ricardo engine at 208 steady state operating conditions are used in this chapter. The specifications of the engine are listed in Table 2.1.

Operating range of the HCCI engine is shown in Figure 4.14. For this study three different blends of Primary Reference Fuels (PRFs) are used. These fuels include PRF0 (n-heptane), PRF20 (20% iso-Octane and 80% n-heptane), and PRF40 (40% iso-Octane and 60% n-heptane). The data includes ultra-lean air-fuel mixtures with fuel equivalence ratio ranging from 0.29 to 0.61. Due to the low compression ratio, the engine can be run at a limited speed and PRF ranges. The knock limit threshold for the studied HCCI Ricardo engine is defined as the pressure rise rate of 7 bar/CAD [10]. The data points in this study have pressure rise rate less than the knock threshold. In addition, external Exhaust Gas Recirculation (EGR) is 0% in this study.

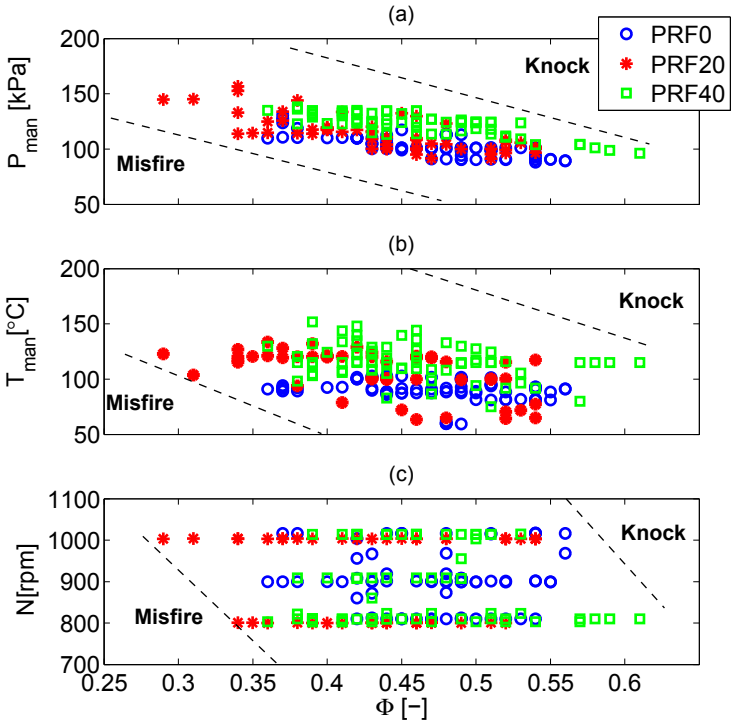

Figure 4.14: Operating range for 208 experimental HCCI data points used in this study. (Ricardo engine)

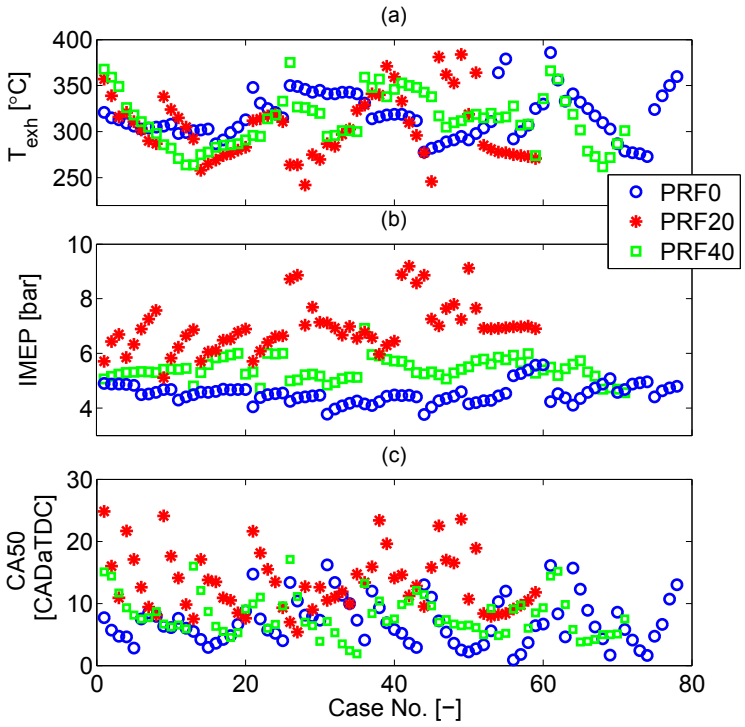

Figure 4.15: Range of engine combustion phasing (CA50), load (gross IMEP), and exhaust gas temperature (Texh) for the experimental data points shown in Figure 4.14. (Ricardo engine)

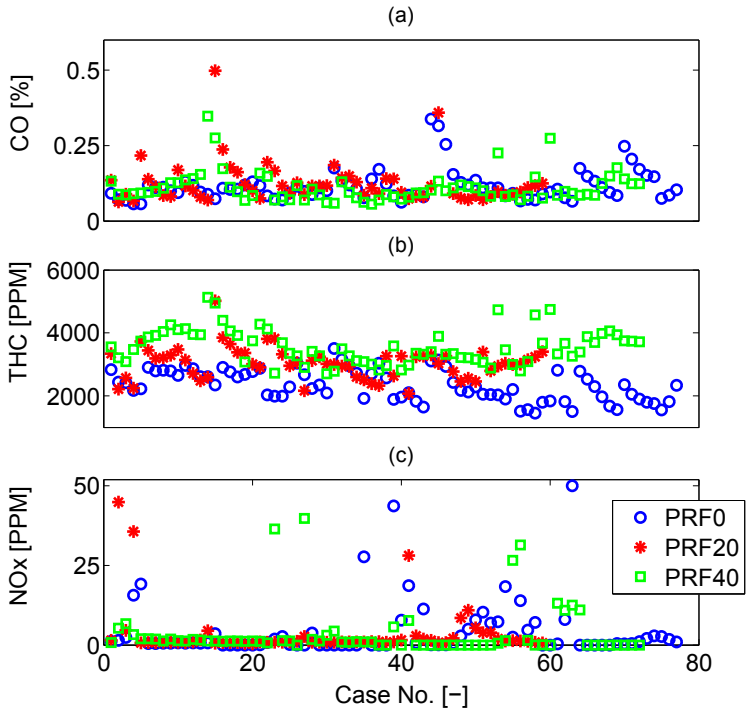

Figure 4.16: Range of engine CO, THC, and NOx exhaust gas concentrations for the experimental data points shown in Figure 4.14. (Ricardo engine)

Range of combustion phasing (CA50) in Figure 4.15 is from 0 to 25 CAD aTDC, the engine load (IMEP) ranges from 3.4 to 9.1 bar, and the exhaust gas temperature (T_{exh}) ranges from 242 to 386 °C. More than 40% of the data points in Figure 4.15 have T_{exh} less than 300 °C. The light-off temperature (the temperature at which the catalyst becomes more than 50 percent effective) is about 250 to 300 °C for most catalysts [37, 38]. To ensure that high THC and CO emissions in HCCI can be mitigated by an oxidation catalyst, it is important to adjust the exhaust gas temperature above the catalyst light-off temperature. In addition, it is necessary to

ensure that the engine generates a minimum amount of THC and CO emissions until the catalyst reaches its fully warm-up condition. Figure 4.16 shows ranges of the engine-out harmful exhaust gas concentrations that expand from 0 to 50 PPM for NOx, 0.05% to 0.50% for CO, and 1452 to 5127 PPM for THC. The experimental data from this section is used for training and validation of the HCCI grey-box model described in Section 4.3.3.

4.3.2 Grey-box Model Description

4.3.2.1 Architecture of Model

In this section, a grey-box model is developed using the serial architecture shown in Figure 4.17. It consists of a CA50-IMEP grey-box model, an ANN T_{exh} model, and an ANN emission model. The CA50-IMEP grey-box model consists of a physical model and an ANN CA50-IMEP model. The T_{exh} grey-box model requires five inputs including engine speed (N), fuel equivalence ratio (ϕ), adiabatic flame temperature (Tad), and T_{exh} from the clear-box model (T_{exhp}), and CA50 from the CA50-IMEP grey-box model ($CA50_g$). The inputs to the grey-box emission model are ϕ, intake manifold pressure (P_{man}), intake manifold temperature (T_{man}), N, and CA50g. The model outputs are CO, THC, and NOx concentrations.

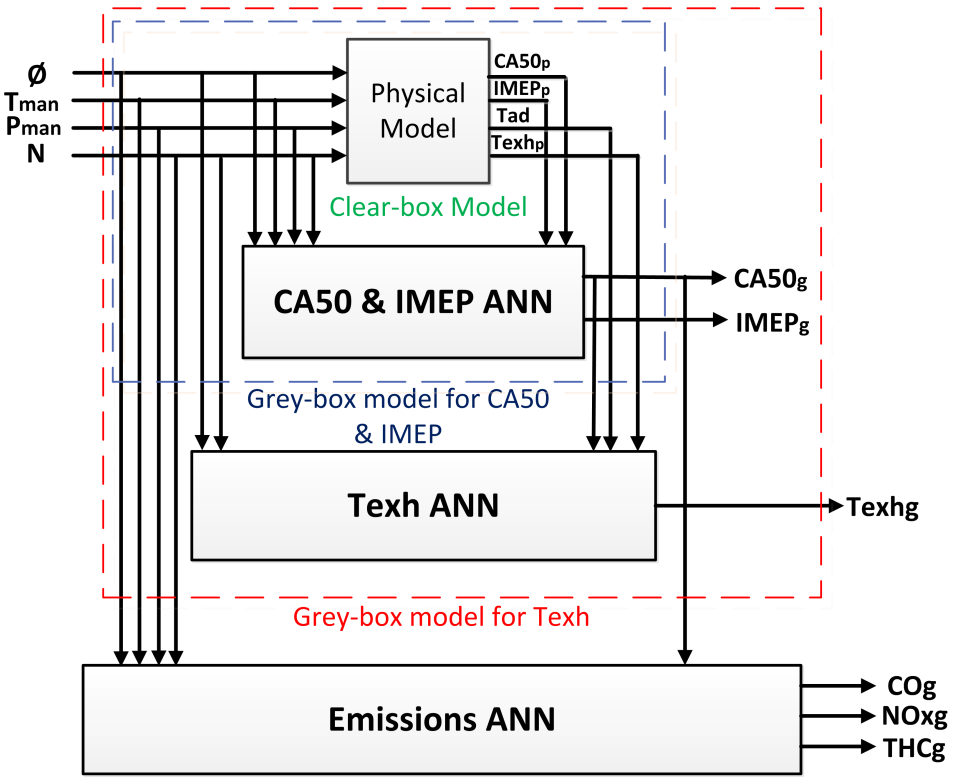

Figure 4.17: Architecture of the grey-box HCCI model.

4.3.2.2 Physical Model

The physical model in the CA50-IMEP grey-box model consists of four physical HCCI models used for predicting $CA50_p$ [9], $IMEP_p$ [2], adiabatic flame temperature (T_{ad}), and T_{exh} [131]. T_{ad} is calculated at constant volume since the HCCI cycle is a closer approximation to constant volume combustion than to constant-pressure combustion. T_{ad} is calculated from the ideal gas law with enthalpy of reactants and specific heat of each of the mixture components for any ϕ and T_{man} of HCCI engine. Details of the

physical models were previously explained in Chapters 2 and 3. The following T_{exh} submodel is used in this chapter [132]:

$$T_{exh} = \frac{T_{evo} + T_{evc}}{2}\left[\frac{2m_{mix}(1 - X_{rg})c_p - h_c A_R}{2m_{mix}(1 - X_{rg})c_p + h_c A_R}\right] + \frac{2h_c A_R}{2m_{mix}(1 - X_{rg})c_p + h_c A_R}T_w \tag{4.21}$$

where, h_c, A_R, and T_w are the convection heat transfer coefficient, heat transfer surface area, and the cylinder wall temperature. ϕ, T_{man}, P_{man}, and N are the dominant engine operating variables that affect CA50, IMEP, Tad, and T_{exh} [9, 26, 37]. Therefore, they are used as the inputs to the clear-box model. The engine operating variables including ϕ and N along with Tad, T_{exhp}, and CA50g are used as the inputs to the T_{exh} ANN model (T_{exhg} is the output). The emissions ANN model receives all the aforementioned engine operating variables and $CA50_g$ to predict the engine-out emissions (CO_g, THC_g, and NOx_g). No EGR is used in this study, thus it is not among the model inputs.

4.3.2.3 Artificial (Black-Box) Model

Structure of the CA50-IMEP, T_{exh}, and emissions ANN models is shown in Figure 4.18. A hyperbolic tangent sigmoid function is used as the activation function for the hidden and output layers. The back-propagation learning algorithm [133] is used for training the ANN models using MATLAB ANN toolbox. The weights are

initially chosen randomly. Then, they are adjusted during several training iterations to minimize a cost function chosen to be the Mean Squared Error (MSE) [133]. The ANN is simulated with the input data and the error is calculated between the estimated output and the actual output. The weights are then updated starting with the output weights and progressing back to the input weights using a gradient descent to minimize the MSE. The process is repeated until a performance goal is achieved. Training is done only for the black-box models; the physical model is run and its outputs are used as the inputs to the black-box models for either training or validation. Therefore, there is no training for the physical parts of the grey-box model.

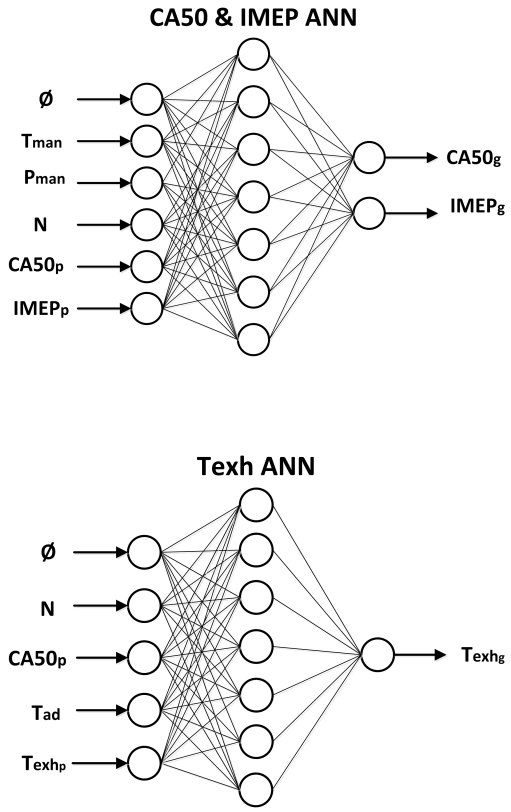

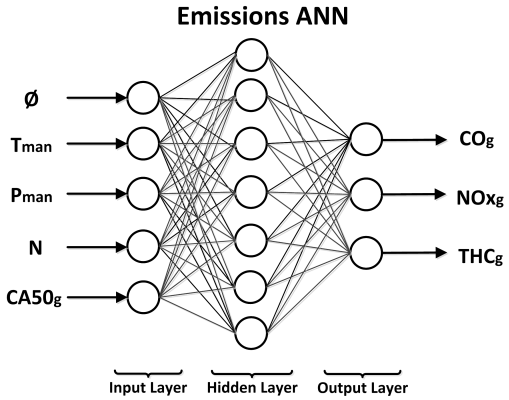

Figure 4.18: Feedfoward Artificial Neural Networks (ANNs) used in this study.

4.3.3 Results and Discussion

The CA50-IMEP, T_{exh}, and emissions ANN models are trained and validated in this section for different PRFs (i.e. PRF0, PRF20, and PRF40) from Ricardo HCCI engine. Then, performance of the developed grey-box models are tested on a different HCCI engine (Yanmar).

4.3.3.1 ANN Structure Design

To design the ANN structure, it is necessary to determine the optimum size of the ANN model and the optimum number of epochs (training iterations) to avoid over-training. For this purpose, in this section the design procedure is illustrated for the

CA50-IMEP ANN model, while the same procedure is used for T_{exh} and Emission ANN models. An ANN with one hidden layer and 25 neurons is selected for the CA50-IMEP model. The number of neurons in the hidden layer is chosen by investigating the training performance as shown in Figure 4.19. For every PRF, the ANN is trained and validated over a range of 1 to 35 hidden neurons (Figure 4.19).

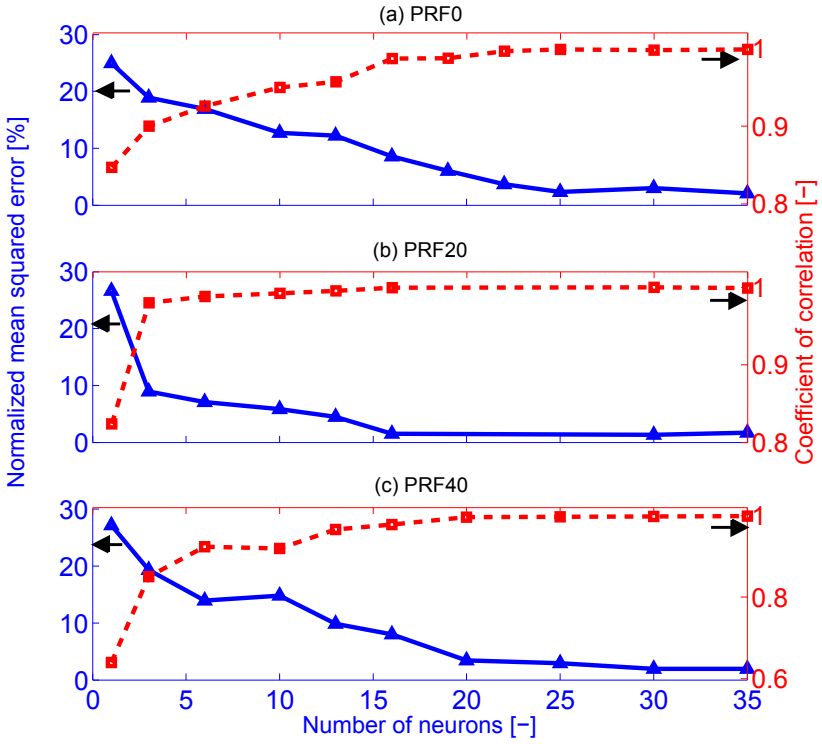

Figure 4.19: Training metrics for the CA50-IMEP ANN model. Normalized MSE in the y-axis is the average of normalized MSE for CA50 and IMEP.

As the number of neurons increases, the MSE decreases and the coefficient of correlation increases. After 25 neurons in the hidden layer, the change in prediction accuracy of the model is minor with increase in the complexity of the network. This

helps in choosing the smallest network size with an acceptable accuracy. A size of 25 neurons in the hidden layer is selected to satisfy a trade-off between the model complexity and accuracy.

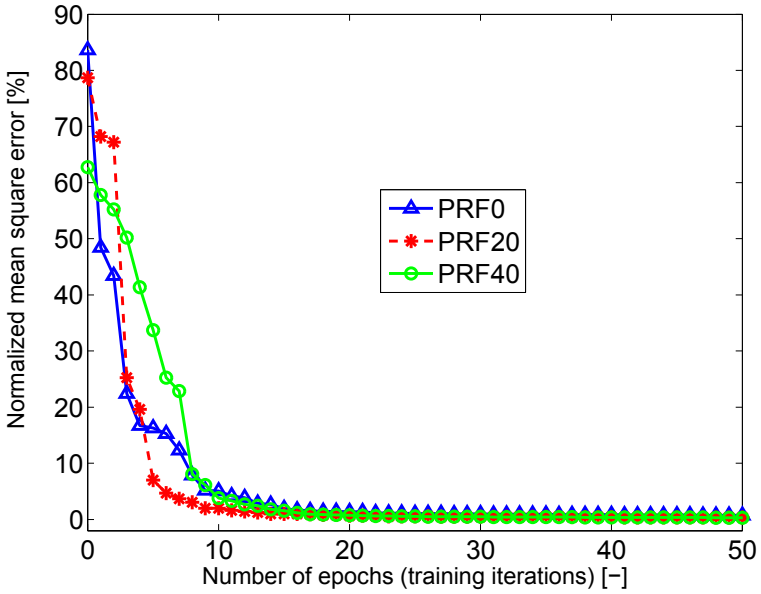

Figure 4.20: Training MSE over iteration history for the CA50-IMEP ANN model. Normalized MSE in the y-axis is the average of normalized MSE for CA50 and IMEP.

The CA50-IMEP ANN model is simulated to find the optimum number of epochs to avoid overtraining. The results are shown in Figure 4.20. Initially, the MSE decreases dramatically with increasing the number of epochs, but then the drop in MSE becomes small and the MSE stays at about a constant value. Optimum number of training iterations is found to be 30, as shown in Figure 4.20.

208 steady-state data points of the Ricardo HCCI engine for three PRFs are used. 75% of the data is used for training while the rest 25% of the data is used to validate

the grey-box models. The training and validation results are discussed in the following Sections 4.3.4 to 4.3.6.

4.3.4 Combustion Phasing and Engine Load (IMEP)

Results of training and validation of the CA50-IMEP grey-box model are shown in Figures 4.21 and 4.22. The accuracy of the grey-box model for predicting CA50 and IMEP is compared with those from the clear-box and the black-box only models in Table 4.4. The term *black-box only model* in this study refers to an independent ANN model with inputs only from the engine operating conditions including T_{man}, P_{man}, N, and ϕ. The *black-box only model* is not part of the grey-box model structure (Figure 4.17) and does not have any inputs from the physical model. The grey-box model shows the best performance in predicting CA50 and IMEP among all the studied types of modeling. Root Mean Squared Error (RMSE) of the grey-box model is 3.3 and 2.1 CAD less compared to the clear-box and black-box only models, respectively. In addition, Standard Deviation (STD) of error for the grey-box model is about 2.3 and 2.1 CAD less than the clear-box and black-box only models, respectively. Similarly, the IMEP prediction of the grey-box model is better than those of its two peers with more than 84% and 60% reduction in RMSE and about 94% and 86% reduction in STD of error compared to the clear-box and black-box only models, respectively.

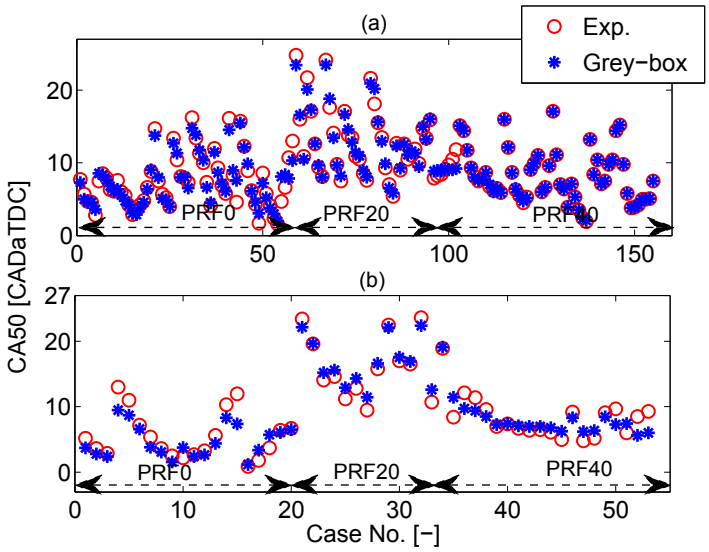

Figure 4.21: Prediction of CA50 for Ricardo engine: (a) training, (b) validation data.

Table 4.4
Comparison of average accuracy of the clear-box, black-box only, and the grey-box models for all fuels for Ricardo engine based on the validation data sets.

Type of Model	Parameter	STD of Error	RMSE
Clear-box	CA50 [CAD]	3.1	4.1
	IMEP [bar]	1.7	1.30
	Texh [°C]	17.0	21.0
	NOx [PPM]	-	-
	CO [%]	-	-
	THC [PPM]	-	-
Black-box only	CA50 [CAD]	2.9	2.9
	IMEP [bar]	0.7	0.50
	Texh [°C]	10.0	13.3
	NOx [PPM]	11	12
	CO [%]	0.14	0.18
	THC [PPM]	1054	1210
Grey-box	CA50 [CAD]	0.8	0.8
	IMEP [bar]	0.1	0.20
	Texh [°C]	5.0	5.3
	NOx [PPM]	4	4
	CO [%]	0.03	0.03
	THC [PPM]	333	394

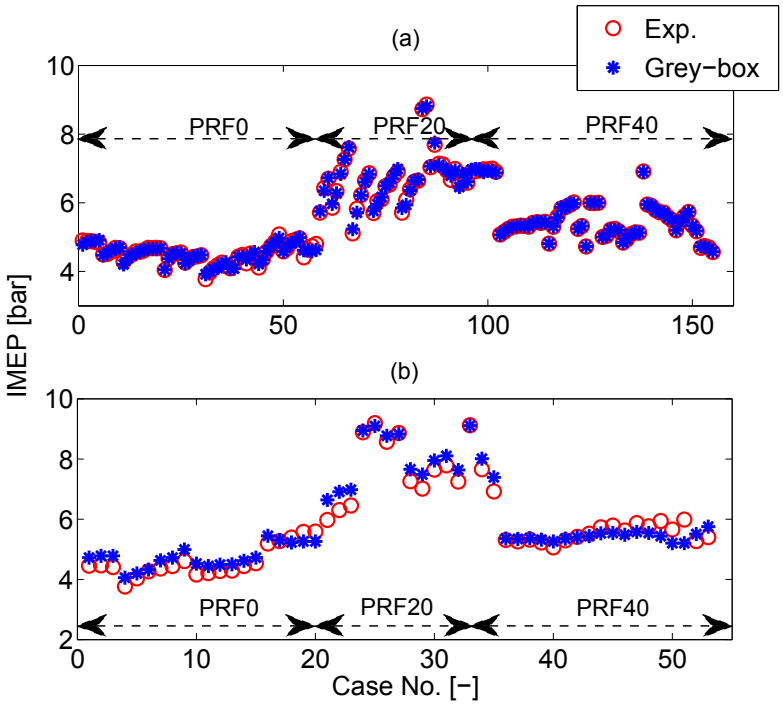

Figure 4.22: Prediction of IMEP for Ricardo engine: (a) training, (b) validation data.

4.3.4.1 Exhaust Gas Temperature

Performance of the T_{exh} grey-box model is shown in Figure 4.23. Table 4.4 compares the average of RMSE and STD of error for all the three PRFs. It shows that there are about 16, 8 °C reductions in RMSE and 12, 5 °C reductions in STD of error in the grey-box model prediction of T_{exh} compared to the clear-box and the black-box only models, respectively. Overall, the T_{exh} grey-box model outperforms its two clear-box and black-box only peers.

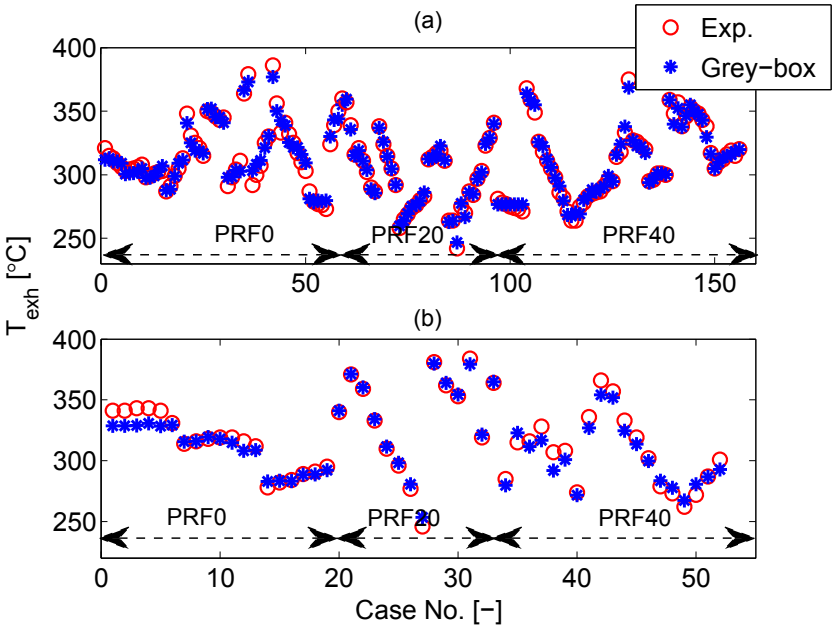

Figure 4.23: Prediction of exhaust gas temperature for Ricardo engine: (a) training, (b) validation data.

4.3.5 Engine-out Emissions

Performance of the grey-box model in predicting the engine-out emissions concentrations are shown in Figures 4.24, 4.25, and 4.26 and indicate the grey-box model can effectively predict concentrations of all the three types of emissions with correct trends and acceptable accuracy. Comparison results in Table 4.4 show that the prediction of CO, THC, and NOx emissions have been improved by more than *three times* using the grey-box emission model compared to the black-box only model. The accuracy of the grey-box model can be improved by training region-based grey-box models for individual HCCI operating regions and then switching between the models depending

on HCCI operating regions.

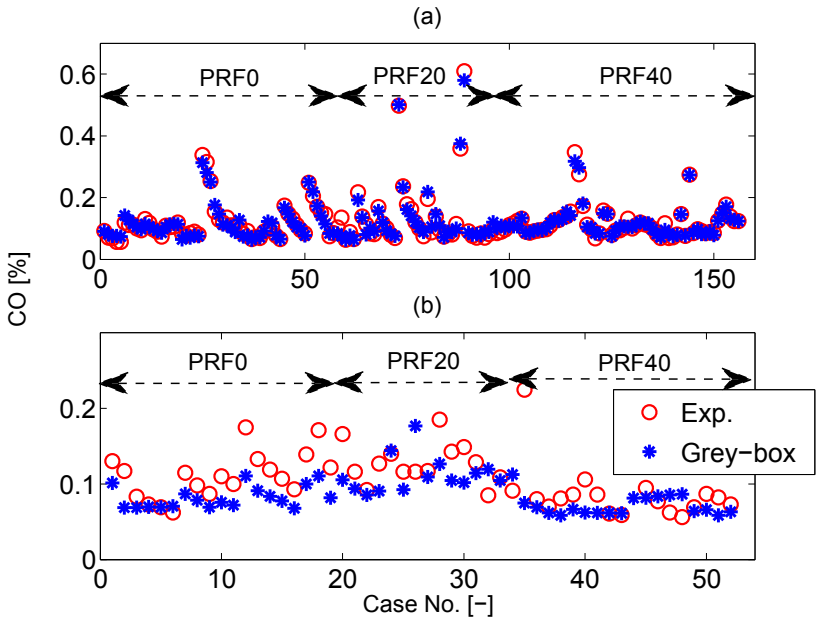

Figure 4.24: Prediction of CO concentration for Ricardo engine: (a) training, (b) validation data.

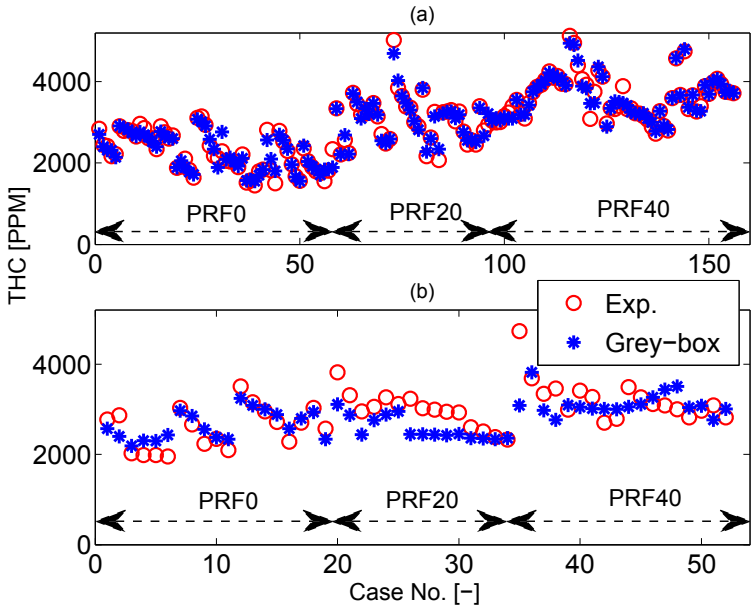

Figure 4.25: Prediction of THC concentration for Ricardo engine: (a) training, (b) validation data.

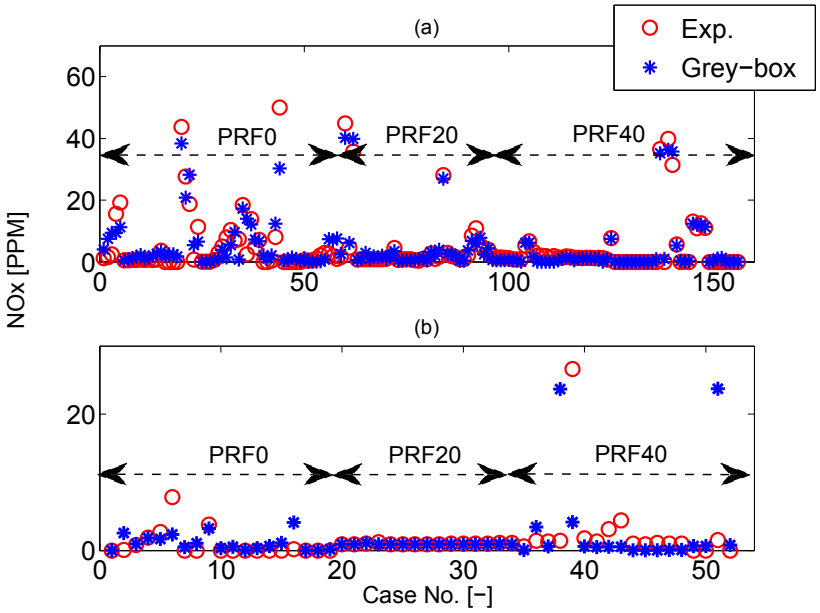

Figure 4.26: Prediction of NOx concentration for Ricardo engine: (a) training, (b) validation data.

4.3.6 Transient Validation

The grey-box models are also validated against the transient HCCI experimental data taken from [131]. The transient validation includes CA50, IMEP, and T_{exh} but does not include engine-out emissions since fast response emission analyses were not at our disposal. Transient validation results for CA50, IMEP, and T_{exh} are shown in Figure 4.27. Accuracy metrics of the grey-box models for this transient operation are listed in Table 4.5 and show that the grey-box model can predict CA50 with the STD of error and RMSE of both less than 2 CAD. While both the STD of error and RMSE for IMEP and T_{exh} are less than 0.1 bar and 3 °C, respectively.

Computation time for the grey-box model for each engine cycle on a 3.2 GHz Intel processor is less than 1 ms. This makes the grey-box model desirable for model-based real time control of HCCI engines.

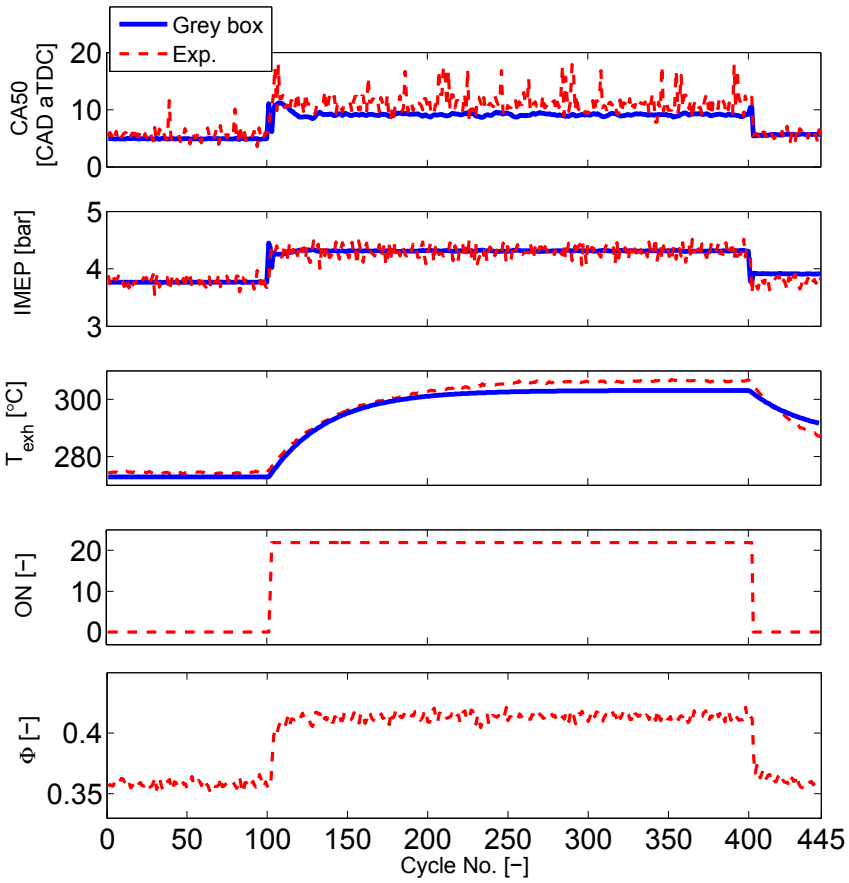

Figure 4.27: Validation of the CA50-IMEP, T_{exh} grey-box models for transient fueling conditions in Ricardo engine (P_m= 110 kPa, T_m= 91 °C, External EGR = 0%, P_{exh}= 99 kPa, N=815 rpm).

Table 4.5
Prediction accuracy metrics for transient validation of the CA50-IMEP and T_{exh} grey-box models for Ricardo engine.

Parameter	STD of Error	RMSE
CA50 (CAD)	1.5	1.6
IMEP (bar)	0.1	0.085
T_{exh} (°C)	1.5	2.2

4.3.7 Validation on a Different HCCI Engine (Yanmar)

The developed grey-box models are also validated for a different HCCI engine. The engine is a single-cylinder four-stroke naturally aspirated, air-cooled Yanmar diesel engine with direct injection capability that was modified for HCCI operation using ethanol fuel. The specifications of this Yanmar engine are listed in Table 4.6. Experimental data for 100 steady state operating conditions from [124, 125] is used in this study.

Table 4.6
Specifications of single cylinder Yanmar L70AE engine.

Parameter	Value (units)
Bore	78 mm
Stroke	62 mm
Compression Ratio	19.5:1
Displacement Volume	0.296 L
Number of Valves	2
IVO/IVC	-155/+59 CAD aBDC
EVO/EVC	-59/-155 CAD aBDC

The Yanmar engine experimental data are shown in Figure 4.28. It covers a large range of operating conditions (CA50= 3 to 16 CAD aTDC, IMEP= 0.41 to 3.1 bar, and T_{exh}=163 to 260 °C). The air-fuel mixture used in this engine is lean (ϕ= 0.23 to 0.35) to avoid knock occurrence. The values of exhaust THC concentration vary from 1139 to 2779 PPM. CO and NOx vary from 0.15% to 0.5% and 0 to 1 PPM, respectively. Given the ultra low level of NOx emission in this engine, NOx prediction is not included in the grey-box modeling.

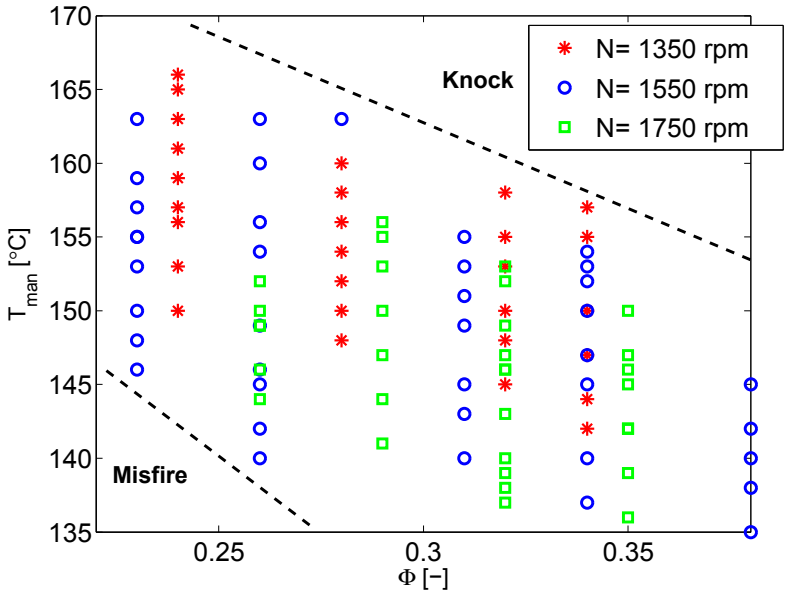

Figure 4.28: Operating range for the HCCI experimental data from Yanmar engine.

CA50-IMEP, T_{exh}, and emissions (CO and THC) grey-box models are developed based on the Yanmar engine experimental data. The design approach of the ANN models are similar to those described in Section 4.3.3.1. The physical model is parameterized and validated for the Yanmar engine; then is used in the grey-box model structure. Prediction performance of the grey-box models are then tested for the Yanmar engine. Results are shown in Figures 4.29, 4.30, and 4.31. Comparison results of the prediction performance for the clear-box, black-box only, and grey-box models are also shown in Table 4.7. The validation results confirm that similarly to the Ricardo engine, the grey-box models outperform the other two peers. The RMSE is improved by about 4.2 CAD, 0.9 bar, and 5 °C for CA50, IMEP, and T_{exh}, respectively compared to the

clear-box model and about 1 CAD, 0.15 bar, and 5 °C compared to the black-box only model. In addition, the grey-box model predicts the CO and THC concentrations with about 50% and 39% less error than the black-box only model.

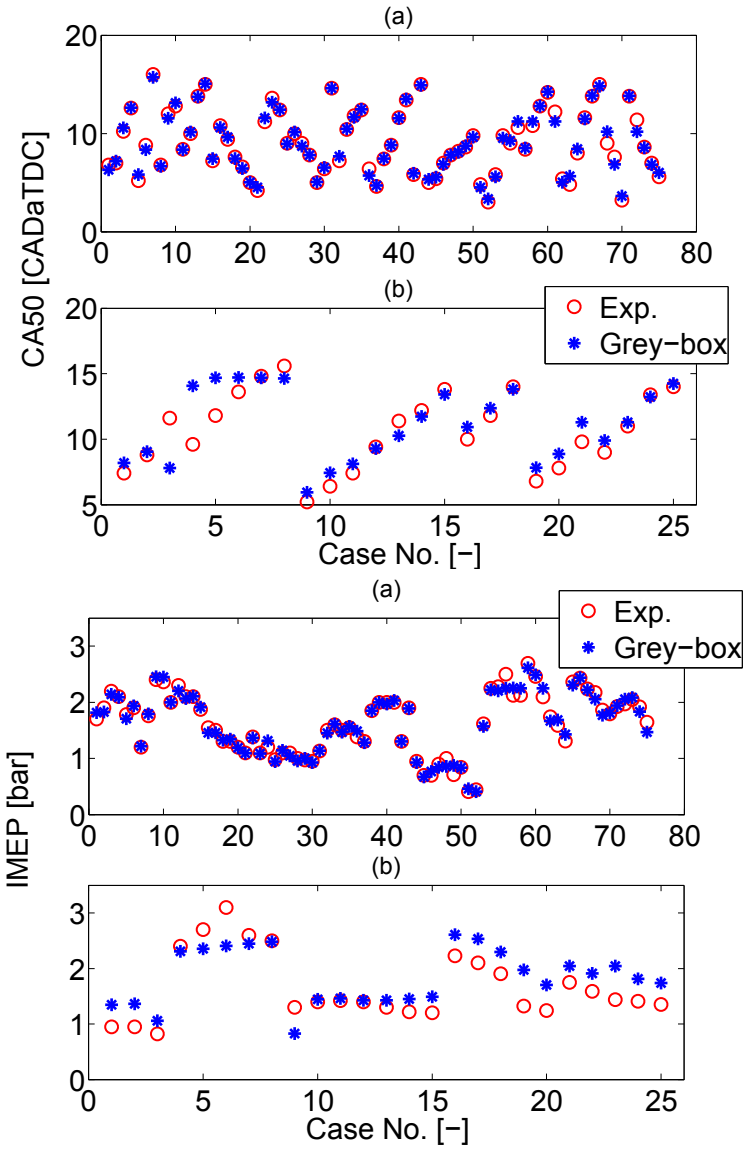

Figure 4.29: Prediction of CA50 and IMEP for Yanmar engine: (a) Training, (b) Validation.

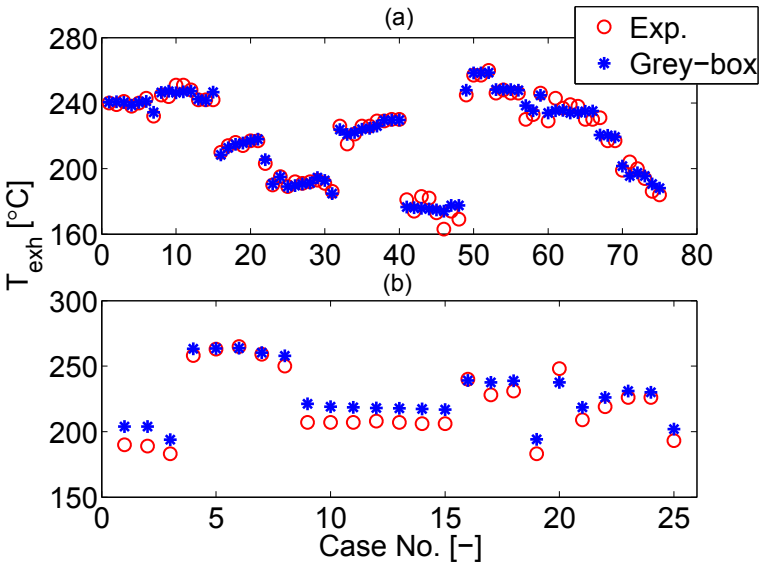

Figure 4.30: Prediction of T_{exh} for Yanmar engine: (a) Training, (b) Validation.

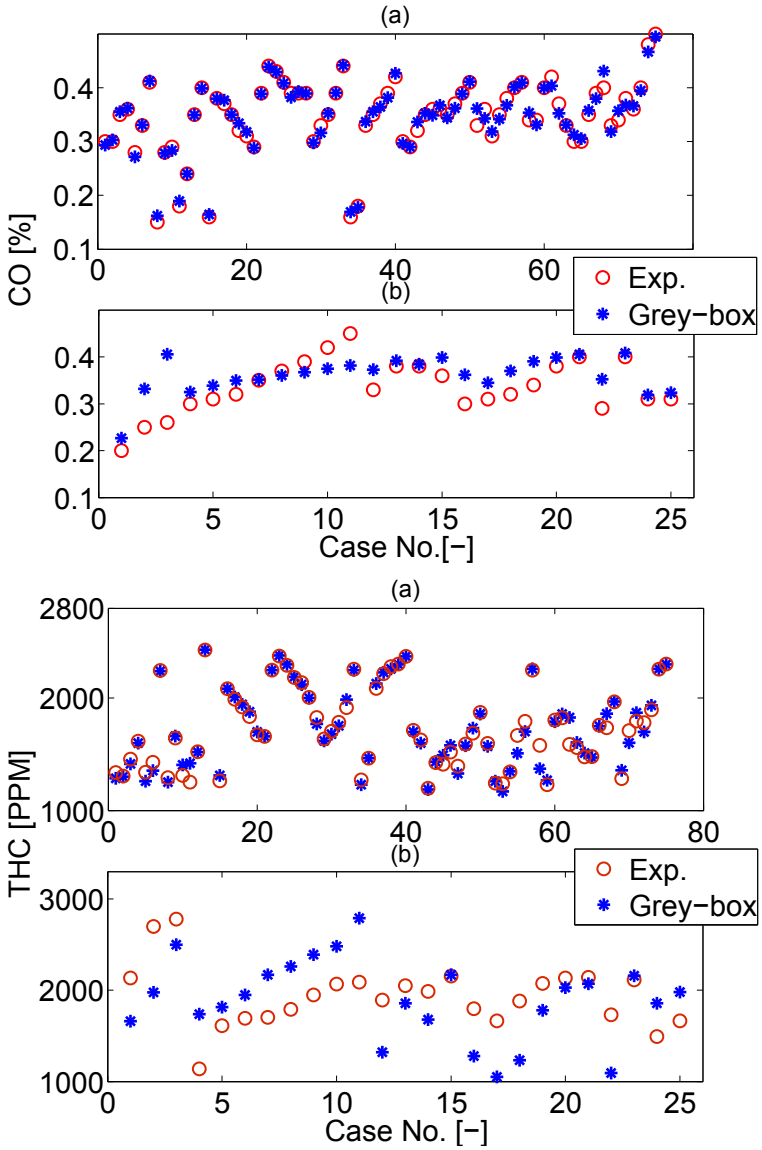

Figure 4.31: Prediction of CO and THC concentration for Yanmar engine: (a) Training, (b) Validation.

Table 4.7
Comparison of average accuracy of the clear-box, black-box only, and the grey-box models for Yanmar engine based on the validation data sets.

Type of Model	Parameter	STD of Error	RMSE
Clear-box	CA50 [CAD]	4.90	5.0
	IMEP [bar]	0.3	1.10
	T_{exh} [°C]	13.7	11.1
	CO [%]	-	-
	THC [PPM]	-	-
Black-box only	CA50 [CAD]	1.40	1.70
	IMEP [bar]	0.2	0.35
	T_{exh} [°C]	11.0	11.0
	CO [%]	0.06	0.1
	THC [PPM]	392	734
Grey-box	CA50 [CAD]	1.20	0.80
	IMEP [bar]	0.2	0.20
	T_{exh} [°C]	9.0	6.5
	CO [%]	0.03	0.05
	THC [PPM]	261	450

4.3.8 Application of HCCI Grey-box Model for Control

In this section, an application of the developed HCCI grey-box models are illustrated for the Ricardo HCCI engine. HCCI emissions are strongly affected by combustion phasing CA50 [10, 125]. In this study, HCCI emissions are indirectly controlled by using an optimum CA50 trajectory. The emission grey-box model from Section 4.3.5 is used in corporation with a Genetic Algorithm (GA) optimization method to find

an optimum CA50. The optimum CA50 at each load (i.e. IMEP) is the indicator for the optimum combustion phasing at which the engine emissions are minimum. NOx emission is typically ultra low in HCCI engines (Figure 4.26) but high CO and THC emissions are major concerns in HCCI engines (Figures 4.24-4.25). Thus, CO and THC are selected as the main optimization targets.

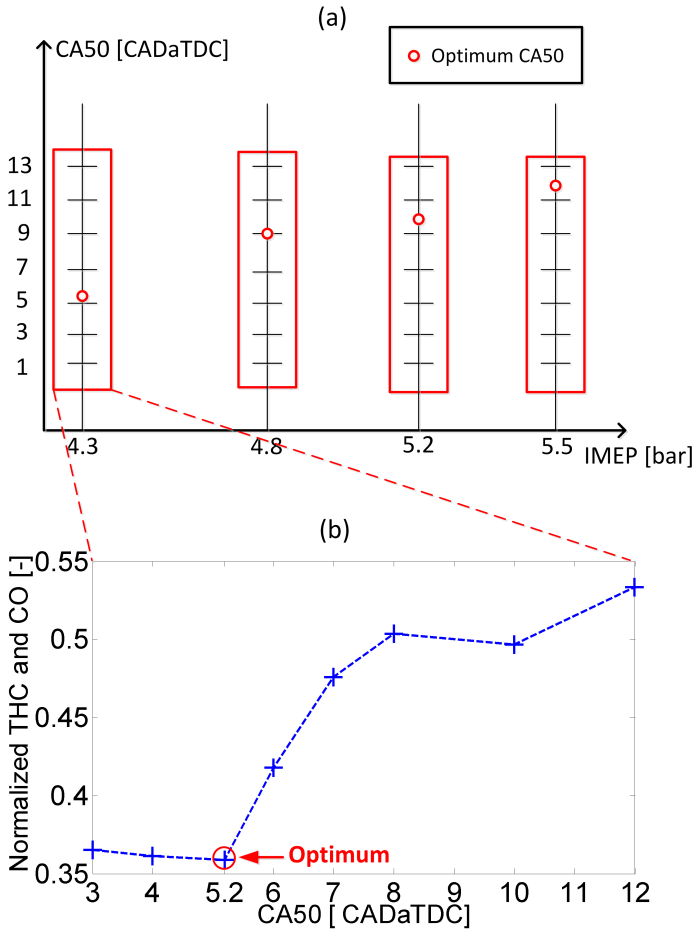

Figure 4.32: (a) Schematic of optimum combustion phasing for a sample engine load variation. (b) Average of normalized THC and CO concentrations versus CA50 at 4.3 bar engine load (baseline condition with varying PRF: P_{man}= 110 kPa, T_{man}= 90 °C, External EGR = 0%, N=850 rpm). The presented emission values are normalized by dividing the emission values over the maximum values of the data at each load for THC and CO, i.e., $\frac{HC}{\|HC\|_\infty}$ and $\frac{CO}{\|CO\|_\infty}$.

A multi-objective optimization method called NSGAII [134] is used in this study. The Grey-box Genetic Algorithm (GB/GA) is run for a given IMEP trajectory while receiving the engine operating conditions such as T_{man}, P_{man}, and N and also predicted

CA50s from the CA50-IMEP grey-box model (Figure 4.17).

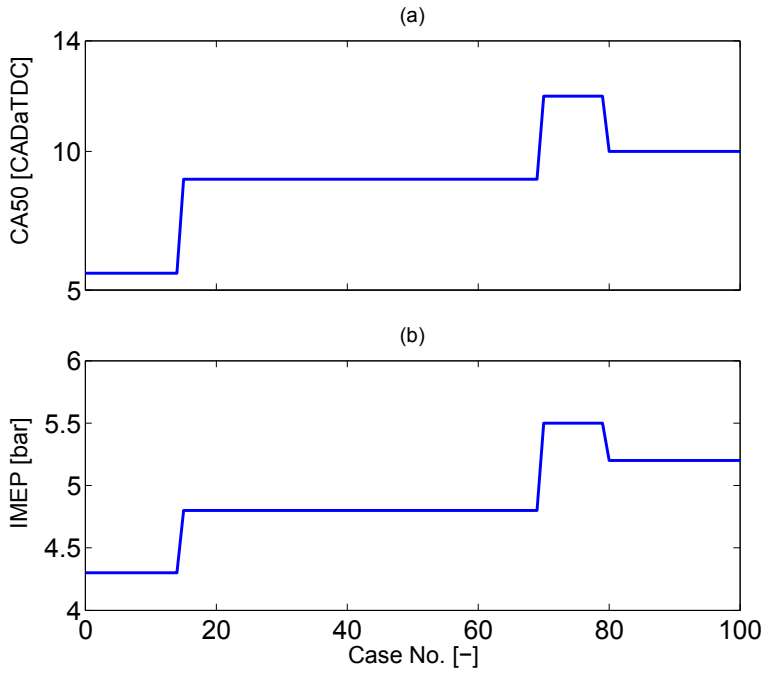

Figure 4.33: Optimum CA50 trajectory (top) from GB/GA algorithm for the load sweep (bottom) from Figure 4.32-a.

Figures 4.32-a and 4.33 show the optimum combustion phasing for a sample engine load variation.Variation of THC and CO emission concentrations for a sample load condition (IMEP=4.3 bar) is illustrated in Figure 4.32-b. Figure 4.32-b shows that the GA algorithm finds the optimum CA50 of 5.2 CADaTDC for minimum THC and CO emissions at this load. A similar approach is done for the other loads of the IMEP trajectory. It should be noted that THC and CO emission trends versus CA50 can vary from one operating region to another. This variation can be caused by changes in in-cylinder gas temperature, mixture dilution level, and coolant (cylinder wall)

temperature [26]. The purpose of this section is to provide a systematic methodology to choose optimum CA50 for HCCI operating regions. The grey-box model offers the capability to train for operating regions; thus, optimum CA50 can be chosen for different HCCI operating regions.

Results in Figure 4.33 show that by moving from low load to higher loads, a more delayed combustion phasing is desired. This can be because at relatively higher load (with higher fuel content), there will be higher in-cylinder temperature resulting in higher combustion temperature which leads to lower THC and CO concentrations [135]. This allows for a higher tolerance for delayed combustion with regard to THC and CO emissions at higher loads. In addition at a higher load, the peak pressure, the ringing intensity, and the knock tendency will be higher. This limits the safe operation range of an HCCI engine at high loads. Thus, using late ignition at higher load helps to avoid unsafe HCCI operation. A known practice [110] is to use high levels of air-fuel mixture dilution at higher loads. This practice results in low ringing intensity due to faster charge expansion at a delayed combustion phasing.

HCCI power output and engine indicated thermal efficiency are typically the highest at intermediate combustion phasings [136]. But as the engine load increases, the optimal combustion phasing to generate highest power and efficiency occurs at a more delayed combustion event [22]. This is mainly because of a tradeoff between

in-cylinder heat transfer losses and unburned species losses as detailed in [22]. In-cylinder heat losses are higher at earlier combustion phasing and unburned species losses increase as combustion occurs later. However, the combustion phasing threshold, at which a sharp increase happens with the amount of unburned species losses, is delayed when the engine load increases. This is because higher in-cylinder temperatures at higher loads reduce unburned species losses [22]. This explains why the optimum CA50 moves towards more delayed combustion as the engine load increases in Figure 4.33.

The optimum CA50 trajectory from GB/GA is then used in a model-based control structure, shown in Figure 4.34. Fuel Octane Number (ON) is manipulated to adjust CA50 by using an integral state feedback controller which is developed based on a physical HCCI model from [2], [9] described in Chapters 2 and 3. IMEP is adjusted by means of a feedforward integral sub-controller in corporation with a ϕ-IMEP map from the physical model. Details for designing these HCCI controllers are found in Chapters 2 and 3.

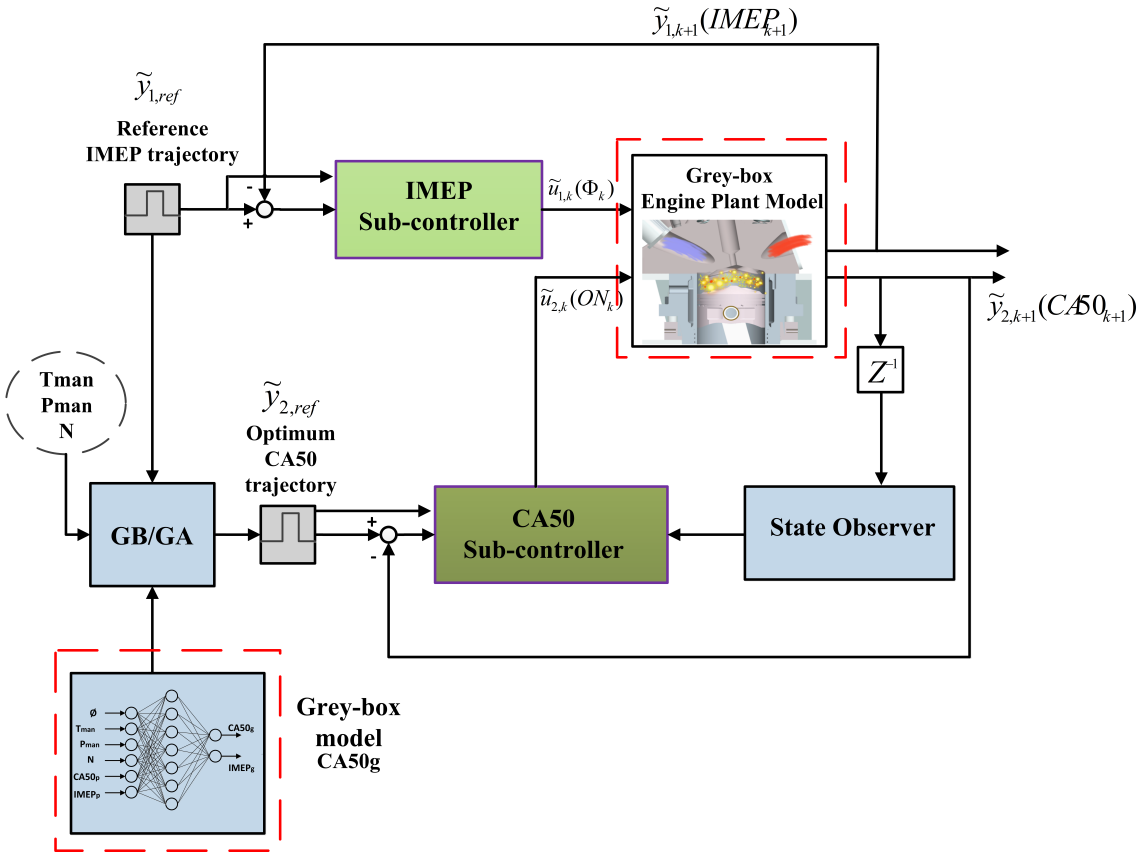

Figure 4.34: Structure of the designed controller.

The designed model-based CA50-IMEP controller is implemented on the grey-box plant model to track the optimum CA50 trajectory. Results of the control simulation are shown in Figure 4.35. Tracking speed for both given IMEP trajectory and the optimum CA50 trajectory are within 3-4 simulation engine cycles while the maximum overshoot is less than 2 CAD for CA50 and 0 bar for IMEP. The engine emissions are also controlled indirectly since the controller tracks the desired CA50 which is chosen such that HCCI emissions will be minimized at each required engine load.

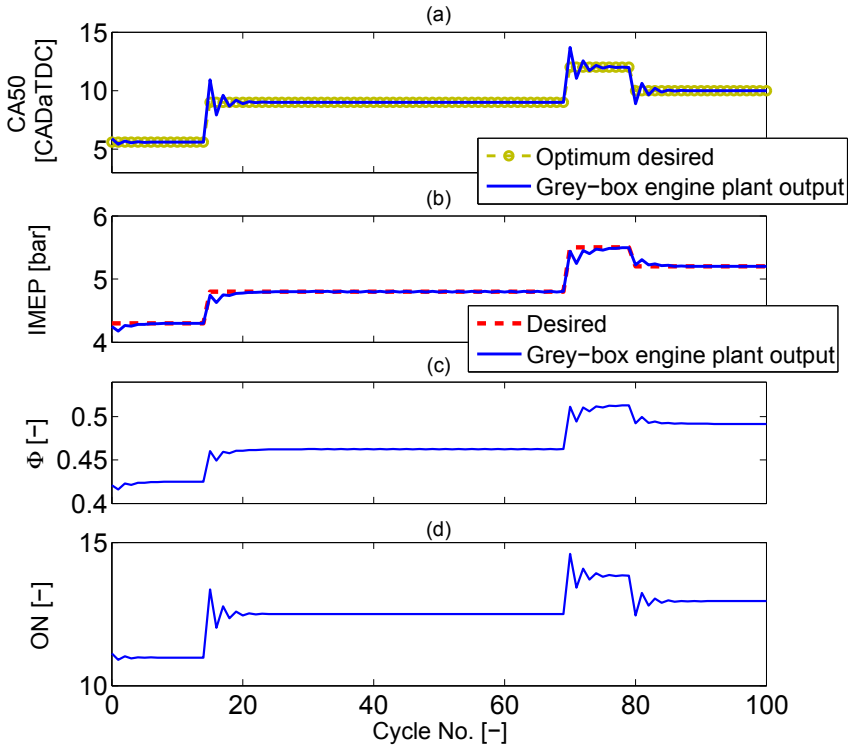

Figure 4.35: Tracking results of optimum CA50 and given IMEP using grey-box model-based controller design in Figure 4.34.

4.4 Summary

A new performance index was proposed for an integrated control of HCCI engines. The performance index incorporates engine load, raw emissions, and exhaust gas temperature (aftertreatment light-off efficiency). To have the optimum performance index at each load (IMEP), an optimum combustion phasing (OCP) algorithm was developed to determine the optimum CA50 trajectory for HCCI control.

The methodology of PI-based HCCI control was illustrated for a blended fuel HCCI engine for IMEP and CA50 control. The experimental data at 214 operating points was used to determine the PI contour plot which was used in the OCP algorithm to calculate optimum CA50 trajectory. The HCCI controller was designed and tested on a previously validated physical engine model. For the case study in this work, a cumulative PI improvement of 11% was shown in comparison to a conventional controller where a constant CA50 is used. The new PI-based control methodology from this work is general and can be applied for different HCCI control applications.

This chapter also presented the first MIMO grey-box model for predicting all the main HCCI engine outputs including CA50, IMEP, T_{exh}, and concentrations of CO, THC, and NOx engine-out emissions. The grey-box models were designed to require minimum efforts for training while providing appropriate accuracy. The grey-box models were validated with extensive experimental data at 309 steady state and transient conditions for two different HCCI engine applications. Here is the summary of the main findings from the grey-box control in this chapter:

† Ricardo HCCI engine with PRF fuels: The validation results show that the emission grey-box model is able to predict CA50, IMEP, T_{exh}, CO, THC, and NOx with the average errors of 0.8 CAD, 0.2 bar, 5.3 °C, 4 PPM, 0.03%, and 394 PPM, respectively. The grey-box models predicts CA50, IMEP, and T_{exh} with more than 80%, 84%, and 74% better accuracy compared to those from the

clear-box (physical) model and 72%, 60%, and 60% improvement in prediction accuracy compared to those from the black-box only model. In addition, the emissions grey-box model predicts CO, THC, and NOx concentrations with three times better accuracy compared to those from the black-box only model.

† Yanmar HCCI engine with ethanol fuel: The grey-box model is capable of predicting the main HCCI engine outputs with average 69% and 45% better accuracy than the clear-box and black-box only models, respectively (for CA50, IMEP, and T_{exh}) and about 45% average better accuracy than the black-box only model for HC and CO concentrations.

† Application of the HCCI grey-box model: The developed grey-box model requires less than 1 ms computation time to run on a 3.2 GHz Intel processor for simulating one HCCI engine cycle. The grey-box model can be used as a virtual engine platform to i) study HCCI engine performance, ii) evaluate and design HCCI controllers in a simulation test-bed. This study illustrated an application of the grey-box model as a virtual engine test-bed for model-based controller design for the Ricardo HCCI engine. A Genetic Algorithm optimization method was applied to simulation results from the grey-box model to determine optimum CA50s leading to minimum HCCI emissions at different engine loads. The optimum CA50 trajectory was then utilized in design of a model-based CA50-IMEP controller to simultaneously control combustion phasing and load while minimizing the HCCI engine-out emissions.

Chapter 5

Integrated Direct Control of Combustion Phasing, Load, and Exhaust Gas Temperature[1]

Precise and integrated cycle-to-cycle control of T_{exh}, load, and combustion phasing is essential for realizing high efficiency HCCI engines, while also maintaining low engine-out emissions. This chapter outlines a model-based control framework for an integrated and direct control of T_{exh}, IMEP, and combustion phasing in an HCCI engine. The discrete COM from Chapter 2 is extended to predict the HCCI outputs on a cycle-to-cycle basis and validated against steady-state and transient experimental

[1]The results of this chapter are partially based on [6] with permission from IEEE as shown in Appendix E, Section E.4.

data from the single cylinder Ricardo engine. In addition, the COM is studied to be computationally efficient for real-time HCCI control.

A three-input three-output controller is designed using a Discrete Sliding Mode Control (DSMC) method to control T_{exh}, IMEP, and combustion phasing by adjusting the intake manifold pressure, fuel mass flow rate, and ratio of two PRFs, respectively. The results indicate the DSMC is capable of maintaining the stability of the engine operation and tracking the desirable HCCI engine outputs. The DSMC is then compared with an empirical PID-based controller.

5.1 Introduction

HCCI control studies in literature are divided into three main groups depending on the number of output control variables: single control, double control, and triple control. Figure 5.1 outlines some major HCCI control studies from these three groups along with the control variables and types of the HCCI controllers designed. In single control studies, one major variable of HCCI combustion phasing is adjusted using a single control input. References [1, 39, 41, 42, 43, 46, 48, 78, 87, 91, 137] are examples of this group. Crank angle by which 50% of the fuel mass is burnt (CA50) is a robust indicator of combustion phasing due to the steep heat release in the main stage of HCCI combustion [80]. Therefore, CA50 is commonly used

in control of HCCI combustion phasing and is also used in this work. Volume at the combustion event (V_{comb}) [49], the crank angle at the peak pressure ($\theta_{P_{max}}$) [50], and the cyclic variability in combustion phasing [138] are other combustion phasing related variables used in HCCI control. The second group includes double control HCCI studies where a secondary variable is controlled in addition to combustion phasing [2, 47, 49, 50, 51, 52, 139, 140]. The secondary variables can be the maximum in-cylinder pressure (P_{max}) [49, 52], IMEP [2, 47], Net Mean Effective Pressure (NMEP) [40, 51], and T_{exh} [5, 52]. IMEP is the major indicator of the engine output work and is used in this work as the second control variable. The third group includes the HCCI control studies on triple control of combustion phasing, load, and T_{exh}. There has been no study in literature on direct triple control of HCCI engines. To the best of the author's knowledge, the work in this chapter is the first study undertaken to develop integrated control of all three main HCCI outputs including CA50, IMEP, and T_{exh}. Figure 5.1 also shows different types of HCCI controllers used in the literature. They are divided into two categories: empirical controllers and model-based controllers. Proportional Integral (PI) [138] and Proportional Integral Derivative (PID) [43, 78] are examples of the first category of HCCI controllers where no model of engine dynamics is incorporated in the controller design. The second category includes model-based controllers, which are designed using HCCI models to consider HCCI engine dynamics. The HCCI models can be empirical like system identification based models [43, 45] or they can be physical like physics-based Control

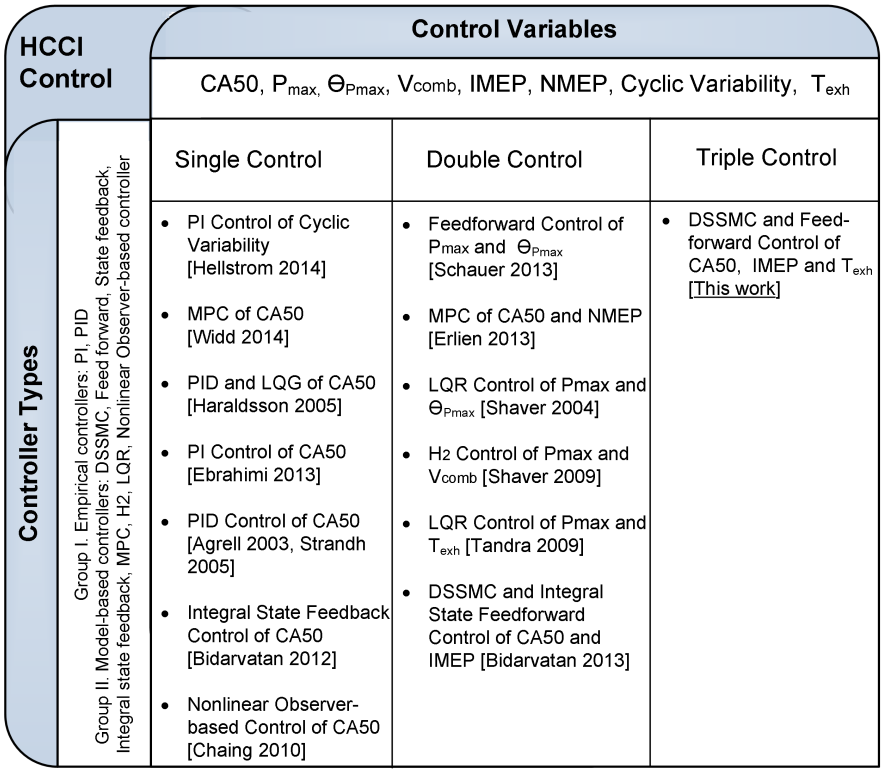

Figure 5.1: Background of HCCI engine control.

Oriented Models (COMs) [81, 82, 83, 85, 141, 142, 143, 144]. Model Predictive Controller (MPC), Sliding Mode Controller (SMC), Linear Quadratic Regulator (LQR), Linear Quadratic Gaussian (LQG), integral state feedback and feedforward controller, H_2 controller, and nonlinear observer based controller are examples of model-based HCCI controllers in the literature. This study develops a new model-based controller denoted as DSSMC (Discrete Suboptimal SMC) and also a new empirical controller (PID) for integrated triple control of HCCI engines.

The contribution from this chapter is twofold. First, an HCCI COM is developed and experimentally validated for predicting cycle-to-cycle T_{exh}, CA50, and IMEP.

Second, a triple model-based controller is designed using a discrete sliding mode control method. Performance of the triple controller for tracking T_{exh}, CA50, and IMEP trajectories is evaluated on a detailed experimentally validated HCCI model. The designed controller can be utilized for real-time control of HCCI engines and can be extended to other HCCI engines once the COM is parameterized for a new engine.

The chapter is presented as follows. In the first section, an extended COM is developed to predict T_{exh}, CA50, and IMEP. Then, the model is experimentally validated at a large number of steady state and transient operating conditions. In the third section, the developed COM is used to design a model-based controller for integrated control of T_{exh}, CA50, and IMEP. In the fourth section, tracking performance of the controller is tested by using a complex physical HCCI model from the previous work [9]. The disturbance rejection properties of the designed controller are also investigated against variations in the engine operating conditions. Finally, the summary from this work is presented.

5.2 Control-Oriented Model (COM) Description

A COM is developed in this section that incorporates physics-based sub-models to capture operation of an HCCI engine on a cycle-to-cycle basis. The HCCI engine process captured by the model consists of five different stages including induction

stroke, compression stroke, combustion period from the start of combustion (SOC) to the end of combustion (EOC), expansion stroke, and exhaust stroke, as shown in Fig. 5.2. Two new sub-models are developed in this work to predict CA50 and T_{exh} as highlighted in red in Fig. 5.2. Furthermore, sub-models from Chapters 2 and 3 are used for the rest of the HCCI model. The COM is parameterized for a single cylinder Ricardo engine with the specifications listed in Table 2.1. The engine operates with a blend of two PRFs, iso-Octane (PRF100) with ON of 100 and n-Heptane (PRF0) with ON of 0. In the following, the two new sub-models of the COM are described and details about the rest of the COM are available in Chapters 2 and 3.

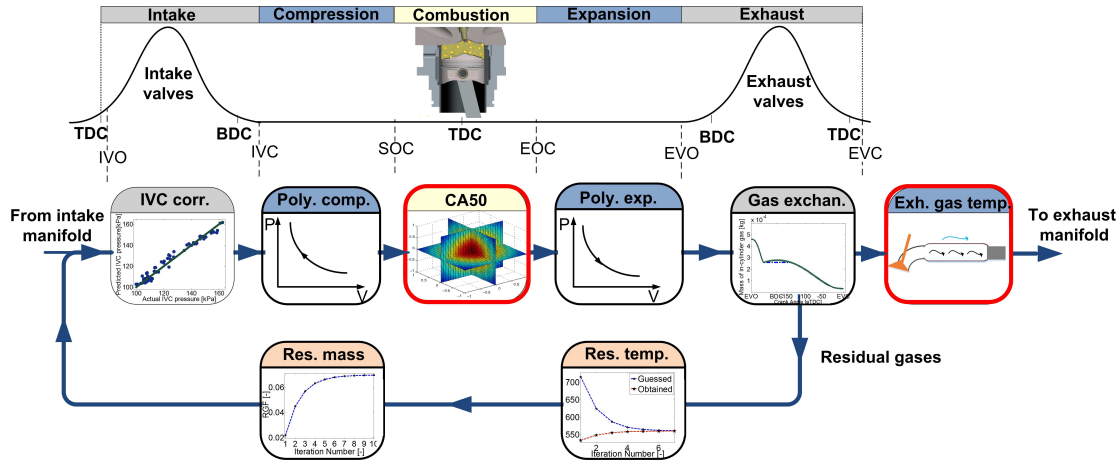

Figure 5.2: Schematic of the COM developed in this study.

5.2.1 CA50 Model

In [96], an MKIM was developed for predicting SOC position for an HCCI engine. MKIM is accurate for predicting SOC, but due to its highly nonlinear structure,

MKIM is limited for controller design. Therefore, a simple fitted empirical correlation using MKIM is developed. This results in condensing MKIM to an empirical correlation. According to [27] and [53], the fuel ON, ϕ, T_{mix}, and P_{ivc} are the dominant factors affecting SOC. Therefore, the following correlation is used to predict SOC:

$$SOC_k = f\left(T_{mix,k}, P_{ivc,k}, ON_{k-1}, \Phi_{k-1}\right) \tag{5.1}$$

where SOC is the crank angle position at SOC and k denotes the current engine cycle. CA50 is then calculated assuming a constant fuel burning rate:

$$CA50_k = SOC_k + 0.5 \times \Delta\Theta_{comb,k} \tag{5.2}$$

where $\Delta\Theta_{comb}$ is the crank angle interval from SOC to EOC. The CA50 also depends on the same dominant factors as SOC. Thus, the following equation is used:

$$CA50_k = g\left(T_{mix,k}, P_{ivc,k}, ON_{k-1}, \Phi_{k-1}\right) \tag{5.3}$$

Fig. 5.3 shows a comparison between the CA50 prediction from the nonlinear MKIM [96] and the new correlation in Eq. (5.3). CA50 is predicted at 38896 different HCCI engine operating conditions for a range of variables shown in Table 5.1.

Then, the simulation data is used to parameterize the CA50 empirical correlation:

$$CA50_k = D_1.\Phi_{k-1}.T_{mix,k} + D_2.P_{ivc,k} + D_3.\Phi_{k-1} + D_4.ON_{k-1} + D_5 \tag{5.4}$$

where constants D_1, D_2, D_3, D_4 and D_5 are 0.617, -0.090, 224.121, 0.252 and 29.618, respectively. The average error, RMSE, and STD of error between the predicted CA50s are 1.3 CAD, 1.5 CAD, and 1.1 CAD respectively. This confirms the reliability of the obtained correlation for predicting CA50 for the region the HCCI engine is parameterized.

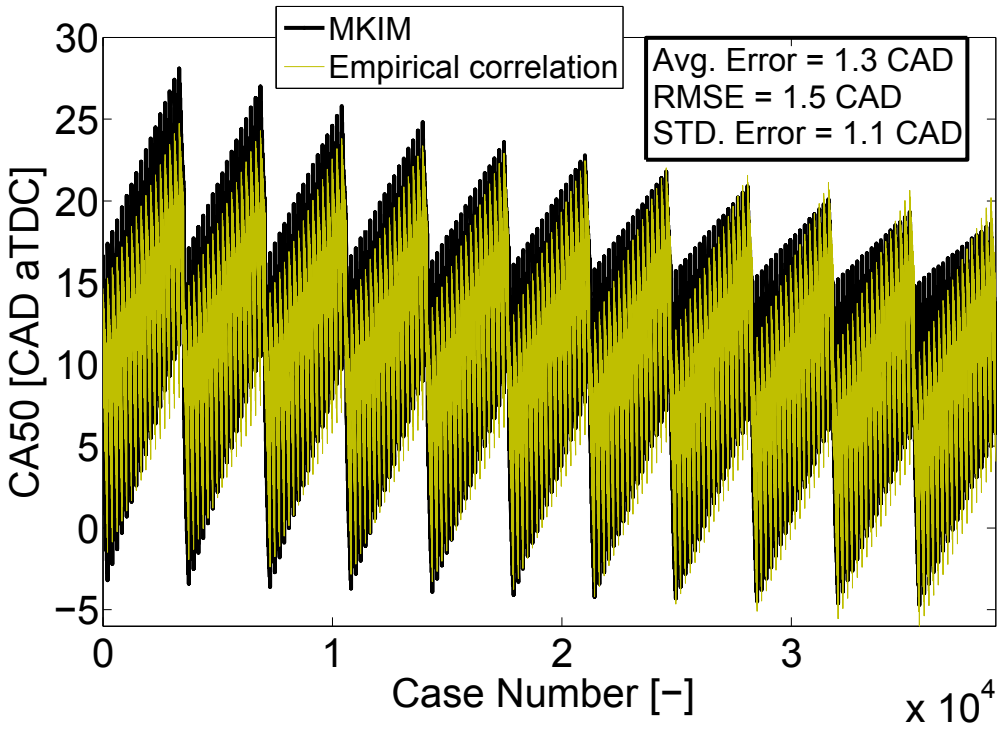

Figure 5.3: Comparisons of CA50 prediction by MKIM with those from the developed CA50 correlation. RMSE and STD stand for Root Mean Square Error and Standard Deviation of prediction error, respectively.

Table 5.1
Range of HCCI engine operating conditions used to parameterize the CA50 correlation.

Parameter	Range	Increment
T_{mix}	390 - 420 °C	2 °C
P_{ivc}	110 - 160 kPa	5 kPa
ON	0 - 40	2.5
Φ	0.3 - 0.6	0.025
N	1000 rpm	0
EGR	0 %	0

5.2.2 Exhaust Gas Temperature (T_{exh}) Model[2]

The COM is extended by adding a new model for calculating T_{exh} in the exhaust gas manifold and before entering a catalytic converter. Fig. 5.4 shows a schematic for the flow of exhaust gases from the exhaust valve to the entry of the catalytic converter. The following assumptions are made for developing the T_{exh} model:

1. The temperature of exhaust gases leaving the combustion chamber is equal to the temperature at exhaust valve closing (T_{evc}).

2. Heat transfer occurs only due to convection between the exhaust gases and the exhaust manifold as shown in Fig. 5.4. The remaining forms of heat transfer are included by a Q_{corr} term.

3. Temperature at point (A) in Fig. 5.4 is assumed to be the mean of T_{evc} and T_{exh}.

[2]This subsection is based on the work in [132].

4. The surface temperature of the exhaust manifold ($T_{surface}$) is constant and equal to the ambient temperature ($T_{ambient}$).

5. Changes in kinetic energy and potential energy in the exhaust manifold are neglected.

The first law of thermodynamics is applied to the control volume in Fig. 5.4. After rearranging the energy equation, the following equation is used to calculate T_{exh}:

$$\begin{aligned} T_{exh,k} = & \frac{hA_{surface}(T_{evc,k} - T_{surface})}{\dot{m}_{exh,k}C_v + (hA_{surface}/2)T_{evc,k}} \\ & + \frac{(\dot{m}_{exh,k}C_v - (hA_{surface}/2))T_{evc,k}}{\dot{m}_{exh,k}C_v + (hA_{surface}/2)T_{evc,k}} \\ & + \frac{Q_{corr}}{\dot{m}_{exh,k}C_v + (hA_{surface}/2)T_{evc,k}} \end{aligned} \tag{5.5}$$

where h and C_v are the convective heat transfer coefficient and average specific heat capacity at constant volume. $\dot{m}_{exh}$ is the mass flow rate of the exhaust gases in the exhaust manifold. $A_{surface}$ is the surface area for the exhaust manifold.

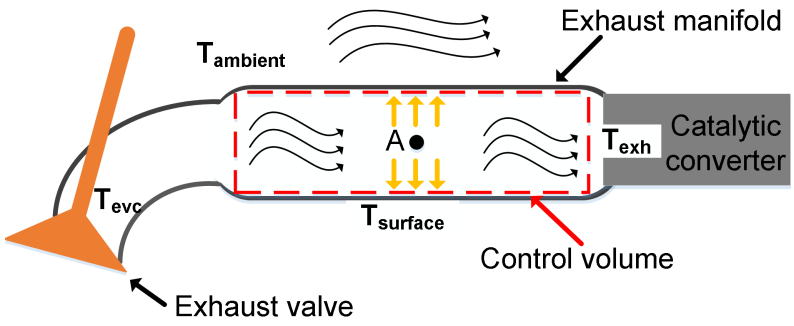

Figure 5.4: A schematic of the control volume for the T_{exh} model.

CA50 submodel and T_{exh} submodel along with other submodels ([1] and [2]) are combined to implement the COM in MATLAB® Simulink. The COM is computationally efficient with simulation time requirement of less than 1 ms for an engine cycle on a 2.67 GHz Intel processor. This makes the COM practical for real-time control of HCCI engines.

5.3 Model Validation

5.3.1 Steady State Validation

The COM is validated against 48 different experimental steady state HCCI conditions with the operating range shown in Table 5.2. Experimental validation results of the COM are shown in Figure 5.5. For each operating condition, the predicted engine outputs by the COM are compared with the average of the measured engine outputs for 300 individual cycles. The cyclic variability for CA50 ranges from 1.8 CAD to 11.1 CAD. The cyclic variability for T_{exh} is around 4 °C. The Coefficient of Variation (COV) of IMEP ranges from 1 % to 5 % for the experimental data in Figure 5.5. Table 5.3 shows the accuracy of the COM for predicting CA50, IMEP and T_{exh} for the 48 steady state HCCI operating conditions. Results show that the COM can predict the three engine output variables with average errors of 1.7 CAD, 0.4 bar,

and 12.4 °C for CA50, IMEP, and T_{exh}, respectively.

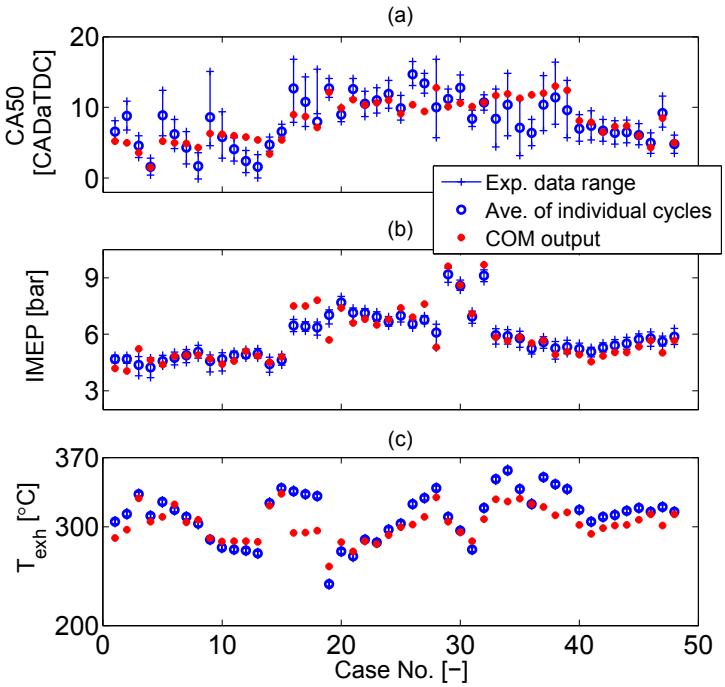

Figure 5.5: Steady state validation of the COM.

Table 5.2
Operating range of the experimental data for steady state validation.

Parameter	Range
ON	0 - 40
Φ	0.3 - 0.6
P_{man}	100 -120 kPa
T_{man}	90 - 140 °C
N	900 - 1000 rpm
External EGR	0 %
Coolant temperature	69 - 85 °C

Table 5.3
Accuracy of the COM for the steady state engine operating conditions in Fig. 5.5.

Parameter	Avg. error	Uncertainty*	RMSE
CA50 (CAD)	1.7	± 2.2	2.2
IMEP (bar)	0.4	± 0.5	0.5
T_{exh} (°C)	12.4	± 13.0	16.0

*Uncertainty is defined as standard deviation of differences between experimental and the COM predicted values.

5.3.2 Transient Validation

Performance of the COM is also tested at a transient engine operating condition. Fig. 5.6 shows the validation results for a step change in fuel ON and Φ. Other parameters including P_{man}, T_{man}, N, and external Exhaust Gas Recirculation (EGR) percentage were kept constant. Table 5.4 shows the accuracy of the COM for predicting CA50, IMEP and T_{exh} for the HCCI engine during the transient condition in Fig. 5.6. From Fig. 5.6, it can be observed that the COM predictions are in very good agreement with the experimental data with average errors of 1.5 CAD, 0.2 bar, and 2.5 °C. Therefore the COM can be used for designing model-based HCCI controllers.

Table 5.4
Accuracy of the COM for the Transient Engine Operation in Fig. 5.6.

Parameter	Avg. error	Uncertainty	RMSE
CA50 (CAD)	1.5	± 1.8	1.9
IMEP (bar)	0.2	± 0.1	0.2
T_{exh} (°C)	2.5	± 2.1	2.9

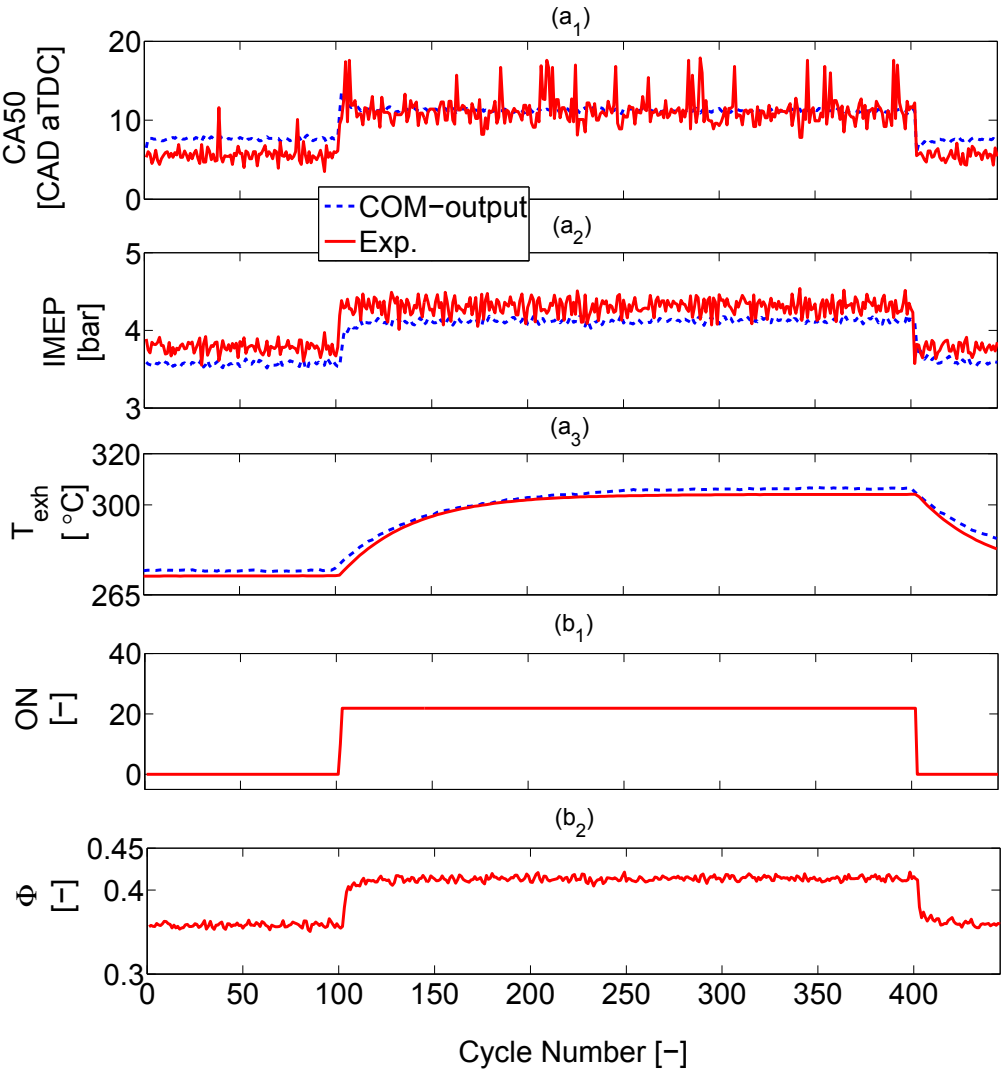

Figure 5.6: Validation of the COM for a transient fueling operating condition. (a_x): Experimental data and model outputs and (b_x): Transient fueling inputs. P_{man}, T_{man}, N and external EGR percentage are 110 kPa, 91 °C, 815 rpm, and 0 %, respectively.

5.4 State-space Representation

The COM is then arranged into a state space form. Both CA50 and T_{exh} models have five states as following:

$$x_1 = [CA50, T_{soc}, P_{soc}, T_{rg}, m_{evc}]^T \tag{5.6}$$

$$x_2 = [T_{evc}, CA50, T_{soc}, P_{soc}, m_{evc}]^T$$

where x_1 and x_2 are the state vectors for the CA50 and T_{exh} models, respectively. The HCCI experimental results from [9, 26] show that ON, fuel mass flow rate ($\dot{m}_f$), and intake manifold pressure (P_{man}) are effective parameters to adjust CA50, IMEP, and T_{exh}, respectively. Therefore, ON and P_{man} are selected as the inputs (u_1 and u_2) for CA50 and T_{exh} control, while $\dot{m}_f$ is selected for the input (u_3) for IMEP control.

The nonlinear COM is then linearized around a nominal operating point shown in Table 5.5. This operating point is selected based on the Ricardo HCCI engine experimental results in [10] to ensure the operating point is located near the engine optimal region with minimal cyclic variations. The resulting linear state-space of CA50 and T_{exh} for two consecutive engine cycles (k and $k+1$) are:

$$x_{k+1} = Ax_k + Bu_k \tag{5.7}$$

$$y_k = Cx_k \tag{5.8}$$

where x, u, and y are the vector of the model states, the input to the plant model, and the output of the model, respectively. State T_{evc} correlates to T_{exh} by using the developed T_{exh} model in Section 5.2. Values of the linear model matrices are presented in Appendix A.4. The linear COM is then used to develop model-based controllers for CA50 and T_{exh} in Section 5.5.

Table 5.5
Nominal operating point around which the nonlinear COM is linearized.

Parameter	**Value**
CA50	10 CAD aTDC
T_{soc}	520 °C
P_{soc}	2364 kPa
T_{rg}	365 °C
m_{evc}	0.0347 g
RGF	6.3 %
ON	20
$\dot{m}_f$	0.097 g/cycle
P_{man}	125 kPa
T_{man}	110 °C
N	1000 rpm
T_{exh}	300 °C
External EGR	0 %

5.5 Controller Design

A triple model-based controller is designed in this section which consists of two types of controllers, discrete sliding mode controller for CA50 and T_{exh} and feedforward integral controller for IMEP. Figure 5.7 shows a schematic of the triple control structure designed in this study. Two state observers are used in the control structure since most of the model states are not easily measurable in practice.

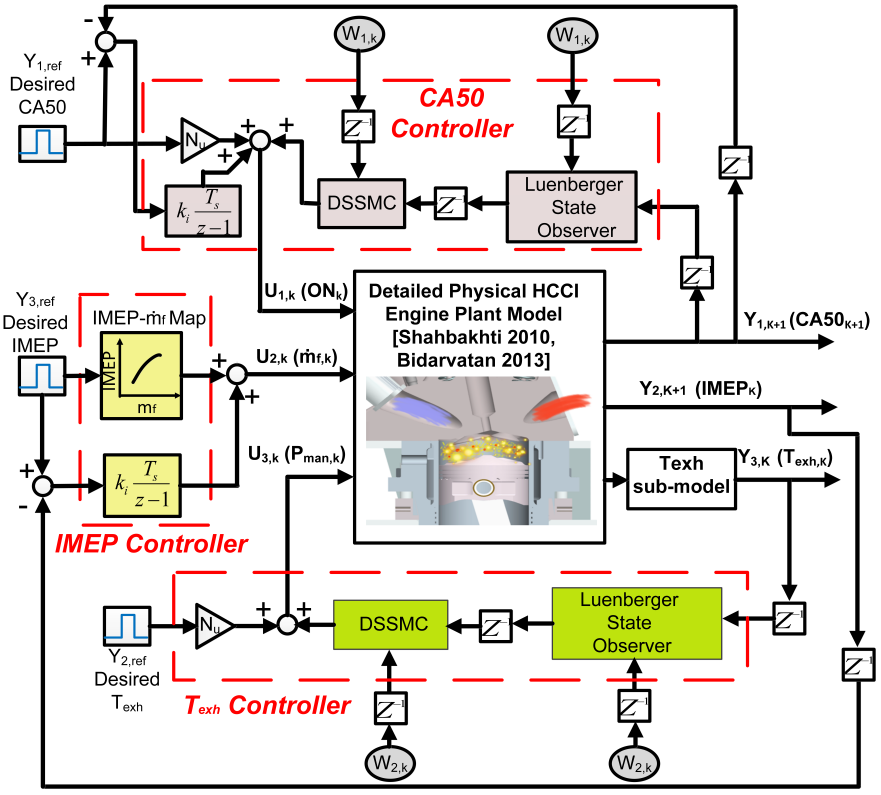

Figure 5.7: Schematic of designed HCCI triple controller.

5.5.1 Discrete Sub-optimal Sliding Mode Control (DSSMC) with Feedforward Gain and Integral Action

DSSMC is a discrete optimization-based control method with the advantage of optimal control and robustness of sliding mode control [101]. Results from Chapter 2 for single control of combustion phasing showed that DSSMC is promising for HCCI control applications. Thus, the DSSMC is used to design $CA50$ and T_{exh} controllers in this chapter.

Details of DSSMC design were explained in Chapter 2. The control law is found using the following equation:

$$u_{sl,k} = -(C_s B)^{-1} \left[C_s A x_k + C_s E w_{k-1,1} \right] + N_u y_{ref} \tag{5.9}$$

where E represents the disturbance matrix and w is the vector of the engine model physical disturbances (w_1 for the CA50 model and w_2 for the T_{exh} model) as shown in Eq. (5.10).

$$w_1 = [P_{man}, \dot{m}_f]^T \tag{5.10a}$$

$$w_2 = [ON, \dot{m}_f]^T \tag{5.10b}$$

In addition, an integral feedforward action (k_i) is added to the CA50 DSSMC to cancel any steady state error. Values of the controller parameters for CA50 are presented in the following:

$$S_{sl,1} = [0.0075, -0.0129, -0.1592, 0.0189, -0.1328] \tag{5.11a}$$

$$N_{u,1} = 3.6023 \quad k_i = 1.8 \tag{5.11b}$$

and for T_{exh} are:

$$S_{sl,2} = [0.009, -0.00001, -0.0008, 0.0697, 0.1659] \tag{5.12a}$$

$$N_{u,2} = -0.5331 \tag{5.12b}$$

5.5.2 Feedforward Integral IMEP Controller

An IMEP-$\dot{m}_f$ map is obtained by running the detailed physical HCCI model [2, 9] for a range of operating conditions to determine the engine's IMEP in response to the changes in the fuel mass rate.

$$u_{ff,k_{map}} = c_1 IMEP_{ref,k} + c_2 \tag{5.13}$$

where $u_{ff_{map}}$ is the control input actuated by the feedforward controller using IMEP-$\dot{m}_f$ map and $IMEP_{ref}$ is the reference IMEP. In addition, an integral gain (K_I) is added to the feedforward controller to cancel any steady state error. Eventually the feedforward control law is calculated by:

$$u_{ff,k} = u_{ff,k_{map}} + u_{ff,k_I} \tag{5.14}$$

where $u_{ff,I}$ is the control input actuated by the integral controller. The final control input (u_{ff}) determines the commanded $\dot{m}_f$ to the engine. Values of the IMEP feedforward controller are:

$$c_1 = 2.136 \quad c_2 = 0.03 \tag{5.15a}$$

$$k_I = 3 \tag{5.15b}$$

5.5.3 State Observer

To estimate the model state variables, two Luenberger state observers [105] are designed. The observed states are then used by the DSSMCs to determine the appropriate control inputs to the engine plant. The model states ($\hat{x}_{1,k+1}$) at *k+1* cycle are

determined using Equation (5.16):

$$\hat{x}_{k+1} = A\hat{x_k} + Bu_k + Ew_k + l(y_k - \hat{y}_k) \tag{5.16}$$

where $\hat{x}_k$ and $\hat{y}_k$ are the estimated states and output from the previous cycle (k), respectively. l is the Luenberger gain vector, that can be determined using a pole placement technique [105]. Values of the Luenberger gain vectors for the CA50 and T_{exh} controllers are shown in the following equations.

$$l_{CA50} = \begin{bmatrix} 0.1629 \\ -2.9301 \\ -91.7526 \\ -0.2194 \\ -0.0012 \end{bmatrix} \tag{5.17a}$$

$$l_{T_{exh}} = \begin{bmatrix} -0.0034 \\ -0.0139 \\ -0.0199 \\ 0.2449 \\ 0 \end{bmatrix} \tag{5.17b}$$

5.5.4 Proportional Integral Derivative (PID)-based Triple Controller

A PID-based triple controller, which consists of three discrete PID controllers, is designed to compare with the developed model-based controller. The PID controller gains (k_p, k_i, and k_d) are initially set using Ziegler and Nichols method [145]. Then, the gains are tuned for optimal control performance. Values of the PID gains are listed in the following.

$$k_{p,ca50} = 1.3, k_{i,ca50} = 2.5, k_{d,ca50} = 0.01 \tag{5.18a}$$

$$k_{p,imep} = 0.009, k_{i,imep} = 0.012, k_{d,imep} = 0.01 \tag{5.18b}$$

$$k_{p,Texh} = 0.65, k_{i,Texh} = 0.6, k_{d,Texh} = -0.001 \tag{5.18c}$$

5.6 Control Results

The experimentally validated detailed physical HCCI model from [2, 9] is used as a testbed (as shown in Figure 5.7) to test the performance of the designed model-based triple controllers. In this section, the tracking performance and the disturbance rejection properties of the controllers are studied for conditions of having single

or simultaneous changes in the desired outputs. In addition, the control results of the model-based triple controller are compared with those of the PID-based triple controller. Tracking performance of controllers are tested for positive and negative step changes in the desired CA50, T_{exh}, and IMEP. Figure 5.8 shows the tracking results of the model-based and PID-based controllers when desired setpoints for CA50, T_{exh}, and IMEP are changed separately. In the first simulation period (cycles 1

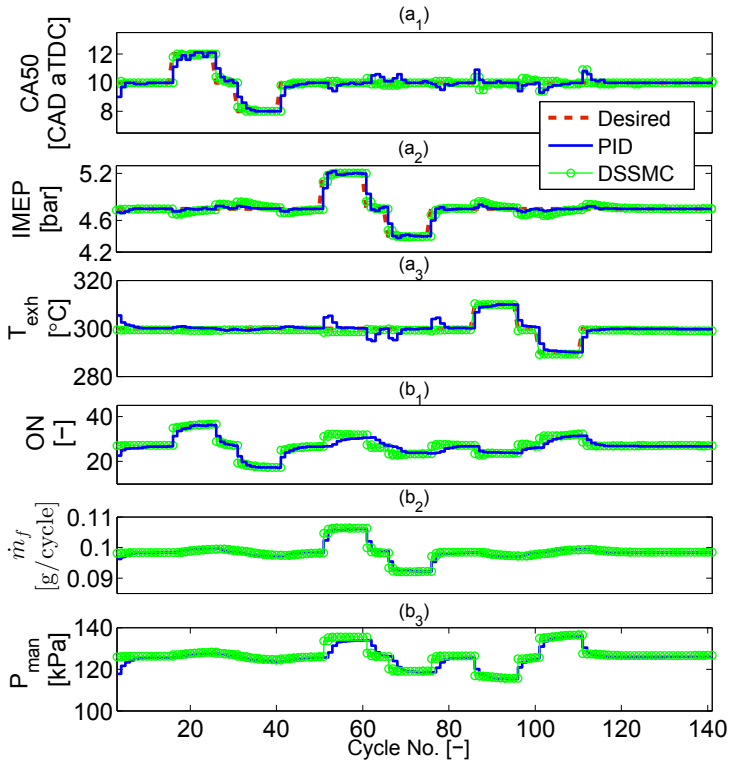

Figure 5.8: Single tracking performance for the triple controllers. (a_x): plant outputs and (b_x): control inputs.

to 40) in Figure 5.8, the tracking performance of the CA50 sub-controller is evaluated by using positive and negative step changes of the desired CA50 setpoints. Constant desired T_{exh} and IMEP (i.e. 300 °C and 4.7 bar) are considered to illustrate how the

IMEP and T_{exh} sub-controllers can regulate the outputs and cancel the disturbance effects of ON variations on T_{exh} and IMEP. In the second simulation period (cycles 41 to 76), the tracking performance of the IMEP sub-controller is studied for positive and negative step changes of the desired IMEP while the CA50 and T_{exh} sub-controllers are responsible to regulate the outputs at the desired constant values of 10 CAD aTDC and 300 °C, respectively. Finally, in the third simulation period (cycles 77 to 110), the tracking performance of the T_{exh} sub-controller is studied for positive and negative step changes and the CA50 and IMEP sub-controllers are responsible to reject the disturbance effects of P_{man} variations and regulate the outputs at the desired constant values of 10 CAD aTDC and 4.7 bar, respectively. Figure 5.9 shows the tracking results for both the model-based and PID-based controllers when CA50, T_{exh}, and IMEP setpoints are simultaneously changed. Quantitative performance metrics for tracking and disturbance rejection of the controllers are shown in Tables 5.6 and 5.7, respectively. Tracking results show the model-based controller can track the reference outputs faster than the PID-based controller with up to 2 and 3 cycles less rise time and settling time, respectively. In addition, the model-based and PID-based controllers have no steady-state error and exhibit no overshoot for tracking CA50 and T_{exh}. However, the PID-based controller has a maximum overshoot of IMEP (0.02 bar) compared to zero IMEP maximum overshoot of the model-based controller. Furthermore, no chattering is observed for the tracking results of the DSSMCs.

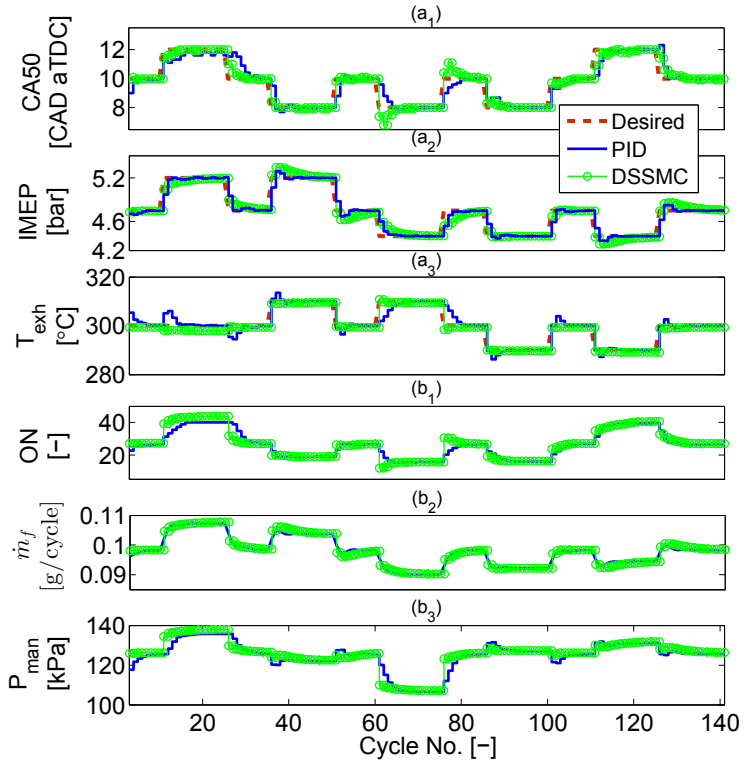

Figure 5.9: Simultaneous tracking performance for the triple controllers. (a_x): plant outputs and (b_x): control inputs.

Table 5.7 shows the metrics of the disturbance rejection performance for the model-based and the PID-based controllers. Simulation results show that the model-based controllers outperform their PID-based peers with 5 and 3 cycles faster disturbance rejection when tracking CA50 and T_{exh} respectively, but the disturbance rejection speed for IMEP is the same at 7 cycles for both controllers. The maximum deviation of CA50 is 0.3 CAD less for the model-based controller compared to the PID-based controller while for IMEP, it is almost the same at 0.05 bar. The maximum deviation of T_{exh} for conditions of having disturbances is 5 °C for the PID-based controller while

the model-based controller is capable to completely cancel the disturbance effects on T_{exh} with 0 °C maximum deviation. Using integral action in the controller design, the maximum steady-state errors of both the model-based and PID-based controllers are zero for all the engine outputs.

Compared to the PID-based triple controller, the model-based controller is able to incorporate knowledge of the system parametric changes. Applying the simple on-line disturbance rejection rule [102] inside the DSSMC structure enhances robustness property of this model-based controller compared to the PID controller. The triple model-based controller can be utilized for other HCCI engines by parameterizing the COM to capture the dynamics of a new engine.

Table 5.6
Tracking performance of the model-based and PID-based controllers.

Controller type	**Output parameter**	**Rise time**	**Settling time**	**Max. overshoot**	**Steady-state error**
PID-based controllers	CA50	3 cycles	4 cycles	0 CAD	0 CAD
	IMEP	2 cycles	4 cycles	0.02 bar	0 bar
	T_{exh}	2 cycles	3 cycles	0 °C	0 °C
Model-based controllers	CA50	1 cycle	1 cycle	0 CAD	0 CAD
	IMEP	1 cycle	1 cycle	0 bar	0 bar
	T_{exh}	1 cycle	1 cycle	0 °C	0 °C

Table 5.7
Disturbance rejection performance of the triple HCCI controllers.

Controller type	Output parameter	Max. absolute deviation	Max. steady -state deviation	Dist. rejection speed
PID-based controllers	CA50	0.7 CAD	0 CAD	6 cycles
	IMEP	0.04 bar	0 bar	7 cycles
	T_{exh}	5 °C	0 °C	4 cycles
Model-based controllers	CA50	0.4 CAD	0 CAD	1 cycle
	IMEP	0.05 bar	0 bar	7 cycles
	T_{exh}	0 °C	0 °C	1 cycle

5.7 Summary

A discrete COM was developed to predict cycle-to-cycle CA50, T_{exh}, and IMEP for a blended fuel HCCI engine. The COM was validated with the HCCI experimental data at 49 steady-state and transient operating conditions. The validation results indicated that the COM can predict CA50, IMEP, and T_{exh} with average errors of 1.6 CAD, 0.3 bar, and 7 °C, respectively. The COM was then utilized to design a triple HCCI controller for tracking the desired cycle-to-cycle CA50, IMEP, and T_{exh}. The triple controller is a model-based engine controller which combines a DSSMC with feedforward gain and integral action for CA50, a feedforward integral controller for IMEP, and a DSSMC for T_{exh} (with the control inputs of fuel ON, $\dot{m}_f$, and P_{man}). Performance of the model-based controller was then studied using a detailed experimentally validated HCCI engine model and compared with those of an optimally tuned PID-based controller. The designed model-based controller could track the

desired output trajectories with up to 4 cycles faster than the PID-based controller while there was no steady-state error observed for both controllers. Performance of the controllers was also studied for rejecting the effects of the disturbances. Simulation results showed that while there was no steady-state deviation for both types of controllers, the model-based controller outperformed its PID-based peer with up to 5 cycles faster disturbance rejection and zero maximum deviation. Given the low computational requirement (<1 ms to simulate an engine cycle on a 2.67 GHz Intel processor) and good prediction accuracy, the new COM and the designed model-based controller are suitable for real-time triple control of HCCI engines.

Chapter 6

Optimal Control of Energy Management in an HEV Integrated with Low Temperature Combustion Engines[1]

In this chapter, the potential energy consumption benefits achieved by the synergy between two advanced powertrain technologies (i.e., LTC and electrification) are studied. For this purpose, a powertrain model for a parallel HEV is developed which includes the sub-models for different components like ICE, E-machine, battery, transmission

[1]The results of this chapter are partially based on [7] with permission from ASME as shown in Appendix E, Section E.5.

system, and vehicle (dynamics). Two different ICE maps are used in the developed HEV powertrain model: 1) ICE map based on the baseline SI engine available at MTU's Energy Mechatronics Lab (EML) and 2) ICE map based on the EML's modified engine that operates in an LTC mode (HCCI). Both ICE map models are built by using the experimental data from engine testing on an AC dynamometer. The E-machine and the battery are sized for the studied ICEs. MPC as an optimal control strategy is designed for management of energy (torque split) between ICE and E-machine. The control strategy is then tested in simulation on two plant powertrain models: 1) LTC-HEV powertrain model and 2) SI-HEV powertrain model, for city driving conditions in a common North American drive cycle. Results are compared to find out the potential energy consumption benefits achieved by integrating LTC and electrification technologies.

6.1 Introduction

There is now a high demand for powertrain technologies with low fuel consumption and low emissions. Parallel HEVs make an important contribution to address this demand, with more than 80% of the total sales of HEVs in the US in 2012 [146]. A parallel HEV shifts ICE operation into the high fuel efficiency or low emission regions by utilizing torque assist from Electric-machine (E-machine) [147]. One well-recognized control challenge in parallel HEVs is the management or control of energy flows from

the two energy sources through the powertrain [148, 149]. A control strategy, which is usually implemented in the vehicle supervisory upper-level controller, is defined as an algorithm that adjusts the torque split between ICE and E-machine. Development of comprehensive torque split strategies is crucial to improve fuel economy in parallel HEVs.

Although LTC engines have benefits of high fuel efficiency and low emissions, they have a limited operating range and can operate mostly at low loads and low speeds [10]. To overcome this challenge, vehicles with LTC engines can be hybridized to operate in a parallel HEV configuration. In this way, E-machine assists in propelling the vehicle at high loads and high speeds by providing torque in addition to the ICE torque through the powertrain. Therefore, there are more opportunities to have benefits of LTC engines. In addition, control of LTC engines is more crucial during vehicle transient operations. Results in Chapters 2, 3, and 5 show that the controller tracking response is in order of several engine cycles. Using the E-machine torque assist during the vehicle transients, LTC engine operates less at transient conditions therefore, less LTC engine control efforts are required. It is anticipated that combining LTC engine and E-machine will lead to fuel economy advantage compared to the conventional HEV. Given all these motivations, the energy consumption benefits achieved in an HCCI-HEV is investigated compared to a baseline SI-HEV in this chapter. To the best of the author's knowledge, this is the first study undertaken for optimal control of energy management in a *parallel* LTC-HEV and analysis of energy

consumption benefits compared to the base-line SI-HEV. It should be noted that fuel economy benefits of HCCI-HEV in *series* and *extended range* configuration have been studied in [150, 151].

The chapter is presented as follows. Section 6.2 describes the HEV model and SI and HCCI experimental maps. Then, details of the design for supervisory energy management control strategies are described in Section 6.3. In Section 6.4, simulation results for using the developed LTC-HEV are presented and compared with those of the baseline SI-HEV. Finally, Section 6.5 summarizes the major findings from this chapter.

6.2 HEV Model Description

Parameters of the parallel HEV in this chapter are listed in Table 6.1. Following sections detail the HEV model that include different component sub-models.

Table 6.1
Parameters of the HEV platform in this chapter.

Parameter	**Value**	**Parameter**	**Value**
M(kg)	1575	n_d (-)	4.53
R_w (m)	0.38	A (m^2)	2.0
C_d (-)	0.3	μ (-)	0.01
P_{amb} (kPa)	88	T_{amb} (°C)	38
R ($\frac{kJ}{kgK}$)	0.287	Q_c (Ah)	5
SOC_i (-)	0.8	V_{oc} (V)	300

6.2.1 Longitudinal Vehicle Dynamics (LVD)

Longitudinal Vehicle Dynamics (LVD) are calculated by using Equations (6.1), (6.2), and (6.3). F_r, F_d, and F_t are rolling resistance, aerodynamic drag, and total traction forces at the wheels, respectively [152]. Eventually in Equation (6.4), the traction torque at the wheels (T_t) is calculated where R_w is the radius of wheels.

$$F_r = \mu W(1 + \frac{\mathbb{V}}{160}) \tag{6.1}$$

$$F_d = \frac{1}{2}\rho C_d A \mathbb{V}^2 \tag{6.2}$$

$$F_t = F_r + F_d + Ma \tag{6.3}$$

$$T_t = F_t R_w \tag{6.4}$$

Where μ and C_d are the rolling resistance coefficient and aerodynamic drag coefficient and ρ is the density of ambient air. $\mathbb{V}$, a, M, W, A are the vehicle velocity, acceleration, gross mass, weight, and front area, respectively.

6.2.2 Transmission System

A transmission system with five speeds is used in this study. The corresponding gear ratios to the gear positions from 1 to 5 are 2.0, 1.0, 0.8, 0.7, and 0.54, respectively. The mechanism for gear-shifting in the HEV system of this study is based on state-flow design. The upper-shift vehicle velocities corresponding to the gear shifts of 1-2, 2-3, 3-4, and 4-5 are 4.5, 9, 14, and 19 m/s, respectively. The down-shift vehicle velocities for the gear shifts of 2-1, 3-2, 4-3, and 5-4 are 3, 7, 12, and 16 m/s, respectively.

6.2.3 E-machine and Battery Models

An E-machine with 75 kW power and with a fixed gear ratio of 2.07 is selected in this work [153]. The E-machine is sized based on the method described in [152] for parallel HEVs. The supervisory controller commands the E-machine torque and the E-machine power request is calculated based on the commanded torque. The power request of E-machine is then used as the input of E-machine model. The E-machine model is a quasi-static model based on a map shown in Figure 6.1.

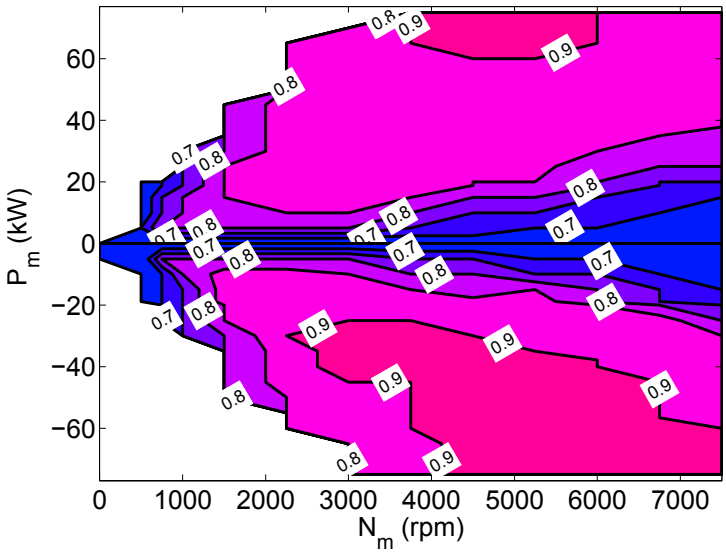

Figure 6.1: Efficiency map of E-machine at motoring and generating modes.

The E-machine motoring efficiency ($\eta_{m,mot}$) or generating efficiency ($\eta_{m,gen}$) is obtained based on the E-machine speed (up to 7500 rpm) and E-machine power request using the map shown in Figure 6.1. The power request of the battery ($P_{bat,req}$) is then estimated based on the E-machine efficiency as follows:

$$\begin{cases} P_{bat,req} = \frac{P_{m_{mot},req}}{\eta_{m,mot}} & (a) \\ P_{bat,req} = P_{m_{gen},req}.\eta_{m,gen} & (b) \end{cases} \tag{6.5}$$

where $P_{m_{mot},req}$ and $P_{m_{gen},req}$ are the power requests of E-machine for motoring and generating modes, respectively. The battery output voltage (V_t) and the battery

current (I_{bat}) are calculated using $P_{bat,req}$ as shown in Equations (6.6) and (6.7) [154].

$$V_b = \sqrt{\mathcal{P}_{b,req}.R_d} \tag{6.6}$$

$$I_b = \frac{V_{oc} - V_b}{R_d} \tag{6.7}$$

Where V_{oc} and R_d are the open circuit voltage of the battery and the battery equivalent resistance, respectively. The State of Charge (SOC) of the battery at moment t is estimated as shown in Equation (6.8).

$$SOC(t) = SOC_i - 100.\frac{\int_0^t I_b(\tau)\ d\tau}{Q_c} \tag{6.8}$$

Where SOC_i and Q_c are the initial state of charge of the battery and the overall energy capacity of the battery, respectively. The battery size is determined by using the design method described in [152] for parallel HEVs.

6.2.4 Experimental ICE Maps

The ICE maps are obtained for the available GM 2.0 L Ecotec LHU SI engine with the specifications listed in Table 6.2. Two combustion modes including 1) the baseline

SI mode and 2) HCCI mode are studied. Both modes are naturally aspirated so no boosting is done for the intake air.

Table 6.2
GM 2.0 L Ecotec LHU SI engine specifications.

Parameter	Value
Bore	86 mm
Stroke	86 mm
Number of cylinders	4
Compression ratio	9.2 : 1
Connecting rod length	145.5 mm
Displacement volume	1998 cc
Clearance volume	61 cc
Valvetrain	DOHC 4 valves/cylinder
Cam phasing mechanism	Hydraulically actuated internal vane type
Intake valve opening	24.5 ° aTDC*
IVC	40 bBDC
Intake valve duration	+55 °
Exhaust valve opening	−70 ° aBDC
Exhaust valve closing	22 ° bTDC
Rated power	220hp (164 kW)@ 5300 rpm
Direct fuel injection	common rail with 100 bar pressure
Port fuel injection pressure	common rail with 3 bar pressure

*after top dead center (TDC) point

6.2.4.1 Engine Test Setup

The LHU Ecotec engine is modified in terms of intake and exhaust loops and additional sets of sensors and actuators are installed on the base engine for monitoring and optimizing engine performance as well as operating the engine at HCCI mode. Fig. 6.2 shows a view of the experimental engine setup. The test cell has an AC

dynamometer with 465 hp capacity. There are data acquisition systems in the test cell which processes the data and displays it on the work station outside the lab. This workstation controls the engine load, dynamometer, air heater, and the coolant heat exchanger. The workstation measures the in-cylinder pressure and monitors temperature of the engine at various locations. The workstation controls the basic engine operation and a prototype engine control unit (ECU) dSPACE Micro AutoBox is used for advanced combustion controls.

Fig. 6.3 shows an overall engine setup along with sensors and actuators. The original sensors and actuators from the production engine are denoted as internal sensors/actuators in this dissertation (e.g. crank position sensor, spark plug, etc.) and sensors/actuators which were installed/calibrated to add further controllability in the HCCI operation are denoted as external sensors/actuators (e.g. in-cylinder pressure sensors, crank shaft encoder, port fuel injectors, EGR valve, combustion phasing estimator, etc.).

The engine is run at 19 different steady-state operating conditions for naturally aspirated HCCI mode and at 54 steady-state operating conditions for naturally aspirated SI mode with the operating range shown in Table 6.3. The steady-state data are used to obtain the engine fuel efficiency map. Figs. 6.4 and 6.5 show the brake torque, engine speed, and Brake Specific Fuel Consumption (BSFC) maps for the naturally aspirated HCCI and SI modes, respectively.

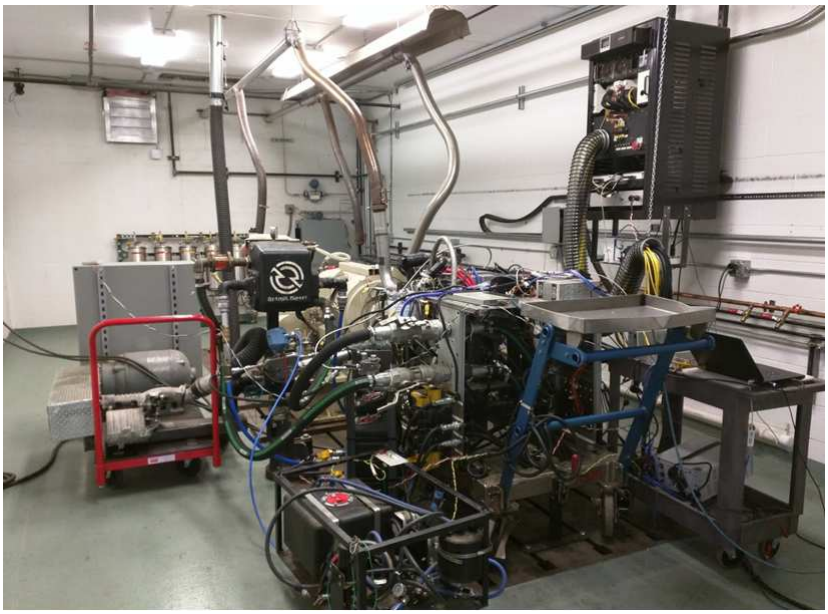

Figure 6.2: LTC engine setup at MTU's Advanced Power Systems Laboratories (APS Labs) test cell.

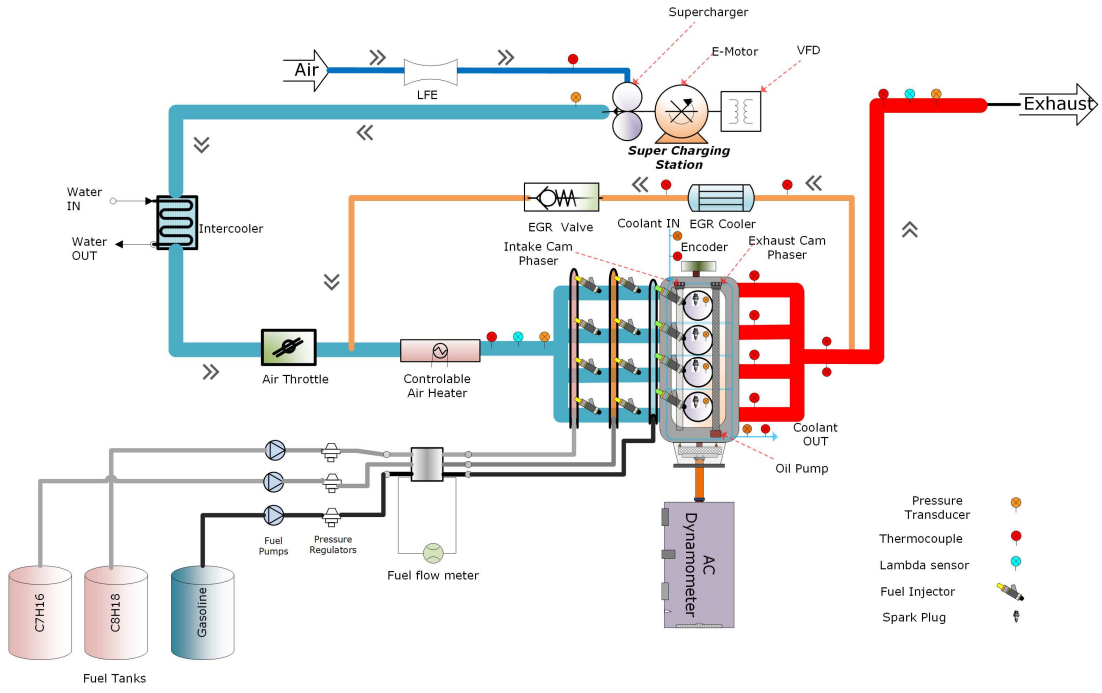

Figure 6.3: Experimental setup for GM Ecotec LHU engine.

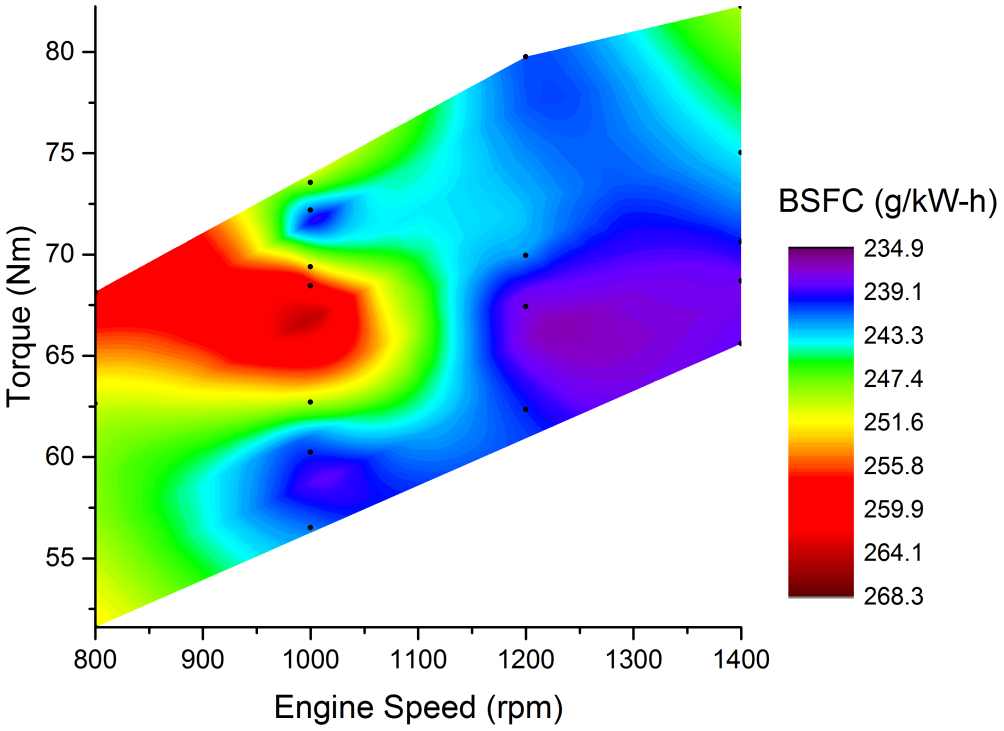

Figure 6.4: Brake torque, speed, and BSFC map for the naturally aspirated HCCI engine.

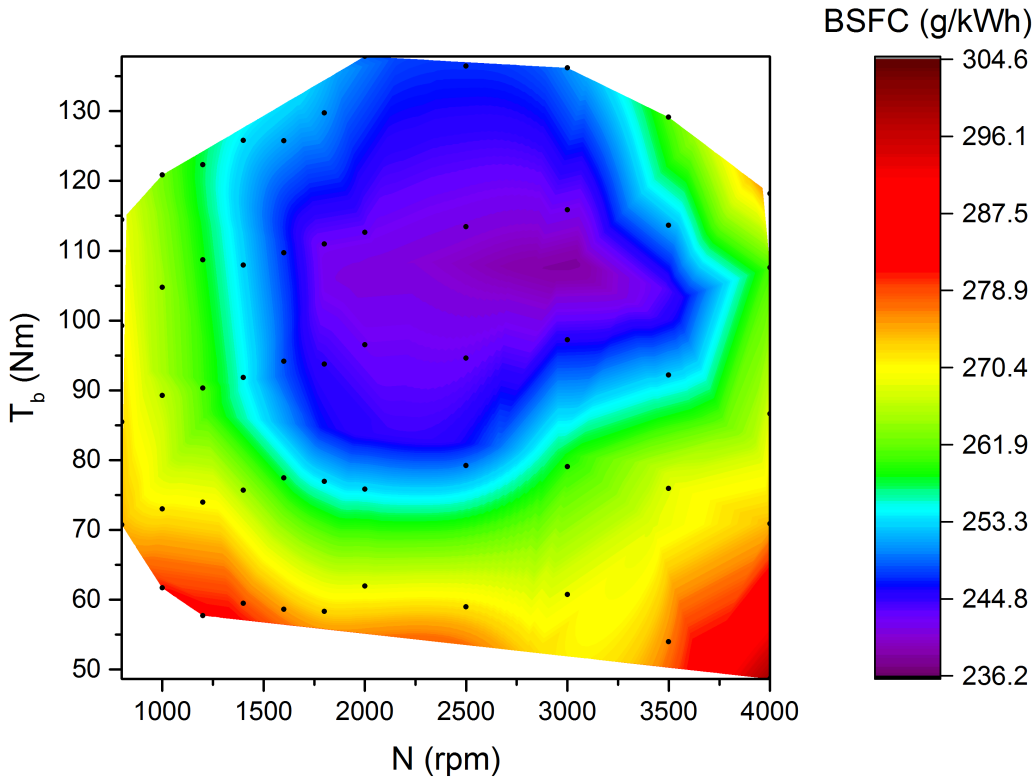

Figure 6.5: Brake torque, speed, and BSFC map for the SI engine.

Table 6.3
Operating range for testing the engine in naturally aspirated HCCI and SI modes on the dynamometer.

Parameter	SI	HCCI
T_{man}	25-40 °C	40 °C
P_{man}	55-95 kPa	90 kPa
N	800-4000 rpm	800-1400 rpm
EGR	0	0
λ	1 (-)	1.83-2.65 (-)

Comparing point-to-point on the two maps show that the HCCI engine has significantly lower fuel consumption compared to the SI engine. For example, at the operating point of N=1000 rpm and T= 62 Nm, the fuel bsfc of the HCCI engine is around 243 $\frac{g}{kWh}$ while for the SI engine is around 290 $\frac{g}{kWh}$. At the operating point of N=1300 rpm and T= 65 Nm, the bsfcs of the HCCI and SI engine are around 236 and 260 $\frac{g}{kWh}$, respectively. Both HCCI and SI maps are used in the parallel HEV powertrain model to design and evaluate the energy management supervisory control strategy.

6.3 Energy Management Controller Development

MPC is used in this study for torque split management between ICE and E-machine as a real-time controller. MPC strategy is obtained based on Dynamic Programmin (DP). Therefore, in this section a brief overview about DP and MPC are presented and then the MPC torque split strategy is designed.

6.3.1 Dynamic Programming for Torque Split Management

DP is a commonly used technique to solve dynamic optimization problems. The main advantage of DP is its ability to handle the constraints and nonlinearity of the

problem while obtaining a globally optimal solution [155]. The DP technique is based on Bellman's principle of optimality [156] which states that the optimal policy can be found if a one-stage subproblem is first solved involving only the last stage and then gradually extend to subproblems involving the last two stages, last three stages, and so forth until the entire problem is solved. In this manner, the overall dynamic optimization problem can be decomposed into a sequence of simpler minimization problems [156]. The energy cost function ($\mathbb{J}$) is defined as follows for parallel HEV torque split management.

$$\mathbb{J}(k) = \int_{t_k}^{t_k+t_p} (\dot{m}_f(t).Q_{hv} + \alpha.P_{_{bat,req}}) \ dt \tag{6.9}$$

subject to:

$$\begin{gathered} T_{e,min} < T_e < T_{e,max}; \quad T_{m,min} < T_m < T_{m,max} \\ N_{e,min} < N_e < N_{e,max}; \quad N_{m,min} < N_m < N_{m,max} \\ SOC_{min} < SOC < SOC_{max}; \quad SOC_{@t=0} = 0.8 \end{gathered} \tag{6.10}$$

Where Q_{hv} is the heating value of fuel. The subscripts min and max denote minimum and maximum, respectively. The first term in Equation (6.9) refers to the fuel energy consumed by the ICE and the second term refers to the battery electrical energy consumption or recharge during the drive cycle. α is a multiplication factor that indicates the equivalent ratio between the battery and ICE energy consumptions.

The value of α affects the decision of the control strategy to use whether ICE or E-machine more than the other, and whether the vehicle is operated in charge sustaining mode or charge depletion mode. In this study, the value of α is selected for a specific charge depletion mode. The control input (u) at time k is the optimal torque split ratio for the ICE that means the ratio of ICE torque request to the total torque request of ICE and E-machine.

For HEV energy management control, moving backward (recursively) from the end of the driving cycle, we need to calculate the optimal cost function at each time step. If N is the last time step of the driving cycle, the cost function at time step N-1 is calculated by:

$$\mathbb{J}(N-1) = \mathbb{J}^*(N) + \mathbb{J}(N \rightarrow N-1) \tag{6.11}$$

where $\mathbb{J}^*(N)$ is the optimal cost-to-go function and $\mathbb{J}(N) \rightarrow (N-1)$ is the stage cost, respectively. Since, the optimal cost-to-go function depends on the system inputs and states at the previous step time (N-1), we need to discretize the input(s) and states(s). Therefore, for this HEV control problem, we need to discretize the torque split ratio space for different possible values. By discretizing the torque split ratio space (0 to 1) into six different possible values, a cost-to-go matrix is found as shown in Figure 6.6. Knowing the velocities through the whole drive cycle, the total requested power is calculated, then depending on the torque split ratio the energy consumption for each

power source and eventually the cost function are calculated.

As it can be seen in Figure 6.6, the optimal cost-to-go function at time N-1 ($\mathbb{J}^*(N-1)$) is the minimum of the summation of optimal cost function at time N and the stage cost from N-1 to N. Only for the first calculation step, the cost at the end of driving cycle is assumed to be zero ($\mathbb{J}^*(N) = 0$), $\mathbb{J}^*(N-1)$ is true for the minimum stage cost. Then, $\mathbb{J}^*(N-1)$ is saved in the cost-to-go matrix. $\mathbb{J}^*(N-2)$ at each torque split ratio (at time N-2) is calculated with the same numerical calculation procedure means to find the minimum of the summation of optimal cost-to-go function for all the grid points at time N-1 and the stage cost from that specific grid point at N-2 to all the grid points at time N-1. For each time step, the feasibility conditions (for inputs and states) shown in Equation (6.10) should be checked. Eventually, a matrix of optimal cost-to-go function is found. Then, at each time step, the minimum of the cost-to-go functions in that column of the matrix is selected as the optimal cost-to-go function at that time and the corresponding torque split ratio is saved as the appropriate control input.

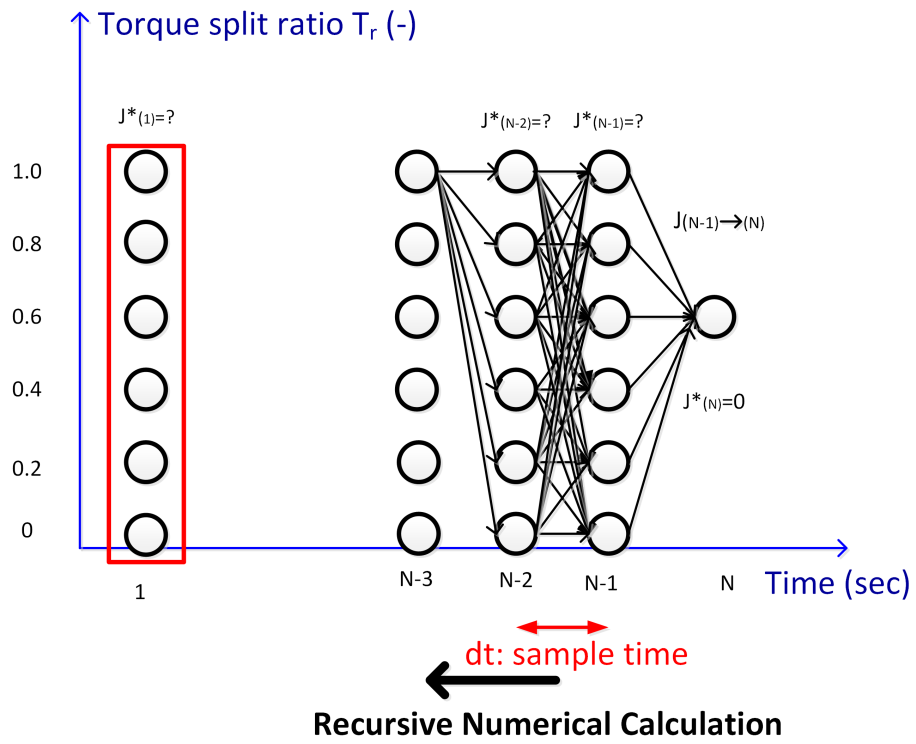

Figure 6.6: Schematic of DP optimization.

6.3.2 MPC Strategy Development

In the MPC technique a window of predicted drive pattern (velocity of the drive cycle comes from GPS) is used. The length of the window is called: "prediction horizon". Therefore, MPC is applicable for real-time torque split control of HEVs. Starting from the beginning of the drive cycle, a DP optimization is executed through the prediction horizon. A vector of optimal torque split ratios is found and the first element of the vector is chosen as the optimal torque split ratio at that time step. At

time k, the MPC strategy determines the optimal $u(k)$ to minimize the cost function in the corresponding prediction horizon. Therefore, the optimal ICE torque request ($T_{e,req}$) is determined by the supervisory HEV MPC as:

$$T_{e,req}(k) = max(0, r_{_T}(k).T_{t,req}) \tag{6.12}$$

where $T_{t,req}$ is the total torque request found from Equation (6.3). The ICE is turned off once the engine torque request becomes zero and the clutch is disengaged. The remaining torque request is provided by the E-machine:

$$T_{m,req}(k) = T_{t,req}(k) - T_{e,req}(k) \tag{6.13}$$

In this chapter, prediction horizon (t_p) of 5 sec [157] and sample time (dt) of 1 sec are used.

6.4 Simulation Results

Two types of HEV powertrain models are used to design and evaluate the energy management MPC: 1) powertrain model with SI engine, and 2) powertrain model with HCCI engine. Simulation results of both cases are then compared in this section.

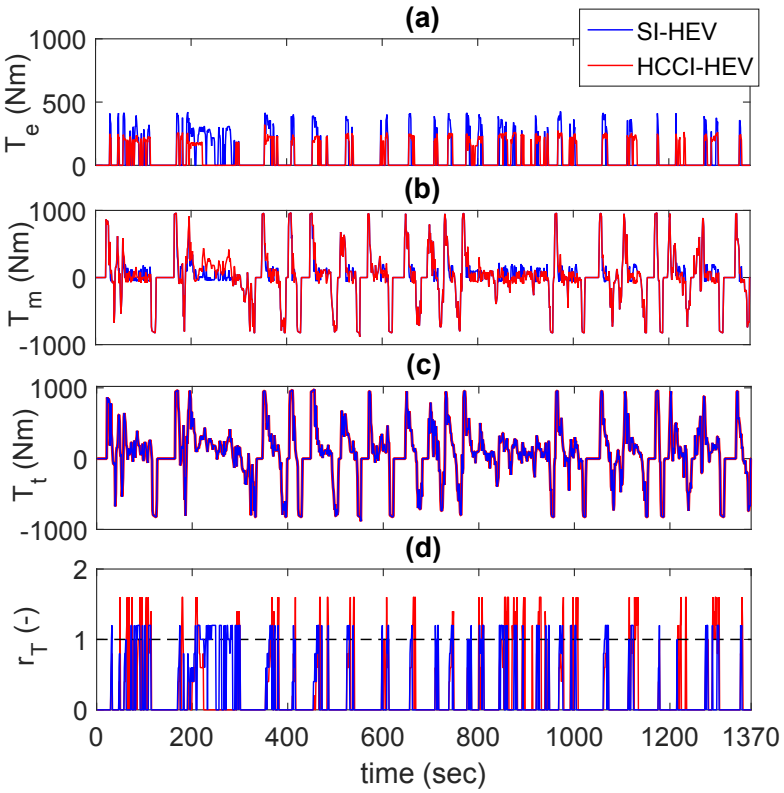

Figure 6.7: Total torque (T_t) at the wheel, ICE torque (T_e) at the wheel, and E-machine torque (T_m) at the wheel and torque split ratio (r_T) for SI-HEV and HCCI-HEV. r_T values higher than 1 represent the battery charging mode by ICE.

Figure 6.7 shows the simulation results for SI-HEV and HCCI-HEV for Urban Dynamometer Driving Schedule (UDDS) drive cycle. Figures 6.7(a) and (b) show the ICE torque (T_e) and E-machine torque (T_m) requests at the wheel commanded by the supervisory energy management controllers, the total torque request at the wheel (T_t), and the torque split ratio (r_T). Results in Figure 6.7 show that for the HCCI-HEV, the ICE is less used at high loads. In addition, the E-machine provides more torque assist during the vehicle accelerations. This is due to the fact that the operating

range of HCCI engine is relatively limited and it does not operate efficiently at high loads. To end this, the E-machine provides more torque during the vehicle transients; thus, the load to the ICE is reduced and HCCI engine can operate more efficiently compared to the SI engine. However, to have a common battery charge depletion mode for both types of HEVs, the HCCI engine needs to do more battery charging. Figure 6.7(d) shows instantaneous r_T for both types of HEVs. The moments at which r_T is greater than '1' are where ICE is charging the battery and it happens more often in the HCCI-HEV, compared to that in the SI-HEV.

Figure 6.8 shows a zoom-in view of Figure 6.7 where ICE is off in the SI-HEV and the vehicle is propelled using the E-machine. However, in the HCCI-HEV, the ICE is not only propelling the vehicle but also charging the battery at the moments where r_T is greater than 1. These battery charging by ICE happens during the conditions where the vehicle is coasting and the ICE load is low since the HCCI engine can operate more efficiently at low loads.

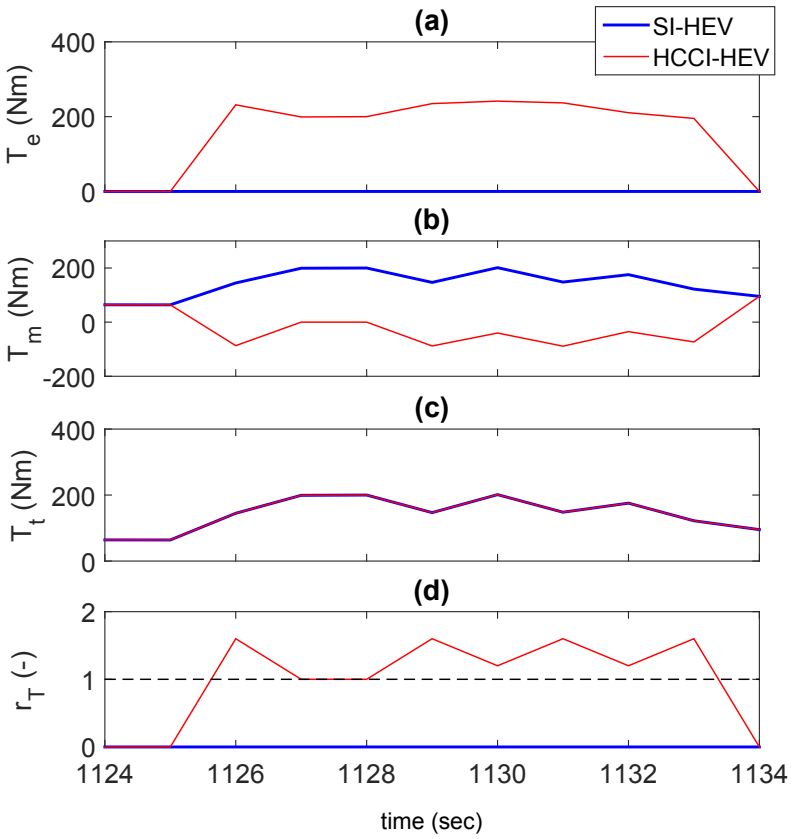

Figure 6.8: A zoom-in view for Figure 6.7.

Figure 6.9 shows the instantaneous fuel consumption for both types of HEVs for the UDDS drive cycle. As can be seen, the HCCI-HEV has lower fuel consumption compared to the SI-HEV during accelerations. This is more noticeable during the simulation period of 200-300 sec as the most significant acceleration with the maximum speed happens during this period of time.

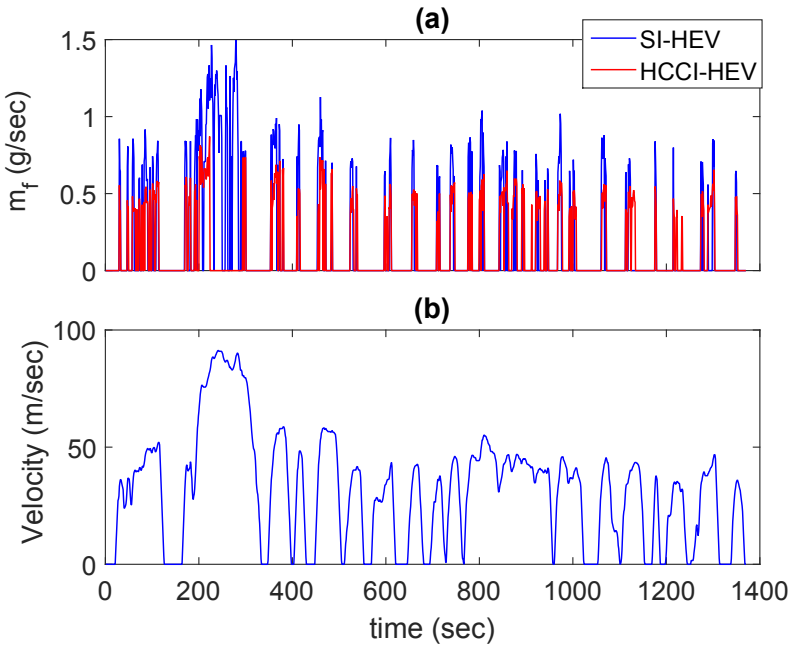

Figure 6.9: Instantaneous fuel consumption and vehicle velocity profile.

Figure 6.10 shows the cumulative fuel consumption ($m_{f,c}$) and battery SOC for both SI-HEV and HCCI-HEV during UDDS drive cycle for a battery charge depletion mode. It can be seen that for both vehicles, the final battery SOC is around 0.69 which is in the desired SOC range ($0.65<SOC<0.95$); however, $m_{f,c}$ for the SI-HEV is 58 g (i.e., 35%) more than the HCCI-HEV. The main fuel consumption difference happens during the period of 200-300 sec as discussed above and then it does not change significantly as the HCCI engine is more used to charge the battery to make the final battery SOC the same as the one for the SI-HEV.

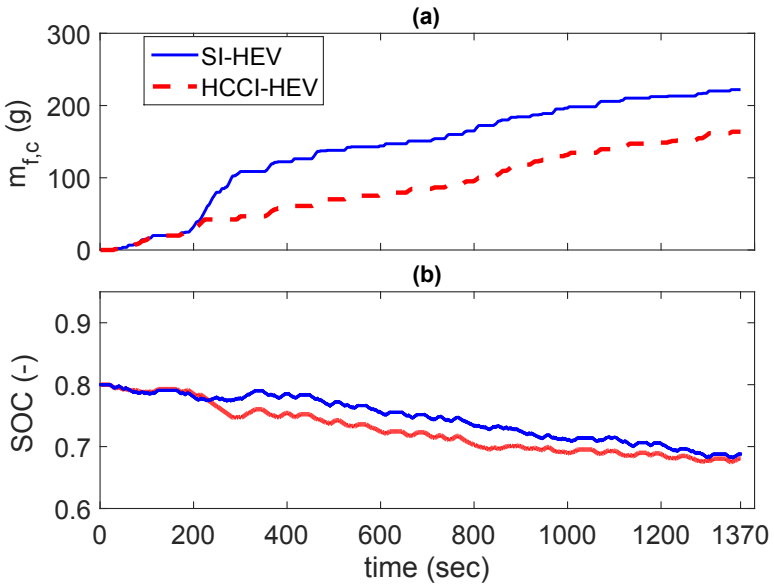

Figure 6.10: Cumulative fuel consumption ($m_{f,c}$)and battery SOC for SI-HEV and HCCI-HEV.

6.5 Summary

In this chapter, the potential fuel consumption benefits achieved by integrating HCCI engine in an HEV powertrain was studied. A parallel HEV powertrain model was developed which includes two types of ICEs: 1) SI engine and 2) HCCI engine. The ICE maps were obtained using the experimental tests on dynamometer. An energy management MPC strategy was developed for both types of HEVs for a battery charge depletion mode during UDDS drive cycle. Simulation results show that during the vehicle transient operations, the HCCI engine is less used compared to the baseline SI engine and the E-machine provides the required torque to reduce the ICE load.

However, the HCCI engine has to charge the battery more during the vehicle low transient operations. Overall, this led to around 26% improvement in the total fuel consumption when using the HCCI-HEV compared to the SI-HEV for UDDS drive cycles.

Chapter 7

Analysis and Control of Energy Management in HEVs by Incorporating Powertrain Dynamics[1]

Energy management strategies in HEVs usually ignore effects of Internal Combustion Engine (ICE) dynamics and rely on static maps for required engine torque-fuel efficiency data. It is uncertain how neglecting these dynamics can affect fuel economy

[1]The results of this chapter are partially based on [7] with permission from ASME as shown in Appendix E, Section E.5.

of an HEV. This chapter addresses this shortcoming by investigating effects of engine dynamics and clutch dynamics on torque split management in a parallel HEV. The control strategy is implemented on an HEV model with an experimentally validated, dynamic ICE model to study how the ICE and clutch dynamics can degrade performance of the HEV control strategy during the transient periods of the vehicle operation. City driving conditions in a common North American drive cycle is used for this purpose and the fuel consumption discrepancy (as a result of the powertrain dynamics) is found. The fuel consumption discrepancy is often overlooked in conventional HEV energy management strategies. An MPC of torque split is developed by incorporating effects of the studied influencing dynamics. The integrated energy management strategy is tested for UDDS and the total energy consumption improvement using this new approach is found.

7.1 Introduction

Previous torque split control strategies for parallel HEVs are categorized into two main groups based on the type of ICE model used for either evaluation or development of the control strategy (Figure 7.1). The first category includes the control strategies based on static map ICE models. These strategies incorporate static maps or steady-state ICE models for the required ICE torque-fuel efficiency data.

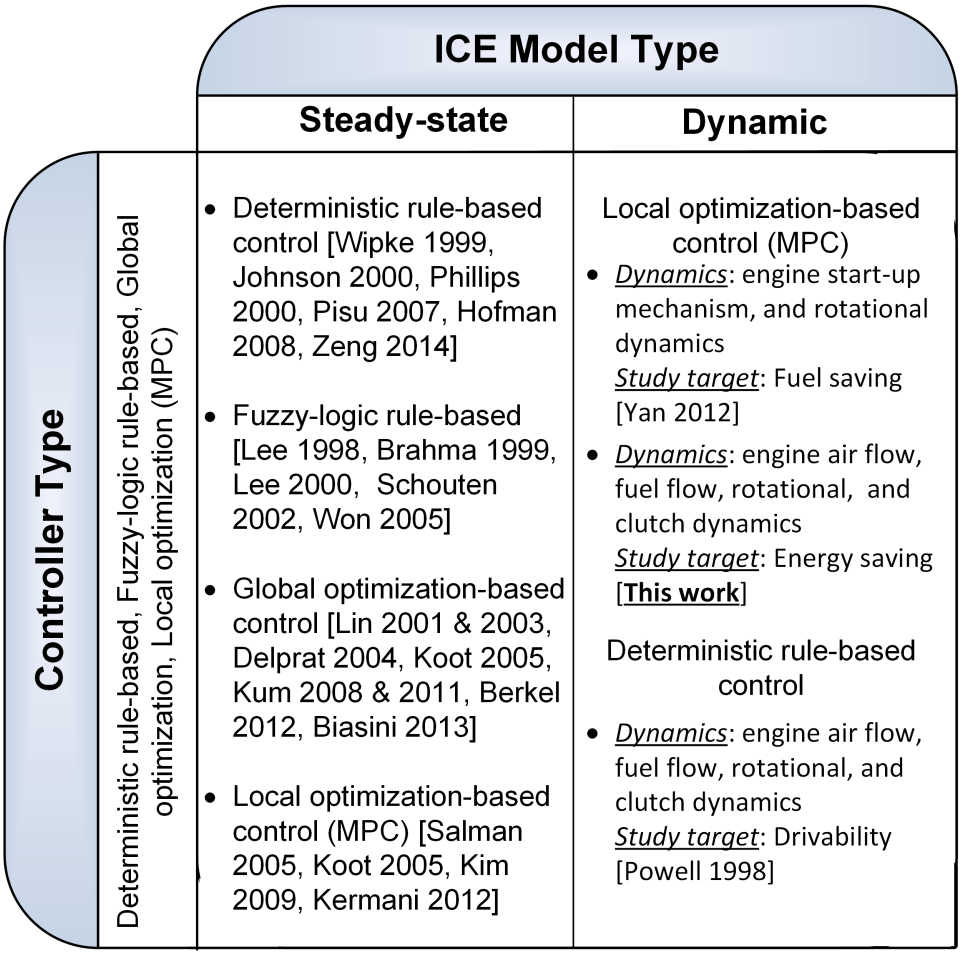

Figure 7.1: Background of torque split control strategies for parallel HEVs.

The major drawback in these strategies is the lack of understanding for the ICE dynamics during transient operations of the vehicle. Neglecting the ICE dynamics can cause a discrepancy between predicted and real fuel consumption and emission results from an HEV. In particular, the torque split strategy in an HEV can deviate from an optimum performance during transient operations when ICE dynamics are

important. This deviation becomes more critical when there are more frequent transitions in driving conditions, as in urban drive cycles. The majority of HEV torque split strategies in the literature belong to the first category and neglect ICE dynamics [61, 63, 66, 71, 72, 147, 158, 159, 160, 161, 162, 163, 164, 165, 166, 167, 168, 169, 170, 171, 172, 173, 174]. This chapter will investigate the effects of ICE dynamics on the outcomes from optimal torque split strategies.

The second category in Figure 7.1 includes the strategies with dynamic ICE models. The HEV models in this category can capture some or most of ICE dynamics during transient vehicle operations. There are few studies in the literature in which partial ICE dynamics, transmission dynamics, and braking dynamics have been incorporated in HEV models [175, 176, 177]. But there are very few studies to capture the powertrain dynamics in the HEV control model in order to develop or evaluate supervisory torque split controllers [178, 179]. In [178], an HEV control model with a steady-state diesel engine sub-model was extended to include transient characteristics of fuel consumption and torque generation by applying correction factors and fitted polynomials. The model was then used in development of the torque split strategy. The results in [178] showed that the diesel engine transient characteristics play an important role in energy management of HEVs during transient operations. The ICE model in [178] only captures partial ICE dynamics including ICE start-up mechanism and rotational dynamics and does not include the effects from other major ICE dynamics on HEV torque split strategy. In [179], Spark Ignition (SI) ICE dynamics including

air flow dynamics, fuel flow dynamics, rotational dynamics, and clutch dynamics were incorporated in the HEV model, but only the vehicle drivability was evaluated and there was no investigation on effects of the dynamics on fuel consumption and torque split control strategy. There has been no study in the HEV literature that integrates a fully dynamic ICE model to capture effects of all major ICE dynamics and clutch dynamics on fuel consumption and the torque split strategies. To the best of the author's knowledge, the material in this chapter presents the first study undertaken to investigate effects of major ICE dynamics along with clutch dynamics on the parallel HEV energy consumption and torque split control strategy. A physical dynamic ICE model from [180, 181] is used in this study. The ICE model captures different engine dynamics including intake air flow dynamics, fuel dynamics, and rotational dynamics. The ICE model is experimentally validated in this study for different throttle openings and various engine loads during both transient and steady-state operations. The dynamic ICE model is integrated with a dynamic clutch model in a parallel HEV platform and will be used as a test bed to evaluate optimal torque split control strategies in this work.

Figure 7.1 also shows different types of controllers used for the torque split control strategies including: deterministic rule-based controllers [147, 158, 159, 160, 161, 162], fuzzy-logic rule-based controllers [72, 163, 164, 165, 166, 168], H_∞ [159], global optimization-based controllers such as Dynamic Programming (DP) [61, 63, 71, 167,

170, 171, 172, 176], and local optimization-based or MPC [66, 173, 174]. This chapter centers on application of MPC for the parallel HEV torque split management. Selection of MPC is due to its capability for real-time control of HEV torque split and handling system constraints. An MPC torque split strategy is developed based on an HEV model and is tested on two different platforms: (i) HEV model using ICE *steady-state* maps, and (ii) HEV model using the ICE *dynamic* model and clutch *dynamic* model. Results for both cases are compared for transient vehicle operations in order to analyze effects of the studied powertrain dynamics. In addition, a new enhanced torque split MPC strategy is designed by incorporating transient characteristics of the vehicle operation based on the HEV model with the ICE dynamic model and the clutch dynamic model. Both baseline and enhanced HEV torque split control strategies are implemented on the HEV model with the ICE dynamic model and the clutch dynamic model to investigate the potential improvement achieved by using the new enhanced controller.

The contribution from this chapter is threefold. First, effects of major ICE dynamics and clutch dynamics on performance of an HEV torque split control strategy are analyzed. Second, this study illustrates potential fuel economy improvement that can be lost by neglecting ICE dynamics in HEV torque split control strategies. Third, a new HEV torque split control strategy is developed by incorporating the effects of the major ICE and clutch dynamics to illustrate improvement in the total HEV energy consumption. The results are presented for Urban Dynamometer Driving

Schedule (UDDS) drive cycle which includes driving conditions with frequent stops, accelerations, and decelerations.

The chapter is presented as follows. Section 7.2 describes the HEV model and the ICE dynamics with experimental validation results of the ICE model. Then, effects of different ICE dynamics and clutch dynamics on fuel consumption are described in Section 7.3. Section 7.4 describes details of MPC torque split strategy development. In Section 7.5, results from implementing the baseline torque split control strategy on the two HEV testbeds including steady-state and dynamic ICE plant models are compared and discussed. Then, the enhanced MPC torque split strategy integrated with the studied dynamics is tested and the potential energy saving improvement is studied. Finally, Section 7.6 summarizes the major findings from this chapter.

7.2 HEV Model Description

Parameters of the parallel HEV in this chapter are the same as those listed in Table 6.1 of Chapter 7. The sub-models for LVD, transmission, E-machine and battery are the same as those from Chapter 7. Following sections detail the new component sub-models of the HEV model that include ICE dynamic model and clutch dynamic model.

7.2.1 ICE Model

The ICE model in this work is a dynamic model for a 4-cylinder gasoline engine with the specifications listed in Table 7.1. Figure 7.2 shows the schematic of the dynamic ICE model which captures ICE dynamics using different sub-models. The ICE dynamics captured by the model include intake air flow dynamics, fuel flow dynamics, and engine rotational dynamics. This dynamic model is a detailed physical-empirical ICE model developed from a large number of ICE dynamometer experiments. In this study, only some major ICE dynamics are presented. Steady-state engine maps of torque and fuel efficiency are obtained using the ICE dynamic model. The steady-state maps are parts of the control model of HEV used to design parallel HEV torque split control strategies.

Table 7.1
Details of the ICE used in this study.

Parameter	**Value**
Number of cylinders (-)	4
Displacement volume ($liter$)	1.76
Bore×stroke ($mm \times mm$)	83×81.5
Compression ratio (-)	9.3
Intake valve opening/closing (°)	32.5 $BTDC$[1]/64.3 $ATDC$[2]
Exhaust valve opening/closing (°)	61 $BTDC$/15 $ATDC$
Maximum torque (Nm)	120 @ 3000 rpm
Maximum power (kW)	62 @ 6000 rpm
Fuel injection system	PFI @ 3 bar

[1] before top dead center; [2] after top dead center

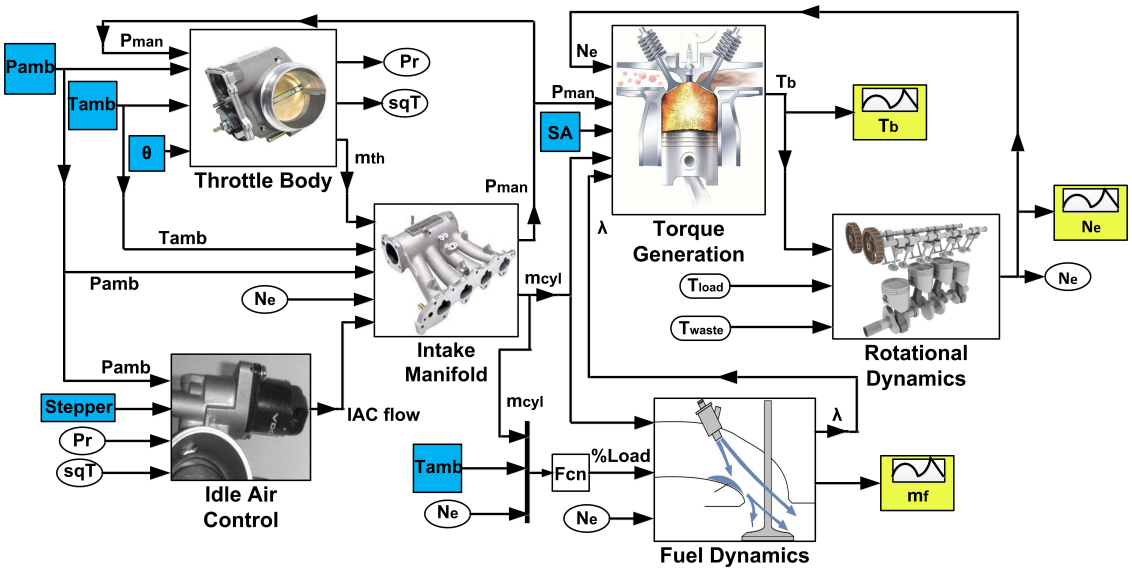

Figure 7.2: An schematic for the dynamic model of ICE.

7.2.1.1 Intake Air Flow Dynamics

The throttle body air flow rate ($\dot{m}_{at}$) is calculated as follows:

$$\dot{m}_{at} = C_D \frac{p_{amb}}{\sqrt{\Theta_{amb}}} \beta_1(\theta)\beta_2(p_r) \tag{7.1}$$

where C_D represents the discharge coefficient, p_{amb} and Θ_{amb} are the ambient pressure and temperature and $p_r = \frac{p_{man}}{p_{amb}}$ is the pressure ratio. The throttle angle (θ) and

p_r affect the air mass flow rate of throttle represented by $\beta_1(\theta)$ and $\beta_2(p_r)$ in Equation (7.1), respectively. Equations (7.2) and (7.3) show how β_1 and β_2 are calculated.

$$\beta_1(\theta) = b_0 + b_1 cos(\theta) + b_2 cos^2(\theta) \tag{7.2}$$

Where coefficients b_0, b_1, and b_2 are 62.56, 0.67, and -62.8, respectively.

$$\beta_2(P_r) = \begin{cases} \frac{1}{0.74}\sqrt{p_r^{0.4404} - p_r^{2.3086}} & if\ p_r \geq 0.41 \\ 1 & if\ p_r < 0.41 \end{cases} \tag{7.3}$$

The pressure of the intake manifold (p_{man}) is estimated based on the throttle body air flow rate and the air flow rate of the cylinder [182, 183]. The air flow rate of the cylinder ($\dot{m}_{ac}$) is calculated by using the following equation [180, 181]:

$$\dot{m}_{ac} = \frac{V_d}{2R\Theta_{man}}[s(N_e)p_{man} - y(N_e)]N_e \tag{7.4}$$

where R, Θ_{man}, N_e, and V_d are the gas constant, intake manifold temperature, ICE speed, and the displacement volume of ICE. Parameters s and y which are functions of engine speed, represent the ICE breathing characteristics. Variation of these parameters versus engine speed is small for conventional SI engines [183]. Therefore,

the average values of the two parameters for this engine are used as following [184]:

$$s_{ave} = 0.933,\ y_{ave} = 0.063\ bar \tag{7.5}$$

7.2.1.2 Fuel Flow Dynamics

The ICE in Table 7.1 is port fuel injection. Thus, the fuel dynamics for transport of the injected fuel to the cylinders are important for transient ICE operations. The fuel transport dynamics are simulated by using approach of x-τ model [185]. A fraction (x) of the total fuel delivered to the ICE intake system is assumed to be deposited on the intake port surfaces. This fuel deposit is in form of fuel film that later enters the cylinder. The fuel film entrance rate is proportional to the mass of fuel film and inversely proportional to fuel evaporation time constant (τ_f) as in Equations (7.6)-(7.8):

$$\dot{m}_f = \dot{m}_{f,v} + \dot{m}_{f,f} \tag{7.6}$$

$$\dot{m}_{f,v} = (1 - x(\Theta_{man}, p_{man}, \Theta_{cool}, N_e))\dot{m}_{f,i} \tag{7.7}$$

$$\ddot{m}_{f,f} = \frac{x(\Theta_{man}, p_{man}, \Theta_{cool}, N_e)\dot{m}_{f,i} - \dot{m}_{f,f}}{\tau_f(\Theta_{man}, p_{man}, \Theta_{cool}, N_e)} \tag{7.8}$$

where $\dot{m}_{f,i}$ represents the mass flow rate of injected fuel and $\dot{m}_{f,v}$ and $\ddot{m}_{f,f}$ are the mass flow rates of the vapor phase and the liquid (fuel film) phase, respectively. Parameters x and τ_f are identified as a function of Θ_{man}, p_{man}, coolant temperature (Θ_{cool}), and N_e [107] and a lookup table map is made to tabulate x and τ_f parameters.

7.2.1.3 Rotational Dynamics

Engine speed variation is calculated using an engine torque balance:

$$\frac{d\omega_e}{dt} = \frac{1}{J_e}(T_{e,i} - T_{e,f/p} - T_{e,l}) \tag{7.9}$$

where J_e is the engine mass moment of inertia and ω_e is the engine speed in $\frac{rad}{s}$. $T_{e,i}$, $T_{e,l}$, and $T_{e,f/p}$ represent the engine indicated torque, load torque, and friction/pumping torque, respectively. A detailed empirical relation that accounts for the torque effects from timing of spark, flow rate of intake air, and mass flow rate of fuel to the engine is used to find $T_{e,i}$ [180, 181]:

$$T_{e,i} = 8027.5\frac{\dot{m}_{ac}}{N_e}\eta_{fc}\ SI\ AFI \tag{7.10}$$

where η_{fc} is the efficiency of the fuel conversion. AFI and SI are the functions represent air fuel ratio influence and spark advance influence, respectively. Friction/pumping torque, $T_{e,f/p}$, is estimated by Equation (7.11).

$$T_{e,f/p} = \frac{V_d}{12560}\ FMEP \tag{7.11}$$

Where $FMEP$ represents the friction mean effective pressure and is found using the experimental data [180].

7.2.1.4 Experimental Validation

The ICE dynamic model is validated for transient changes in the throttle opening position (θ) as shown in Figures 7.3 and 7.4.

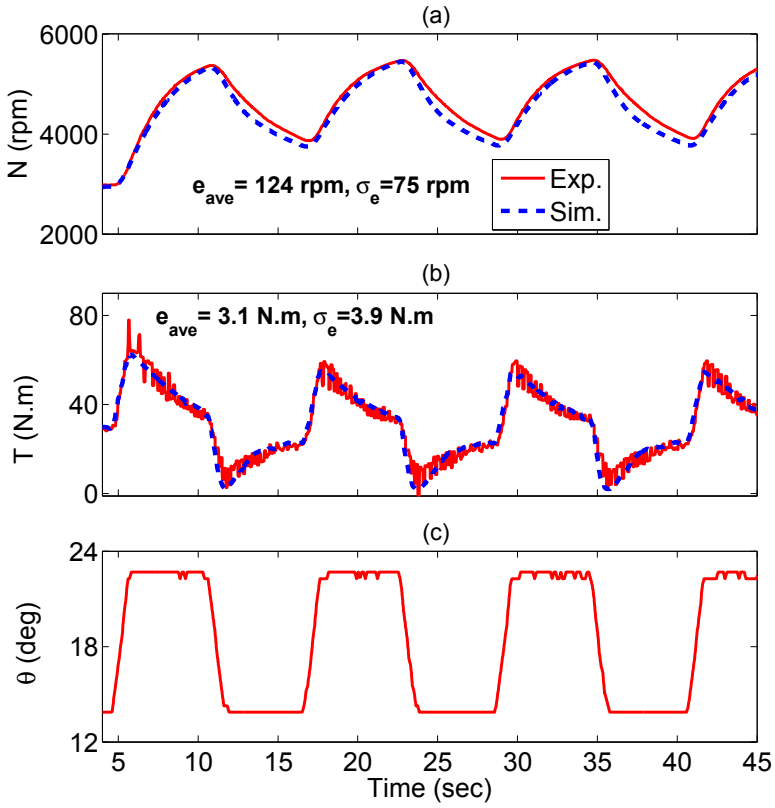

Figure 7.3: ICE experimental validation for speed and brake torque at $T_{e,l}$=30 N.m (e_{ave}=average error, σ_e=standard deviation of error).

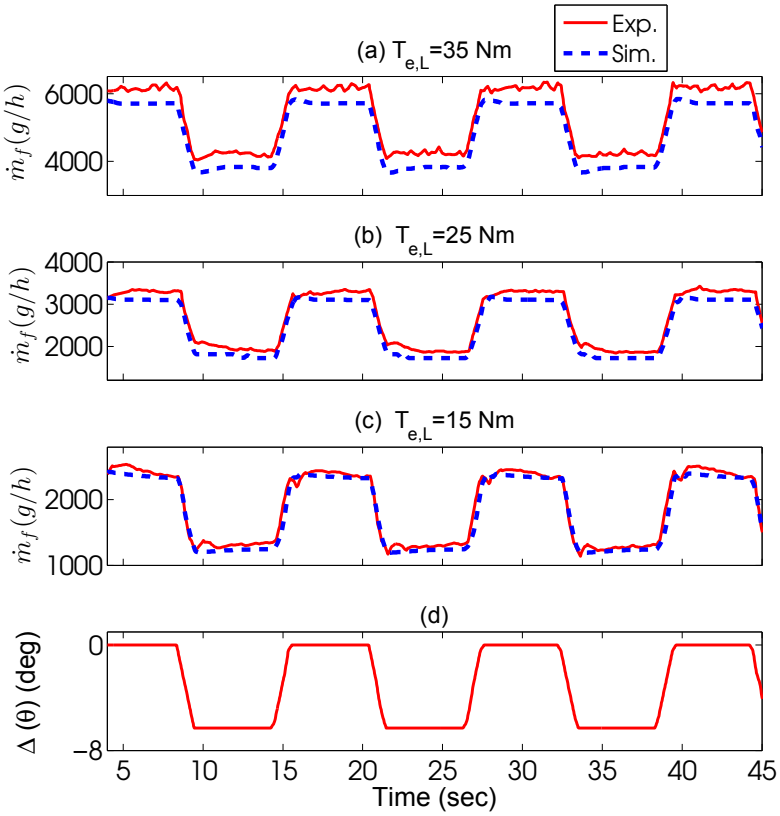

Figure 7.4: ICE experimental validation for fuel consumption at two loads (a) $T_{e,l}$= 35 N.m, N=3296-3670 rpm , θ_i= 18.9°, (b) $T_{e,l}$= 25 N.m, N=2297-2754 rpm, θ_i= 12.2°, (c) $T_{e,l}$= 15 N.m, N=1238-1788 rpm, θ_i= 9.6°, (d) throttle angle change: $\Delta(\theta)$=θ_t-θ_i.

Figure 7.3 shows validation results of the ICE model for speed and torque at 30 Nm ICE load ($T_{e,l}$). Results in Figure 7.3 show capability of the model to predict transient behavior of ICE speed and torque with average errors (e_{ave}) of 124 rpm and 3.1 Nm, respectively. The standard deviations of error (σ_e) are 75 rpm and 3.9 Nm for the ICE speed and torque, respectively. Figure 7.4 shows ICE model validation for transient and steady-state conditions in the throttling opening at different ICE loads. $\bar{e}_{ave}$ of the model in the fuel consumption prediction at three different ICE loads is 205.5

g/h with average error of $\bar{\sigma}_e = \pm 95.1$ g/h (Table 7.2). Results in Table 7.2 show an average of less than 6.0% error in the fuel consumption prediction for the ICE model in this study. Therefore, the ICE model is accurate for fuel consumption prediction during transient conditions.

Table 7.2
Accuracy of fuel consumption prediction in Figure 7.4.

Experiment	$e_{ave}[g/h]$	$\sigma_e[g/h]$	$e_{re}{}^{1}[\%]$
(a)	393.8	139.7	7.8
(b)	160.9	77.0	6.3
(c)	62.0	68.6	3.5

[1]Relative error (i.e., absolute value of error divided by the measured value)

7.2.2 Clutch Model

The acceleration for the engine crank shaft is found by including the clutch parameters:

$$\frac{d\omega_e}{dt} = \frac{1}{J_e + J_c}(T_{e,i} - T_{e,f/p} - T_{e,l} - T_c) \tag{7.12}$$

where J_c is the clutch moment of inertia and T_c is the clutch torque. T_c is zero when the clutch is not engaged. T_c is found by using Equation (7.13) when the clutch is

slipping and using Equation (7.14) when the clutch is fully engaged [179].

$$T_c = k_{ayl}\left[\int |(\omega_e - \omega_c)|dt\right]\left[|(\omega_e - \omega_c)|(-.0005) + 1\right] \\ f(|(\omega_e - \omega_c)|) \tag{7.13}$$

$$T_c = \left[k_{ay2}\int (\omega_e - \omega_c)dt\right] + k_{ayp}(\omega_e - \omega_c) \tag{7.14}$$

Where, ω_c is the clutch speed at engine side in $\frac{rad}{s}$, k_{ayl} is slipping stiffness constant for engine side of shaft in $\frac{Nm}{rad}$, k_{ay2} is synchromesh engaged damping constant in $\frac{Nms}{rad}$, and $f(\omega_e - \omega_c)$ is the normalized clutch capacity [179].

7.3 Effects of Powertrain Dynamics on Fuel Consumption

Effects of the powertrain dynamics (described in Section 7.2) on ICE fuel consumption are discussed in this section. Figure 7.5 shows effects of air flow dynamics for a transient condition of 5° throttle opening (θ) that resembles a condition of vehicle acceleration.

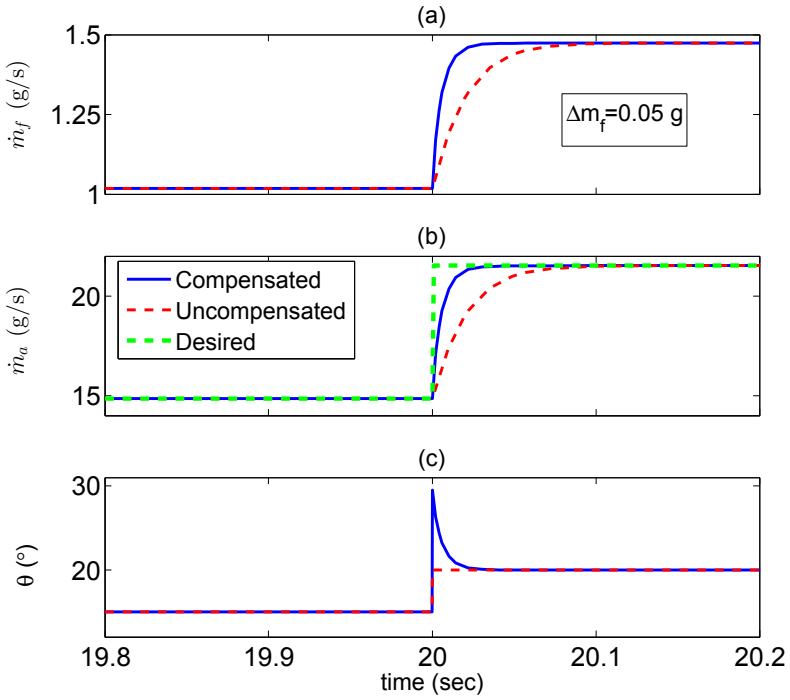

Figure 7.5: Effects of air flow dynamics on required injected fuel.

As seen, due to the air flow dynamics, the air mass flow rate ($\dot{m}_a$) does not increase immediately (red dashed line in Figure 7.5-b) compared to the desired step change in air mass flow rate (green dashed line in Figure 7.5-b). This causes a discrepancy in the engine speed. Therefore, the throttle controller needs to compensate for this discrepancy by further throttle opening that results in compensated $\dot{m}_a$ in Figure 7.5-b. This causes 0.05 g more fuel consumption as fuel-air equivalence ratio (ϕ) is required to remain constant (i.e., ϕ=1 in the SI engine operation). This fuel penalty is ignored when steady-state map of ICE is used in HEV energy management strategies.

Figure 7.6 shows effects of fuel flow dynamics for ICE cold start conditions (x=0.47

and τ=1.3 s) and fully warm-up conditions (x=0.2 and τ=0.3 s) [186]. Results in Figure 7.6 are shown for a desired step change of 0.28 $\frac{g}{sec}$ in the rate of inducted fuel into the cylinders, that resembles a vehicle acceleration condition. The fuel injector controller based on steady-state map injects the same amount of fuel that needs to get inducted into the cylinders. However, less fuel is inducted into the cylinders due to the dynamics of the fuel transport. As a result, a drop in the ϕ occurs and it leads to an engine torque drop. The fuel compensator, which takes into account fuel transport dynamics, injects more fuel to compensate for this ϕ drop. This leads to higher fuel consumption as ϕ is required to remain constant. Increased fuel consumption of 0.23 g and 0.06 g are found for the dynamic ICE model at cold start and fully warm-up conditions, respectively compared to the baseline steady-state model. These fuel penalties are ignored by steady-state map of ICE.

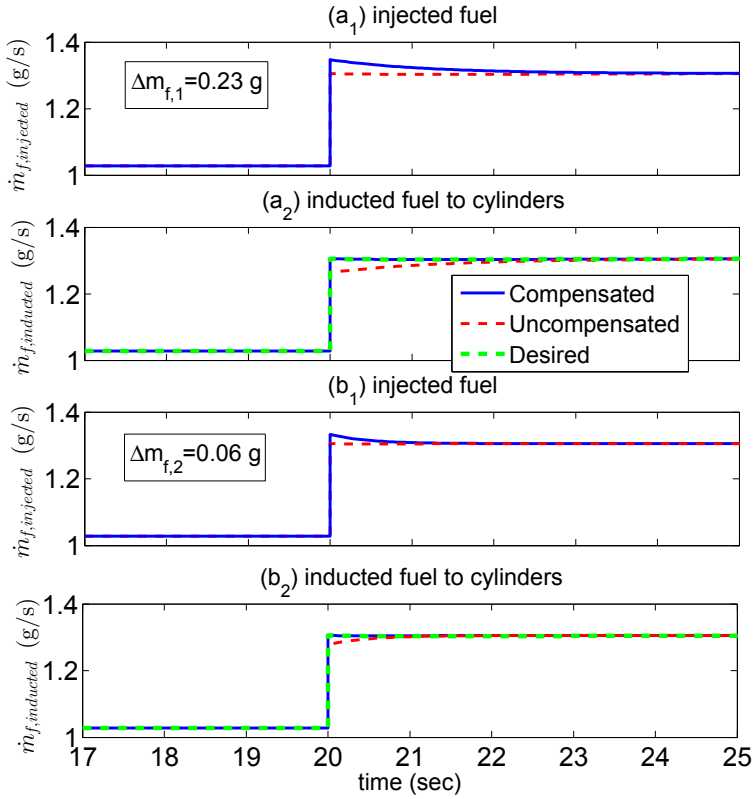

Figure 7.6: Effects of fuel flow dynamics on required injected fuel: (a) Cold start (T_{cool}=-15 °C); (b) Fully warm-up (T_{cool}=80 °C)

Figure 7.7 shows combined effects of air flow dynamics, fuel flow dynamics, and engine rotational dynamics. The target is to change the engine speed from 1580 rpm to 1930 rpm at 50 Nm load torque. This means 2° throttle angle (θ) opening based on the steady-state map. However, Figure 7.7 indicates the actual required θ to achieve this goal. Due to the air flow dynamics, the air mass flow rate does not increase immediately that means a discrepancy in the engine speed. Therefore, the throttle controller compensates for this discrepancy by further opening the throttle. This causes more fuel consumption as ϕ should remain stoichiometric (i.e., ϕ=1). In addition, more fuel

should be injected in this transient fueling condition due to fuel transport dynamics. Due to the ICE rotational dynamics, the ICE output speed becomes different than the speed of the steady-state model. This engine speed discrepancy can cause discrepancy in the vehicle speed. The vehicle speed discrepancy needs to be compensated by the HEV energy management system (i.e., further opening the throttle to provide the required torque). Overall, combination of these three major engine dynamics leads to 0.3 g more fuel consumption compared to the steady-state model/map.

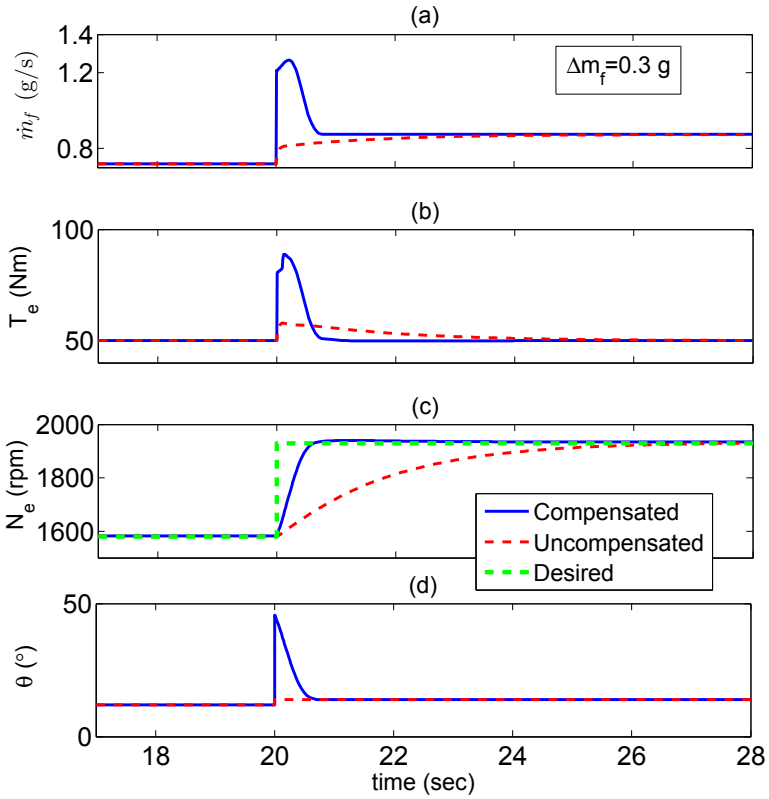

Figure 7.7: Effects of air flow dynamics, fuel flow dynamics, and rotational dynamics on required injected fuel.

Figure 7.8 shows combined effects of the air flow dynamics, fuel flow dynamics, ICE

rotational dynamics and clutch dynamics for a desired vehicle acceleration from 0 to 70 $\frac{km}{h}$. During clutch slipping and engagement, which depends on the difference in speed between the ICE side shaft and the final drive side shaft, there is significant energy dissipation that is ignored in the steady-state HEV powertrain model. The HEV energy management system needs to compensate for this loss. Compensated torque is shown by solid line in Figure 7.8-c. Overall, the effects of engine and clutch dynamics lead to around 3.1 g fuel penalty for the studied acceleration condition. This fuel penalty can not be seen when evaluation is based on steady-state maps. The effects of ignoring engine and clutch dynamics in UDDS drive cycle will be studied later in Section 7.5.1.

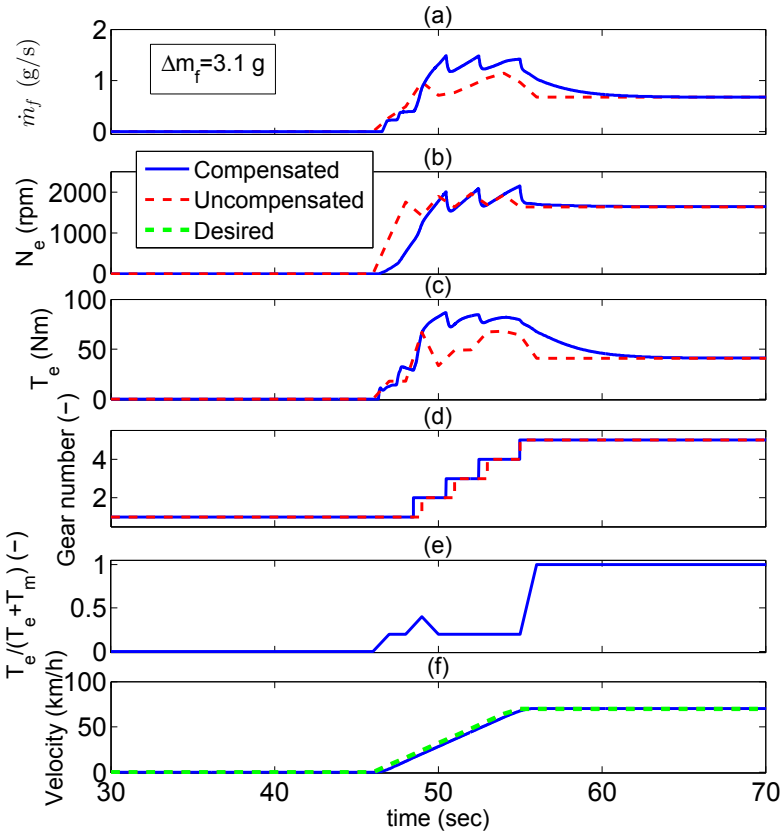

Figure 7.8: Effects of air flow dynamics, fuel flow dynamics, rotational dynamics, and clutch dynamics on required injected fuel.

7.4 Control Strategy Development

Figure 7.9 shows the flow of power and interactions between the supervisory controller and different components of the parallel HEV powertrain of this work. The control strategy of torque split determines the torque requests from ICE and E-machine, the engine ON/OFF status, the transmission gear ratio, and the clutch engagement status.

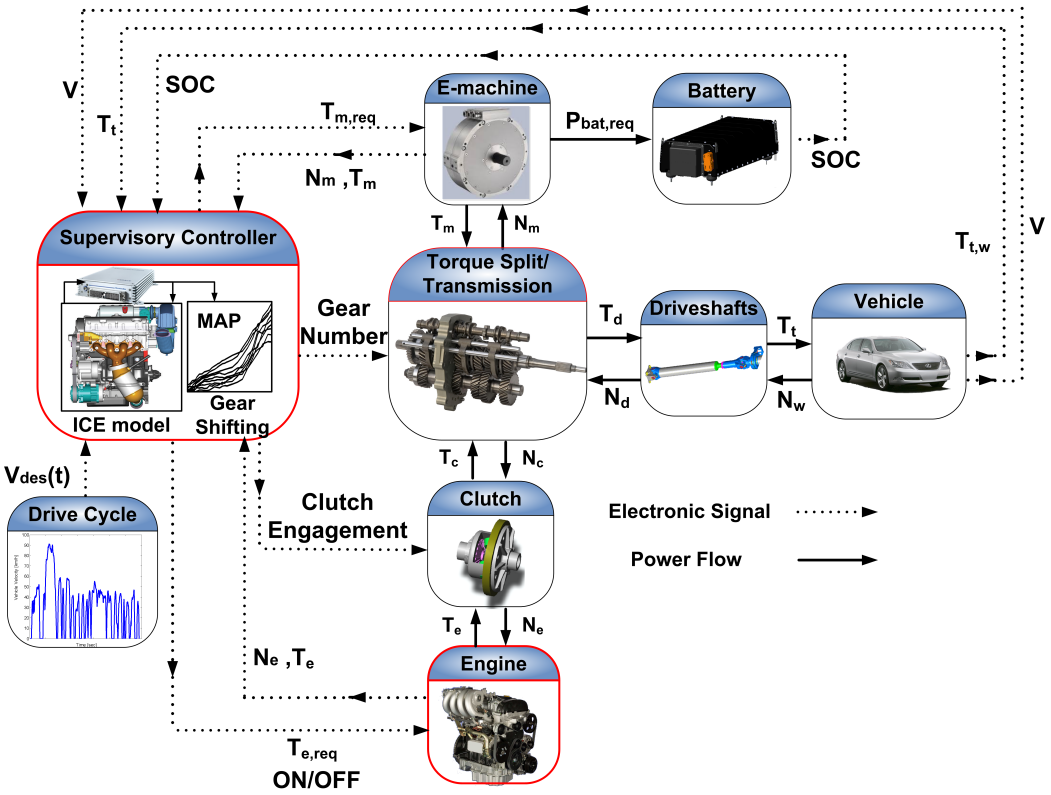

Figure 7.9: Control signals and power flow for the parallel HEV in this work.

MPC is employed in this work as a strong tool for parallel HEV real-time optimal energy management control. Furthermore, MPC is capable to handle different constraints in the vehicle operation [187]. To develop MPC strategy for HEV energy management control, the future driving conditions need to be predicted. This can be realized by means of a Global Positioning System (GPS) [188, 189]. The MPC of this work is designed using two HEV control models: 1) the HEV model based on the steady-state ICE maps and 2) the HEV model based on the dynamic ICE model and clutch model.

7.4.1 MPC Ignoring Dynamics

The prediction horizon (t_p) used in this study is 5 sec [157]. The sample time of 1 sec is used to discretize the HEV model for the purpose of computational efficiency. Equation (7.15) shows the cost function for the k^{th} prediction horizon.

$$\mathbb{J}_{st}(k) = \int_{t_k}^{t_k+t_p} (\dot{m}_f(t).Q_{hv} + \alpha.P_{_{bat,req}})\ dt \tag{7.15}$$

subject to:

$$\begin{gathered} T_{e,min} < T_e < T_{e,max} \\ T_{m,min} < T_m < T_{m,max} \\ N_{e,min} < N_e < N_{e,max} \\ N_{m,min} < N_m < N_{m,max} \\ SOC_{min} < SOC < SOC_{max} \\ SOC_{@t=0} = 0.8 \end{gathered} \tag{7.16}$$

Where Q_{hv} represents the gasoline fuel heating value. The subscripts max and min denote maximum and minimum, respectively. Equation (7.15) consists of two terms: the first term refers to the ICE fuel energy consumption. The second term refers to

the electrical energy consumption or recharge of the battery. α is a multiplication factor that represents the equivalent ratio between the energy consumptions of the battery and the ICE. Depending on the value of α, the decision of the control strategy to propel the vehicle by using whether ICE or E-machine more than the other, is different. It also affects the control strategy decision to operate the vehicle in charge depletion mode or charge sustaining mode. The optimal control input (u) is the optimal ICE torque split ratio ($r_{_T}$) that means the optimal ratio of ICE torque request to the total traction torque request of ICE and E-machine.

At time k, $u(k)$ is determined by the MPC strategy so that the cost function in the corresponding prediction horizon is minimized. The supervisory HEV controller determines the optimal ICE torque request ($T_{e,req}$) as shown in (7.17).

$$T_{e,req}(k) = max(0, r_{_T}(k).T_{t,req}) \tag{7.17}$$

Where $T_{t,req}$ is the total traction torque request from Equation (6.3). The supervisory controller turns off the ICE and disengages the clutch once the ICE torque request by the control strategy becomes zero. The remaining torque request is provided by the E-machine:

$$T_{m,req}(k) = T_{t,req}(k) - T_{e,req}(k) \tag{7.18}$$

7.4.2 MPC Accounting for Dynamics

The supervisory control strategy is enhanced by including characteristics of the studied powertrain dynamics. The energy cost function in Equation (7.15) is modified by adding a fuel penalty term ($\dot{m}_{f,pen}$) for the vehicle transient conditions. This term is found using the HEV model which includes the dynamics of ICE and clutch. The fuel penalty term is developed based on a map of engine speed change (i.e., ΔN_e for time duration of 1 sec) and the engine torque as shown in Equation (7.19).

$$\mathbb{J}_{dyn}(k) = \int_{t_k}^{t_k+t_p} [(\dot{m}_f(t) + \dot{m}_{f,pen}(\Delta N_e, T_e)).Q_{hv} + \alpha.P_{bat,req}]\ dt \tag{7.19}$$

Similar to the MPC method described for the steady-state supervisory controller, the optimal torque split ratio and the torque requests of the ICE and the E-machine are determined so that the modified cost function defined in (7.19) is minimized. Section 7.5 compares the steady-state and dynamic torque split controllers.

7.5 CONTROL RESULTS

First, the developed steady-state MPC strategy is implemented on two HEV testbeds. The HEV testbeds include (i) steady-state ICE maps and (ii) dynamic ICE model

integrated with the dynamic clutch model. As a lower-level ICE controller, there is a Proportional Integral (PI) throttle controller in the dynamic HEV plant. This controller receives the ICE torque request determined by the HEV supervisory controller and then it adjusts the throttle opening to follow the desired ICE torque. Effects of the powertrain dynamics on fuel consumption during the vehicle transient operations are studied by comparing the control results for these two cases. Then, two HEV torque split control strategies are implemented on the same dynamic HEV model. The two control strategies include (i) the enhanced controller (Section 7.4.2) and (ii) the baseline steady-state controller (Section 7.4.1). Results of testing these two control strategies are compared to study the energy saving improvement that can be achieved by integrating the new supervisory control design with the powertrain dynamics.

7.5.1 Effects of Powertrain Dynamics

This study investigates the fuel consumption discrepancy between the two HEV testbeds including (i) steady-state ICE maps and (ii) dynamic ICE and clutch models. UDDS drive cycle is used in this work. UDDS includes several transient operations of vehicle including aggressive accelerations and decelerations; therefore, it is used to study the effect of powertrain dynamics. The baseline steady-state HEV controller is tested on both steady-state and dynamic HEV testbeds. Figure 7.10 shows the

velocity profile of the vehicle and two control inputs including the ICE torque split ratio and the ICE ON/OFF status commanded by the steady-state HEV controller. It is observed that the strategy turns the ICE off and recharges the battery by utilizing the E-machine when the vehicle decelerates during the stops and decelerations. It also commands the E-machine to provide torque assist during some conditions of vehicle launch. Figure 7.11 shows simulation results of testing the controller on both HEV testbeds. The drive cycle velocity profile is successfully tracked for both HEV testbeds (Figure 7.11-e). Figure 7.11 shows the instantaneous fuel consumption, transmission gear number, ICE speed and torque of both HEV plant models. As shown in Figure 7.11, during accelerations, the ICE torque and speed for the steady-state and dynamic HEV plant models do not match completely and the instantaneous fuel consumption of the dynamic HEV testbed is greater compared to that of the steady-state HEV testbed. This difference is due to the effects of ICE dynamics and clutch dynamics during the transients of the drive cycle as previously detailed in Section 7.3. The ICE and clutch dynamics are ignored in the steady-state HEV control strategy.

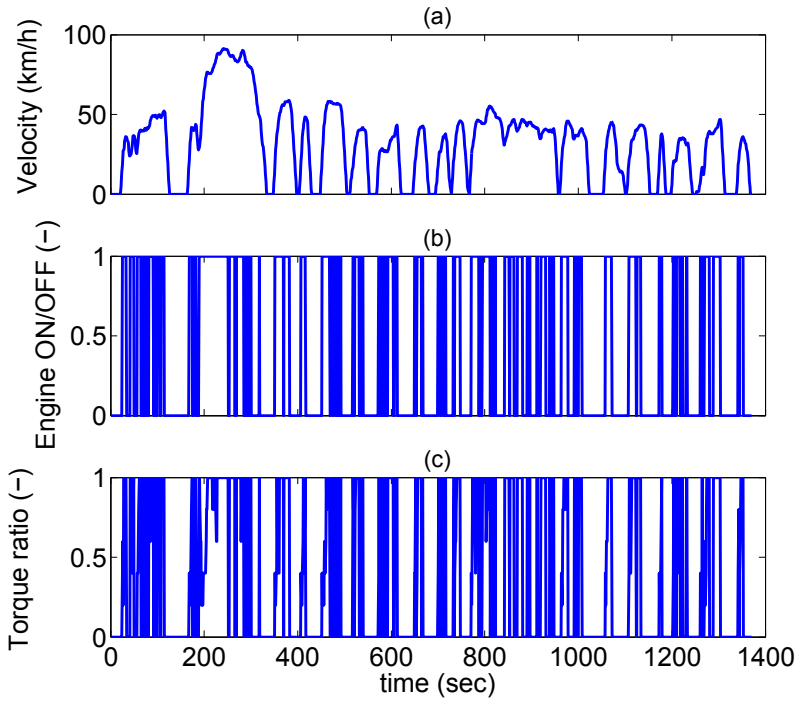

Figure 7.10: Torque split ratio and engine ON/OFF status ("1" means 'ON' and "0" means 'OFF') for UDDS drive cycle commanded by the HEV steady-state supervisory controller.

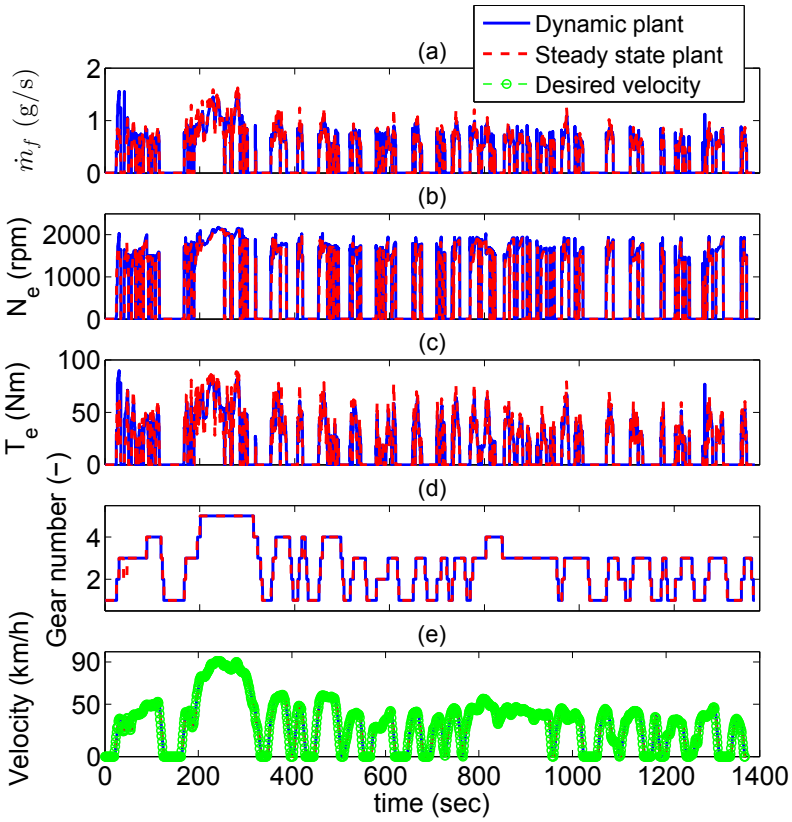

Figure 7.11: Testing the steady-state supervisory controller on two HEV testbeds: (i) HEV plant model using ICE *steady-state* maps, and (ii) HEV plant model using the ICE and clutch *dynamic* models.

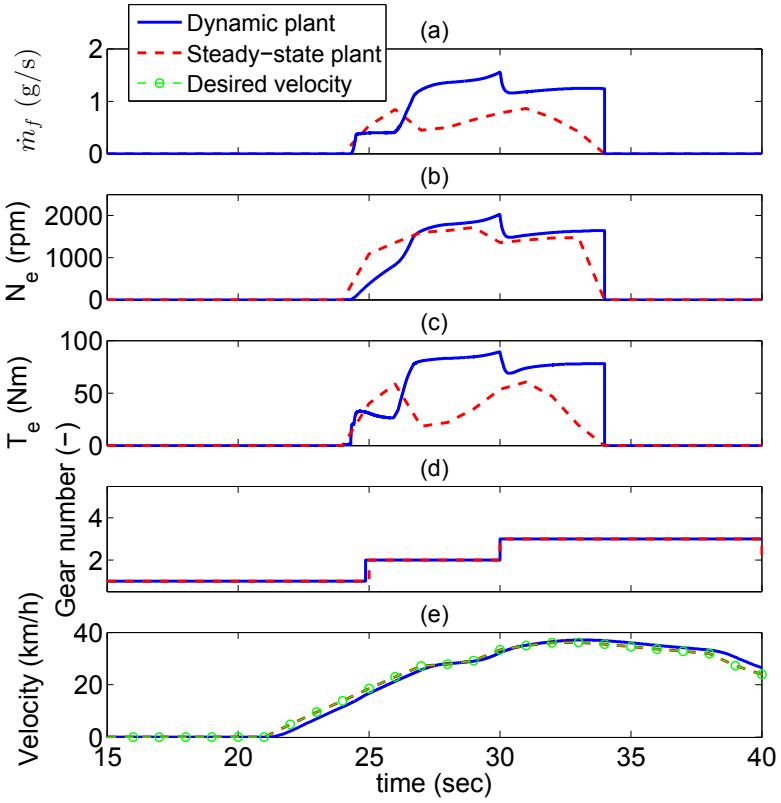

Figure 7.12: Zoom-in view of Figure 7.11 from 15 sec to 40 sec.

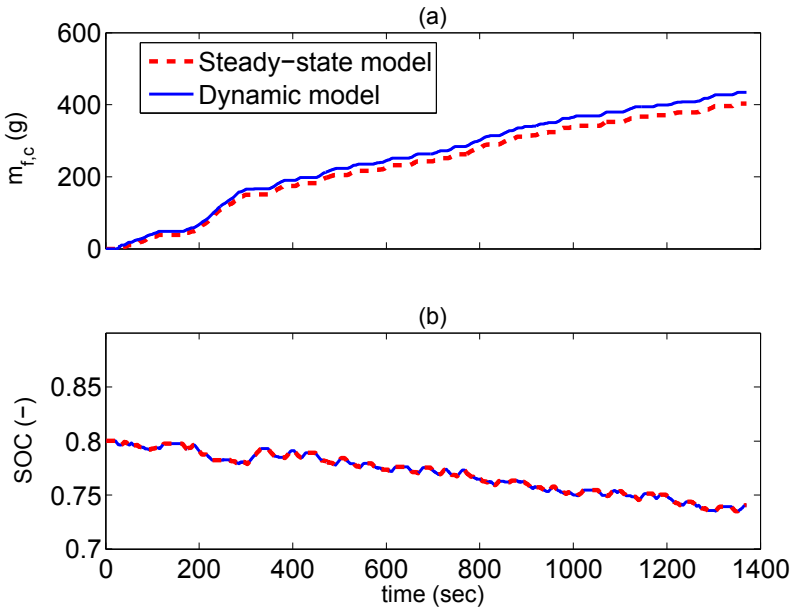

Figure 7.13: Cumulative fuel consumption and SOC for UDDS drive cycle, using the steady-state supervisory controller.

For more investigation of the discrepancy between two HEV plant models, a zoom-in view of Figure 7.11 from 15 sec to 40 sec is shown in Figure 7.12. As seen, at the beginning of vehicle acceleration, the ICE speed of the dynamic HEV testbed increases gradually with lag compared to the engine speed of the steady-state HEV plant. This is because of the effect of the powertrain dynamics that do not let the engine speed change immediately as discussed in Section 7.3. Then, the ICE controller in the dynamic HEV testbed compensates for this effect by further throttle opening and consequently injecting more fuel. This leads to further increase in the ICE torque compared to that of the steady-state HEV testbed. Eventually, the ICE instantaneous fuel consumption for the dynamic HEV testbed becomes greater than

that of the steady-state HEV testbed. Figure 7.13 compares the cumulative fuel consumption ($m_{f,c}$) of the HEV plants for UDDS drive cycle. The results show that there is a discrepancy of 32 g or 7.8 % more cumulative fuel consumption if the torque split control strategy is designed based on the steady-state map of ICE. The discrepancy between dynamic and steady-state fuel consumption is expected to significantly increase for drive cycles with more frequent transient vehicle operations. Figure 7.13-b shows the battery SOC changes within the desired range $0.7 < SOC < 0.9$ based on the constraints in Equation (7.16). The torque request of the E-machine is the same for both plant models; thus, the SOC is identical for both models.

7.5.2 Effects of Controller Design

The control strategy (Section 7.4.2), which accounts for the studied powertrain dynamics is tested for UDDS drive cycle on the HEV plant model including the ICE and clutch dynamics.

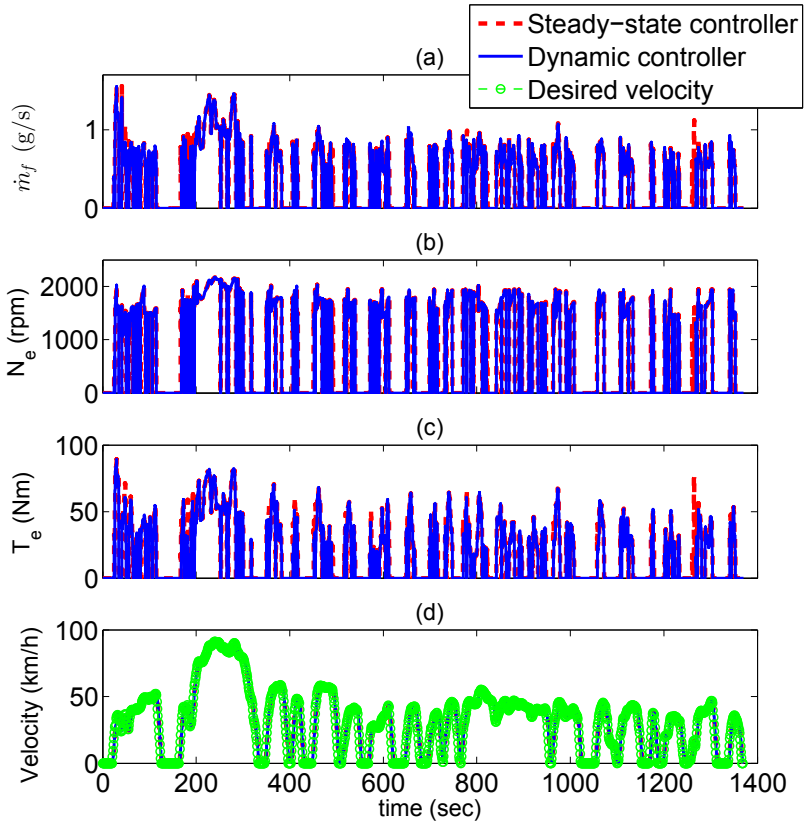

Figure 7.14: Testing dynamic and steady-state HEV supervisory controllers (Section 7.4) on the dynamic HEV plant model for UDDS drive cycle.

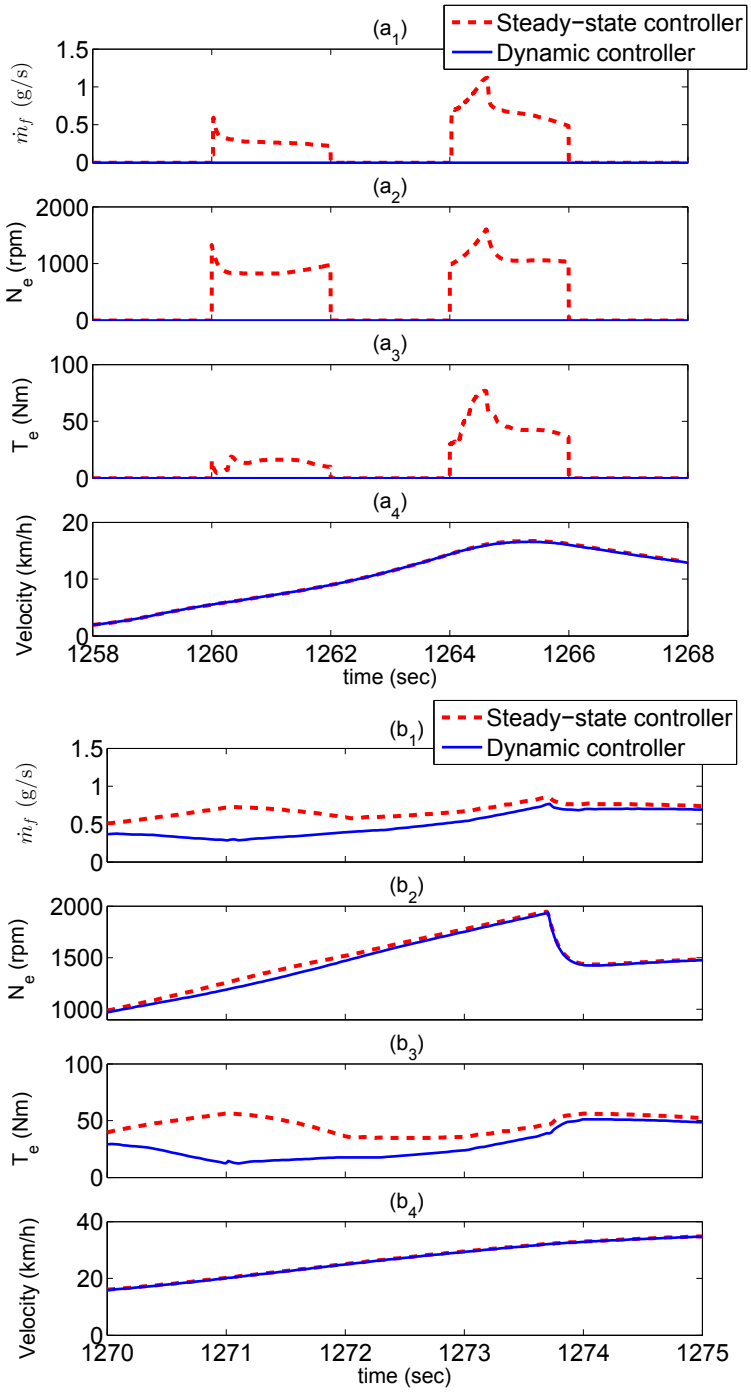

Figure 7.15: Zoom-in views of Figure 7.14 for (a) 1258-1268 sec and (b) 1270-1275 sec.

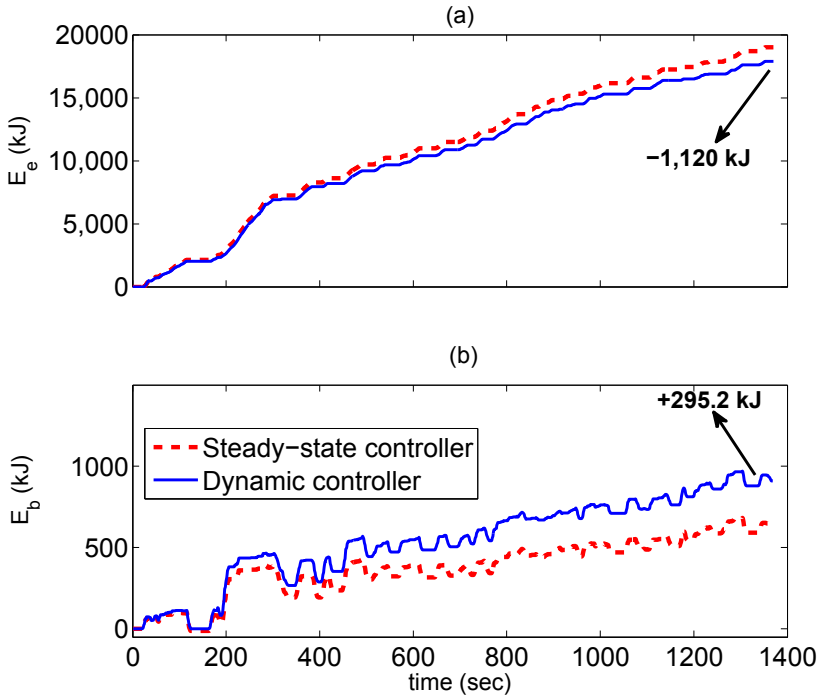

Figure 7.16: Cumulative ICE and battery energy consumption.

Results are then compared with those of testing the steady-state HEV controller on the same dynamic HEV plant model. Figure 7.14 shows the velocity profile of the vehicle, the engine torque requests commanded by both supervisory controllers (Section 7.4) for UDDS drive cycle. Furthermore, the ICE speed and the instantaneous fuel consumption resulted from both HEV supervisory controllers are shown in Figure 7.14. As seen in the figure, the vehicle velocity in the drive cycle is successfully tracked for both cases. In addition, in Figure 7.14-d during some transient conditions (e.g., 406 sec) of vehicle launch, the commanded engine torque by the steady-state HEV controller is greater than that of the dynamic HEV controller while the engine

speeds are almost the same; thus, there is more instantaneous fuel consumption when the steady-state controller is applied compared to when the dynamic controller is applied.

For a more detailed study, two zoom-in views of Figure 7.14 are shown in Figure 7.15 for two time periods of 1258 sec to 1268 sec and 1270 sec to 1275 sec. For the vehicle *transient* condition in Figure 7.15-a, the dynamic HEV supervisory controller keeps the engine off and propels the vehicle by running the E-machine so there is no ICE fuel consumption while the steady-state HEV controller commands the ICE to provide torque for propelling the vehicle. The zoom-in view in Figure 7.15-b shows another example of the transient condition of the vehicle velocity. As seen, the dynamic HEV controller commands less ICE torque than the steady-state HEV controller; therefore, the instantaneous fuel consumption is less than the one resulted from testing the steady-state controller. Since the dynamic HEV supervisory controller has the knowledge of the ICE dynamics and clutch dynamics during such transient vehicle operations, it commands the E-machine to provide the remaining torque to attenuate the adverse effect of the ICE and clutch dynamics on fuel consumption.

For a comprehensive comparison between performance of the two HEV controllers, it is necessary to compare the total energy consumption of both ICE and E-machine. Figure 7.16 shows cumulative ICE energy consumption (E_e) and cumulative battery energy consumption (E_b) for UDDS drive cycle. In total, using the dynamic HEV

supervisory controller, the cumulative ICE energy consumption is 1,120 kJ less and the battery cumulative energy consumption is 295.2 kJ more than the steady-state HEV controller. Overall, using the dynamic HEV supervisory controller leads to 4.2% reduction in the total energy consumption. The results of energy saving depend on the level of hybridization which means in case of more battery usage, less effects from powertrain dynamics on the total energy consumption are anticipated.

7.6 Summary

This study investigated the effects of major engine dynamics and clutch dynamics on performance of a parallel HEV torque split control strategy. The studied ICE dynamics include airflow dynamics, fuel flow dynamics, and rotational dynamics. An ICE dynamic model was built and experimentally validated. This study developed two different HEV testbeds by using (i) steady-state ICE maps, and (ii) dynamic ICE model integrated with a dynamic clutch model. MPC energy management strategies were developed based on the steady-state and dynamic HEV model. The control strategies were tested on both HEV plant models for UDDS drive cycle. Here are the findings from this work for the conditions studied:

† The effect of ICE dynamics and clutch dynamics resulted in about 8% higher cumulative fuel consumption when the strategy was tested on the dynamic HEV

platform for the UDDS drive cycle. This revealed the importance of ICE and clutch dynamics for the HEV torque split control strategy, while it is a common practice ([61, 63, 66, 71, 72, 147, 158, 159, 160, 161, 162, 163, 164, 165, 166, 167, 168, 169, 170, 171, 172, 173, 174]) to use steady-state ICE map data and ignore the ICE dynamics and clutch dynamics.

† Although the desired vehicle velocity profile was successfully met for both steady-state and dynamic plants, there was a lag in the engine speed change of the dynamic HEV plant during the transient conditions of the vehicle launch as a result of the effect of the ICE dynamics and clutch dynamics. The ICE controller in the dynamic HEV plant model compensates for this effect by further opening the throttle (i.e., injecting more fuel) to keep stoichiometric air-fuel ratio.

† A new HEV torque split control strategy was designed by incorporating the effects of the studied powertrain dynamics. The effect of ICE dynamics and clutch dynamics were considered by modifying the optimization cost function and adding a map of fuel penalty for transient vehicle operations. This provides a simple way to incorporate these dynamics into torque split control strategy of HEVs.

† Both enhanced and baseline HEV torque split controllers were tested on the HEV plant model including the dynamic ICE and clutch models. Results of testing both HEV controllers were compared for UDDS drive cycle. The results

show that using the enhanced controller leads to more than 4% improvement in the total energy consumption of the vehicle, compared to the baseline steady-state controller. This shows the potential energy saving benefit of integrating knowledge of the powertrain dynamics into the HEV torque split controller design.

Chapter 8

Conclusion and Future Work

Model-based control of HCCI engine was conducted for simultaneous control of multiple engine variables. In addition, the potential fuel economy benefits achieved by integrating HCCI engine technology with electrification technology was studied. Finally, the effects of powertrain dynamics on HEV energy management control strategy were investigated. Major results and contributions from this thesis are summarized in this chapter and recommendations for further work are outlined.

8.1 Conclusions

The analysis of the results in this thesis leads to the following findings and conclusions:

8.1.1 COM Development and Model-based Control of HCCI Engines

- A thermodynamics-based NCOM was developed for predicting cycle-to-cycle combustion phasing for a blended-fuel HCCI engine. The model consists of different sub-models that capture the operation of the whole HCCI cycle starting from the intake stroke to the exhaust stroke. The NCOM was validated against both a detailed physical model and a large number of experimental measurements at steady-state and transient operating conditions. Validation results showed sufficient accuracy of the model in predicting HCCI combustion phasing with an average error of less than 2 CAD and high computational efficiency with computational time requirement of less than 1 ms for a simulation engine cycle on a 2.67 GHz Intel processor. These results showed that the NCOM is suitable to design a model-based HCCI combustion controller for real-time control applications.

  The NCOM was then linearized around a nominal operating point. A discrete sub-optimal sliding mode controller along with feed-forward gain was designed to control HCCI combustion phasing in a range of operating conditions.

The controller adjusts the injected ratio of two PRFs (i.e., iso-Octane and n-Heptane) to change the fuel octane number and obtain a desired CA50. Performance of the controller was compared with a manually tuned PI controller by testing on a more detailed physical plant model. Simulation results showed that the designed sliding mode controller regulates CA50 within a maximum of 3 engine cycles with no overshoot or chattering which is two cycles faster than the PI controller. A Kalman filter was developed and added to the DSSMC structure to estimate the model states and attenuate the measurement noise effects. Tracking performance of the controllers was compared for a condition of having measurement noise with STD of 1.5 CAD. Results showed that the DSSMC with Kalman filter has better performance with around 0.4 CAD less cyclic variation. Subject to step disturbances, the designed DSSMC outperforms the PI controller for rejecting step disturbances of engine load, intake temperature, and engine speed with around 3, 0.5, and 2.5 CAD less maximum deviations and 3,1, and 3 cycles faster disturbance rejection. Considering all these findings, the designed DSSMC appears promising for real-time HCCI combustion phasing control.

- The NCOM from Chapter 2 was extended to predict cycle-to-cycle IMEP and CA50 for a blended fuel HCCI engine. The COM was validated with the HCCI experimental data at 57 steady state and 3 transient operating conditions. The validation results showed that the COM can predict CA50 and IMEP with an

average error of 1.4 CAD and 0.2 bar, respectively. The COM is computationally efficient and it only requires 0.2 ms to simulate an engine cycle on a 2.67 GHz Intel processor. A two-input two-output HCCI controller was then designed based on the extended COM for tracking desired cycle-to-cycle IMEP and CA50. The new controller is a model-based engine controller which combines a DSMC with a feed-forward integral controller. Results showed that the designed controller can track the desired IMEP and CA50 trajectory in a maximum of 4 engine cycles. No overshoot and chattering were observed in the sliding mode control of combustion phasing. Performance of the controller was also evaluated under physical disturbances when the intake manifold temperature and the engine speed suddenly change. The simulation results showed that the controller can reject these two physical disturbances in 3 to 6 engine cycles, while maintaining CA50 and IMEP deviation within 1.5 CAD and 0.1 bar. Given the low computational time and good prediction accuracy, the new COM and the designed model-based combustion plashing and load controllers are suitable for real-time HCCI engine control.

- A new performance index was proposed for an integrated control of HCCI engines. The performance index incorporates engine load, raw emissions, and exhaust gas temperature (aftertreatment light-off efficiency). To have the optimum performance index at each load (IMEP), an optimum combustion phasing (OCP) algorithm was developed to determine the optimum CA50 trajectory for

HCCI control to minimize the engine tailpipe emissions. The PI includes raw emission index and aftertreatment efficiency index. Raw emissions include CO, uHC, and NO_x. Aftertreatment efficiency depends on T_{exh}. The methodology of PI-based HCCI control was illustrated for a blended fuel HCCI engine for IMEP and CA50 control. The experimental data at 214 operating points was used to determine the PI contour plot which was used in the OCP algorithm to calculate optimum CA50 trajectory. Performance of the OCP algorithm was studied for different scenarios of local low load sweep or high load sweep and load sweep from low load region to high load region. The HCCI controller was designed and tested on a previously validated physical engine model. For the case study in this work, a cumulative PI improvement of 11% was shown in comparison to a conventional controller where a constant CA50 is used. The new PI-based control methodology from this work is general and can be applied for different HCCI control applications. It was also observed that higher PI improvement can be achieved by relaxing the constraints on CA50 change or PI change in one step. The PI-based control methodology helps to reduce the costly control calibration efforts by indirect control of engine emissions.

- A MIMO grey-box model was developed for predicting all the main HCCI engine outputs including CA50, IMEP, T_{exh}, and concentrations of CO, THC, and NOx engine-out emissions. The grey-box models were designed to require minimum efforts for training while providing appropriate accuracy. The grey-box

models were validated with extensive experimental data at 309 steady state and transient conditions for 2 different HCCI engine applications: a Ricardo HCCI engine with PRFs and a Yanmar HCCI engine with ethanol fuel. The validation results for the Ricardo HCCI engine with PRFs showed that the emission grey-box model is able to predict CA50, IMEP, T_{exh}, CO, THC, and NO_x with the average errors of 0.8 CAD, 0.2 bar, 5.3 °C, 0.03%, 394 PPM, and 4 PPM, respectively. The grey-box models predict CA50, IMEP, and T_{exh} with more than 80%, 84%, and 74% better accuracy compared to those from the clear-box (physical) model and 72%, 60%, and 60% improvement in prediction accuracy compared to those from the black-box only model. In addition, the emissions grey-box model predicts CO, THC, and NOx concentrations with three times better accuracy compared to those from the black-box only model. For the Yanmar HCCI engine with ethanol fuel, the grey-box model is capable of predicting the main HCCI engine outputs with average 69% and 45% better accuracy than the clear-box and black-box only models, respectively (for CA50, IMEP, and T_{exh}) and about 45% average better accuracy than the black-box only model for HC and CO concentrations.

Application of the HCCI grey-box model for HCCI engine control was then studied. The developed grey-box model requires less than 1 ms computation time to run on a 3.2 GHz Intel processor for simulating one HCCI engine cycle. The grey-box model was used as a virtual engine platform to i) study HCCI

engine performance, ii) evaluate and design HCCI controllers in a simulation test-bed. This study illustrated an application of the grey-box model as a virtual engine test-bed for model-based controller design for the Ricardo HCCI engine. In addition, a Genetic Algorithm optimization method was applied to simulation results from the grey-box model to determine optimum combustion phasing (i.e., CA50) leading to minimum HCCI emissions at different engine loads. The optimum CA50 trajectory was then utilized in design of a model-based CA50-IMEP controller to simultaneously control combustion phasing and load while minimizing the HCCI engine-out emissions. This is another methodology presented for indirect control of HCCI engine variables in order to reduce the costly calibration efforts.

- The discrete COM from Chapter 3 was extended by adding a physics-based sub-model to predict cycle-to-cycle T_{exh} for a blended fuel HCCI engine. The COM was validated with the HCCI experimental data at 49 steady-state and transient operating conditions. The validation results indicated that the COM can predict CA50, IMEP, and T_{exh} with average errors of 1.6 CAD, 0.3 bar, and 7 °C, respectively. The COM was then utilized to design a triple HCCI controller for tracking the desired cycle-to-cycle CA50, IMEP, and T_{exh}. The triple controller is a model-based engine controller which combines a DSSMC with feedforward gain and integral action for CA50, a feedforward integral controller for IMEP, and a DSSMC for T_{exh} (with the control inputs of fuel ON, $\dot{m}_f$, and P_{man}).

Performance of the model-based controller was then studied using a detailed experimentally validated HCCI engine model and compared with those of an optimally tuned PID-based controller. The designed model-based controller could track the desired output trajectories with up to 4 cycles faster than the PID-based controller while there was no steady-state error observed for both controllers. Performance of the controllers was also studied for rejecting the effects of the disturbances. Simulation results showed that while there was no steady-state deviation for both types of controllers, the model-based controller outperformed its PID-based peer with up to 5 cycles faster disturbance rejection and zero maximum deviation. Given the low computational requirement (<1 ms to simulate an engine cycle on a 2.67 GHz Intel processor) and good prediction accuracy, the new COM and the designed model-based controller are suitable for real-time triple control of HCCI engines.

8.1.2 Energy Management Control in HEVs

- This study investigated the potential fuel consumption benefits achieved by integrating HCCI engine technology and HEV. Two parallel HEV powertrain models integrated with 1) an HCCI engine map and 2) an SI engine map are developed and used to design and evaluate energy management MPC strategy. Fuel consumption performance of both HEVs are compared for a battery charge depletion mode during UDDS drive cycle. The results showed that the HCCI

engine is less used at high vehicle loads and the E-machine compensates by providing more torque assist. However, HCCI engine charges the battery more at low loads. Overall, using the HCCI-HEV, the fuel consumption is improved by 26%.

- This study investigated the effects of major engine dynamics and clutch dynamics on performance of a parallel HEV torque split control strategy. The studied ICE dynamics include airflow dynamics, fuel flow dynamics, and rotational dynamics. An ICE dynamic model was built and experimentally validated. This study developed two different HEV testbeds by using (i) steady-state ICE maps, and (ii) dynamic ICE model integrated with a dynamic clutch model. MPC energy management strategies were developed based on the steady-state and dynamic HEV model. The control strategies were tested on both HEV plant models for UDDS drive cycle. The effect of ICE dynamics and clutch dynamics resulted in about 8% higher cumulative fuel consumption when the strategy was tested on the dynamic HEV platform for the UDDS drive cycle. This revealed the importance of ICE and clutch dynamics for the HEV torque split control strategy. Although the desired vehicle velocity profile was successfully met for both steady-state and dynamic plants, there was a lag in the engine speed change of the dynamic HEV plant during the transient conditions of the vehicle launch as a result of the effect of the ICE dynamics and clutch dynamics. The ICE controller in the dynamic HEV plant model compensates

for this effect by further opening the throttle (i.e., injecting more fuel) to keep stoichiometric air-fuel ratio. A new HEV torque split control strategy was designed by incorporating the effects of the studied powertrain dynamics. The effect of ICE dynamics and clutch dynamics were considered by modifying the optimization cost function and adding a map of fuel penalty for transient vehicle operations. This provides a simple way to incorporate these dynamics into torque split control strategy of HEVs. Both enhanced and baseline HEV torque split controllers were tested on the HEV plant model including the dynamic ICE and clutch models. Results of testing both HEV controllers were compared for UDDS drive cycle. The results show that using the enhanced controller leads to more than 6% improvement in the total energy consumption of the vehicle, compared to the baseline steady-state controller. This shows the potential energy saving benefit of integrating knowledge of the powertrain dynamics into the HEV torque split controller.

8.2 Major Thesis Contributions

The major contributions of this thesis are outlined below:

- Developed and experimentally validated a new COM for control of combustion phasing in a blended fuel HCCI engine; showed the first application of sliding

mode control for control of HCCI combustion phasing.

- Extended a COM to predict both combustion phasing and load in a blended fuel HCCI engine; validated the COM for a large number of HCCI steady-state and transient operating conditions.

- Developed two novel methodologies for integrated HCCI engine control based on i) an integrated performance index and ii) grey-box modeling; developed a new algorithm to determine OCP trajectory for HCCI control based on the developed performance index

- developed the first MIMO grey-box model that can predict major HCCI engine output variables including CA50, IMEP, T_{exh}, CO, NO_x, and THC.

- Illustrated the applications of both proposed performance index-based and grey-box model-based methodologies for integrated control of IMEP, CA50, and emissions in an HCCI engine.

- Extended an HCCI COM by developing a T_{exh} sub-model and experimentally validated the extended COM for predicting cycle-to-cycle T_{exh}, CA50, and IMEP; designed a triple model-based controller using a discrete sliding mode control method; evaluated performance of the triple controller for tracking T_{exh}, CA50, and IMEP trajectories on a detailed experimentally validated HCCI model.

- Studied the potential fuel consumption benefits achieved by integrating HCCI

technology with HEV by developing two HEV powertrain models with 1) HCCI engine map and 2) baseline SI engine to design and evaluate an energy management MPC strategy; compared the fuel consumption of both HEVs for a battery charge depletion mode during UDSS drive cycle.

- Analyzed effects of major ICE dynamics and clutch dynamics on performance of an HEV torque split control strategy; illustrated the potential fuel economy improvement that can be lost by neglecting ICE dynamics in HEV torque split control strategies; developed a new HEV torque split control strategy by incorporating the effects of the major ICE and clutch dynamics to illustrate improvement in the total HEV energy consumption.

8.3 Future Work

- The fuel consumption benefits of LTC-HEV can be studied using different types of LTC like RCCI and PCCI and compared with other types of LTC-HEV, SI-HEV, and CI-HEV.

- The designed model-based HCCI engine controllers in this work could be experimentally implemented on the actual engine setup.

- The COM could be extended for the operating conditions utilizing VVA and external EGR; the model-based controller with other actuators like VVA could

be designed and implemented for real-time HCCI engine control.

- The second law (exergy) efficiency could be added to the HCCI performance index for fuel economy improvement and saving exhaust exergy for applications such as Combined Heat and Power (CHP).

- A more detailed and dynamic battery model could be added to the HEV control model to study the effects of the battery dynamics on the HEV energy management control strategy.

- The effects of the powertrain dynamics could be incorporated to the HEV energy management control strategy for a battery charge sustaining mode condition.

References

[1] M. Bidarvatan, M. Shahbakhti, S.A. Jazayeri, and C.R. Koch. Cycle-to-cycle Modeling and Sliding Mode Control of Blended Fuel HCCI Engine. *Control Engineering Practice*, 24:79–91, March 2014.

[2] M. Bidarvatan and M. Shahbakhti. Two-input Two-output Control of Blended Fuel HCCI Engines. SAE Paper No. 2013-01-1663, 2013a.

[3] M. Bidarvatan, V. Thakkar, M. Shahbakhti, B. Bahri, and A.A. Aziz. Grey-box Modeling of HCCI Engines. *Applied Thermal Engineering*, 70(1):397–409, 2014.

[4] M. Bidarvatan and M. Shahbakhti. Gray-box Modeling for Performance Control of an HCCI Engine with Blended Fuels. *Journal of Engineering for Gas Turbines and Power*, 136(10):101510, 2014.

[5] M. Bidarvatan and M. Shahbakhti. Integrated HCCI Engine Control Based on a Performance Index. *ASME Journal of Engineering for Gas Turbines and Power*, 136(10):101601, 2014.

[6] M. Bidarvatan, D. Kothari, and M. Shahbakhti. Integrated Cycle-to-Cycle Control of Exhaust Gas Temperature, Load, and Combustion Phasing in an HCCI Engine . In *Proceedings of the 2015 American Control Conference*, 2015.

[7] M. Bidarvatan and M. Shahbakhti. Impact of Engine Dynamics on Torque Split Management of a Hybrid Electric Vehicle. In *Proceedings of the 2014 ASME Dynamic Systems and Control Conference*, DSCC paper 2014-6283, 2014.

[8] G.D. Neely, S. Sasaki, Y. Huang, J.A. Leet, and D.W. Stewart. New Diesel Emission Control Strategy to Meet US Tier 2 Emissions Regulations. SAE Paper 2005-01-1091, 2005.

[9] M. Shahbakhti and C.R. Koch. Physics Based Control Oriented Model for HCCI Combustion Timing. *AMSE Journal of Dynamic Systems, Measurement, and Control*, 132(2), 2010.

[10] M. Shahbakhti and C.R. Koch. Characterizing the Cyclic Variability of Ignition Timing in a Homogeneous Charge Compression Ignition Engine Fuelled with n-Heptane/iso-Octane Blend Fuels. *International Journal of Engine Research*, 9(5):361–397, 2008.

[11] M. Bidarvatan and M. Shahbakhti. Analysis and Control of Torque Split in Hybrid Electric Vehicles by Incorporating Powertrain Dynamics. *IEEE Transaction on Vehicular Technology*, submitted in May 2015, under review.

[12] Global Anthropogenic Non-CO2 Greenhouse Gas Emissions: 1990 - 2030. *http://www.epa.gov/climatechange/Downloads/EPAactivities*. 2012.

[13] Intergovernmental Panel on Climate Change), WG III Fifth Assessment Report. *https://www.ipcc.ch/report/ar5/*. 2014.

[14] United States Environmental Protection Agency. EPA and NHTSA Set Standards to Reduce Greenhouse Gases and Improve Fuel Economy for Model Years 2017-2025 Cars and Light Trucks. Office of Transportation and Air Quality, August 2012.

[15] United States Environmental Protection Agency. EPA Sets Tier 3 Tailpipe and Evaporative Emission and Vehicle Fuel Standards. Office of Transportation and Air Quality, March 2014.

[16] D.N. Tsinoglou, O.A. Haralampous, G.C. Koltsakis, and Z.C. Samaras. Model-based Optimization Methods of Combined DPF+ SCR Systems. SAE Paper No. 2007-24-0098, 2007.

[17] J.H. Kim, R.D. Reitz, and S.W. Park. Improvements in the Performance and Pollutant Emissions for Stoichiometric Diesel Combustion Engines Using a Two-pray-angle Nozzle. *Proceedings of the Institution of Mechanical Engineers, Part D: Journal of Automobile Engineering*, 224(8):1113–1122, 2010.

[18] S. Sasaki, T. Ito, and S. Iguchi. Smokeless Rich Combustion by Low Temperature Oxidation in Diesel Engines. In *Proceedings of the 9^{th} Aachen Colloquium Automobile and Engine Technology*, 2000.

[19] J.E. Dec. Advanced Compression-ignition EnginesUnderstanding the In-cylinder Processes. *Proceedings of the Combustion Institute*, 32(2):2727–2742, 2009.

[20] R. Hanson, S. Kokjohn, D. Splitter, and R.D. Reitz. Fuel Effects on Reactivity Controlled Compression Ignition (RCCI) Combustion at Low Load. *SAE International Journal of Engines*, 4(2011-01-0361):394–411, 2011.

[21] D. Splitter, R. Hanson, S. Kokjohn, and R.D. Reitz. Reactivity Controlled Compression Ignition (RCCI) Heavy-duty Engine Operation at Mid-and High-loads with Conventional and Alternative Fuels. SAE Paper 2011-01-0363, 2011.

[22] S. Saxena, I.D. Bedoya, N. Shah, and A. Phadke. Understanding Loss Mechanisms and Identifying Areas of Improvement for HCCI Engines Using Detailed Exergy Analysis. *ASME J. Eng. Gas Turbines Power*, 135(9), 2013.

[23] F. Zhao, F. Asmus, D.N. Assanis, J.E. Dec, J.A. Eng, and P.M. Najt. Homogeneous Charge Compression Ignition (HCCI) Engines. SAE Paper PT-94, 2003.

[24] H. Zhao. HCCI and CAI Engines for the Automotive Industry. Elsevier, 2007.

[25] R.H. Stanglmaier and C.E. Roberts. Homogeneous Charge Compression Ignition (HCCI): Benefits, Compromises, and Future Engine Applications. SAE Paper No. 1999-01-3682, 1999.

[26] M. Shahbakhti, A. Ghazimirsaied, and C.R. Koch. Experimental Study of Exhaust Temperature Variation in a Homogeneous Charge Compression Ignition Engine. *Proceedings of the Institution of Mechanical Engineers, Part D: Journal of Automobile Engineering*, 224(9):1177–1197, 2010.

[27] M. Shahbakhti, R. Lupul, and C.R. Koch. Sensitivity Analysis and Modeling of HCCI Auto-ignition Timing. In *Proceeding of the Fifth IFAC Symposium on Advances in Automotive Control*, pages 303–310, 2007.

[28] M. Shahbakhti. Modeling and Experimental Study of an HCCI Engine for Combustion Timing Control. PhD thesis, University of Alberta, 2009.

[29] M. Yao, Z.-Q. Zheng, B. Zhang, and Z. Chen. The Effect of PRF Fuel Octane Number on HCCI Operation. SAE Paper No. 2004-01-2992, 2004.

[30] X.-C. Lü, W. Chen, Y.-C. Hou, and Z. Huang. Study on the Ignition, Combustion and Emissions of HCCI Combustion Engines Fueled with Primary Reference Fuels. SAE Paper No. 2005-01-0155, 2005.

[31] L. Koopmans, O. Backlund, and I. Denbratt. Cycle to Cycle Variations: Their Influence on Cycle Resolved Gas Temperature and Unburned Hydrocarbons

from a Camless Gasoline Compression Ignition Engine. SAE Paper No. 2002-01-0110, 2002.

[32] L. Xingcai, H. Yuchum, J. Libin, Z. Linlin, and H. Zhen. Heat Release Analysis on Combustion and Parametric Study on Emissions of HCCI Engines Fueled with 2-propanol/n-heptane Blend Fuels. *Energy and Fuels*, 20(5):1870–1878, 2006.

[33] G.T. Kalghatgi and R.A. Head. Combustion Limits and Efficiency in a Homogeneous Charge Compression Ignition Engine. *International Journal of Engine Research*, 7(3):215–236, 2006.

[34] A. Jungkunz, H.-H. Liao, N. Ravi, and J.C. Gerdes. Reducing Combustion Variation of Late-phasing HCCI with Cycle-to-cycle Exhaust Valve Timing Control. In *Advances in Automotive Control*, pages 815–820, 2010.

[35] M. Shahbakhti, A. Ghazimirsaied, and C.R. Koch. Modeling Ranges of Cyclic Variability for HCCI Ignition Timing Control. In *Proceedings of the 2011 ASME Dynamic Systems and Control Conference*.

[36] S. Williams, L. Hu, T. Nakazono, H. Ohtsubo, and M. Uchida. Oxidation Catalysts for Natural Gas Engine Operating Under HCCI or SI Conditions. *SAE International Journal of Fuels and Lubricants*, 1(1):326–337, 2009.

[37] J.B. Heywood. Internal Combustion Engine Fundamentals. McGraw-Hill New York, 1998.

[38] V. Ferrari, H. Rabinowitz, S. Siemund, T. Collinq, and B. Campbell. Achieving EURO III and EURO IV with Ultra-low Precious Metal Loadings. SAE Paper No. 2007-01-2565, 2007.

[39] A. Widd, K. Ekholm, P. Tunestål, and R. Johansson. Physics-based Model Predictive Control of HCCI Combustion Phasing Using Fast Thermal Management and VVA. *IEEE Transactions on Control Systems Technology*, 20(3):688–699, 2012.

[40] N. Ravi, H-H. Liao, A.F. Jungkunz, A. Widd, and J.C. Gerdes. Model Predictive Control of HCCI Using Variable Valve Actuation and Fuel Injection. *Control Engineering Practice*, 20(4):421–430, 2012a.

[41] C-J. Chiang, A.G. Stefanopoulou, and M. Jankovic. Nonlinear Observer-based Control of Load Transitions in Homogeneous Charge Compression Ignition Engines. *IEEE Transactions on Control Systems Technology*, 15(3):438–448, 2007.

[42] C-J. Chiang, C-C. Huang, and M. Jankovic. Discrete-time Cross-term Forwarding Design of Robust Controllers for HCCI Engines. In *Procceding of the 2010 American Control Conference*, pages 2218–2223, 2010.

[43] P. Strandh, J. Bengtsson, R. Johansson, P. Tunestål, and B. Johansson. Variable Valve Actuation for Timing Control of a HCCI Engine. SAE Paper No. 2005-01-0147, 2005.

[44] J.O. Olsson, P. Tunestål, and B. Johansson. Closed-loop control of an HCCI engine. SAE Paper No. 2001-01-1031, 2001a.

[45] A. Audet and C.R. Koch. Actuator Comparison for Closed Loop Control of HCCI Combustion Timing. SAE Paper No. 2009-01-1135, 2009.

[46] M. Bidarvatan, M. Shahbakhti, and S.A. Jazayeri. Model-based Control of Combustion Phasing in an HCCI Engine. *SAE International Journal of Engines*, 5(3):1163–1176, 2012.

[47] N. Ravi, M.J. Roelle, H-H. Liao, A.F. Jungkunz, C-F. Chang, S. Park, and J.C. Gerdes. Model-based Control of HCCI Engines Using Exhaust Recompression. *IEEE Transactions on Control Systems Technology*, 18(6):1289–1302, 2010.

[48] G. Haraldsson, P. Tunestål, and B. Johansson. Transient Control of a Multi Cylinder HCCI Engine During a Drive Cycle. SAE Paper No. 2005-01-0153, 2005.

[49] G.M. Shaver, J.C. Gerdes, and M. Roelle. Physics-based Modeling and Control of Residual-affected HCCI Engines. *ASME Journal of Dynamic Systems, Measurement, and Control*, 131(2), 2009.

[50] G.M. Shaver, J.C. Gerdes, and M. Roelle. Physics-based Closed-loop Control of Phasing, Peak Pressure and Work Output in HCCI Engines Utilizing Variable Valve Actuation. In *Proceeding of the 2004 American Control Conference*, pages 150–155, 2004.

[51] N. Ravi, H-H. Liao, A.F. Jungkunz, C-F. Chang, H-H. Song, and J.C. Gerdes. Modeling and Control of an Exhaust Recompression HCCI Engine Using Split Injection. *ASME Journal of Dynamic Systems, Measurement, and Control*, 134(1), 2012b.

[52] V. Tandra and N. Srivastava. Optimal Peak Pressure and Exhaust Temperature Tracking Control for a Two-zone HCCI Engine Model with Mean Burn Duration. SAE Paper No. 2009-01-1130, 2009.

[53] P. Gorzelic, E. Hellström, A.G. Stefanopoulou, and L. Jiang. Model-based Feedback Control for an Automated Transfer Out of SI Operation During SI to HCCI Transitions in Gasoline Engines. In *Proceeding of the 5th Annual Dynamic Systems and Control Conference*, 2012.

[54] C. Fang, F. Yang, M. Ouyang, G. Gao, and L. Chen. Combustion Mode Switching Control in a HCCI Diesel Engine. *Applied Energy*, 110:190–200, 2013.

[55] J. Wang. Hybrid Robust Air-path Control for Diesel Engines Operating Conventional and Low Temperature Combustion Modes. *IEEE Transactions on Control Systems Technology*, 16(6):1138–1151, 2008.

[56] U. Asad, P. Divekar, X. Chen, M. Zheng, and J. Tjong. Mode Switching Control for Diesel Low Temperature Combustion with Fast Feedback Algorithms. *SAE International Journal of Engines*, 5(3):850–863, 2012.

[57] L. Tribioli, M. Barbieri, R. Capata, E. Sciubba, E. Jannelli, and G. Bella. A

Real Time Energy Management Strategy for Plug-in Hybrid Electric Vehicles based on Optimal Control Theory. *Journal of Energy Procedia*, 45:949–958, 2014.

[58] A. Sciarretta, L. Serrao, P.C. Dewangan, P. Tona, EN.D. Bergshoeff, C. Bordons, L. Charmpa, P.h. Elbert, L. Eriksson, T. Hofman, et al. A control Benchmark on the Energy Management of a Plug-in Hybrid Electric Vehicle. *Control Engineering Practice*, 29:287–298, 2014.

[59] M. Shams-Zahraei, A.Z. Kouzani, S. Kutter, and B. Bäker. Integrated Thermal and Energy Management of Plug-in Hybrid Electric Vehicles. *Journal of Power Sources*, 216:237–248, 2012.

[60] X. Yang and G.G. Zhu. A Two-zone Control Oriented SI-HCCI Hybrid Combustion Model for the HIL Engine Simulation. In *the proceeding of 2011 American Control Conference (ACC)*, pages 973–978, 2011.

[61] D. Kum, H. Peng, and N.K. Bucknor. Supervisory Control of Parallel Hybrid Electric Vehicles for Fuel and Emission Reduction. *Journal of Dynamic Systems, Measurement, and Control*, 133(6):061010, 2011.

[62] J.T.B.A. Kessels, M.W.T. Koot, P.P.J. van den Bosch, and D.B. Kok. Online Energy Management for Hybrid Electric Vehicles. *IEEE Transactions on Vehicular Technology*, 57(6):3428–3440, 2008.

[63] M. Koot, J.T.B.A. Kessels, B. de Jager, W.P.M.H. Heemels, P.P.J. Van den

Bosch, and M. Steinbuch. Energy Management Strategies for Vehicular Electric Power Systems. *IEEE Transactions on Vehicular Technology*, 54(3):771–782, 2005.

[64] A. Yonekawa, M. Ueno, O. Watanabe, and N. Ishikawa. Development of New Gasoline Engine for ACCORD Plug-in Hybrid. SAE Paper No. 2013-01-1738, 2013.

[65] N. Kawamoto, K. Naiki, T. Kawai, T. Shikida, et al. Development of New 1.8-liter Engine for Hybrid Vehicles. SAE Paper No. 2009-01-1061, 2009.

[66] S. Kermani, S. Delprat, T.-M. Guerra, R. Trigui, and B. Jeanneret. Predictive Energy Management for Hybrid Vehicle. *J. of Control Eng. Practice*, 20(4):408–420, 2012.

[67] D.F. Opila, X. Wang, R. McGee, R.B. Gillespie, J.A. Cook, and J.W. Grizzle. An Energy Management Controller to Optimally Trade Off Fuel Economy and Drivability for Hybrid Vehicles. *IEEE Transactions on Control Systems Technology*, 20(6):1490–1505, 2012.

[68] R. Johri, A. Salvi, and Z. Filipi. Optimal Energy Management for a Hybrid Vehicle Using Neuro-dynamic Programming to Consider Transient Engine Operation. In *Proceeding of the 2011 ASME Dynamic Systems and Control Conference.*

[69] I.J. Albert, E. Kahrimanovic, and A. Emadi. Diesel Sport Utility Vehicles with

Hybrid Electric Drive Trains. *IEEE Transactions on Vehicular Technology*, 53(4):1247–1256, 2004.

[70] G. Rizzoni, L. Guzzella, and B.M. Baumann. Unified Modeling of Hybrid Electric Vehicle Drivetrains. *IEEE/ASME Transactions on Mechatronics*, 4(3):246–257, 1999.

[71] C.-C. Lin, H. Peng, J.W. Grizzle, and J.-M. Kang. Power Management Strategy for a Parallel Hybrid Electric Truck. *IEEE Trans. on Control Sys. Tech.*, 11(6):839–849, 2003.

[72] A. Brahma, B. Glenn, Y. Guezennec, T. Miller, G. Rizzoni, and G. Washington. Modeling, Performance Analysis and Control Design of a Hybrid Sport-utility Vehicle. In *Proceeding of the IEEE Int. Conf. on Control Applications*.

[73] N. Jalil, N.A. Kheir, and M. Salman. A Rule-based Energy Management Strategy for a Series Hybrid Vehicle. In *Proceedings of the 1997 American Control Conference*.

[74] B. Lawler, E. Ortiz-Soto, R. Gupta, H. Peng, and Z.S. Filipi. Hybrid Electric Vehicle Powertrain and Control Strategy Optimization to Maximize the Synergy with a Gasoline HCCI Engine. *SAE International Journal of Engines*, 4(1):1115–1126, 2011.

[75] K. Ahn, J. Whitefoot, A. Babajimopoulos, E. Ortiz-Soto, and P.Y. Papalambros. Homogeneous Charge Compression Ignition Technology Omplemented in

a Hybrid Electric Vehicle: System Optimal Design and Benefit Analysis for a Power-split Architecture. *Proceedings of the Institution of Mechanical Engineers, Part D: Journal of Automobile Engineering*, 227(1):87–98, 2013.

[76] A. Delorme, A. Rouseau, T. Wallner, E. Ortiz-Soto, A. Babajimopolous, and D. Assanis. Evaluation of Homogeneous Charge Compression Ignition (HCCI) Engine Fuel Savings for Various Electric Drive Powertrains. In *Proceeding of the 25th World Battery, Hybrid and Fuel Cell Electric Vehicle Symposium and Exhibition*, 2010.

[77] J.O. Olsson, P. Tunestål, G. Haraldsson, and B. Johansson. A Turbo Charged Dual Fuel HCCI Engine. SAE Paper No. 2001-01-1896, 2001b.

[78] F. Agrell, H.E. Ångström, B. Eriksson, J. Wikander, and J. Linderyd. Integrated Simulation and Engine Test of Closed-loop HCCI Control by Aid of Variable Valve Timings. SAE Paper No. 2003-01-0748, 2003.

[79] P. Strandh, J. Bengtsson, R. Johansson, P. Tunestål, and B. Johansson. Cycle-to-cycle Control of a Dual Fuel HCCI Engine. SAE Paper No. 2004-01-0941, 2004.

[80] J. Bengtsson, P. Strandh, R. Johansson, P. Tunestål, , and B. Johansson. Hybrid Modeling of Homogeneous Charge Compression Ignition (HCCI) Engine Dynamics - a Survey. *Int. J. of Control*, 80(11):1814–1847, 2007.

[81] D.J. Rausen, J.-M. Kang, J.A. Eng, A.G. Stefanopoulou, and T.-W. Kuo. A

Mean-value Model for Control of Homogeneous Charge Compression Ignition (HCCI) Engines. *Journal of Dynamic Systems, Measurement, and Control*, 127(3):355–362, 2005.

[82] G.M. Shaver, P.A. Caton, C.F. Edwards, J.C. Gerdes, and M.J. Roelle. Dynamic Modeling of Residual-Affected Homogeneous Charge Compression Ignition Engines with Variable Valve Actuation. *Journal of Dynamic Systems, Measurement, and Control*, 127(3):374–381, 2005.

[83] G.M. Shaver, M.J. Roelle, and C.J. Gerdes. Modeling Cycle-to-cycle Dynamics and Mode Transition in HCCI Engines with Variable Valve Actuation. *Control Engineering Practice*, 14(3):213–222, 2006.

[84] J.-M. Kang and M. Druzhinina. HCCI Engine Control Strategy with External EGR. In *the Proeeding of 2010 American Control Conference (ACC)*.

[85] H. Ma, H-M. Xu, and J-H. Wang. Real-time Control Oriented HCCI Engine Cycle-to-cycle Dynamic Modelling. *International Journal of Automation and Computing*, 8(3):317–325, 2011.

[86] K. Ebrahimi, C.R. Koch, and A. Schramm. A Control Oriented Model with Variable Valve Timing for HCCI Combustion Timing Control. SAE Paper No. 2013-01-0588, 2013a.

[87] K. Ebrahimi and C.R. Koch. HCCI Combustion Timing Control with Variable

Valve Timing. In *Proceeding of the 2013 American Control Conference*, pages 4429–4434, 2013b.

[88] G.M. Shaver. Stability Analysis of Residual-affected HCCI Using Convex Optimization. *Control Engineering Practice*, 17(12):1454–1460, 2009.

[89] K. Ebrahimi and C.R. Koch. Model Predictive Control for Combustion Timing and Load Control in HCCI Engines. SAE Paper 2015-01-0822, 2015.

[90] J. Bengtsson, P. Strandh, R. Johansson, P. Tunestål, and B. Johansson. Hybrid Control of Homogeneous Charge Compression Ignition (HCCI) Engine Dynamics. *International journal of control*, 79(05):422–448, 2006.

[91] M. Bidarvatan, M. Shahbakhti, and S.A. Jazayeri. Optimal Integral State Feedback Control of HCCI Combustion Timing. *Int. Journal of Automotive Engineering*, 1(3), 2011.

[92] G.M. Shaver, M. Roelle, and J.C. Gerdes. Decoupled Control of Combustion Timing and Work Output in Residual-affected HCCI Engines. In *Proceedings of the 2005 American Control Conference*, pages 3871–3876. IEEE, 2005.

[93] A. Widd, H.-H. Liao, J.C. Gerdes, P. Tunestal, and R. Johansson. Control of Exhaust Recompression HCCI Using Hybrid Model Predictive Control. In *Proceedings of the 2011 American Control Conference*, pages 420–425. IEEE, 2011.

[94] Z. Jia and I. Denbratt. Experimental Investigation of Natural Gas-Diesel Dual-Fuel RCCI in a Heavy-Duty Engine. *SAE International Journal of Engines*, 8(2015-01-0838):797–807, 2015.

[95] R.D. Reitz and G. Duraisamy. Review of High Efficiency and Clean Reactivity Controlled Compression Ignition (RCCI) Combustion in Internal Combustion Engines. *Progress in Energy and Combustion Science*, 46:12–71, 2015.

[96] K. Swan, M. Shahbakhti, and C.R. Koch. Predicting Start of Combustion Using a Modified Knock Integral Method for an HCCI Engine. SAE Paper No. 2006-01-1086, 2006.

[97] C. Milosavljević. General Conditions for the Existence of a Quasi-sliding Mode on the Switching Hyperplane in Discrete Variable Structure Systems. *Automation and Remote Control*, 46(3):307–314, 1985.

[98] H. Sira-Ramirez. Non-linear Discrete Variable Structure Systems in Quasi-sliding Mode. *International Journal of Control*, 54(5):1171–1187, 1991.

[99] G. Golo and C. Milosavljević. Robust Discrete-time Chattering Free Sliding Mode Control. *Systems & Control Letters*, 41(1):19–28, 2000.

[100] A. Bartoszewicz. Discrete-time Quasi-sliding-mode Control Strategies. *IEEE Transactions on Industrial Electronics*, 45(4):633–637, 1998.

[101] W.-C. Yu and G.-J. Wang. Discrete Sliding Mode Controller Design Based on

the LQR Suboptimal Approach with Application on AC Servo Motor. *Journal of the Chinese Institute of Engineers*, 29(5):873–882, 2006.

[102] W.-C. Su, S.V. Drakunov, and U. Ozguner. An O (T 2) Boundary Layer In Sliding Mode for Sampled-data Systems. *IEEE Transactions on Automatic Control*, 45(3):482–485, 2000.

[103] K. Youcef-Toumi and O. Ito. A Time Delay Controller for Systems with Unknown Dynamics. *ASME Journal of Dynamic Systems, Measurement, and Control*, 112(1):133–142, 1990.

[104] H. Elmali and N. Olgac. Sliding Mode Control with Perturbation Estimation (SMCPE): A New Approach. *International Journal of Control*, 56(4):923–941, 1992.

[105] G.F. Franklin, M.L. Workman, and D. Powell. Digital Control of Dynamic Systems. *2nd edition, Addison-Wesley, 1997.*

[106] S.M. Bozic. Digital and Kalman Filtering: an Introduction to Discrete-time Filtering and Optimum Linear. *Halsted Press, New York, NY, 1994.*

[107] M. Shahbakhti and C.R. Koch. Dynamic Modeling of HCCI Combustion Timing in Transient Fueling Operation. *SAE Int. J.of Engines*, 2(1):1098–1113, 2009.

[108] H.-H. Liao, A. Widd, N. Ravi, A.F. Jungkunz, J.-M. Kang, and J.C. Gerdes.

Control of Recompression HCCI with a Three Region Switching Controller. *Control Engineering Practice*, 21(2):135–145, 2013.

[109] E. Jean, V. Leroy, G. Montenegro, A. Onorati, and M. Laurell. Impact of Ultra Low Thermal Inertia Manifolds on Emission Performance.

[110] M. Sjöberg and J.E. Dec. Influence of EGR Quality and Unmixedness on the High-load Limits of HCCI Engines. *SAE International Journal of Engines*, 2(1):492–510, 2009.

[111] J.E. Dec and Y. Yang. Boosted HCCI for High Power Without Engine Knock and With Ultra-low NOx Emissions-using Conventional Gasoline. *SAE International Journal of Engines*, 3(1):750–767, 2010.

[112] T. Johansson, B. Johansson, P. Tunestål, and H. Aulin. HCCI Operating Range in a Turbo-charged Multi Cylinder Engine with VVT and Spray-guided DI. SAE Paper No. 2009-01-0494, 2009.

[113] T. Kuboyama, Y. Moriyoshi, K. Hatamura, J. Takanashi, Y. Urata, and T. Yamada. A Study of Newly Developed HCCI Engine With Wide Operating Range Equipped With Blowdown Supercharging System. *SAE International Journal of Engines*, 5(2011-01-1766):51–66, 2011.

[114] P. Erduranl M. Sahir Salman M. Gölcü, Y. Sekmen. Artificial Neural-network Based Modeling of Variable Valve-timing in a Spark-ignition Engine. *Applied Energy*, 81(2):187–197, 2005.

[115] A. Parlak, Y. Islamoglu, H. Yasar, and A. Egrisogut. Application of Artificial Neural Network to Predict Specific Fuel Consumption and Exhaust Temperature for a Diesel Engine. *Applied Thermal Engineering*, 26(8):824–828, 2006.

[116] C. Sayin, H.M. Ertunc, M. Hosoz, I. Kilicaslan, and M. Canakci. Performance and Exhaust Emissions of a Gasoline Engine Using Artificial Neural Network. *Applied Thermal Engineering*, 27(1):46–54, 2007.

[117] N. Kara Togun and S. Baysec. Prediction of Torque and Specific Fuel Consumption of a Gasoline Engine by Using Artificial Neural Networks. *Applied Energy*, 87(1):349–355, 2010.

[118] J. Porteiro, J. Collazo, D. Patiño, and J.L. Míguez. Diesel Engine Condition Monitoring Using a Multi-net Neural Network System with Nonintrusive Sensors. *Applied Thermal Engineering*, 31(17):4097–4105, 2011.

[119] A. Çay, Y.and Çiçek, F. Kara, and S. Sağiroğlu. Prediction of Engine Performance for an Alternative Fuel Using Artificial Neural Network. *Applied Thermal Engineering*, 37:217–225, 2012.

[120] B. Liu, C. Zhao, F. Zhang, T. Cui, and J. Su. Misfire Detection of a Turbocharged Diesel Engine by Using Artificial Neural Networks. *Applied Thermal Engineering*, 55:26–32, 2013.

[121] Y. Choi and J-Y. Chen. Fast Prediction of Start-of-combustion in HCCI with

Combined Artificial Neural Networks and Ignition Delay Model. *Proceedings of the Combustion Institute*, 30(2):2711–2718, 2005.

[122] M. Mirhassani, X. Chen, A. Tahmasebi, and M. Ahmadi. On Control of HCCI Combustion-neural Network Approach. In *Proceeding of the 2006 IEEE International Conference on Control Applications*, pages 1669–1674, 2006.

[123] V.M. Janakiraman, X. Nguyen, and D. Assanis. Nonlinear Identification of a Gasoline HCCI engine Using Neural Networks Coupled with Principal Component Analysis. *Applied Soft Computing*, 13(5):2375–2389, 2013.

[124] B. Bahri, A.A. Aziz, M. Shahbakhti, and M.F. Muhamad Said. Understanding and Detecting Misfire in an HCCI Engine Fuelled with Ethanol. *Applied Energy*, 108:24–33, 2013a.

[125] B. Bahri, A.A. Aziz, M. Shahbakhti, and M.F. Muhamad Said. Analysis and Modeling of Exhaust Gas Temperature in an Ethanol Fuelled HCCI Engine. *Journal of Mechanical Science and Technology*, 27(11):3531–3539, 2013b.

[126] S. Zhang, G. Zhu, Y. Yoon, and Z. Sun. A Control Oriented Charge Mixing and HCCI Combustion Model for Internal Combustion Engines. *ASME Journal of Dynamic Systems, Measurement, and Control*, 2:321–327, 2012.

[127] P. Kirchen, M. Shahbakhti, and C.R. Koch. A Skeletal Kinetic Mechanism for PRF Combustion in HCCI Engines. *Combustion Science and Technology*, 179(6):1059–1083, 2007.

[128] N.P. Komninos, D.T. Hountalas, and D.A. Kouremenos. Description of In-cylinder Combustion Processes in HCCI Engines Using a Multi-zone Model. SAE Paper No. 2005-01-0171, 2005.

[129] D.L. Flowers, S.M. Aceves, J. Martinez-Frias, and R.W. Dibble. Prediction of carbon monoxide and hydrocarbon emissions in iso-octane HCCI engine combustion using multizone simulations. *Proceedings of the Combustion Institute*, 29(1):687–694, 2002.

[130] M. Bidarvatan and M. Shahbakhti. Grey-box modeling for HCCI engine control. In *Proceedings of the 2013 ASME Internal Combustion Engine Division Fall Technical Conference*, ASME Paper No. ICEF2013-19097, 2013b.

[131] M. Dehghani Firoozabadi, M. Shahbakhti, C.R. Koch, and S.A. Jazayeri. Thermodynamic Control-oriented Modeling of Cycle-to-cycle Exhaust Gas Temperature in an HCCI Engine. *Applied Energy*, 110:236–243, 2013.

[132] D. Kothari. Experimental Setup and Controller Design for an HCCI Engine. MS thesis, Michigan Technological University, 2014.

[133] S. Haykin. Neural Networks and Learning Machines. Prentice Hall New York, 2009.

[134] K. Deb, A. Pratap, S. Agarwal, and T. Meyarivan. A Fast and Elitist Multiobjective Genetic Algorithm: NSGA-II. *IEEE Transactions on Evolutionary Computation*, 6(2):182–197, 2002.

[135] S. Saxena and I. Bedoya. Fundamental Phenomena Affecting Low Temperature Combustion and HCCI Engines, High Load Limits and Strategies for Extending these Limits. *Progress in Energy and Combustion Science*, 39:457–488, 2013.

[136] M. Shahbakhti, A. Ghazimirsaied, A. Audet, and C.R. Koch. Combustion Characteristics of Butanol/n-Heptane Blend Fuels in an HCCI Engine. In *Proceedings of Combustion Institute - Canadian Section*, 2010.

[137] A. Widd, H.-H. Liao, J.C. Gerdes, P. Tunestål, and R. Johansson. Hybrid Model Predictive Control of Exhaust Recompression HCCI. *Asian Journal of Control*, 16(2):370–381, 2014.

[138] E. Hellström, J. Larimore, S. Jade, A.G. Stefanopoulou, and L. Jiang. Reducing Cyclic Variability While Regulating Combustion Phasing in a Four-Cylinder HCCI Engine. *IEEE Transactions on Control Systems Technology*, 3(22):1190–1197, 2014.

[139] F.X. Schauer, T. Zimmer, M. Bachhuber, M. Scheller, Y. Yamasaki, K. Oryoji, and G. Wachtmeister. Development of a Model-Based HCCI Control Strategy for an Engine with a Fully Variable Valve Train. SAE Paper 2013-01-1667, 2013.

[140] S.M. Erlien, A.F. Jungkunz, and J.C. Gerdes. Multicylinder HCCI Control with Coupled Valve Actuation Using Model Predictive Control. *ASME Journal of Dynamic Systems, Measurement, and Control*, 135(5), 2013.

[141] Y. Yoon, Z. Sun, S. Zhang, and G.G. Zhu. A Control-Oriented Two-Zone Charge Mixing Model for HCCI Engines With Experimental Validation Using an Optical Engine. *ASME Journal of Dynamic Systems, Measurement, and Control*, 136(4):041015, 2014.

[142] S. Zhang, G. Zhu, and Z. Sun. A Control-Oriented Charge Mixing and Two-Zone HCCI Combustion Model. *IEEE Transactions on Vehicular Technology*, 63(3):1079–1090, 2014.

[143] Y. Fengjun and J. Wang. Enabling Air-Path Systems for Homogeneous Charge Compression Ignition (HCCI) Engine Transient Control. In *Procceding of the 2009 ASME Dynamic Systems and Control Conference*, pages 873–880, 2009.

[144] S. Chen and Y. Fengjun. Combustion Phasing and Work Output Modeling for Homogeneous Charge Compression Ignition (HCCI) Engines. In *Procceding of the 2014 American Control Conference*, pages 843–848, 2014.

[145] J.G. Ziegler and N.B. Nichols. Optimum Settings for Automatic Controllers. *ASME Journal of Dynamic Systems, Measurements, and Control*, 115:220–222, 2008.

[146] T. Hutchinson, S. Burgess, and G. Herrmann. Current Hybrid-electric Powertrain Architectures: Applying Empirical Design Data to Life Cycle Assessment and Whole-life Cost Analysis. *J. of Applied Energy*, 119:314–329, 2014.

[147] V.H. Johnson, K.B. Wipke, and D.J. Rausen. HEV Control Strategy for Real-time Optimization of Fuel Economy and Emissions. SAE Paper 2000-01-1543, 2000.

[148] F.R. Salmasi. Control Strategies for Hybrid Electric Vehicles: Evolution, Classification, Comparison, and Future Trends. *IEEE Tranaction on Vehicular Technology*, 56(5):2393–2404, 2007.

[149] K. Çağatay Bayindir, M.A. Gözüküçük, and A. Teke. A Comprehensive Overview of Hybrid Electric Vehicle: Powertrain Configurations, Powertrain Control Techniques and Electronic Control Units. *J. of Energy Conversion and Management*, 52(2):1305–1313, 2011.

[150] A. Solouk, M. Shahbakhti, and M.J. Mahjoob. Energy Management and Control of a Hybrid Electric Vehicle With an Integrated Low Temperature Combustion (LTC) Engine. In *Proceedings of the ASME 2014 Dynamic Systems and Control Conference*, pages V002T20A005–V002T20A005. American Society of Mechanical Engineers, DSCC Paper 6286, 2014.

[151] A. Solouk and M. Shahbakhti. Modeling and Energy Management of an HCCI based Powertrain for Series Hybrid and Extended Range Electric Vehicles. *International Journal of Powertrains*, 29 pages, accepted in October 2015, 2015.

[152] M. Ehsani, Y. Gao, and A. Emadi. *Modern Electric, Hybrid Electric, and Fuel Cell Vehicles: Fundamentals, Theory, and Design.* CRC press, 2009.

[153] M. Ehsani, K.M. Rahman, and H.A. Toliyat. Propulsion System Design of Electric and Hybrid Vehicles. *IEEE Trans. on Ind. Elec.*, 44(1):19–27, 1997.

[154] D. Linden. *Handbook of Batteries*. McGraw-Hill, New York, 1995.

[155] D.P. Bertsekas. *Dynamic Programming and Optimal Control*. Athena Scientific, 1995.

[156] R.A.D.S Bellman. *Applied Dynamic Programming*. Princeton University Press, 1962.

[157] H. Borhan, A. Vahidi, A. Phillips, M. Kuang, and I. Kolmanovsky. Predictive Energy Management of a Power-split HEV. In *Proc. of ACC*, pages 3970–3976, 2009.

[158] K.B. Wipke, M.R. Cuddy, and S.D. Burch. ADVISOR 2.1: a User-friendly Advanced Powertrain Simulation Using a Combined Backward/forward Approach. *IEEE Transaction on Vehicular Technology*, 48(6):1751–1761, 1999.

[159] P. Pisu and G. Rizzoni. A Comparative Study of Supervisory Control Strategies for Hybrid Electric Vehicles. *IEEE Trans. on Control Sys. Tech.*, 15(3):506–518, 2007.

[160] A.M. Phillips, M. Jankovic, and K.E. Bailey. Vehicle System Controller Design for a Hybrid Electric Vehicle. In *Proc. of the 2000 IEEE Int. Conf. on Control Applications*, pages 297–302, 2000.

[161] T. Hofman, M. Steinbuch, R.M. van Druten, and A.F.A. Serrarens. Rule-based Equivalent Fuel Consumption Minimization Strategies for Hybrid Vehicles. In *Proc. of the 17th IFAC World Congress*, pages 5652–5657, 2008.

[162] X. Zeng, N. Yang, Y. Peng, Y. Zhang, and J. Wang. Research on Energy Saving Control Strategy of Parallel Hybrid Loader. *Journal of Automation in Construction*, 38:100–108, 2014.

[163] H.-D. Lee and S.-K. Sul. Fuzzy-logic-based Torque Control Strategy for Parallel-type Hybrid Electric Vehicle. *IEEE Transactions on Industrial Electronics*, 45(4):625–632, 1998.

[164] H.-D. Lee, E.-S. Koo, S.-K. Sul, J.-S. Kim, M. Kamiya, H. Ikeda, S. Shinohara, and H. Yoshida. Torque Control Strategy for a Parallel-hybrid Vehicle Using Fuzzy Logic.

[165] J.-S. Won and R. Langari. Intelligent Energy Management Agent for a Parallel Hybrid Vehicle- Part II: Torque Distribution, Charge Sustenance Strategies, and Performance Results. *IEEE Transaction on Vehicular Technology*, 54(3):935–953, 2005.

[166] A. Poursamad and M. Montazeri. Design of Genetic-fuzzy Control Strategy for Parallel Hybrid Electric Vehicles. *Journal of Control Engineering Practice*, 16(7):861–873, 2008.

[167] D. Kum, H. Peng, and N. Bucknor. Modeling and Control of Hybrid Electric

Vehicles for Fuel and Emission Reduction. In *Proceedings of the 2008 ASME Dynamic Systems and Control Conference*, DSCC paper 2008-2179, 2008.

[168] N.J. Schouten, M.A. Salman, and N.A. Kheir. Fuzzy Logic Control for Parallel Hybrid Vehicles. *IEEE Trans. on Control Sys. Tech.*, 10(3):460–468, 2002.

[169] C.-C. Lin, J.-M. Kang, J.W. Grizzle, and H. Peng. Energy Management Strategy for a Parallel Hybrid Electric Truck. In *Proc. of the 2001 ACC*, pages 2878–2883, 2001.

[170] S. Delprat, J. Lauber, T. Marie Guerra, and J. Rimaux. Control of a Parallel Hybrid Powertrain: Optimal Control. *IEEE Transaction on Vehicular Technology*, 53(3):872–881, 2004.

[171] K. Van Berkel, T. Hofman, B. Vroemen, and M. Steinbuch. Optimal Control of a Mechanical Hybrid Powertrain. *IEEE Transaction on Vehicular Technology*, 61(2):485–497, 2012.

[172] R. Biasini, S. Onori, and G. Rizzoni. A Near-optimal Rule-based Energy Management Strategy for Medium Duty Hybrid Truck. *Int. J. of Powertrains*, 2(2):232–261, 2013.

[173] M. Salman, M.-F. Chang, and J.-S. Chen. Predictive Energy Management Strategies for Hybrid Vehicles. In *Proceedings of the IEEE Vehicular Power and Propulsion Conference*, 2005.

[174] T.S. Kim, C. Manzie, and R. Sharma. Model Predictive Control of Velocity and Torque Split in a Parallel Hybrid Vehicle. In *Proc. of IEEE International Conference on Systems, Man and Cybernetics*, pages 2014–2019, 2009.

[175] X. Wei, P. Pisu, G. Rizzoni, and S. Yurkovich. Dynamic Modeling of a Hybrid Electric Drivetrain for Fuel Economy, Performance and Driveability Evaluations. In *Proceedings of the 2003 ASME International Mechanical Engineering Congress and Exposition*, pages 443–450, 2003.

[176] O. Barbarisi, E.R. Westervelt, F. Vasca, and G. Rizzoni. Power Management Decoupling Control for a Hybrid Electric Vehicle. In *Proceedings of 44th IEEE Conference on Decision and Control and 2005 European Control Conference*, pages 2012–2017, 2005.

[177] P. Pisu, K. Koprubasi, and G. Rizzoni. Energy Management and Drivability Control Problems for Hybrid Electric Vehicles. In *Proceedings of 44th IEEE Conference on Decision and Control and 2005 European Control Conference*, pages 1824–1830. IEEE, 2005.

[178] F. Yan, J. Wang, and K. Huang. Hybrid Electric Vehicle Model Predictive Control Torque-split Strategy Incorporating Engine Transient Characteristics. *IEEE Transaction on Vehicular Technology*, 61(6):2458–2467, 2012.

[179] B.K. Powell, K.E. Bailey, and S.R. Cikanek. Dynamic Modeling and Control

of Hybrid Electric Vehicle Powertrain Systems. *IEEE Transactions on Control Systems*, 18(5):17–33, 1998.

[180] S.A. Jazayeri, M.S. Rad, and S. Azadi. Development and Validation for Mean Value Engine Models. In *Proc. of the ASME 2005 ICEF Tech. Conf.*, pages 19–28, 2005.

[181] A. Sahraeian, M. Shahbakhti, A.R. Aslani, S.A. Jazayeri, S. Azadi, and A.H. Shamekhi. Longitudinal Vehicle Dynamics Modeling on the Basis of Engine Modeling. SAE paper No. 2004-01-1620, 2004.

[182] E. Hendricks and S.C. Sorenson. Mean Value Modelling of Spark Ignition Engines. SAE paper No. 900616, 1990.

[183] E. Hendricks, A. Chevalier, M. Jensen, S.C. Sorenson, D. Trumpy, and J. Asik. Modeling of the Intake Manifold Filling Dynamics. SAE paper No. 960037, 1996.

[184] M. Sharifirad, S.A. Jazayeri, and M. Shahbakhti. Automatic Driver Design and Longitudinal Dynamic Simulation for Passenger Cars. SAE paper No. 2006-01-1015, 2006.

[185] C.F. Aquino. Transient A/F Control Characteristics of the 5 Liter Central Fuel Injection Engine. SAE paper No. 810494, 1981.

[186] M. Shahbakhti, M. Ghafuri, A.R. Aslani, A. Sahraeian, S.A. Jazayeri, and

S. Azadi. A Method to Determine Fuel Transport Dynamics Model Parameters in Port Fuel Injected Gasoline Engines During Cold Start and Warm-up Conditions. *ASME Journal of Engineering for Gas Turbines and Power*, 132(7), 2010.

[187] A. Sciarretta and L. Guzzella. Control of Hybrid Electric Vehicles. *IEEE Control systems Magazine*, 27(2):60–70, 2007.

[188] A. Fotouhi, R. Yusof, R. Rahmani, S. Mekhilef, and N. Shateri. A Review on the Applications of Driving Data and Traffic Information for Vehicles Energy Conservation. *Ren. and Sust. Energy Rev.*, 37:822–833, 2014.

[189] S.K. Reghunath, D. Sharma, and A.S. Athreya. Optimal Gearshift Strategy using Predictive Algorithm for Fuel Economy Improvement. SAE paper 2014-01-1743, 2014.

Appendix A

Model Parameters

A.1 Chapter 2

A.1.1 Fuel Properties and Average Specific Heat Capacities and Gas Constants of In-cylinder Air-fuel Mixture

A.1.2 Constants of P_{ivc} and T_{ivc} Correlations (Eq. (2.1) and Eq. (2.2)

a= 0.027 b= 0.046 c= 0.005

Table A.1
Fuel and in-cylinder gas properties

Subscript	C_v [kJ/kg]	R [kJ/kgK]	LHV [kJ/kg]	ρ [kg/m^3]
iso	-	-	4.434 e+4	6.900 e+2
nH	-	-	4.456 e+4	6.820 e+2
nc	7.700 e-1	-	-	-
rg	8.180 e-1	-	-	-
ivc	-	2.860 e-1	-	-
soc	-	2.890 e-1	-	-
eoc	-	2.870 e-1	-	-
evc	-	2.893 e-1	-	-

Table A.2
Values of constants for T_{ivc} correlation

constant	PRF0	PRF10	PRF20	PRF40
a_1	-7.300 e-3	-1.700 e-3	-1.700 e-3	-7.000 e-4
a_2	1.482	4.073 e-1	5.533 e-1	3.470 e-1
a_3	1.103 e+2	1.012 e+2	1.134 e+2	1.123 e+2
b_1	-1.488 e-1	-4.310 e-2	-1.164 e-1	-5.100 e-3
b_2	-8.500 e-2	-1.620 e-2	-4.260 e-2	-1.750 e-2
b_3	9.200 e-3	2.400 e-3	2.000 e-4	1.200 e-3

A.1.3 Linear COM Matrices

$$A = \begin{bmatrix} 0.0063 & -0.0050 & 0.0019 & -0.0226 & -116.30 \\ -0.0025 & 0.0020 & -0.0007 & 0.0090 & 46.49 \\ -0.0273 & 0.0219 & -0.0083 & +0.0990 & 507.50 \\ +0.040 & -0.0320 & 0.0121 & -0.0411 & -743.10 \\ 0 & 0 & 0 & 0 & 0.0441 \end{bmatrix} \tag{A.1}$$

$$B = \begin{bmatrix} 0.3280 & -0.1311 & -1.4320 & 0.5830 & -0.00003 \end{bmatrix}^T$$

$$C = \begin{bmatrix} 1 & 0 & 0 & 0 & 0 \end{bmatrix}$$

A.1.4 CA50 Correlation

Constant coefficients of Eq. (2.12) are C_1= -0.67, C_2= 219.0, C_3= 0.328, C_4= 28.4. Here is a discussion on these constant coefficients: There is a direct relation between ON and the auto ignition phasing as an increase in ON leads to delay in combustion phasing [10, 41]. The positivity of C_3 conveys such a trend. On the other hand, based on the experimental results on the same studied engine in [45], there is an approximate linear relation between variations of CA50 and the inducted fuel mixture ON. The results in [45] show that the sensitivity of this linear relation is approximately constant at different operating conditions which justfies the constant value of C_3.

HCCI combustion has a compression ignition nature and an increase in T_{mix} leads to earlier combustion phasing and vice versa. Negative value of C_2 implies such a negative relation between variations of CA50 and T_{mix}. Simulation results of MKIM from the physical model show an approximate linear relation between CA50 and T_{mix} (Fig.A.1). Such an approximate linear relation is also been seen in other studies [41, 47]. Any increase in the amount of inducted fuel energy which can be implicated by

ϕ leads to an advance in combustion phasing [10, 41]. Value of $(C_1 T_{mix} + C_2)$ as the coefficient of ϕ is negative in the normal operating range of this engine, which justifies such a negative relation.

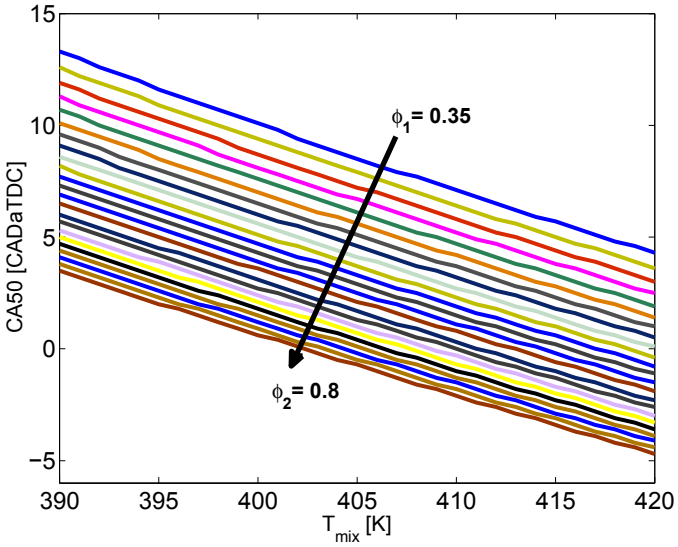

Figure A.1: MKIM simulation (ON= 5, N= 800 rpm).

A.2 Chapter 3

A.2.1 Linear COM Matrices

$$A = \begin{bmatrix} 0.0176 & -0.0044 & 0.0016 & -0.0216 & -99.75 \\ -0.0225 & 0.0056 & -0.0021 & 0.0276 & 127.50 \\ -0.2428 & 0.0607 & -0.0232 & 0.2987 & 1376 \\ 0.1235 & -0.0309 & 0.01182 & -0.0421 & -699.80 \\ 0 & 0 & 0 & 0 & 0.0436 \end{bmatrix} \tag{A.2}$$

$$B = \begin{bmatrix} 0.3280 & -0.4193 & -4.5240 & 0.6262 & 0 \end{bmatrix}^T$$

$$C = \begin{bmatrix} 1 & 0 & 0 & 0 & 0 \end{bmatrix}$$

A.3 Chapter 4

A.3.1 Linear COM Matrices

$$A = \begin{bmatrix} 4.1e-2 & -4.6e-3 & 1.6e-3 & -2.1e-2 & -9.2e+1 \\ -1.1e-1 & 1.3e-2 & -4.5e-3 & 6.0e-2 & 2.6e+2 \\ -1.4 & 1.5e-1 & -5.4e-2 & 7.2e-1 & 3.1e+3 \\ 2.9e-1 & -3.3e-2 & 1.1e-2 & -4.7e-2 & -6.6e+2 \\ -2.0e-5 & 2.3e-6 & -7.9e-7 & 3.3e-6 & 4.5e-2 \end{bmatrix} \tag{A.3}$$

$$B = \begin{bmatrix} 3.28e-1Z & -9.28e-1 & -1.10e+1 & 7.17e-1 & -4.92e-5 \end{bmatrix}^T$$

$$C = \begin{bmatrix} 1 & 0 & 0 & 0 & 0 \end{bmatrix}$$

A.4 Chapter 5

A.4.1 Linear COM Matrices

A.4.1.1 CA50 Linear Model

$$A_1 = \begin{bmatrix} 0.024 & -0.006 & 0.002 & -0.021 & -140.8 \\ -0.034 & 0.008 & -0.002 & 0.030 & 201.9 \\ -0.425 & 0.108 & -0.036 & 0.370 & 2484 \\ 0.140 & -0.035 & 0.012 & -0.044 & -818.6 \\ -7.6e^{-6} & 1.95e^{-6} & -6.55e^{-7} & -2.44e^{-6} & 0.0446 \end{bmatrix}$$

$$B_1 = \begin{bmatrix} 0.289 \\ -0.498 \\ -6.139 \\ 0.7289 \\ 3.9e^{-}5 \end{bmatrix}$$

$$C_1 = \begin{bmatrix} 1 & 0 & 0 & 0 & 0 \end{bmatrix}$$

A.4.1.2 T_{exh} Linear Model

$$A_2 = \begin{bmatrix} -0.044 & 0.140 & -0.035 & 0.012 & -818.6 \\ -0.021 & 0.024 & -0.006 & 0.002 & -140.8 \\ -0.030 & -0.034 & -0.008 & -0.002 & 201.9 \\ 0.370 & -0.425 & 0.108 & -0.0365 & 2484 \\ -2.44e^{-6} & -7.6e^{-6} & 1.95e^{-6} & -6.55e^{-7} & 0.0446 \end{bmatrix}$$

$$B_2 = \begin{bmatrix} -1.826 \\ -0.015 \\ -0.164 \\ 14.1 \\ 3.7e^{-}4 \end{bmatrix}$$

$$C_2 = \begin{bmatrix} 1 & 0 & 0 & 0 & 0 \end{bmatrix}$$

Appendix B

LTC Engine Instrumentation and Calibration in dSPACE

The engine instrumentation and calibration was done as a joint work with Mr. Kaushik Kannan, Mr. Jayant Kumar Arora, and Dr. Hamit Solmaz.

B.1 Port Fuel Injectors Calibration

Eight port fuel injectors on two common rails for iso-Octane and n-Heptane for four cylinders (4 injectors on each common rail) are wired as shown in Figure B.1. The pressure for port fuel injection is 3 bars and they are calibrated in dSPACE by using

the reference fuel flow rate data from a Micro Motion fuel flow meter as shown in Figure B.2. Figure B.3 shows the calibration results for the port fuel injectors for iso-Octane and n-Heptane. Gain and offset for the injectors are found by using the actuated pulse width (i.e., injection duration) in ms versus the measured fuel flow rate from the reference fuel flow meter. After calibrating the injectors for both

Figure B.1: Port fuel injectors installed and wired on the common rail.

PRFs, an algorithm is developed to calculate the injected fuel mass for each PRF when the values of the total fuel mass and the fuel mixture ON are given to the dSPACE controller. Given that the fuel ON is the volumetric ratio of iso-Octane to the total mixture of iso-Octane and n-Heptane:

$$ON = \frac{V_{iso}}{V_{iso} + V_{nH}} = \frac{\frac{m_{iso}}{\rho_{iso}}}{\frac{m_{iso}}{\rho_{iso}} + \frac{m_{nH}}{\rho_{nH}}} \tag{B.1}$$

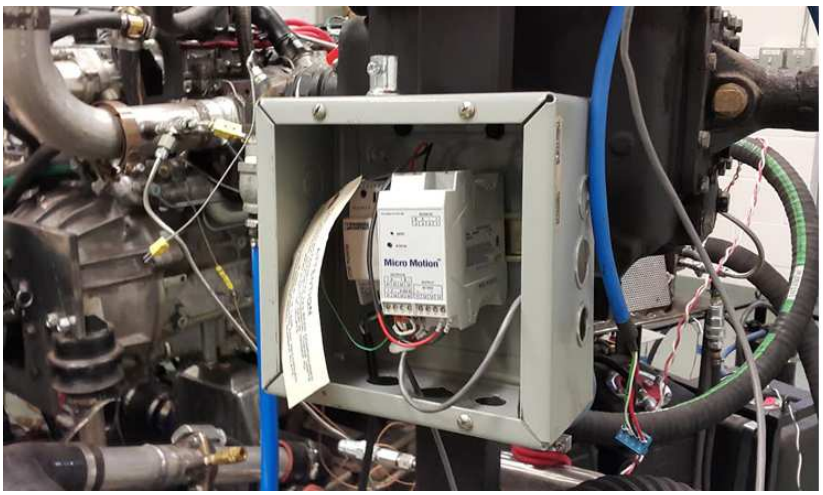

Figure B.2: Fuel flow meter used to calibrate the port fuel injectors.

where ρ_{iso} and ρ_{nH} are the densities of iso-Octane and n-Heptane, respectively. In addition, the given value of the total injected mass is:

$$m_t = m_{iso} + m_{nH} \tag{B.2}$$

From these two equations, the required injected mass for each PRF (m_{iso} and m_{nH}) are found and based on the port fuel injection calibration for each PRF, the suitable injection duration is actuated.

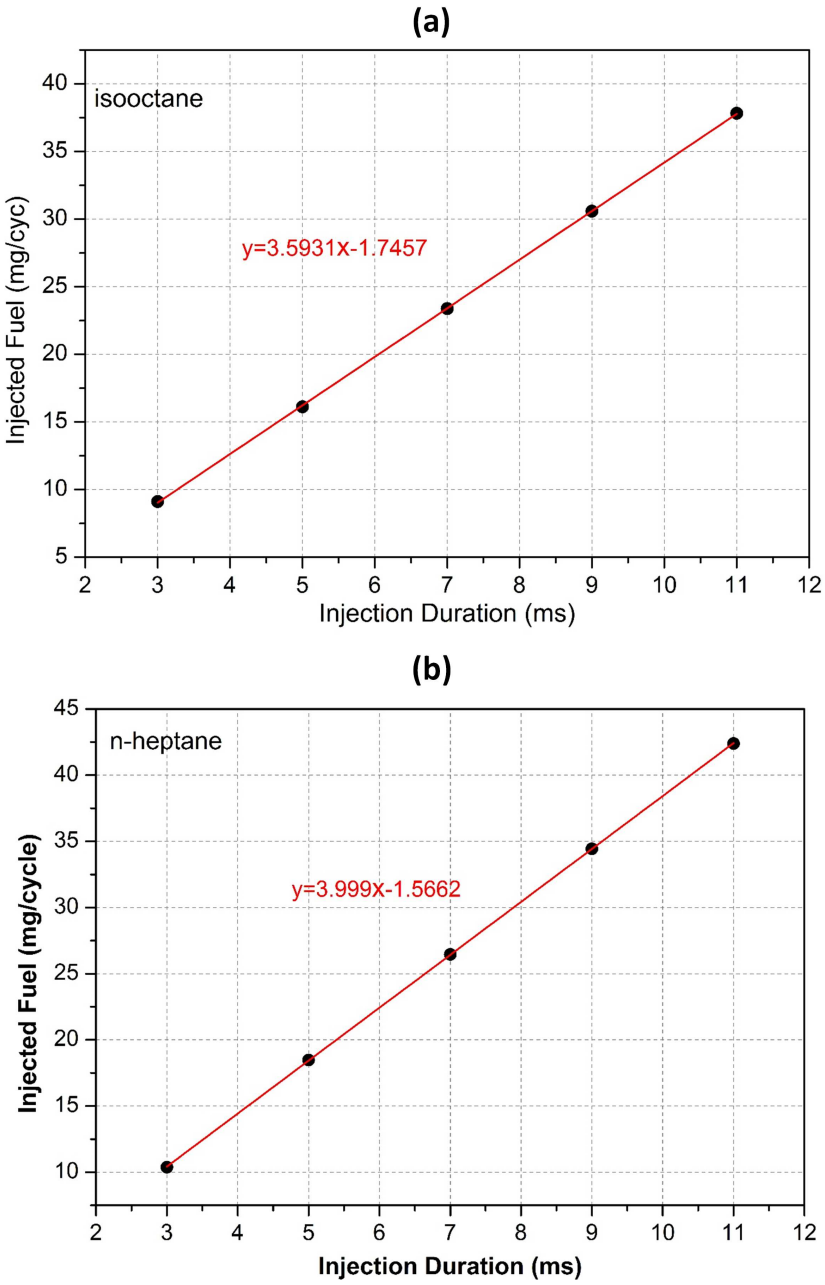

Figure B.3: PFI calibration results for (a) iso-Ocatne and (b) n-Heptane.

B.2 EGR Valve Installation, Calibration, and Filtering

The EGR valve is connected to the inlet air path through an EGR line as shown in Figure B.4. The EGR valve sensor (i.e., pintle position) is calibrated in dSPACE for two specific positions of 0% and 100% openings. Then, a PI controller is added in the dSPACE model and tuned to control the EGR valve position as shown in Figure B.5. A low pass filter is also added to attenuate the effects of noise on the measured pintle position signal. The tuned values of the PI controller gains are: k_p=0.5 and k_i=0.3. The performance of the EGR valve controller is tested for the desired EGR valve positions of 0-25-50-70-100 % as shown in Figure B.6. Results show a promising performance with the maximum overshoot, rise time, and steady-state error of 0 %, 0.12 sec, 3 sec, and 1 %, respectively.

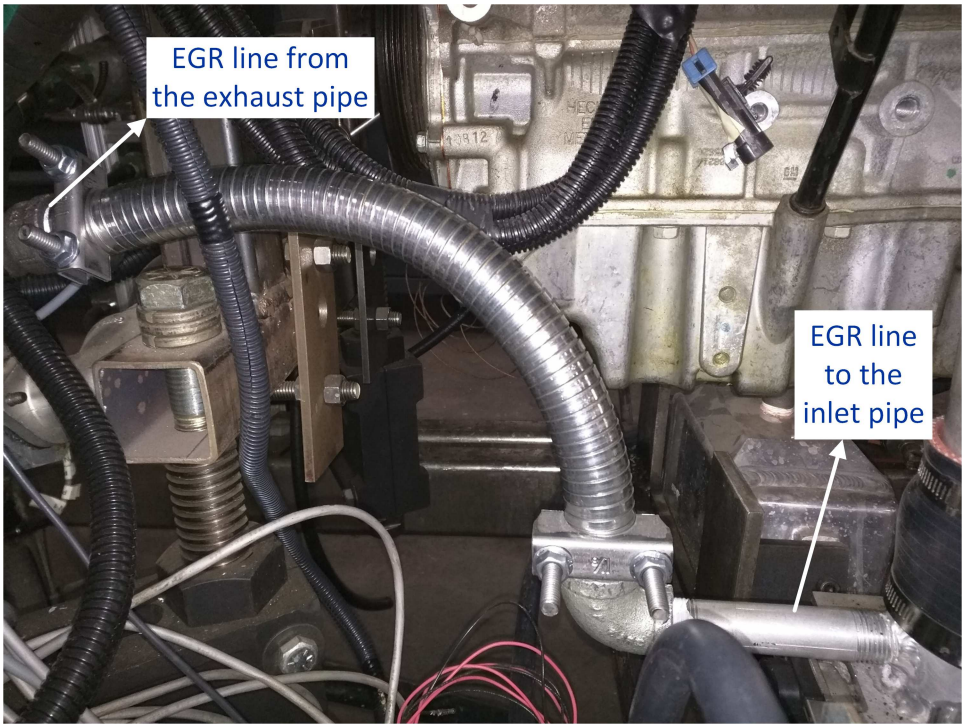

Figure B.4: EGR connecting line.

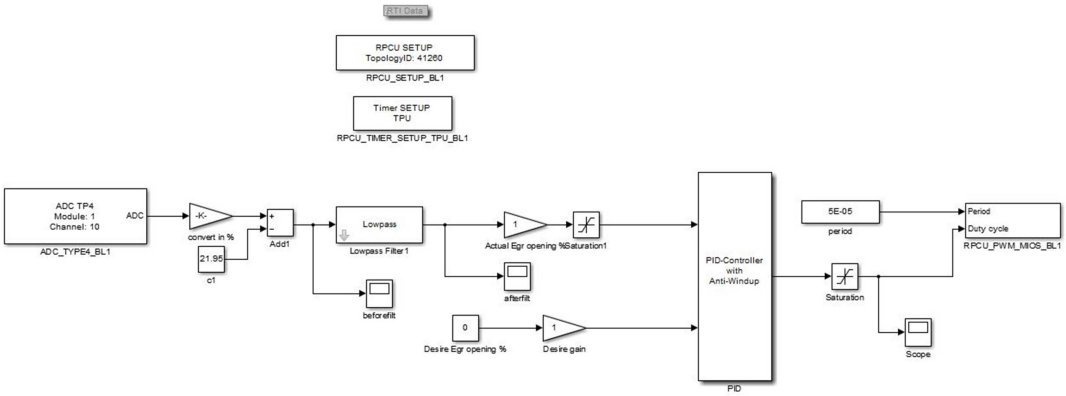

Figure B.5: EGR valve controller in dSPACE.

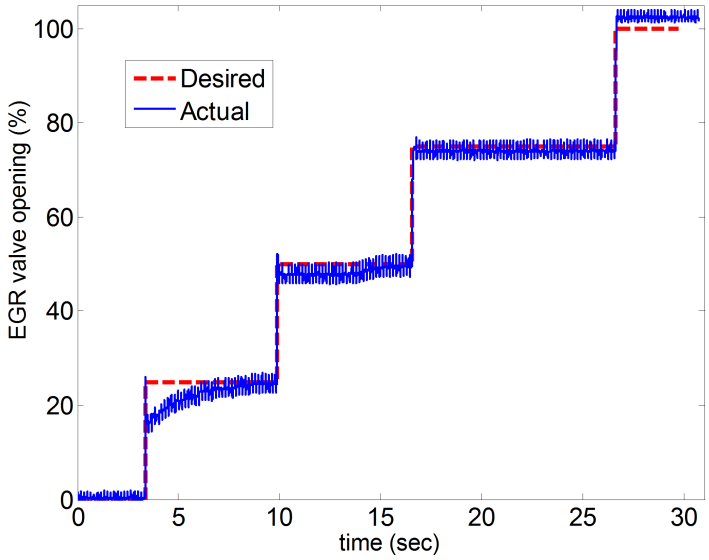

Figure B.6: Implementation results of the EGR valve controller.

Appendix C

PhD Publications

C.1 Peer Reviewed Journal Papers

C.1.1 Published Journal Papers

1. M. Bidarvatan, V. Thakkar, M. Shahbakhti, B. Bahri, A.A. Aziz, "Grey-box Modeling of HCCI Engines", Applied Thermal Engineering, Vol. 70, Issue 1, pages 397-409, Sept. 2014.

2. M. Bidarvatan, M. Shahbakhti, "Integrated HCCI Engine Control based on a Performance Index", ASME Journal of Engineering for Gas Turbines and Power, 12 pages, Vol. 136, Issue 10, Oct. 2014.

3. M. Bidarvatan, M. Shahbakhti, "Grey-Box Modeling for Performance Control of a HCCI Engine with Blended Fuels", ASME Journal of Engineering for Gas Turbines and Power, 10 pages, Vol. 136, Issue 10, Oct. 2014.

4. M. Bidarvatan, M. Shahbakhti, S.A. Jazayeri, C.R. Koch, "Cycle-to-Cycle Modeling and Sliding Mode Control of Blended-Fuel HCCI Engine", Journal of Control Engineering Practice, Vol. 24, Pages 7991, Mar. 2014.

C.1.2 Submitted Journal Papers

1. M. Bidarvatan and M. Shahbakhti, "Analysis and Control of Torque Split in Hybrid Electric Vehicles by Incorporating Powertrain Dynamics", 13 pages, Submitted to IEEE Transactions on Vehicular Technology, May 2015.

C.2 Refereed Conference Papers

C.2.1 Published Conference Papers

1. M. Bidarvatan, D. Kothari, M. Shahbakhti , "Analysis and Control of Torque Split in Hybrid Electric Vehicles by Incorporating Powertrain Dynamics", 2015

ASME Dynamic Systems and Control Conference, 10 pages, October 28-30, 2015, Columbus, Ohio, USA.

2. M. Bidarvatan and M. Shahbakhti, "Integrated Cycle-to-Cycle Control of Exhaust Gas Temperature, Load, and Combustion Phasing in an HCCI Engine", 6 pages, 2015 American Control Conference, Jul. 1-3, 2015, Chicago, IL, USA.

3. M. Bidarvatan and M. Shahbakhti, "Impact of Engine Dynamics on Torque Split Management of a Hybrid Electric Vehicle", ASME Dynamic Systems and Control Conference, 10 pages, Oct. 22-24, 2014, San Antonio, Texas, USA.

4. M. Bidarvatan, V. Thakkar, M. Shahbakhti, "Grey-box Modeling and Control of HCCI Engine Emissions", American Control Conference, 6 pages, Jun. 4-6, 2014, Portland, OR, USA.

5. M. Bidarvatan, M. Shahbakhti, "Integrated HCCI Engine Control based on a Performance Index", ASME Internal Combustion Engine Division Fall Technical Conference, Paper No. ICEF2013-19097, 11 pages, Oct. 13-16, 2013, Dearborn, Michigan, USA.

6. M. Bidarvatan, M. Shahbakhti, "Grey-Box Modeling for HCCI Engine Control", ASME Internal Combustion Engine Division Fall Technical Conference, Paper No. ICEF2013-19107, 10 pages, Oct. 13-16, 2013, Dearborn, Michigan, USA.

7. M. Bidarvatan, M. Shahbakhti, "Two-Input Two-Output Control of Blended Fuel HCCI Engines", Proceeding of SAE World Congress, SAE Paper No. 2013-01-1663, 15 pages, April 16-18, 2013, Detroit, USA.

C.2.2 Submitted Conference Papers

1. M. Razmara, M. Bidarvatan, M. Shahbakhti, R. Robinett, "Innovative Exergy-based Control of Combustion Phasing in ICEs", submitted to 2016 SAE World Congress, Detroit, MI.

2. M. Razmara, M. Bidarvatan, M. Shahbakhti, R. Robinett, "Novel Exergy-Wise Predictive Control of Internal Combustion Engines", Submitted to 2016 American Control Conference, Boston.

Appendix D

Program and Data File Summary

Following files were used for this thesis. Data is arranged in form of tables.

D.1 Chapter 1

Table D.1
Figure files.

File name	File description
LTCMap.png	Figure 1.1
HCCIControlGroups.vsd	Figure 1.3
HCCIControlBackground.vsd	Figure 1.4
ThesisOrganization.vsd	Figure 1.5

D.2 Chapter 2

Table D.2
Figure files.

File name	File description
HCCIBackground.vsd	Figure 2.1
physical_vs_NCOM_Conditions.fig	Figure 2.3
Verification.fig	Figure 2.4
Mean_Value_CA50.fig	Figure 2.5
DynamicValidCA50_Phi.fig	Figure 2.6
DynamicValidCA50_ON.fig	Figure 2.7
DynamicValidCA50_PhiON.fig	Figure 2.8
DynamicValidCA50_ON_LCOM.fig	Figure 2.9
controlstructure_CA50control.vsd	Figure 2.10
kp_over_Rise.fig	Figure 2.11
ki_over_Rise.fig	Figure 2.12
Tracking_NoDist_NoNoise.fig	Figure 2.13
Observer.fig	Figure 3.6
Tracking_Noisy.fig	Figure 2.15
CA50_robustness_to_phi.fig	Figure 2.16
CA50_robustness_to_Tman.fig	Figure 2.17
CA50_robustness_to_rpm.fig	Figure 2.18

Table D.3
Experimental data files.

File name	File description
57data_points.mat	Steady-state experimental data in Figure 2.5
ExpData_DynamicModeling.mat	Transient experimental data in Figures 2.6, 2.6, and 2.6

Table D.4
MATLAB script and Simulink files.

File name	File description
CA50DynamicModeling_Cyclic_LCOM.m	Script to call LCOM function and plotting
CA50DynamicModeling_VO_LCOM.m	LCOM
CA50DynamicModeling_Cyclic_NCOM.m	Script to call NCOM function and plotting
CA50DynamicModeling_VO_NCOM.m	NCOM
CA50DynamicModeling_Cyclic.m	Script to call physical model function and plotting
CA50DynamicModeling_VO.m	Physical model
Sliding_lqr_physicmodel.mdl	Control Simulink model

D.3 Chapter 3

Table D.5
Figure files.

File name	File description
Ch3_ControlBackground.vsd	Figure 3.1
different_trends.fig	Figure 3.2
CA50_IMEP_MV_Validation.fig	Figure 3.3
DynamicValidCA50IMEP_PhiChange.fig	Figure 3.4
DynamicValidCA50IMEP_ONChange.fig	Figure 3.5
DynamicValidCA50IMEP_PhiONChange.fig	Figure 3.6
Ch3_ControlStructure.vsd	Figure 3.7
Tracking_single.fig	Figure 3.8 (a)
Tracking_simultaneous.fig	Figure 3.8 (b)
Observer_single.fig	Figure 3.9 (a)
Observer_simultaneous.fig	Figure 3.9 (b)
DistRejec_Tman.fig	Figure 3.10
DistRejec_rpm.fig	Figure 3.11

Table D.6
Experimental data files.

File name	File description
57data_points.mat	Steady-state experimental data in Figure 3.3
ExpData_DynamicModeling.mat	Transient experimental data used in Figures 3.4, 3.5, and 3.6

Table D.7
MATLAB script and Simulink files.

File name	File description
CA50DynamicModeling_Cyclic.m	Script to call COM function and plotting
CA50DynamicModeling_VO.m	COM
observer.m	State observer function
sliding_lqr.m	Sliding mode controller function
sliding_lqr.mdl	Control Simulink model
physic_model.m	Physical plant model

D.4 Chapter 4

Table D.8
Figure files (Part 1).

File name	File description
Ch4_HCCIControlBackground.vsd	Figure 4.1
Ch4_Pm_Tm_Phi.fig	Figure 4.2
Ch4_AllOutputsDataRange.fig	Figure 4.3
Ch4_AllOutputsDataRange.fig	Figure 3.4
Ch4_Sensitivity.fig	Figure 4.4
Ch4_RawEmissions.fig	Figure 4.5
Ch4_AEIndex.fig	Figure 4.6
Ch4_PI.fig	Figure 4.7
OCP.vsd	Figure 4.8
Trajec_LowLoad.fig	Figure 4.9 (a)
Trajec_HighLoad.fig	Figure 4.9 (b)
Ch4_Trajec.fig	Figure 4.10
Ch4_ControlStructure.vsd	Figure 4.11
Ch4_Tracking.fig	Figure 4.12
BackgroundCh4Part2.vsd	Figure 4.13
Ch4_Pm_Tm_N_range_Ricardo.fig	Figure 4.14
CA50_IMEP_Texh_Ricardo.fig	Figure 4.15
EmissionsRange_Ricardo.fig	Figure 4.16
GB_structure.vsd	Figure 4.17
ANN.vsd	Figure 4.18

Table D.9
Figure files (Part 2).

File name	File description
error_vs_node.fig	Figure 4.19
error_vs_epoch.fig	Figure 4.20
error_vs_node.fig	Figure 4.19
CA50_Ricardo.fig	Figure 4.21
IMEP_Ricardo.fig	Figure 4.22
Texh_Ricardo.fig	Figure 4.23
CO_Ricardo.fig	Figure 4.24
THC_Ricardo.fig	Figure 4.25
NOx_Ricardo.fig	Figure 4.26
GBTransient.fig	Figure 4.27
Phi_Tm_N_Yanmar.fig	Figure 4.28
CA50_Yanmar.fig	Figure 4.29
IMEP_Yanmar.fig	Figure 4.29
Texh_Yanmar.fig	Figure 4.30
CO_Yanmar.fig	Figure 4.31
THC_Yanmar.fig	Figure 4.31
Schematic_CA50_IMEP.tif	Figure 4.32
Control_Trajectory.fig	Figure 4.33
Figure_CS_GBox.vsd	Figure 4.34
Control_Tracking.fig	Figure 4.35

Table D.10
Experimental data files.

File name	File description
all_with_limited_nox.mat	Steady-state experimental data used in Figures 4.2 4.14

Table D.11
MATLAB script and Simulink files.

File name	File description
ContourPlotting.m	Contour plotting code
observer.m	State observer function
controller_pi_statefeedback.mdl	Control Simulink model
physic_model.m	Physical plant model
FF.m	Feedforward controller
net.m	ANN model
data_ON0, data_ON20, data_ON40	Data file for ANN simulation

D.5 Chapter 5

Table D.12
Figure files.

File name	File description
Ch5_ControllerBackground.vsd	Figure 5.1
Road_MaP.vsd	Figure 5.2
CA50_correlation.fig	Figure 5.3
ExhaustPipediagram.vsdx	Figure 5.4
Ch5_SSValid.fig	Figure 5.5
COM_transient_validation.fig	Figure 5.6
ControllerStructure.vsd	Figure 5.7
SingleTracking.fig	Figure 5.8
SimultaneousTracking.fig	Figure 5.9

Table D.13
Experimental data files.

File name	File description
ProcessedExpData.mat	Steady-state experimental data used in Figure 5.5
ExpData DynamicModeling.mat	Transient experimental data used in Figure 5.6

Table D.14
MATLAB script and Simulink files.

File name	File description
CA50Modeling_MeanValue.m	Mean value engine model
CA50DynamicModeling_Cyclic.m	Script to call COM function and plotting
CA50DynamicModeling_VO.m	COM
observer.m	State observer function
observer_for_Trg.m	T_{exh} state observer function
sliding_lqr.m	Sliding mode controller function
sliding_for_Trg.m	T_{exh} sliding mode controller function
All_PID_controller.slx	PID Control Simulink model
DSSMC_controller.slx	SMC Simulink model
TexhFormulaA_3in_3out_model.m	Physical plant model

D.6 Chapter 6

Table D.15
Figure files.

File name	File description
EM_Op_Eff.fig	Figure 6.1
ICETestSetup.png	Figure 6.2
ExperimentalTestSetup.vsdx	Figure 6.3
HCCI_naturally_aspirated_T40.png	Figure 6.4
Si_map.png	Figure 6.5
DP.vsd	Figure 6.6
rT_Tew_Tmw_Ttw.fig	Figure 6.7
rT_Tew_Tmw_Ttw_Zoomin.fig	Figure 6.8
mf_Vel.fig	Figure 6.9
mfc_SOC.fig	Figure 6.10

Table D.16
Experimental data files.

File name	File description
HCCI_NA_Tm40.mat	Steady-state HCCI data in Figure 6.4
SI_map.mat	Steady-state SI data used in Figure 6.5
rpm_HCCImap_Tm40.mat	HCCI engine speed map
T_HCCImap_Tm40.mat	HCCI engine torque map
bsfc_HCCImap_Tm40.mat	HCCI engine bsfc map
rpm_SIImap_Tm40.mat	SI engine speed map
T_SImap_Tm40.mat	SI engine torque map
bsfc_SImap_Tm40.mat	SI engine bsfc map
UDDS_Cycle.mat	UDDS drive cycle

Table D.17
MATLAB script and Simulink files.

File name	File description
Controller.m	Optimal HEV controller
Plant_Model_Control.m	HEV plant model

D.7 Chapter 7

Table D.18
Figure files.

File name	File description
Ch7_Background.vsd	Figure 7.1
ICE_Model.vsd	Figure 7.2
ICE_valid_T_N_theta.fig	Figure 7.3
ICE_valid_mf_deltaTheta.fig	Figure 7.4
Airflow.fig	Figure 7.5
Fueldynamics.fig	Figure 7.6
Airflow_FuelFlow_Rotation.fig	Figure 7.7
VelocityChange.fig	Figure 7.8
Ch7_Control_Scheme.vsd	Figure 7.9
UDDS_flag_Tratio.fig	Figure 7.10
UDDS_complete.fig	Figure 7.11
UDDS_complete_zoomin.fig	Figure 7.12
UDDS_SOCmf.fig	Figure 7.13
dynctrl_ssctrl_UDDS.fig	Figure 7.14
dynctrl_ssctrl_UDDS_zoomin.fig	Figure 7.15 (a)
dynctrl_ssctrl_UDDS_zoomin_part2.fig	Figure 7.15 (b)
dynctrl_ssctrl_UDDS_Ee_Eb.fig	Figure 7.16

Table D.19
Experimental data files.

File name	File description
look1.mat	ICE data file for validation in Figures 7.3 and 7.4
rpm_engine_map.mat	ICE speed map
torque_engine_map.mat	ICE torque map
bsfc_engine_map.mat	ICE bsfc map
UDDS_Cycle.mat	UDDS drive cycle
ENG.mat	ICE data file for Simulink run

Table D.20
MATLAB script and Simulink files.

File name	File description
Controller.m	Optimal HEV controller
Plant_Model.m	HEV plant model

D.8 Appendix B

Table D.21
Figure files.

File name	File description
PFICommonRails.png	Figure B.1
FuelFlowMeter.png	Figure B.2
PFICalibration.png	Figure B.3
EGRConnection.png	Figure B.4
EGRController.vsdx	Figure B.5
EGRResult.png	Figure B.6

Table D.22
Experimental data files.

File name	File description
mgpercycle.xlsx	Experimental data for the calibration of the port fuel injectors

Appendix E

Letters of Permission

E.1 Letter of Permission for [1] (Chapter 2 and Figure 2.2)

ELSEVIER LICENSE
TERMS AND CONDITIONS

Nov 19, 2015

This is a License Agreement between Mehran Bidarvatan ("You") and Elsevier ("Elsevier") provided by Copyright Clearance Center ("CCC"). The license consists of your order details, the terms and conditions provided by Elsevier, and the payment terms and conditions.

All payments must be made in full to CCC. For payment instructions, please see information listed at the bottom of this form.

Supplier	Elsevier Limited The Boulevard,Langford Lane Kidlington,Oxford,OX5 1GB,UK
Registered Company Number	1982084
Customer name	Mehran Bidarvatan
Customer address	910 R.L. Smith Building HOUGHTON, MI 49931
License number	3752591036780
License date	Nov 19, 2015
Licensed content publisher	Elsevier
Licensed content publication	Control Engineering Practice
Licensed content title	Cycle-to-cycle modeling and sliding mode control of blended-fuel HCCI engine
Licensed content author	M. Bidarvatan,M. Shahbakhti,S.A. Jazayeri,C.R. Koch
Licensed content date	March 2014
Licensed content volume number	24
Licensed content issue number	n/a
Number of pages	13
Start Page	79
End Page	91
Type of Use	reuse in a thesis/dissertation
Portion	full article
Format	both print and electronic
Are you the author of this Elsevier article?	Yes
Will you be translating?	No
Title of your thesis/dissertation	PHYSICS-BASED MODELING AND CONTROL OF POWERTRAIN SYSTEMS INTEGRATED WITH LOW TEMPERATURE COMBUSTION ENGINES
Expected completion date	Dec 2015

Estimated size (number of pages)	310
Elsevier VAT number	GB 494 6272 12
Permissions price	0.00 USD
VAT/Local Sales Tax	0.00 USD / 0.00 GBP
Total	0.00 USD

Terms and Conditions

INTRODUCTION

1. The publisher for this copyrighted material is Elsevier. By clicking "accept" in connection with completing this licensing transaction, you agree that the following terms and conditions apply to this transaction (along with the Billing and Payment terms and conditions established by Copyright Clearance Center, Inc. ("CCC"), at the time that you opened your Rightslink account and that are available at any time at http://myaccount.copyright.com).

GENERAL TERMS

2. Elsevier hereby grants you permission to reproduce the aforementioned material subject to the terms and conditions indicated.

3. Acknowledgement: If any part of the material to be used (for example, figures) has appeared in our publication with credit or acknowledgement to another source, permission must also be sought from that source. If such permission is not obtained then that material may not be included in your publication/copies. Suitable acknowledgement to the source must be made, either as a footnote or in a reference list at the end of your publication, as follows:
"Reprinted from Publication title, Vol /edition number, Author(s), Title of article / title of chapter, Pages No., Copyright (Year), with permission from Elsevier [OR APPLICABLE SOCIETY COPYRIGHT OWNER]." Also Lancet special credit - "Reprinted from The Lancet, Vol. number, Author(s), Title of article, Pages No., Copyright (Year), with permission from Elsevier."

4. Reproduction of this material is confined to the purpose and/or media for which permission is hereby given.

5. Altering/Modifying Material: Not Permitted. However figures and illustrations may be altered/adapted minimally to serve your work. Any other abbreviations, additions, deletions and/or any other alterations shall be made only with prior written authorization of Elsevier Ltd. (Please contact Elsevier at permissions@elsevier.com)

6. If the permission fee for the requested use of our material is waived in this instance, please be advised that your future requests for Elsevier materials may attract a fee.

7. Reservation of Rights: Publisher reserves all rights not specifically granted in the combination of (i) the license details provided by you and accepted in the course of this licensing transaction, (ii) these terms and conditions and (iii) CCC's Billing and Payment terms and conditions.

8. License Contingent Upon Payment: While you may exercise the rights licensed immediately upon issuance of the license at the end of the licensing process for the transaction, provided that you have disclosed complete and accurate details of your proposed use, no license is finally effective unless and until full payment is received from you (either by publisher or by CCC) as provided in CCC's Billing and Payment terms and conditions. If full payment is not received on a timely basis, then any license preliminarily granted shall be deemed automatically revoked and shall be void as if never granted. Further, in the event that you breach any of these terms and conditions or any of CCC's Billing and Payment terms and conditions, the license is automatically revoked and shall be void as

if never granted. Use of materials as described in a revoked license, as well as any use of the materials beyond the scope of an unrevoked license, may constitute copyright infringement and publisher reserves the right to take any and all action to protect its copyright in the materials.
9. Warranties: Publisher makes no representations or warranties with respect to the licensed material.
10. Indemnity: You hereby indemnify and agree to hold harmless publisher and CCC, and their respective officers, directors, employees and agents, from and against any and all claims arising out of your use of the licensed material other than as specifically authorized pursuant to this license.
11. No Transfer of License: This license is personal to you and may not be sublicensed, assigned, or transferred by you to any other person without publisher's written permission.
12. No Amendment Except in Writing: This license may not be amended except in a writing signed by both parties (or, in the case of publisher, by CCC on publisher's behalf).
13. Objection to Contrary Terms: Publisher hereby objects to any terms contained in any purchase order, acknowledgment, check endorsement or other writing prepared by you, which terms are inconsistent with these terms and conditions or CCC's Billing and Payment terms and conditions. These terms and conditions, together with CCC's Billing and Payment terms and conditions (which are incorporated herein), comprise the entire agreement between you and publisher (and CCC) concerning this licensing transaction. In the event of any conflict between your obligations established by these terms and conditions and those established by CCC's Billing and Payment terms and conditions, these terms and conditions shall control.
14. Revocation: Elsevier or Copyright Clearance Center may deny the permissions described in this License at their sole discretion, for any reason or no reason, with a full refund payable to you. Notice of such denial will be made using the contact information provided by you. Failure to receive such notice will not alter or invalidate the denial. In no event will Elsevier or Copyright Clearance Center be responsible or liable for any costs, expenses or damage incurred by you as a result of a denial of your permission request, other than a refund of the amount(s) paid by you to Elsevier and/or Copyright Clearance Center for denied permissions.

LIMITED LICENSE

The following terms and conditions apply only to specific license types:
15. **Translation**: This permission is granted for non-exclusive world **English** rights only unless your license was granted for translation rights. If you licensed translation rights you may only translate this content into the languages you requested. A professional translator must perform all translations and reproduce the content word for word preserving the integrity of the article.
16. **Posting licensed content on any Website**: The following terms and conditions apply as follows: Licensing material from an Elsevier journal: All content posted to the web site must maintain the copyright information line on the bottom of each image; A hyper-text must be included to the Homepage of the journal from which you are licensing at http://www.sciencedirect.com/science/journal/xxxxx or the Elsevier homepage for books at http://www.elsevier.com; Central Storage: This license does not include permission for a scanned version of the material to be stored in a central repository such as that provided by Heron/XanEdu. Licensing material from an Elsevier book: A hyper-text link must be included to the Elsevier homepage at http://www.elsevier.com . All content posted to the web site must maintain the copyright information line on the bottom of each image.

Posting licensed content on Electronic reserve: In addition to the above the following clauses

are applicable: The web site must be password-protected and made available only to bona fide students registered on a relevant course. This permission is granted for 1 year only. You may obtain a new license for future website posting.

17. **For journal authors:** the following clauses are applicable in addition to the above:

Preprints:

A preprint is an author's own write-up of research results and analysis, it has not been peer-reviewed, nor has it had any other value added to it by a publisher (such as formatting, copyright, technical enhancement etc.).

Authors can share their preprints anywhere at any time. Preprints should not be added to or enhanced in any way in order to appear more like, or to substitute for, the final versions of articles however authors can update their preprints on arXiv or RePEc with their Accepted Author Manuscript (see below).

If accepted for publication, we encourage authors to link from the preprint to their formal publication via its DOI. Millions of researchers have access to the formal publications on ScienceDirect, and so links will help users to find, access, cite and use the best available version. Please note that Cell Press, The Lancet and some society-owned have different preprint policies. Information on these policies is available on the journal homepage.

Accepted Author Manuscripts: An accepted author manuscript is the manuscript of an article that has been accepted for publication and which typically includes author-incorporated changes suggested during submission, peer review and editor-author communications.

Authors can share their accepted author manuscript:

- immediately
  - via their non-commercial person homepage or blog
  - by updating a preprint in arXiv or RePEc with the accepted manuscript
  - via their research institute or institutional repository for internal institutional uses or as part of an invitation-only research collaboration work-group
  - directly by providing copies to their students or to research collaborators for their personal use
  - for private scholarly sharing as part of an invitation-only work group on commercial sites with which Elsevier has an agreement
- after the embargo period
  - via non-commercial hosting platforms such as their institutional repository
  - via commercial sites with which Elsevier has an agreement

In all cases accepted manuscripts should:

- link to the formal publication via its DOI
- bear a CC-BY-NC-ND license - this is easy to do
- if aggregated with other manuscripts, for example in a repository or other site, be shared in alignment with our hosting policy not be added to or enhanced in any way to appear more like, or to substitute for, the published journal article.

Published journal article (JPA): A published journal article (PJA) is the definitive final record of published research that appears or will appear in the journal and embodies all value-adding publishing activities including peer review co-ordination, copy-editing, formatting, (if relevant)

pagination and online enrichment.

Policies for sharing publishing journal articles differ for subscription and gold open access articles:

Subscription Articles: If you are an author, please share a link to your article rather than the full-text. Millions of researchers have access to the formal publications on ScienceDirect, and so links will help your users to find, access, cite, and use the best available version.

Theses and dissertations which contain embedded PJAs as part of the formal submission can be posted publicly by the awarding institution with DOI links back to the formal publications on ScienceDirect.

If you are affiliated with a library that subscribes to ScienceDirect you have additional private sharing rights for others' research accessed under that agreement. This includes use for classroom teaching and internal training at the institution (including use in course packs and courseware programs), and inclusion of the article for grant funding purposes.

Gold Open Access Articles: May be shared according to the author-selected end-user license and should contain a CrossMark logo, the end user license, and a DOI link to the formal publication on ScienceDirect.

Please refer to Elsevier's posting policy for further information.

18. **For book authors** the following clauses are applicable in addition to the above: Authors are permitted to place a brief summary of their work online only. You are not allowed to download and post the published electronic version of your chapter, nor may you scan the printed edition to create an electronic version. **Posting to a repository:** Authors are permitted to post a summary of their chapter only in their institution's repository.

19. **Thesis/Dissertation**: If your license is for use in a thesis/dissertation your thesis may be submitted to your institution in either print or electronic form. Should your thesis be published commercially, please reapply for permission. These requirements include permission for the Library and Archives of Canada to supply single copies, on demand, of the complete thesis and include permission for Proquest/UMI to supply single copies, on demand, of the complete thesis. Should your thesis be published commercially, please reapply for permission. Theses and dissertations which contain embedded PJAs as part of the formal submission can be posted publicly by the awarding institution with DOI links back to the formal publications on ScienceDirect.

Elsevier Open Access Terms and Conditions

You can publish open access with Elsevier in hundreds of open access journals or in nearly 2000 established subscription journals that support open access publishing. Permitted third party re-use of these open access articles is defined by the author's choice of Creative Commons user license. See our open access license policy for more information.

Terms & Conditions applicable to all Open Access articles published with Elsevier:

Any reuse of the article must not represent the author as endorsing the adaptation of the article nor should the article be modified in such a way as to damage the author's honour or reputation. If any changes have been made, such changes must be clearly indicated.

The author(s) must be appropriately credited and we ask that you include the end user license and a DOI link to the formal publication on ScienceDirect.

If any part of the material to be used (for example, figures) has appeared in our publication with credit or acknowledgement to another source it is the responsibility of the user to ensure their reuse complies with the terms and conditions determined by the rights holder.

Additional Terms & Conditions applicable to each Creative Commons user license:

E.2 Letter of Permission for [2] (Chapter 3)

Mehran Bidarvatan <mbidarva@mtu.edu>

Permission Request for SAE Paper 2013-01-1663

Monica Nogueira <Monica.Nogueira@sae.org> Tue, Dec 1, 2015 at 6:03 PM
To: Mehran Bidarvatan <mbidarva@mtu.edu>
Cc: Rhonda Buzard <Rhonda.Buzard@sae.org>

Dear Mehran Bidarvatan:

The permission to use the SAE Technical Paper 2013-01-1663 is hereby granted for the specific use indicated in your email.

Please note that permission is also subject to the following terms and conditions:

--Permission is granted for non-exclusive English language rights, and for the specific title indicated in your email (academic dissertation)

--Permission is required for new requests, or further use of the material.

--The SAE material must be clearly identified and include the following statement “Reprinted with permission from SAE International.”

--We also request that you include a complete reference to the SAE document in the reference section of your report.

--This permission does not cover any third party copyrighted work which may appear in the material requested.

--Licensor’s use of this material, in whole or in part, is entirely its responsibility, and SAE International does not warrant or is not responsible for any use of the material.

Kind regards,

Monica

Monica Nogueira

Content Acquisition Manager

Multimedia

SAE INTERNATIONAL

400 Commonwealth Drive

Warrendale, PA 15096

o +1.724.772.7525

m +1.412.996.5809

e Nogueira@sae.org

www.sae.org

From: Mehran Bidarvatan [mailto:mbidarva@mtu.edu]
Sent: Thursday, November 19, 2015 1:51 PM
To: copyright
Subject: Permission Request for SAE Paper 2013-01-1663

[Quoted text hidden]

E.3 Letters of Permission for [3, 4, 5] (Chapter 4)

MichiganTech

Mehran Bidarvatan <mbidarva@mtu.edu>

Permission Request for ASME Paper GTP-14-1101

Beth Darchi <DarchiB@asme.org> Wed, Nov 25, 2015 at 10:07 AM
To: Mehran Bidarvatan <mbidarva@mtu.edu>

Dear Prof. Bidarvatan,

It is our pleasure to grant you permission **to use all or any part of** the following ASME materials:

- Gray-Box Modeling for Performance Control of an HCCI Engine With Blended Fuels, by M. Bidarvatan; M. Shahbakhti, J. Eng. Gas Turbines Power. 2014; 136(10)
- Integrated HCCI Engine Control Based on a Performance Index, by M. Bidarvatan; M. Shahbakhti, J. Eng. Gas Turbines Power. 2014; 136(10)
- Impact of Engine Dynamics on Torque Split Management of a Hybrid Electric Vehicle, by Mehran Bidarvatan; Mahdi Shahbakhti, Paper number DSCC2014-6283

cited in your letter for inclusion in a PhD dissertation entitled Physics-based Modeling and Control of Powertrain Systems Integrated with Low Temperature Combustion Engines to be published by Michigan Technological University.

Permission is granted for the specific use as stated herein and does not permit further use of the materials without proper authorization. Proper attribution must be made to the author(s) of the materials. **Please note**: if any or all of the figures and/or Tables are of another source, permission should be granted from that outside source or include the reference of the original source. ASME does not grant permission for outside source material that may be referenced in the ASME works.

As is customary, we request that you ensure full acknowledgment of this material, the author(s), source and ASME as original publisher. Acknowledgment must be retained on all pages printed and distributed.

Many thanks for your interest in ASME publications.

Sincerely,

ASME SETTING THE STANDARD

Beth Darchi
Publishing Administrator
ASME
2 Park Avenue, 6th Floor

ELSEVIER LICENSE
TERMS AND CONDITIONS

Nov 19, 2015

This is a License Agreement between Mehran Bidarvatan ("You") and Elsevier ("Elsevier") provided by Copyright Clearance Center ("CCC"). The license consists of your order details, the terms and conditions provided by Elsevier, and the payment terms and conditions.

All payments must be made in full to CCC. For payment instructions, please see information listed at the bottom of this form.

Supplier	Elsevier Limited The Boulevard,Langford Lane Kidlington,Oxford,OX5 1GB,UK
Registered Company Number	1982084
Customer name	Mehran Bidarvatan
Customer address	910 R.L. Smith Building HOUGHTON, MI 49931
License number	3752591395879
License date	Nov 19, 2015
Licensed content publisher	Elsevier
Licensed content publication	Applied Thermal Engineering
Licensed content title	Grey-box modeling of HCCI engines
Licensed content author	M. Bidarvatan,V. Thakkar,M. Shahbakhti,B. Bahri,A. Abdul Aziz
Licensed content date	5 September 2014
Licensed content volume number	70
Licensed content issue number	1
Number of pages	13
Start Page	397
End Page	409
Type of Use	reuse in a thesis/dissertation
Intended publisher of new work	other
Portion	full article
Format	both print and electronic
Are you the author of this Elsevier article?	Yes
Will you be translating?	No
Title of your thesis/dissertation	PHYSICS-BASED MODELING AND CONTROL OF POWERTRAIN SYSTEMS INTEGRATED WITH LOW TEMPERATURE COMBUSTION ENGINES

Expected completion date	Dec 2015
Estimated size (number of pages)	310
Elsevier VAT number	GB 494 6272 12
Permissions price	0.00 USD
VAT/Local Sales Tax	0.00 USD / 0.00 GBP
Total	0.00 USD
Terms and Conditions	

INTRODUCTION

1. The publisher for this copyrighted material is Elsevier. By clicking "accept" in connection with completing this licensing transaction, you agree that the following terms and conditions apply to this transaction (along with the Billing and Payment terms and conditions established by Copyright Clearance Center, Inc. ("CCC"), at the time that you opened your Rightslink account and that are available at any time at http://myaccount.copyright.com).

GENERAL TERMS

2. Elsevier hereby grants you permission to reproduce the aforementioned material subject to the terms and conditions indicated.

3. Acknowledgement: If any part of the material to be used (for example, figures) has appeared in our publication with credit or acknowledgement to another source, permission must also be sought from that source. If such permission is not obtained then that material may not be included in your publication/copies. Suitable acknowledgement to the source must be made, either as a footnote or in a reference list at the end of your publication, as follows:
"Reprinted from Publication title, Vol /edition number, Author(s), Title of article / title of chapter, Pages No., Copyright (Year), with permission from Elsevier [OR APPLICABLE SOCIETY COPYRIGHT OWNER]." Also Lancet special credit - "Reprinted from The Lancet, Vol. number, Author(s), Title of article, Pages No., Copyright (Year), with permission from Elsevier."

4. Reproduction of this material is confined to the purpose and/or media for which permission is hereby given.

5. Altering/Modifying Material: Not Permitted. However figures and illustrations may be altered/adapted minimally to serve your work. Any other abbreviations, additions, deletions and/or any other alterations shall be made only with prior written authorization of Elsevier Ltd. (Please contact Elsevier at permissions@elsevier.com)

6. If the permission fee for the requested use of our material is waived in this instance, please be advised that your future requests for Elsevier materials may attract a fee.

7. Reservation of Rights: Publisher reserves all rights not specifically granted in the combination of (i) the license details provided by you and accepted in the course of this licensing transaction, (ii) these terms and conditions and (iii) CCC's Billing and Payment terms and conditions.

8. License Contingent Upon Payment: While you may exercise the rights licensed immediately upon issuance of the license at the end of the licensing process for the transaction, provided that you have disclosed complete and accurate details of your proposed use, no license is finally effective unless and until full payment is received from you (either by publisher or by CCC) as provided in CCC's Billing and Payment terms and conditions. If full payment is not received on a timely basis, then any license preliminarily granted shall be deemed automatically revoked and shall be void as if never granted. Further, in the event that you breach any of these terms and conditions or any of CCC's

Billing and Payment terms and conditions, the license is automatically revoked and shall be void as if never granted. Use of materials as described in a revoked license, as well as any use of the materials beyond the scope of an unrevoked license, may constitute copyright infringement and publisher reserves the right to take any and all action to protect its copyright in the materials.

9. Warranties: Publisher makes no representations or warranties with respect to the licensed material.

10. Indemnity: You hereby indemnify and agree to hold harmless publisher and CCC, and their respective officers, directors, employees and agents, from and against any and all claims arising out of your use of the licensed material other than as specifically authorized pursuant to this license.

11. No Transfer of License: This license is personal to you and may not be sublicensed, assigned, or transferred by you to any other person without publisher's written permission.

12. No Amendment Except in Writing: This license may not be amended except in a writing signed by both parties (or, in the case of publisher, by CCC on publisher's behalf).

13. Objection to Contrary Terms: Publisher hereby objects to any terms contained in any purchase order, acknowledgment, check endorsement or other writing prepared by you, which terms are inconsistent with these terms and conditions or CCC's Billing and Payment terms and conditions. These terms and conditions, together with CCC's Billing and Payment terms and conditions (which are incorporated herein), comprise the entire agreement between you and publisher (and CCC) concerning this licensing transaction. In the event of any conflict between your obligations established by these terms and conditions and those established by CCC's Billing and Payment terms and conditions, these terms and conditions shall control.

14. Revocation: Elsevier or Copyright Clearance Center may deny the permissions described in this License at their sole discretion, for any reason or no reason, with a full refund payable to you. Notice of such denial will be made using the contact information provided by you. Failure to receive such notice will not alter or invalidate the denial. In no event will Elsevier or Copyright Clearance Center be responsible or liable for any costs, expenses or damage incurred by you as a result of a denial of your permission request, other than a refund of the amount(s) paid by you to Elsevier and/or Copyright Clearance Center for denied permissions.

LIMITED LICENSE

The following terms and conditions apply only to specific license types:

15. **Translation**: This permission is granted for non-exclusive world **English** rights only unless your license was granted for translation rights. If you licensed translation rights you may only translate this content into the languages you requested. A professional translator must perform all translations and reproduce the content word for word preserving the integrity of the article.

16. **Posting licensed content on any Website**: The following terms and conditions apply as follows: Licensing material from an Elsevier journal: All content posted to the web site must maintain the copyright information line on the bottom of each image; A hyper-text must be included to the Homepage of the journal from which you are licensing at http://www.sciencedirect.com/science/journal/xxxxx or the Elsevier homepage for books at http://www.elsevier.com; Central Storage: This license does not include permission for a scanned version of the material to be stored in a central repository such as that provided by Heron/XanEdu. Licensing material from an Elsevier book: A hyper-text link must be included to the Elsevier homepage at http://www.elsevier.com . All content posted to the web site must maintain the copyright information line on the bottom of each image.

Posting licensed content on Electronic reserve: In addition to the above the following clauses are applicable: The web site must be password-protected and made available only to bona fide students registered on a relevant course. This permission is granted for 1 year only. You may obtain a new license for future website posting.

17. **For journal authors:** the following clauses are applicable in addition to the above:

Preprints:

A preprint is an author's own write-up of research results and analysis, it has not been peer-reviewed, nor has it had any other value added to it by a publisher (such as formatting, copyright, technical enhancement etc.).

Authors can share their preprints anywhere at any time. Preprints should not be added to or enhanced in any way in order to appear more like, or to substitute for, the final versions of articles however authors can update their preprints on arXiv or RePEc with their Accepted Author Manuscript (see below).

If accepted for publication, we encourage authors to link from the preprint to their formal publication via its DOI. Millions of researchers have access to the formal publications on ScienceDirect, and so links will help users to find, access, cite and use the best available version. Please note that Cell Press, The Lancet and some society-owned have different preprint policies. Information on these policies is available on the journal homepage.

Accepted Author Manuscripts: An accepted author manuscript is the manuscript of an article that has been accepted for publication and which typically includes author-incorporated changes suggested during submission, peer review and editor-author communications.

Authors can share their accepted author manuscript:

- immediately
  - via their non-commercial person homepage or blog
  - by updating a preprint in arXiv or RePEc with the accepted manuscript
  - via their research institute or institutional repository for internal institutional uses or as part of an invitation-only research collaboration work-group
  - directly by providing copies to their students or to research collaborators for their personal use
  - for private scholarly sharing as part of an invitation-only work group on commercial sites with which Elsevier has an agreement
- after the embargo period
  - via non-commercial hosting platforms such as their institutional repository
  - via commercial sites with which Elsevier has an agreement

In all cases accepted manuscripts should:

- link to the formal publication via its DOI
- bear a CC-BY-NC-ND license - this is easy to do
- if aggregated with other manuscripts, for example in a repository or other site, be shared in alignment with our hosting policy not be added to or enhanced in any way to appear more like, or to substitute for, the published journal article.

Published journal article (JPA): A published journal article (PJA) is the definitive final record of published research that appears or will appear in the journal and embodies all value-adding

publishing activities including peer review co-ordination, copy-editing, formatting, (if relevant) pagination and online enrichment.

Policies for sharing publishing journal articles differ for subscription and gold open access articles:

Subscription Articles: If you are an author, please share a link to your article rather than the full-text. Millions of researchers have access to the formal publications on ScienceDirect, and so links will help your users to find, access, cite, and use the best available version.

Theses and dissertations which contain embedded PJAs as part of the formal submission can be posted publicly by the awarding institution with DOI links back to the formal publications on ScienceDirect.

If you are affiliated with a library that subscribes to ScienceDirect you have additional private sharing rights for others' research accessed under that agreement. This includes use for classroom teaching and internal training at the institution (including use in course packs and courseware programs), and inclusion of the article for grant funding purposes.

Gold Open Access Articles: May be shared according to the author-selected end-user license and should contain a CrossMark logo, the end user license, and a DOI link to the formal publication on ScienceDirect.

Please refer to Elsevier's posting policy for further information.

18. **For book authors** the following clauses are applicable in addition to the above: Authors are permitted to place a brief summary of their work online only. You are not allowed to download and post the published electronic version of your chapter, nor may you scan the printed edition to create an electronic version. **Posting to a repository:** Authors are permitted to post a summary of their chapter only in their institution's repository.

19. **Thesis/Dissertation**: If your license is for use in a thesis/dissertation your thesis may be submitted to your institution in either print or electronic form. Should your thesis be published commercially, please reapply for permission. These requirements include permission for the Library and Archives of Canada to supply single copies, on demand, of the complete thesis and include permission for Proquest/UMI to supply single copies, on demand, of the complete thesis. Should your thesis be published commercially, please reapply for permission. Theses and dissertations which contain embedded PJAs as part of the formal submission can be posted publicly by the awarding institution with DOI links back to the formal publications on ScienceDirect.

Elsevier Open Access Terms and Conditions

You can publish open access with Elsevier in hundreds of open access journals or in nearly 2000 established subscription journals that support open access publishing. Permitted third party re-use of these open access articles is defined by the author's choice of Creative Commons user license. See our open access license policy for more information.

Terms & Conditions applicable to all Open Access articles published with Elsevier:

Any reuse of the article must not represent the author as endorsing the adaptation of the article nor should the article be modified in such a way as to damage the author's honour or reputation. If any changes have been made, such changes must be clearly indicated.

The author(s) must be appropriately credited and we ask that you include the end user license and a DOI link to the formal publication on ScienceDirect.

If any part of the material to be used (for example, figures) has appeared in our publication with credit or acknowledgement to another source it is the responsibility of the user to ensure their reuse complies with the terms and conditions determined by the rights holder.

Additional Terms & Conditions applicable to each Creative Commons user license:

CC BY: The CC-BY license allows users to copy, to create extracts, abstracts and new works from the Article, to alter and revise the Article and to make commercial use of the Article (including reuse and/or resale of the Article by commercial entities), provided the user gives appropriate credit (with a link to the formal publication through the relevant DOI), provides a link to the license, indicates if changes were made and the licensor is not represented as endorsing the use made of the work. The full details of the license are available at http://creativecommons.org/licenses/by/4.0.

CC BY NC SA: The CC BY-NC-SA license allows users to copy, to create extracts, abstracts and new works from the Article, to alter and revise the Article, provided this is not done for commercial purposes, and that the user gives appropriate credit (with a link to the formal publication through the relevant DOI), provides a link to the license, indicates if changes were made and the licensor is not represented as endorsing the use made of the work. Further, any new works must be made available on the same conditions. The full details of the license are available at http://creativecommons.org/licenses/by-nc-sa/4.0.

CC BY NC ND: The CC BY-NC-ND license allows users to copy and distribute the Article, provided this is not done for commercial purposes and further does not permit distribution of the Article if it is changed or edited in any way, and provided the user gives appropriate credit (with a link to the formal publication through the relevant DOI), provides a link to the license, and that the licensor is not represented as endorsing the use made of the work. The full details of the license are available at http://creativecommons.org/licenses/by-nc-nd/4.0. Any commercial reuse of Open Access articles published with a CC BY NC SA or CC BY NC ND license requires permission from Elsevier and will be subject to a fee.

Commercial reuse includes:

- Associating advertising with the full text of the Article
- Charging fees for document delivery or access
- Article aggregation
- Systematic distribution via e-mail lists or share buttons

Posting or linking by commercial companies for use by customers of those companies.

20. **Other Conditions**:

v1.8

Questions? customercare@copyright.com or +1-855-239-3415 (toll free in the US) or +1-978-646-2777.

E.4 Letter of Permission for [6] (Chapter 5)

E.5 Letter of Permission for [7] (Chapters 6 and 7)

Michigan Tech

Mehran Bidarvatan <mbidarva@mtu.edu>

Permission Request for ASME Paper GTP-14-1101

Beth Darchi <DarchiB@asme.org> Wed, Nov 25, 2015 at 10:07 AM
To: Mehran Bidarvatan <mbidarva@mtu.edu>

Dear Prof. Bidarvatan,

It is our pleasure to grant you permission **to use all or any part of** the following ASME materials:

- Gray-Box Modeling for Performance Control of an HCCI Engine With Blended Fuels, by M. Bidarvatan; M. Shahbakhti, J. Eng. Gas Turbines Power. 2014; 136(10)
- Integrated HCCI Engine Control Based on a Performance Index, by M. Bidarvatan; M. Shahbakhti, J. Eng. Gas Turbines Power. 2014; 136(10)
- Impact of Engine Dynamics on Torque Split Management of a Hybrid Electric Vehicle, by Mehran Bidarvatan; Mahdi Shahbakhti, Paper number DSCC2014-6283

cited in your letter for inclusion in a PhD dissertation entitled Physics-based Modeling and Control of Powertrain Systems Integrated with Low Temperature Combustion Engines to be published by Michigan Technological University.

Permission is granted for the specific use as stated herein and does not permit further use of the materials without proper authorization. Proper attribution must be made to the author(s) of the materials. **Please note**: if any or all of the figures and/or Tables are of another source, permission should be granted from that outside source or include the reference of the original source. ASME does not grant permission for outside source material that may be referenced in the ASME works.

As is customary, we request that you ensure full acknowledgment of this material, the author(s), source and ASME as original publisher. Acknowledgment must be retained on all pages printed and distributed.

Many thanks for your interest in ASME publications.

Sincerely,

ASME SETTING THE STANDARD

Beth Darchi
Publishing Administrator
ASME
2 Park Avenue, 6th Floor